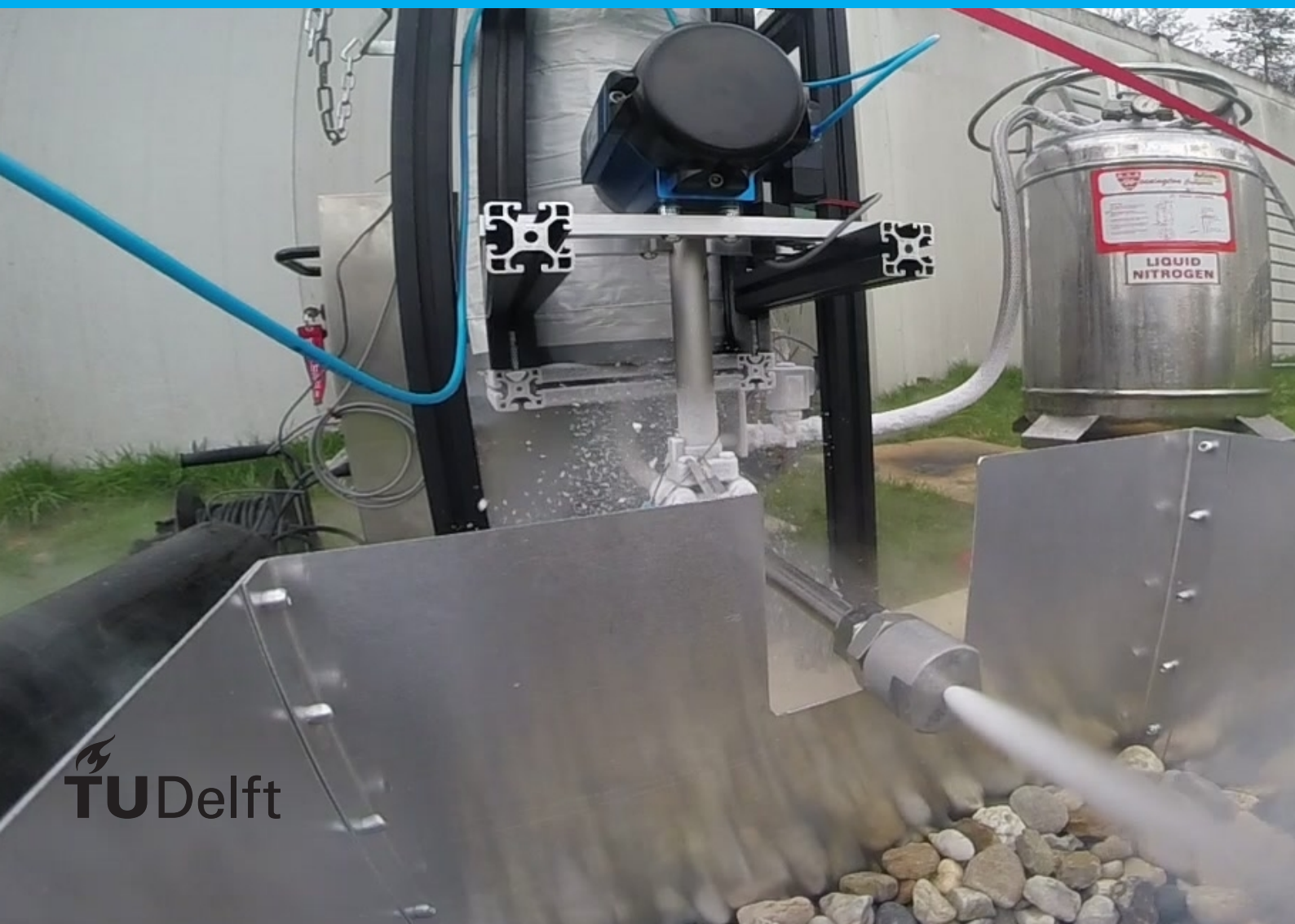# Cryogenic propellant tank pressurization

Practical investigation on the tank collapse factor for small, high-pressure, cryogenic rocket propellant tanks

R.J.G. Hermsen

Master thesis report
Faculty of Aerospace Engineering
Department of Space Engineering

TUDelft

Cryogenic propellant tank pressurization

Practical investigation on the tank collapse factor for small, high-pressure, cryogenic rocket propellant tanks

by

R.J.G. Hermsen

to obtain the degree of Master of Science
at the Delft University of Technology,
to be defended publicly on the 29th of June, 2017 at 9:00.

Student number: 4016165
Project duration: April 4, 2016 – May 11, 2017
Thesis committee: Prof. Dr. E.K.A. Gill,   TU Delft, chair
                    Ir. B.T.C. Zandbergen,   TU Delft, supervisor
                    Ir. R. Noomen,   TU Delft

TUDelft

*"Capabilities drive requirements, regardless of
what the systems engineering textbooks say."*
—
Akin's laws of spacecraft design, number 38

*"I would have written a shorter letter, but
I did not have the time."*
—
Blaise Pascal

Acknowledgements

It has been a pleasure to conduct the research described in this thesis at the TU Delft. The freedom of choice in subject has made it possible to select a project and a course of action that I enjoyed very much. It was fantastic, although sometimes very hard, to combine some theoretical work with a large practical project. I am happy that I was able to structure my thesis in this way, as I am of the opinion that every TU Delft student should get more in contact with the practical side of engineering. It's good to now and then sit down, read books, do simulations and write papers, but as an engineer you also need to go out and build stuff.

I first of all need to thank my supervisor, Barry Zandbergen, who has overall been a large support during this thesis. His advice, critical questions, and extensive feedback have very much improved the quality of the work done. Also his persistence has led to numerous improvements on the final report and to the completion of the paper about this research, to be presented at EUCASS 2017.

Furthermore I am extremely grateful for the existence of the organization Delft Aerospace Rocket Engineering (DARE). The society offers the chance for personal and intellectual development. The knowledge gained there is both theoretical and practical. It teaches not only on technical aspects, but also on social and organizational points. Through the creative and inspiring environment that DARE has offered me for my time at the university, I have been able to develop myself on all fronts. I would not be the person I am now without the society DARE and its members.

For this thesis specifically DARE has assisted on many fronts. The society made it possible to construct the full test setup, to conduct all the tests required to make the setup work, and to conduct all the tests to validate the simulation. From the people in the society, a number can be mentioned in particular. These are Felix Lindemann, Angelos Karagiannis and Martin Olde as safety officers, Jeroen Wink and Bastiaan Bom for hardware acquisition, Radu Florea for his extensive help with setting up the capacitive sensor measurement and with the cRIO and LabView code in general, and the Cryogenics project members (Akhil, Andrea, Arthur, Daniel, Dion, Eoghan, Joshua, Jorgis, Juan, Krijn, Mathijs, Nick, Rano, Rolf, Simon and Tobias).

Also a big thank you should go out to two TU Delft staff members who helped out tremendously during the practical side of the thesis: Kees, from the Dreamhall, for all the production tips and assistance, and Michel van den Brink from the Process & Energy department for his assistance during the tests.

Finally I want to thank my girlfriend, for having patience with me while I spent so much of my time working on DARE and on this project. I want to thank my parents and my brother for their continuous support. (They must by now have been very much wondering why this graduating was taking so long.)

R.J.G. Hermsen
Delft, June 2016

Summary

Delft University of Technology, and its student project Delft Aerospace Rocket Engineering (DARE) in particular, are interested in simple, low-cost options to explore space. DARE is working towards becoming the first student society worldwide that reaches the edge of space (100 km). For this it will likely need to use liquid oxygen as an oxidizer, but it also needs to rely on pressure-fed systems, as it has not yet developed propellant pumps. Due to the cryogenic temperatures of the liquid oxygen (~180°C), the pressurant gas (helium) that is injected into the tank for pressurization cools down significantly, which means more gas is needed to maintain the pressure.

The effect of heat transfer on the amount of helium required is not well known, but is very important for small-scale, high-pressure tanks. To make an effect design of a rocket it needs to be known how much helium is required. This thesis has as goal to investigate this theoretically and by means of practical tests. Next to establishing the amount of gas needed, it is beneficial to investigate how the amount required can be reduced. To this purpose different injection methods are investigated during the tests: Radial, axial and vortex. It is hypothesised that axial injection may be more efficient than the commonly used radial injection.

The effect of the heat transfer (and other non-ideal effects) on the amount of pressurant gas required is characterized by the so called "collapse factor". This factor has a value between 1.0 and 2.0 when taken from literature. The large uncertainty in this factor means that an engineer needs to take a design safety margin of over 10% on its rocket mass, and over 15% on the rocket length. Reducing the uncertainty in this parameter has as effect that a far more efficient design can be created.

To reduce this uncertainty a set of models is created, with the goal to develop a tool that is simple, easy to use, and computationally inexpensive, that can predict the pressurant gas collapse factor within 10%. Models are constructed as a lumped parameter model, or as an extended 1D model, where ullage volume is divided into horizontal or vertical slices. During the development it is found that the heat transfer cannot be well predicted by means of existing correlations due to the extreme temperatures and pressures in the tank. It is realized that radial injection reinforces the natural convection pattern in the tank, likely increasing heat transfer. Axial injection destroys this convective pattern and thus has likely less heat transfer.

For the conduction of the experiments a 30 L cryogenic propellant tank, with associated feed system, is designed and constructed. The tank is suspended in a test bench and equipped with a large amount of sensors, including 16 thermocouples and a custom designed and made capacitive liquid level sensor. During the tests the tank is filled with liquid nitrogen. This is then pressurized with helium up to ~30 bar of pressure for 60 s. This is followed by 50 s of pressurized expulsion of the liquid nitrogen where all thermodynamic processes in the tank are monitored.

From the tests it is learned that for radial injection the collapse factor is around 15% higher than for axial injection. This is due to the different temperature distributions in the ullage gas. The measurements show stronger vertical temperature gradients for the radial tests. This results in high heat transfer because the relatively high temperature gas comes in contact with the tank wall. For axial tests the vertical gradient is lower and the radial gradient is far greater, resulting in colder gas near the wall, and thus lower heat transfer. The tests with the vortex tube injection were unfortunately not successful.

The comparison of the test data and the simulation shows that it is possible to predict the tank collapse factor within 10% accuracy for the axial injection tests. The simulation consistently under-predicts the tank collapse factor, indicating that the heat transfer is likely underestimated in the simulation. The more accurate prediction from the simulation can be used to reduce the uncertainties due to collapse factor in total rocket mass from 10% to below 2.5%, and in total rocket length from 15% to below 4%.

Contents

List of Abbreviations

BSPP	British Standard Pipe, Parallel (thread)
BSPT	British Standard Pipe, Tapered (thread)
BV	Bleed Valve
CFD	Computational Flow Dynamics
CGR	Compressed Gas Regulator
CJC	Cold Junction Compensation (for thermocouples)
CP	Command Post
cRIO	Compact RIO (NI instrument, can also refer to the DARE cRIO assembly as a whole)
DARE	Delft Aerospace Rocket Engineering
FIFO	First In First Out
FPGA	Field Programmable Gate Array
FV	Fill Valve
HEOS	Helmholtz Equation Of State
I_{sp}	Specific Impuls
MV	Main Valve
LCH4	Liquid Methane
LN2	Liquid Nitrogen
LOx	Liquid Oxygen
LPM	Lumped Parameter Model
NI	National Instruments
OF	Oxidizer to fuel ratio
PSRV	Pressure Safety Relief Valve
PSU	Power Supply Unit
PV	Pressurization Valve
PTFE	Polytetrafluoroethylene (brand name: Teflon)
PU	Polyurethane
RSE	Relative Standard Error
SSE	Space Systems Engineering
TW	Oxidizer to fuel ratio
VI	Virtual Instrument (LabView)

Rocket engine tank pressurization

Rocket engine tank pressurization deals with the injection or generation of some form of gas in a rocket engine propellant tank to keep this tank at a required pressure level. The pressure in the tank is either required to keep a net positive suction head at a propellant pump inlet, or to function as the direct force to inject the propellant into the combustion chamber.[58] As is clear by the title of the thesis, the research described in this report deals with cryogenic propellant tanks under high pressure. More specifically, it is aimed to investigate the pressurization of a liquid oxygen propellant tank for pressure-fed rocket engines by means of the injection of helium gas. The extreme conditions in the propellant tank of simultaneously high pressure and cryogenic temperatures results in a complex interaction of the pressurant gas with the tank and the propellant that can have significant impact on the sizing of the complete rocket system. This specific domain of tank pressurization has not been investigated in detail and certainly practical experiments are scarce. However, to design an efficient sounding rocket using liquid oxygen, it is essential that the pressurization system is well understood. That is where this thesis research aims to contribute.

This introduction chapter aims to highlight all the different aspects of rocket engine tank pressurization, the previous research conducted on the subject, and the research goals for this thesis. Large parts of the literature on the subject has already been investigated and reported on in the literature study preceding this thesis.[33, 34]

First, in section 1.1 the student society Delft Aerospace Rocket Engineering (DARE) is introduced. This organization at Delft University of Technology conducts rocketry research on a sounding rocket scale. Its activities are the main drivers for this research. Delft university is the main facilitator that enables the research. Second, in section 1.2 the tank pressurization system and associated literature is elaborated. The main problem statement that is the reason for the current research is explained here. This problem statement is evolved into the research goal and the research questions that are given in section 1.3. In section 1.4 the research plan is presented, and finally section 1.5 on report structure gives an overview of how the performed research and the results are presented in this report.

1.1. DARE: Students reaching to space

Delft Aerospace Rocket Engineering is a student society and "DreamTeam" at Delft University of Technology. It is formed by a group of volunteers that work on practical rocket technology next to their studies. DARE was founded in 2001, and has achieved a number of milestones over the years. The first of these was the launch of the Stratos 1 sounding rocket in 2009 to 12.5 km altitude. At that point this was the European altitude record for amateur rocketry. This was again broken by the launch of Stratos II+ in October 2015: 21.5 km. Since that time however, the European altitude record was (finally) taken over by a different group: The HyEnD student group of the University of Stuttgart launched the HEROS 3 rocket to 32.3 km

altitude in November 2016. DARE is however still looking to regain this record and has started work on the Stratos 3 and future technology development projects to achieve this goal. DARE is aiming to eventually become the first student society to reach space.[1, 5].

The Stratos 1 rocket was a two-stage sounding rocket based on a solid rocket propellant using sorbitol and potassium nitrate. Stratos II+ was a single stage hybrid rocket engine that used nitrous oxide as oxidizer, and a mix of sorbitol, paraffin, and aluminium powder as fuel [63]. From the Stratos II project, and the currently ongoing Stratos 3 project, DARE has build up a good expertise with N_2O. This substance however has its limitations as an oxidizer, and DARE is looking at more energetic replacements for this in the future. It is thought that this is a required step to eventually be able to launch a rocket into space. The most promising candidate for this is liquid oxygen (LOx), which is used in virtually all large launch vehicles. The use of this cryogenic liquid however brings with it a myriad of challenges that need to be solved by careful investigation.[62]

To lay the foundation work for this, a number of senior DARE members, working towards their master thesis, decided to focus on different aspects of the design of a rocket using a cryogenic oxidizer. This is supported by the department of Space Engineering, as part of the department's focus on small launchers and possible game-changer technology in launcher design for small satellites. At time of writing, one thesis in this project line has already been completed, on the design of regenerative cooling in a LOx-methane engine[22].

The research that is the topic of this report was started after a literature study concerning cryogenic rocket engine feed systems[33]. Many practical things were learned from this literature study, but mostly it was instrumental in identifying the topic of this thesis: The pressurization of a cryogenic propellant tank for a pressure-fed sounding rocket. DARE currently does not have the technology ready to use pump systems on-board a rocket. Development on this subject is just getting started, and thus it is not feasible to implement any such technology quickly in a rocket to get back the European altitude record, or to get students to space. Instead building a pressure-fed engine using stored pressurized gas is for now the best option for DARE. However to use stored pressurized gas effectively, it needs to be known how much of this gas is actually needed. To investigate this is the subject of this master thesis.

1.2. The problem of tank pressurization

Tank pressurization is required for both pump and pressure fed rocket propulsion. For pump-fed systems the tank pressure is needed to maintain a positive suction head for the pump. Pressures usually range between 1 to 4 bar overpressure. For pressure-fed systems it forms the main driving force to push propellant into the combustion chamber. Pressure-fed systems have been used to pressures over 100 bar. There are various methods to maintain a high pressure in a propellant tank during expulsion, but the most common one is to use a stored pressurized gas, usually helium, that is injected into the propellant tank from the top.[58, 65] Most research on tank pressurization has been done for either tanks for pump-fed systems, operating at low pressures, or for tanks in a zero-g environment, using storable propellants.

For DARE however, the goal is to implement a tank pressurization system in a small scale, high pressure tank, using a cryogenic propellant. There is relatively little data available to predict how much pressurant gas is required to pressurize and empty such a tank. Knowing how much pressurant gas is needed is however essential to make an effective design for a sounding rocket. (The effect of the pressurant amount on system level sizing is discussed extensively in chapter 2.) If the pressurization system is designed too large, the system will become too heavy and bulky, while if the system is designed too small, it can lead to loss of pressure near the end of the burn, which results in less engine performance.

1.2.1. Tank pressurization in literature

Tank pressurization is a widely studied subject. Research of it has been ongoing for a long time already and continues to this day. The standard work on the subject is, in my opinion, the book "Rocket propellant and pressurization systems" by Elliot Ring, published in 1964[52]. His work is a basic introduction into everything related to tank pressurization, and is a good starting point for research on the subject. Virtually all important physical phenomena involved are discussed, such as tank loading accuracy, tank pressurization, liquid temperature gradients, etc. Furthermore a lot of attention is focussed on analytical expressions to make estimations for all these effects. These kinds of expressions are still

very useful to any modern rocket scientist working on rocket designs. Tank pressurization is also a subject treated in general rocket propulsion books, but usually these do not go into the details of the matter[36, 58, 65].

The focus of this study is how much pressurant gas is required to pressurize and empty a propellant tank. Important in this is how effectively the pressurant gas is used. There are thermodynamic relations available to describe the ideal situation of pressurization and expulsion (see chapter 2) but these do not take into account non-ideal gas effects and, more importantly for cryogenics, heat transfer. The ideal relations represent a '100% efficiency' case for inert gas pressurization systems. Effects like heat transfer usually reduce this efficiency, meaning more pressurant gas is required. The so called tank collapse factor (K) is a figure of merit that quantifies the inefficiencies. The tank collapse factor is defined as the ratio of the actual gas mass flowing into the tank during pressurization and expulsion versus the ideal gas mass flowing into the tank[20]. The collapse factor can be defined by equation 1.1. In this equation m_u is the amount of gas that flows into the ullage volume. For more details on this expression and other analytical relations regarding tank pressurization, please see appendix B.

$$K \equiv \frac{(m_u)_{real}}{(m_u)_{ideal}} \tag{1.1}$$

The collapse factor is a single efficiency factor that includes all non-ideal effects influencing the amount of pressurant gas. A collapse factor of unity means the system is working as efficiently as the ideal thermodynamic process. A collapse factor above unity means it is working less efficient. E.g. a factor $K = 1.5$ means the system requires 1.5 times as much pressurant gas compared to the ideal case. In systems working near environment temperatures a collapse factor near one is usually applicable. Any losses in efficiency are compensated by heat transfer from the environment towards the expanding pressurant gas. Energy is flowing into the system, improving its efficiency compared to the ideal case, which does not include any heat transfer. In contrast, for systems at which the temperature difference between pressurant gas and the propellant/propellant tank is large, such as in cryogenic systems, the heat transfer will draw energy from the gas and thus lowering the efficiency.

A recent study that gives a good overview of practical efforts into tank pressurization is given by De Quay and Hodge[21] in 2010. They present an excellent overview table of experimentally determined collapse factors collected from literature from around 1966 till 1998. They split the data in those for liquid hydrogen tanks, and other liquids (LN2, LOx, LCH4). Only the latter set is of interest here. From their data it is clear that most tests conducted in the past were for large tanks (ranging from 100 L to 40 m^3), and relatively low pressures (in general around 3.5 bar). Collapse factors gathered by De Quay are in the range of 1 to 5.25. The real high values of 5.25 and 4.1 are for LCH4 pressurized with N2 and LOx pressurized with N2 respectively. These combinations of gasses are generally just not a good idea due to the pressurant condensing or dissolving (see appendix A.2). The other values that are of relevance are between 1 and 2.6, with the most representable ones with respect to the application studied in this thesis roughly between 1 and 2.

Clear from the study by De Quay and Hodge[21] is as well the scarcity of experimental results, specifically on high pressure systems. De Quay takes this as argument to go and do research on high pressure systems which he has documented in his PhD thesis[20]. He had conducted tests with pressurization systems and modelled these as well. However his tests and models are for spherical tanks of 10 m^3 and 19 m^3, running at pressures between roughly 350 bar to 550 bar, and having a tank wall thickness of 35 cm to 40 cm. The simulations he constructed are indeed unique in the fact that he takes into account the temperature distribution across the thickness of the tank wall, but except for his extreme test setup, it is unlikely that such effects are of major importance to the pressurization systems in any other case.

The most practical and recent work (from after the period covered in the evaluation by De Quay and Hodge) has been done by Ludwig and Dreyer at ZARM in Bremen[43] and Wang et al. in China[59, 60]. Ludwig and Dreyer unfortunately only investigated pressurization, not emptying. They use an LN2 tank that is very well instrumented with a large number of thermocouples to measure temperature gradients, but only have done tests with pressurization of LN2 to 4 bar maximum. Wang et al. have conducted pressurization and emptying tests with large scale tanks, which are also out of the range of interest for this work.

Next to these papers, the most important work in the field of pressurization and emptying of tanks has been done in the 1960s. Next to the book by Ring[52], this included work on hydrogen tanks by Stochl et al. [56], and the experimental and analytical work by Nein and Thompson[46]. Also a very interesting document is the paper by DeWitt et al. [25] which discusses pressurant injection in more detail. This paper is discussed in the next section (1.2.2).

In more recent times, the study of tank pressurization has mainly focussed on propellant storage in zero-g (such as Van Dresar and Stochl[26]), and on full CFD simulations of the pressurization and emptying of a specific rocket tank (such as the work by Ahuja et al.[9]). An important name when it comes to lumped parameter simulations of pressurization and emptying is that of Majumdar, who has published on simulations conducted with the NASA GFSSP code[44].

In the paper of De Quay and Hodge[21] and the PhD thesis of De Quay[20] also detailed descriptions of the parameters affecting collapse factor are given. In the paper it is cited that "The predominant property where spatial distribution has significant effects is temperature"[21]. Among the parameters of influence mentioned are horizontal and vertical temperature gradients in the ullage, and the effect of different forms of pressurant gas injection. He discusses the effect of pressurant gas injection methods by references to literature, but he does not make definitive statements on what method is more effective in which situation, and he does not conduct further research into it. Based on the work by De Quay and Hodge it was hypothesized for this research project that heat transfer in the ullage will play a more significant role in the determination of the tank collapse factor than it does in the commonly studied cases. There are four main reasons to expect heat transfer to be more significant in the case of pressure-fed, cryogenic, small-scale rockets. These are:

1. High pressure in the propellant tank

2. Large temperature difference between the 'warm' pressurant gas and the cold propellant and cold tank wall.

3. Large area to volume ratio of the ullage due to the small diameter of the tank

4. Large heat capacity of the propellant tank, because of its thick walls and bulkheads, designed to withstand the high pressures.

These properties of the system all have as effect that heat transfer plays a more important role in the pressurant gas consumption, making the prediction of the amount required harder, as it deviates further from ideal gas predictions. From this it is concluded that the temperature distribution in the ullage gas is of major importance in the determination of the collapse factor.

1.2.2. Pressurant injection methods

One of the main design parameters of a pressurization system that influences ullage temperature distribution is the method of pressurant gas injection. The pressurant gas is sprayed into the top of the propellant tank via a pressurant injector. As described by Huzel[36], the most common shape of the injector is that of a radial diffuser. The radial diffuser injects pressurant radially so that disturbance of the propellant surface by the incoming gas is minimized. This can either be done via a simple plate that deflects the incoming gas stream, or by means of a slightly more complicated construction such as a sintered metal block, akin to a filter. The radial injection method is shown schematically on the left of figure 1.1. The radial injection seems to have as effect that the temperature profile in the ullage gas does not show radial variations, but does show a strong vertical gradient.[25] I.e. the gas is cold near the propellant surface, and warm near the top of the tank, but there is hardly any temperature difference between the gas at the wall and the gas at the centre.

Other variations exist, including axial injection. This is the most simple method: gas is injected via an open port straight along the tank axis. The axial injection is shown in the middle in figure 1.1.

An important paper on the subject of pressurant injection methods is the NASA technical note from 1966 by DeWitt, Stochl and Johnson on the effectiveness of different pressurant injectors[25]. This is a paper not discussed by De Quay[21]. The paper by DeWitt et al. is of particular interest for this research as it is the only paper that could be found that is focussed on the effect of injection methods. They tested six types of different injector geometries. They also conducted tests with a tank of similar scale as what is proposed by DARE. The tank they used was 0.68 m diameter and 2 m high. Tests

were however conducted with liquid hydrogen as propellant and gaseous hydrogen as pressurant. Their results indicated that a straight tube injector resulted in the least amount of pressurant required. They attributed this to (1) the evaporation of propellant when it came in contact with the pressurant gas and (2) the radial temperature profile created by this injector, where the temperature gradient meant the gas was warm at the tank centreline and cold near the walls. The cold gas temperatures at the wall resulted in low heat transfer from gas to the wall, and so to lower pressurant requirements.

It is interesting to see that, in contrast to what DeWitt et al. propose[25], nearly all simulation efforts assume that there exist hardly any radial temperature gradients in the tank. Assuming no radial temperature distribution is the main justification for developing 1D-simulations. Nearly all experimental papers point to the use of a radial diffuser as injector type, if the used injector type is mentioned at all. This injector type will indeed create a near uniform radial temperature distribution and might indeed be most suited for large, low-pressure, thin-walled tanks. However, the experiments from DeWitt et al. indicate that a non-uniform radial distribution might be far more beneficial. They indicated that their theoretical analysis worked well for radial diffuser types, but that a model needs to be developed for the mixing effects of the axial injection.
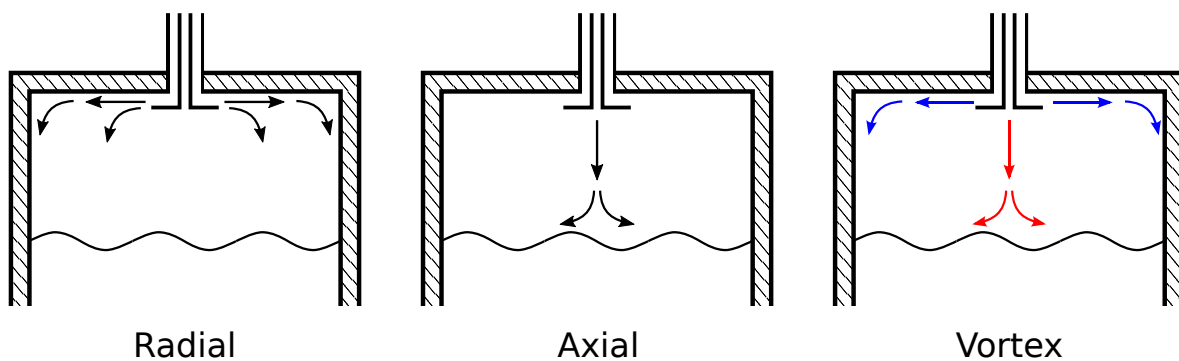
Figure 1.1: A schematic representation of the three injector types that will be researched during this thesis. The arrows indicate the gas flow direction from the injector.

Based on the analysis by DeWitt et al. regarding the temperature gradients, and inspired by upon a small 'note-in-passing' in the book of Huzel[36], a third possible method of injection was thought of. This involves a so called Ranque-Hilsch-vortex-tube. A vortex tube is a simple and light mechanical construction without moving parts that splits an incoming gas flow into a cold and a warm gas stream[35]. Huzel suggests to use this system to protect cold cryogenic tank structural members from the incoming hot pressurant gas. The idea considered for this project however is to use a vortex tube specifically to introduce a large radial temperature gradient in the pressurant ullage. This is expected to provide an even higher temperature gradient than axial injection, and thus an even lower heat loss to the tank wall. The way the gas is prosed to be injected after it is split into a hot and cold stream by the vortex tube is shown on the right in figure 1.1. The vortex tube itself, including associated literature, is explained in detail in chapter 6.

Based on this information it has been decided to investigate three different injection methods and to look at their effect in pressurant usage and collapse factor. All three are displayed graphically in figure 1.1. The main focus is on the first two injection methods: Radial and axial injection. The design for the injector body was mainly based to accommodate all three types of injection methods in one design, being able to switch between them without needing to open the tank (see section 5.3). For the radial injection method gas is only injected from the side, and flows along the top bulkhead into the tank. For axial injection the central port is used to directly blow the helium down along the tank axis. The vortex tube is a kind of combination of the two. First the gas stream is split in a hot and cold stream via a vortex tube (not displayed in this figure). Then the cold stream is injected radially, and the warm stream is injected axially. Within this thesis the main focus is on the difference between radial and axial injection.

1.3. Research goal and research question

As explained in section 1.2, it is currently not well known how much pressurant gas is needed to pressurize and empty a small cryogenic propellant tank. The collapse factor that determines the efficiency of the pressurization is estimated to be somewhere between 1 and 2[21], but there are no clear methods available to determine its value more precisely. However, as the amount of pressurant required is directly proportional to the collapse factor, this uncertainty is of large influence on the sizing of the total rocket system. (See chapter 2 for a quantification of its effect.)

The main focus of this research is to reduce the impact of this uncertainty, which will allow for better designed rocket systems. Reducing the impact of the collapse factor can be done by reducing the uncertainty in its value, and by trying to reduce its absolute value. Modelling and experiments can be used to reduce the uncertainty, and different gas injection methods seem a promising way to reduce the factor itself. This focus can be formalized and quantified in the main research goal:

> **To provide DARE and the TU Delft with the means to predict the tank collapse factor for cryogenic tank pressurization systems within 10% accuracy and to investigate the effect of the pressurant injector on the tank collapse factor.**

The 10% mark in accuracy for the research goal has been chosen as it is thought that this is a feasible level that can be achieved during the research period, while it is also a significant improvement over the current estimates.

Based on this goal a number of research questions can be formulated that work towards achieving the goal. These questions are:

1. What is the (quantified) influence of the collapse factor and its uncertainty on the design of a rocket system?

2. How can the collapse factor be modelled by analytical and numerical methods?

3. How do the physical processes that take place during pressurization and emptying of the tank influence collapse factor?

4. Which pressurant gas injection method realizes the lowest collapse factor? Is axial injection indeed more efficient than the commonly used radial injection method?

Answering these questions will generate a better understanding of the physical processes that are ongoing in a propellant tank during pressurized expulsion, which in turn allows to predict how much pressurant gas is needed. Knowing how the amount of pressurant gas required is affected by different parameters of the system will allow to design a more optimized sounding rocket system.

1.4. Research plan

To answer the research questions, tank pressurization and pressurized expulsion need to be investigated. Such an investigation can be done via simulations or via practical experiments. Making a simulation is however not a sure way to achieve a good result. It is hypothesized that the difficulty in estimating the pressurant mass is due to heat transfer inside the tank. This heat transfer is closely related to the temperature distribution and the flow patterns inside the ullage volume. Heat transfer, temperature distribution and flow patterns are difficult subjects to investigate numerically, any simulation developed for this would require some form of experimental validation to make sure that the code can be trusted.

The first step in the investigation is to quantify the influence of the collapse factor on a rocket design: If a pressurization system needs to be sized for a sounding rocket going to space, what size will that rocket be?

After this is defined, a first simulation attempt can be made. A simulation of a propellant tank system can be structured in a number of ways. The most simple one is a lumped parameter model. Here certain sections of the tank (such as propellant volume, ullage volume, tank wall, etc.) can be simulated as discreet sections with homogeneous properties such as temperature and pressure. Heat transfer in the ullage can be estimated via empirical heat transfer relations. If a simulation like this can provide accurate results when compared to experimental data, this would be a valuable result. The simpler

the simulation method, the easier it is to implement it in a design iteration process for sizing a rocket system.

A lumped parameter model can be further extended by splitting sections of the model into a large number of smaller, equal sections. For example, the tank ullage can be split into stacked horizontal slices, where each slice can have its own temperature and mass. Splitting tank ullage and tank wall into multiple sections is expected to enhance the accuracy of the simulation, as it is more suited to cover the temperature gradients that are expected to play a role in the pressurant usage. The split of the ullage could even be varied between stacked horizontal slices, or concentric vertical rings to try and predict vertical or radial temperature gradients respectively. These temperature distributions in turn are expected to represent radial and axial gas injection.

After this the next logical step in simulation would be to add a second dimension and perform a full CFD analysis of the system. This is however considered out of the scope of this thesis, as this would be akin to optimizing a certain system design instead of trying to find general rules to predict gas usage. Next to this the amount of work involved in creating such a simulation would be substantial and would likely merit a full thesis research all on its own.

When a model is constructed it needs to be checked with experimental evidence before it can be trusted in any way to make design predictions in reality. To conduct such an investigation a test setup needs to be build. This setup much have a tank that can hold cryogenic propellant under large pressure, have a pressurization system using a pressurant gas, and a feed system to allow the loading, pressurization and discharge of all fluids. The system must be instrumented to collect sufficient data on the pressurization and expulsion process. And most importantly: The system must be save to operate.

The test setup needs to be fully designed and constructed from scratch, as there is virtually no experience with cryogenic systems within DARE. When the system is constructed it then needs to be tested, debugged and operated during the eventual validation tests.

Finally the results from the validation tests can be compared to test data and conclusions can be drawn on how well the code functions. Based on the data recorded during the tests it should be possible to get a good understanding of the processes in the tank and how they effect the amount of pressurant gas required. With the test results and the simulations it should be possible to make a good estimated of the amount of pressurant gas required.

1.5. Report structure

This report is structured to present the research in a logical order. This chapter (1) has introduced the research question, goal and the research plan.

Chapter 2 deals with the influence of the collapse factor on the design of a sounding rocket. To do this, a study on the sizing of a sounding rocket is conducted. The rocket investigated should be capable of breaking the European altitude record, or reaching the 100 km mark. This chapter also elaborates a few analytical expressions from literature related to pressurization systems, which are used in this system sizing.

Chapter 3 takes the lessons learned from literature and the estimated sizing from the systems engineering study and uses these in the construction of a computer program to simulate the pressurization and expulsion of a cryogenic propellant tank. The program is verified using the analytical expressions. Simulations results and a sensitivity study are presented.

The next four chapters dive into the practical aspects of this thesis. First the test plan is defined in chapter 4. In chapter 5 the test setup design, construction and validation are described. A small in-depth intermezzo on the vortex tube, including a literature study on its sizing, and subsystem tests on the tube, is presented in chapter 6. Chapter 7 then contains the main results from this report: The results and conclusions from the validation tests using the constructed test setup.

Chapters 8 and 9 conclude this report. The first gives a comparison of the results from the practical tests and the simulations. The last gives the overall conclusions and recommendations of the report.

At the end a number of appendices is also included, that describe the way the experimental datasets were processed in detail, an overview of the man-hours spend on production, an abstract for a EUCASS 2017 paper, and a full copy of the test procedures (amongst other things).

2

System sizing for a liquid oxygen
sounding rocket

Before a detailed investigation on pressurization systems can begin, it needs to be determined what the range of applicability for the system needs to be: What kind of rocket systems are we considering? What are their main parameters? And how does the tank collapse factor influence the design?

For this, the long-term goal of the student society DARE can be considered: To be the first students to launch a rocket into space. In this context "into space" is defined as achieving an altitude of more than 100 km above the Earth's surface. For a less demanding goal in terms of rocket size, a short-term goal of the society could also be looked at: Breaking the student altitude record in Europe. Currently this is set at 32.3 km[5]. To achieve these goals DARE wants to develop a sounding rocket using liquid oxygen as an oxidizer.

This section of the report discusses possible designs suited to achieve this goal. The focus is on the main sizing parameters of a pressure fed bi-propellant liquid rocket engine, using LOx as oxidizer and using helium as pressurant. A large number of possible designs are evaluated using a simple Python script. These designs show the need for the current investigation on pressurization systems, and shows the ranges for which a helium pressurization system design tool should give credible results.

The script logic is explained in section 2.1, including some more in-depth explanation of some of the (analytical) subroutines. Section 2.2 discusses the assumptions made within the script, the values and ranges for parameters, and the reasoning behind these values. The resulting designs obtained for both the design cases (space and altitude record) are described and discussed in section 2.3. The conclusions drawn from the script, and the resulting sizing ranges for a pressurization system are discussed in section 2.4.

2.1. Design evaluation script

The design evaluation script is a small, simple analysis script to evaluate the possible designs for a liquid oxygen - ethanol sounding rocket. The main logic of the script is shown schematically in figure 2.1.

The script starts with a number of input parameters that are set by the user. These include various natural constants, properties of materials, system size parameters and the collapse factor for the LOx tank. After this it enters a loop in which it varies the combustion chamber pressure, thrust, and burn time over the specified ranges (see table 2.1).

The first step is then to evaluate the engine performance parameters. Based on the combustion chamber pressure the script selects the resulting I_{sp} and OF ratio for the combustion of LOx and ethanol (95%). It does this via a cubic spline interpolation from a list of values for I_{sp} and OF that have been determined using the RPA Lite code[1]. The list is generated with steps of 5 bar in chamber pressure for each new entry. The values are generated for sea-level altitude, using a fixed nozzle expansion ratio of 8.

---

[1]RPA v1.2 Lite edition: `http://www.propulsion-analysis.com/index.htm`
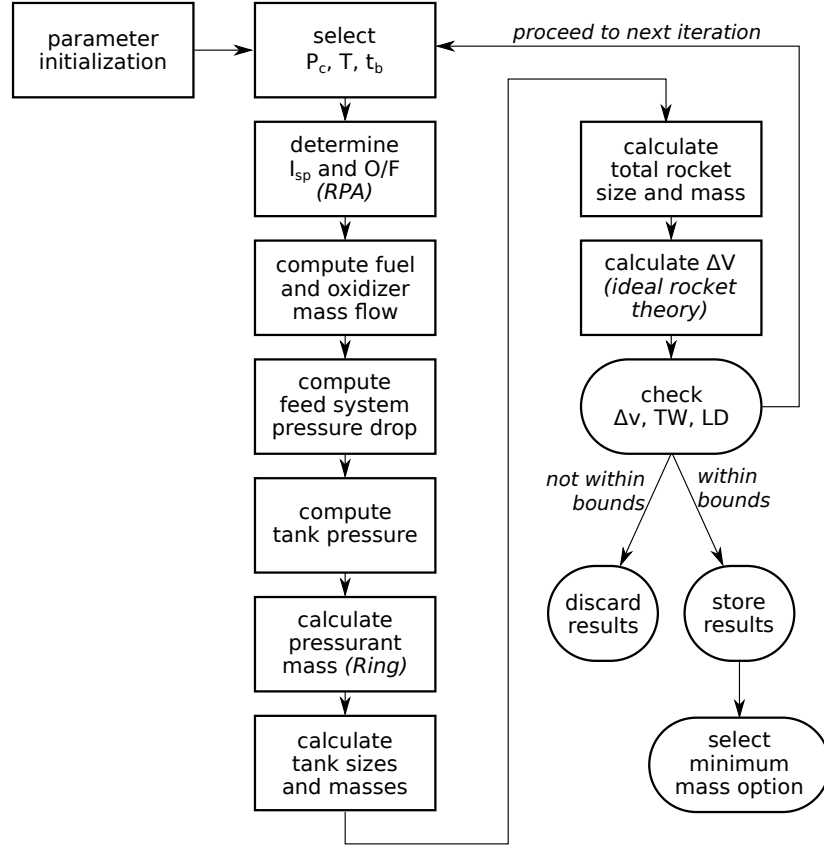
Figure 2.1: A flow chart for the rocket sizing simulation. After parameter initialization the script loops through a fixed range of values for combustion chamber pressure P_c, thrust T and burn time t_b.

Based on the OF ratio and the input values for thrust and burn time, the fuel and oxidizer mass flows and total propellant masses are determined. These mass flows are then used to estimated a feed-system pressure drop. This pressure drop consists of the sum of pressure drops of the injector (20% of P_c), a solenoid valve ($k = 340$ [18]), and 3 m of tubing (inner diameter of 30 mm). This is done for the LOx and ethanol lines individually. The tank pressures for both tanks are then computed as the sum of the combustion pressure and the feed system pressure drops.

Now that the pressures in the tank and the volumes of the tank are known, the pressurant gas mass can be estimated. This is done using the standard ideal relation for the pressurant mass as provided by Sutton[58], but with the correction for gas compressibility as given by Ring[52]. This standard relation is multiplied by the collapse factor (K) to account for all non-ideal effects. The resulting relation is given by equation 2.1. In this equation m_0 is the starting mass of helium in the pressurant tank, P_u is the pressure in the propellant tank, V_{prop} is the initial volume of the propellant (note that this does not include the initial ullage volume), R is the specific gas constant (2077 J kg^{-1} K^{-1} for helium), T_0 is the initial temperature of the pressurant gas, γ is the ratio of specific heats for the gas (1.66 for helium), Z_0 is the initial compressibility of the gas, P_{pres} is the final pressure in the pressurant tank, and P_0 is the initial pressure in the pressurant tank. For more details on this equation and its derivation, please see appendix B.2.

$$m_0 = K\frac{P_u V_{prop}}{RT_0}\left(\frac{\gamma}{1 - Z_0 P_{pres}/P_0}\right) \tag{2.1}$$

Based on the result from this equation the volume of the pressurant tank can be determined. The volumes and lengths of the propellant tanks are determined from the total propellant masses, the propellant densities, the specification for the initial ullage volume and the rocket diameter. Based on the rocket diameter and the tank pressures, the tank wall thickness's are determined, and from this the total tank masses follow.

The total masses of the tanks, fluids, and the auxiliary systems (see table 2.1) are summed to get the total rocket mass. A similar summation is done for the length. And finally the total amount of velocity change (Δv) for the rocket is computed using ideal rocket theory (Tsiolkovsky; impulsive shot). A fixed amount of aerodynamic losses and a variable amount of gravity losses ($= g \cdot t_b$) are subtracted from this.

When all these calculations are then completed, the script evaluates if the rocket generates sufficient Δv to achieve the target altitude. Furthermore it checks if the rocket falls within bounds for thrust-over-weight and length-over-diameter ratios. If the rocket meets all criteria, its results are stored for later evaluation. If not, they are discarded. The script then proceeds to the next combination of P_c, T and t_b and repeats until it has worked through all combinations.

When all cases have been worked out, the scripts looks back at the list of rocket designs meeting all criteria and selects from these the option with the minimum mass. This is the design that it gives as output.

2.2. Design restrictions and assumptions

The design evaluation script is a relatively simple setup to determine the effect of the collapse factor. The script relies on a number of assumptions on system design and on system parameters. This section of the report gives an overview of all these assumptions and parameters and explains why they were chosen as such. The main reference case for most of the assumptions is the Stratos II sounding rocket, which is elaborated in 2.2.1. The design restrictions are summarized in section 2.2.2, and the parameter values or boundaries are given in section 2.2.3.

2.2.1. Stratos II+

The Stratos II+ sounding rocket was designed and developed over the years 2010-2015 at the society DARE. The rocket was launched successfully on the 16th of October 2015 to the then record altitude for European amateur rocketry at 21.5 km. The rocket used a hybrid rocket engine with N_2O as oxidizer and a mixture of sorbitol, paraffin and aluminium as fuel.[63] The rocket was 200 mm in outer diameter and 6.92 m long. The top section, of 1.43 m length, was of an outer diameter of 160 mm. It housed the payloads, the flight computer, and the recovery system. The bottom section consisted of a tank of 4 m long, and a combustion chamber of 1.14 m (incl. nozzle). The rocket had a start mass of 185 kg, a burn-out mass of 100 kg, and an empty mass of 86 kg. The rocket engine that powered Stratos II+ delivered approximately 180 kNs of total impulse over 23 s of burn time. Based on the flight data and the flight simulations of Stratos II+, the total drag losses for the rocket can be estimated at around 530 m/s, and the total gravity losses at around 220 m/s.

Figure 2.2: Lift-off of the Stratos II+ rocket in 2015.

The parameters of this rocket, plus the lessons learned during the development and launch of the rocket are used as main guidelines during this system sizing of a LOx-powered sounding rocket system.

2.2.2. Design restrictions

The following is a list of design choices that determine the shape and form of the rocket under consideration in the design evaluation script.

Engine configuration: Bi-propellant liquid, pressure-fed

The main simulations were conducted for pressure-fed systems, but some simulations were conducted to investigate the effect of a pump for the fuel. Mostly to show how much the design can improve by using such a system. In these simulations the pressure for the fuel tank was set at a constant 5 bar

and a mass of 5 kg was added for pump and power source (electrical pump).

Pressurant gas: Helium
Helium is considered to be the only realistic pressurant gas for this system. See appendix A.2 for more details on this selection.

Oxidizer: Liquid Oxygen
See appendix A.1 for more details on this selection.

Fuel: Ethanol (95%)
The fuel for the rocket has been selected to be ethanol (95%), which is a mix of ethanol with 5% mass of water. This is considered the most realistic fuel option for a bi-propellant liquid for DARE at the moment and was thus selected. Kerosene would be another reasonable option, but is less likely. For this simulation its properties would be comparable to that of Ethanol except for the OF ratio. Methane is not a good option for pressure fed rocket engines. See appendix A.1 for more details on fuel selection.

Propellant tanks: Aluminium, cylindrical, flat bulkhead tanks
The propellant tanks were assumed to be "classical DARE" tank design with a cylindrical tank wall and flat bulkheads that are attached with radial bolts. The bulkheads are assumed to have constant thickness while the tank wall thickness is determined from the required tank pressure times a safety factor.

Pressurant tank: Carbon fibre, cylindrical, spherical endcaps
For the pressurant tank it is assumed that it can be made as a lightweight carbon fibre tank.

Pressure regulation
The fuel tank and oxidizer tank both are fed from the same pressurant tank, but with different pressure regulators (i.e. both tanks can run at different pressures). The pressure in the pressurant tank should remain at 5 bar above the highest of the two tank pressures at the end of the burn.

2.2.3. Parameter values
Table 2.1 gives an overview of the various design parameters that have either fixed values or that are varied within certain bounds. The choices for certain values and/or their ranges are explained in the subsequent text. The estimates that are felt to introduce the largest inaccuracies are those on rocket engine performance and aerodynamic drag losses.

Collapse factor
As discussed in section 1.2.1, the uncertainty on this parameter is rather large. The parameter however also has a large influence on the design, and needs to be known better to make a good design for a rocket. The parameter is set to 1 for the pressurant flowing into the ethanol tank. For the liquid oxygen tank it is varied between 1 and 2 manually between various simulation cases to show the effect of this parameter. The values at which it was evaluated were 1, 1.3, 1.5 and 2.

Length over diameter ratio
An important figure of merit for rockets is their length over diameter ratio (a.k.a. aspect ratio). This is a figure that gives an indication of the rocket shape. Too low an aspect ratio means that the rocket has relatively more frontal surface, and thus likely more air drag. Air drag is a major component of the velocity losses in the flight of a sounding rocket, as could be observed with Stratos II+. A too high aspect ratio generally gives difficulties in structural design to make the rocket straight and to give it enough bending stiffness. A high aspect ratio is also something that is believed to have been a reason for some oscillating eigenmodes observed during the flight of Stratos II+. Stratos II+ had an aspect ratio of approximately 34.5, which is considered to be a very high value.[29] For the system sizing in this thesis a maximum aspect ratio of 32 was selected.

Table 2.1: Parameter values for the system sizing script. Parameters are either treated as a constant, fixed value or are selected from within a range. The selection within the range is done either by the script or by the user. Detailed explanations for these values and the criteria for selection from within a range are given in the text.

Parameter	Unit	Lower bound	Fixed value	Upper bound
Collapse factor (LOx tank)	-	1		2
Collapse factor (fuel tank)	-		1	
Length over diameter ratio (LD)	-	0		32
Thrust to weight ratio (TW)	-	4		6.5
Combustion chamber pressure (P_c)	bar	15		35
Thrust (T)	kN	10		35
Burn time (t_c)	s	15		60
Rocket diameter	m	0.2		0.4
Target altitude ("Students to space")	km		120	
Target altitude ("Record altitude")	km		50	
Drag losses	m/s		750	
Prop. tank bulkhead thickness	mm		20	
Prop. tank wall safety factor	-		1.5	
Prop. tank initial ullage volume	%		10	
Pres. tank wall safety factor	-		1.5	
Pres. tank initial temperature	°C		20	
Pres. tank initial pressure	bar		200	
Pres. tank pressure surplus (end of burn)	bar		5	
Injector pressure drop (% of P_c)[36]	%		20	
Payload mass (incl. nosecone structure, flight computer, and recovery system)	kg		25	
Engine mass (chamber, igniter, valves, etc.)	kg		40	
Engine length	m		0.6	
Inter-tank spacing	m		0.3	
Nosecone length	m		1.5	
Fuel pump mass (incl. power source)	kg		5	
Fuel tank pressure (when using pump)	bar		5	
Nozzle expansion ratio (RPA setting)	-		8	

Thrust to weight ratio

The thrust to weight ratio at lift-off is another figure of merit for a rocket and is mostly of consideration for rockets lacking any form of active control. These types of rockets need to be guided by a launch tower at lift-off. They need to achieve sufficient velocity by the time they leave the tower so that their aerodynamic stability can keep them sufficiently on course. To do this a minimum thrust to weight ratio is often assumed in design. For DARE, which is has not flown a rocket with full control capabilities yet, this ratio is often set at around 5, so that the rocket can achieve sufficient speed in a launch tower of around 6 m (the DARE launch tower). For Stratos II+ this ratio was around 5.5. A maximum of thrust to weight ratio can also be set. This can be done to limit the acceleration of the rocket in the early phases of flight, so that the aerodynamic drag does not rise disproportionally large.

During the system sizing in this thesis the minimum thrust to weight ratio was set to 4. This was done under the assumption that, before the rocket becomes reality, DARE is also able to develop some methods of control that will permit this lower thrust to weight ratio. The maximum thrust to weight ratio has been set to 6.5 to limit excessive aerodynamic forces on the rocket.

Combustion chamber pressure (P_c)

The combustion chamber pressures is varied by the iteration in the script between 15 bar and 35 bar. The lower bound is chosen as a minimum value to prevent the possibility of nozzle flow separation in the lower atmosphere. The upper value is chosen because combustion pressures above this does not seem feasible; higher combustion pressures lead to higher tank pressures and thus heavier tanks.

Thrust (T)
The thrust is varied by the script iteration between 10 kN and 35 kN. The lower bound is chosen because, with the set thrust to weight ratio minimum of 4, a rocket with a lower thrust, and thus lower weight, does not seem feasible. The upper bound has been chosen as a upper limit of what should be achievable for DARE (and this value is likely a high estimate). The thrust is assumed constant.

Burn time (t_c)
The burn time is varied between 15 s and 60 s. The lower bound represents an absolute minimum on required burn time to avoid large drag in the lower part of the atmosphere. The upper bound of this is extended relatively far to cover all possible cases in this aspect.

Rocket diameter
The rocket diameter was chosen to be within a range of 20 cm to 40 cm. These were judged to be reasonable bounds within which DARE will be able to construct a rocket. The preference however is to minimize the diameter of the rocket, mainly to limit the amount of aerodynamic drag during the flight. To achieve this, the rocket diameter was varied in steps of 1 cm to find an approximate minimal value of the diameter for which the script could still find design results for all of the evaluated cases (section 2.3). The diameters used were 32 cm for the students to space rocket, and 28 cm for the altitude record rocket.

Target altitude
The target altitude designed for is 120 km when evaluation designs for getting to space (which is an higher target to ensure the 100 km can certainly be reached). Or 50 km when evaluating designs for getting the European altitude record.

Drag losses
The aerodynamic drag is also difficult to predict, and would required a master thesis research on its own. Instead a very simple estimate is chosen: The aerodynamic losses from Stratos II+ ($\sim$530 m/s) are taken, and increased by a factor of 1.5 to allow for slightly larger diameters. The drag losses are set to 750 m/s. Comparing to Stratos II+ this is felt to be a reasonable estimate for rocket diameters under 300 mm, but is likely an underestimate for larger diameters.

Specific impuls (I_{sp})
The I_{sp} is computed in RPA using the combustion chamber pressure and the fixed expansion ratio. The I_{sp} value is taken to be that at sea-level. The values for sea level are chosen because the rocket lifts of at sea level and for most of its burn time cruises through the lower parts of the atmosphere. With higher altitude, the I_{sp} will actually increase, and thus this is a conservative estimate.

2.3. Rocket design options

To get ranges for the design parameters for a cryogenic tank pressurization system, designs are evaluated with the design parameters within the ranges described in the previous section. These designs are evaluated for collapse factors of 1.0 (minimal case), 1.3 (nominal expected case), 1.5, and 2.0 (maximum case).

For the "students to space" rocket the design altitude has been put at 120 km. Using the script a minimal diameter was selected on which all design cases with the different collapse factors would give possible designs solutions. This diameter was found to be 0.32 m. All rocket designs found by the script for the various values of K are displayed graphically in figure 2.3, and their main parameters are displayed in table 2.2.

Next to the fully pressure fed design cases, two extra cases have been evaluated using a fuel pump. Case number 5 has a diameter of 0.32 m and the nominal value of the collapse factor of 1.3. An extra design case with a reduced diameter of 0.28 m has also been evaluated (case 6), as this would likely be the preferred design option when a pump is available, to limit aerodynamic drag.

What immediately becomes clear from figure 2.3 is that the uncertainty in collapse factor has a large effect on the total length of the rocket. Between a collapse factor of 1 and 2 the total length increases with 15%. From table 2.2 it can be seen that the mass of the rocket also increases with increasing collapse factor, although less so than the length. Mass increases with 10%. At the engine
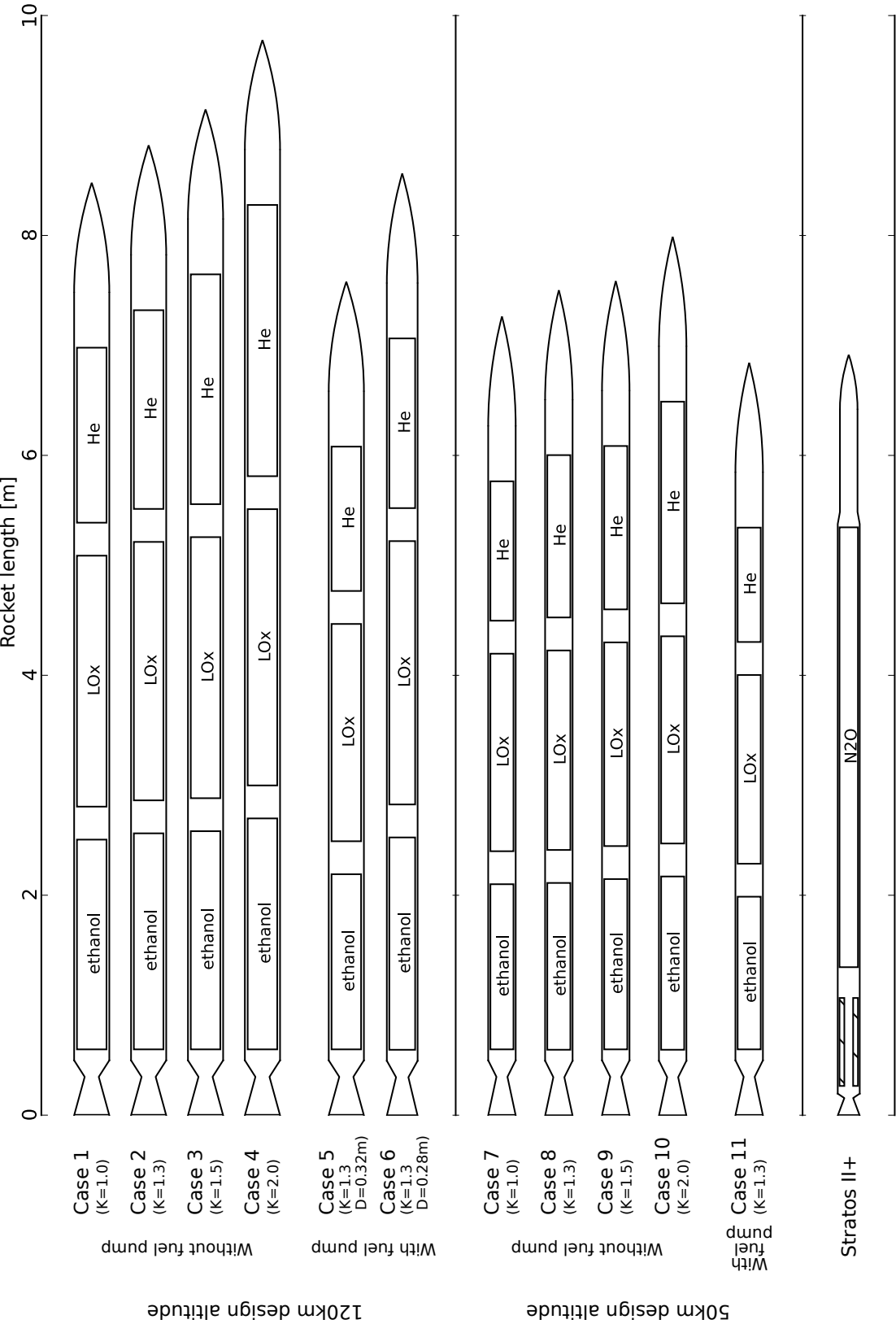
Figure 2.3: The rocket design cases generated with the design evaluation script drawn schematically to illustrate the relative dimensions of the tanks, the rockets, and the effect of the uncertainty in the collapse factor K. The Stratos II+ rocket drawn at the bottom is shown as a reference to given an impression of size. Fins on the rockets are not drawn.

Table 2.2: Sizing parameters resulting from the design evaluation script for rockets designed to achieve 120km altitude.

		No fuel pump				Fuel pump	
Case number		1	2	3	4	5	6
Diameter	m	0.32	0.32	0.32	0.32	0.32	0.28
Collapse factor	-	1.0	1.3	1.5	2.0	1.3	1.3
Thrust	kN	27.0	27.6	28.2	29.5	23.8	22.0
Burn time	s	23.7	23.7	23.5	23.3	24.2	24.2
L/D	-	26.5	27.6	28.4	30.5	23.7	30.5
T/W	-	6.5	6.5	6.5	6.5	6.5	6.5
Pressures							
Combustion	bar	25.2	24.6	24.0	23.2	30.6	30.4
LOx tank	bar	32.8	32.2	31.7	31.0	38.6	38.1
Fuel tank	bar	32.1	31.5	30.8	30.1	5.0	5.0
Masses							
Rocket full	kg	423	434	442	463	373	344
Propellant	kg	278 (66%)	286 (66%)	292 (66%)	306 (66%)	240 (64%)	222 (64%)
Helium	kg	3.5 (0.8%)	4.1 (0.9%)	4.5 (1.0%)	5.6 (1.2%)	2.8 (0.8%)	2.6 (0.8%)
LOx tank	kg	28 (6.5%)	28 (6.4%)	28 (6.3%)	28 (6.1%)	28 (7.5%)	24 (7.0%)
Fuel tank	kg	24 (5.7%)	24 (5.6%)	24 (5.5%)	25 (5.3%)	11 (2.9%)	9 (2.5%)
Helium tank	kg	25 (5.8%)	27 (6.2%)	29 (6.5%)	33 (7.1%)	22 (5.9%)	18 (5.1%)
Lenghts							
Rocket	m	8.5	8.8	9.1	9.8	7.6	8.5
LOx tank	m	2.3 (27%)	2.3 (27%)	2.4 (26%)	2.5 (26%)	2.0 (26%)	2.4 (28%)
Fuel tank	m	1.9 (23%)	2.0 (22%)	2.0 (22%)	2.1 (21%)	1.6 (21%)	1.9 (23%)
Helium tank	m	1.6 (19%)	1.8 (21%)	2.0 (22%)	2.5 (25%)	1.3 (17%)	1.5 (18%)
Volumes							
LOx tank	l	174	174	181	189	151	137
Fuel tank	l	143	151	151	159	126	114
Helium tank	l	117	137	149	186	95	86

parameters it is seen that burn times remains fairly unchanged. Combustion chamber pressure drops with increasing collapse factor. The optimum design shifts to lower chamber pressures because this lowers the pressure in the oxidizer tank, and thus also reduces the amount of helium required for pressurization via formula 2.1. The helium tank volume and mass go up 60% between the two extreme cases and in this way impacts the design sufficiently to cause this shift in optimum. The helium tank increase does not go linearly with the collapse factor, because the collapse factor for the fuel is kept at 1.

At the same time thrust increases with increasing collapse factor. This can be explained by the thrust to weight ratio: For all cases this value is at the maximum of 6.5, and thus the thrust is linearly increasing with the increasing mass of the rocket. This is a result of the simplifications made in the script. Gravity losses decrease with decreasing burn time, but the script does not incur the penalty of higher drag that this would normally also bring about. Therefore it has no proper feedback to limit thrust.

Cases 5 and 6 are interesting to inspect because of the large contrast they provide with the nominal case (number 2). The cases with pump show a decrease in total system mass of 15% and 20%. All tanks have reduced in size, and combustion chamber pressure and oxygen tank pressure went up. The effect of changing collapse factor is however still just as influential as with the fully pressure-fed cases. Changing the collapse factor between 1.0 and 2.0 increases rocket length by around 16% and increases rocket mass with 9%. These cases are not displayed in the figures or the tables.

Important to note on pressures is as well the influence of the feed system and injector pressure drop. The full rocket design is quite sensitive to this pressure drop, as any increase in it, increases the tank pressures or decreases chamber pressure. The first effect couples back into the sizes and

Table 2.3: Sizing parameters resulting from the design evaluation script for rockets designed to achieve 50km altitude.

Case number		No fuel pump				Fuel pump
		7	8	9	10	11
Diameter	m	0.25	0.25	0.25	0.25	0.25
collapse factor	-	1.0	1.3	1.5	2.0	1.3
T	kN	15.2	15.5	15.6	15.9	14.7
tb	s	20.6	20.4	20.2	20.2	20.6
L/D	-	29.1	30.0	30.3	32.0	27.4
T/W	-	6.4	6.5	6.5	6.5	6.5
Pressures						
Combustion	bar	26.8	26.8	24.4	24.6	29.0
LOx tank	bar	33.0	33.0	30.2	30.5	35.6
Fuel tank	bar	32.8	32.8	30.0	30.2	5.0
Masses						
Rocket full	kg	240	243	245	250	231
Propellant	kg	134 *(56%)*	135 *(56%)*	138 *(57%)*	141 *(56%)*	128 *(55%)*
Helium	kg	1.7 *(0.7%)*	2.0 *(0.8%)*	2.0 *(0.8%)*	2.5 *(1.0%)*	1.4 *(0.6%)*
LOx tank	kg	14 *(6.0%)*	15 *(6.0%)*	14 *(5.7%)*	14 *(5.7%)*	15 *(6.4%)*
Fuel tank	kg	13 *(5.4%)*	13 *(5.3%)*	12 *(5.1%)*	13 *(5.0%)*	6.4 *(2.8%)*
Helium tank	kg	12 *(5.0%)*	13 *(5.4%)*	13 *(5.4%)*	15 *(6.1%)*	11 *(4.6%)*
Lengths						
Rocket	m	7.3	7.5	7.6	8.0	6.8
LOx tank	m	1.8 *(25%)*	1.8 *(24%)*	1.9 *(24%)*	1.9 *(24%)*	1.7 *(25%)*
Fuel tank	m	1.5 *(21%)*	1.5 *(20%)*	1.5 *(20%)*	1.6 *(20%)*	1.4 *(20%)*
Helium tank	m	1.3 *(17%)*	1.5 *(20%)*	1.5 *(20%)*	1.8 *(23%)*	1.0 *(15%)*
Volumes						
LOx tank	l	83	83	88	88	79
Fuel tank	l	70	70	70	74	67
Helium tank	l	57	67	67	84	46

masses of the propellant tanks, and also heavily influences the size and mass of the helium tank. The second effect has a high effect on performance in this design evaluation because sea level thrust is assumed. Within the script the propellant lines and valves have been set relatively large to reduce the pressure drop in the lines to roughly 2 to 3 bar.

It is furthermore interesting to note that the total mass of the helium inside the tank is in all cases less than 1.5% of the total rocket mass. So although the amount of helium on board changes by more than 50%, it only has effect on the total mass of the rocket by virtue of the mass of the tank in which it is contained. Overall it is clear that the helium tank has a large effect on the shape and size of the rocket. Basically all three tanks in the rocket are of similar volume.

A similar analysis has been conducted for designs aiming to break the student amateur record. The design altitude for these cases has been set at 50 km. The minimal diameter found for these cases was 0.25 m. For the cases with a fuel pump, the diameter could not be further reduced, as the beneficial effect of a fuel pump becomes of less importance the smaller the rocket becomes. The cases found are displayed in figure 2.3, with the corresponding values shown in table 2.3.

Again it is directly clear that the collapse factor has a large effect on the total length and mass of the rocket. The increase is however smaller than that found for cases 1 through 4. The difference in length is 10% between cases 7 and 10, while the mass increases with 4%.

Similar trends in the variables can be observed, although they are all less strong. They are largely limited by the maximum specified thrust to weight ratio of 6.5, except for case 7, which goes just under this value. Case 10 is instead limited by the maximum length over diameter ratio of 32, and the trends of decreasing chamber pressures and tank pressures is therefore not valid for this case.

Case 11 shows the evaluated design with a pump in the fuel line. The advantage of the pump is

visible, but is less of a significance as it was between cases 2 and 5. The effect is mainly on the length of the rocket, which decreases with 10% because of the pump. This is mainly due to the helium tank that reduces 30% in volume.

2.4. Conclusions and recommendations

Using the design evaluation script it is clear that the design of a pressure fed, cryogenic rocket is highly dependent on the value of the tank collapse factor. From the evaluation it is clear that, although it is a bipropellant engine, the rocket would need three similar sized tanks. The tank containing the helium for pressurization is just as big and just as heavy as the LOx and ethanol tanks. Although the helium is stored at a much higher pressure, its tank mass turns out to be roughly the same only because it was assumed that the helium tank could be constructed out of carbon fibre, instead of aluminium. Overall this simple analysis already shows that quite quickly the usage of pumps has the potential to offer large advantages in the design of a rocket. Pursuing the design of a small pump is highly recommended for the society DARE, but for now a working design is unfortunately not yet in range.

For now DARE will however need to rely on pressure-fed rocket engine systems and it is thus important to get a grip on the estimation of the collapse factor. The analysis done with this script shows that the current uncertainty in collapse factor can result in 10% under- or overestimation of the tank rocket mass during design, and even a 15% mismatch in rocket length. This effect even holds when a pump is used for the ethanol fuel. Clearly the uncertainty in the collapse factor needs to be addressed.

If future researchers are going to look into more detailed design of a LOx-ethanol rocket it is recommended that more effort is put into the simulation of aerodynamic drag and the effect of altitude on the engine performance. The estimations used within this script are likely a good ball-park figure, but certainly when burn time is increased (and thus part of the burn time is higher up in the Earth's atmosphere) the results might deviate quite substantially.

Using the designs generated with the script, and evaluating their designs from tables 2.2 and 2.3, the following parameter ranges have been selected for which a useful pressurization system sizing tool should give reliable results:

1. Tank pressures in the liquid oxygen tank vary between 30 bar and 40 bar.

2. Tank diameters range between 0.25 m and 0.32 m.

3. Liquid oxygen tank volumes range between 80 L and 190 L. (Using 10% ullage.)

4. Helium tank volumes range between 60 L and 190 L.

5. Rocket burn time is between 20 s and 25 s.

Of these ranges the biggest uncertainty is likely to be found in the rocket burn time. As the script does not do a trajectory or aerodynamic analysis it is optimizing towards an instantaneous shot (because it uses ideal rocket theory) and is only limited by the maximum thrust to weight ratio of 6.5. If aerodynamic analysis is done this likely decreases thrust and increases burn time for the rocket. If, via this analysis, the thrust to weight ratio would drop towards the set minimum of 4.0, the burn time would likely increase with around a factor of 6.5/4.0 to give values in the range of 27s to 34s.

3

Numerical simulations

The analytical approaches to tank pressurization as available from literature (section 2.1) offer a first order estimated on the amount of pressurant gas required. However, as is evident from the spread in tank collapse factor, the uncertainty in the amount is still sufficiently large that it significantly affects the size of the whole rocket (chapter 2). To get a more accurate estimates for the collapse factor of a certain rocket system, a numerical simulation program was developed during this thesis. In this chapter the structure of the program is elaborated. The performance of the code is evaluated with respect to a simulation case that matches the hardware test setup (chapter 5). Based on the simulation results it is concluded that the code generates plausible predictions for tank pressure and propellant mass over time, as well as a credible prediction for the collapse factor.

It has been chosen to develop the code in the Python programming language (version 2.7.10), making use of the CoolProp thermodynamic library for Python (version 6.0.0)[13]. These are both open-source, freely available packages that are used extensively in academic research (and it is software which the author was familiar). It has been chosen to start development from a lumped parameter model and to then further develop this into 1D.

Lumped parameter models are relatively straightforward models that are the common first approach to take for the analysis of thermodynamic systems. An example of such a model can already be found with Ring in 1964[52], in his discussion of tank pressurization. The model developed here has much to thank to Ring, but improves on it by being able to use modern day computing power and more advanced numerical tools and thermodynamic databases (more on the comparison between the work of Ring and this work in section 3.1).

A 1D code is the logical next step in development from a lumped parameter model, and is often implemented to investigate tank pressurization[21, 44, 60]. However, as mentioned in the literature discussion (section 1.2.1), the available codes are not developed with the high pressures and small dimensions in mind during this research. The next step onwards from 1D would be further development into multiple dimensions, but as indicated in the research plan (1.4) this is not within the scope of this thesis.

Section 3.1 starts with an introduction of the simulations created. It concerns various versions of a code that has been developed from a so called lumped parameter model into various versions of 1D simulation models. The general setup of the programs and some of the main assumptions are describe in this section.

The heat and mass transfer assumptions, mostly in relation to the ullage gas in the tank, are a bit more complicated in nature and merit their own section in this chapter: section 3.2. The heat transfer assumptions are also considered the most uncertain assumptions within the model.

Section 3.3 describes the verification of the simulation's subsystems and the simulation as a whole. In the discussion of the typical output graphs of the code it also gives a clear explanation of the various processes ongoing during the whole pressurization and expulsion.

The results of the simulation for the hardware test setup are described in 3.4. Here also the different versions of the code are compared to each other. Section 3.5 presents a sensitivity analysis

relating the influence of input parameters to various output parameters. Finally the conclusion and recommendations for future work are presented in section 3.6.

3.1. Lumped parameter and 1D models

This section of the report describes the way the various computer models are structured and implemented. Section 3.1.1 elaborates the lumped parameter model (LPM), which is the basic model that has been developed during this thesis. Based on this first model a number of improvements were made that essentially developed the lumped parameter model into a 1D simulation of the system. The step by step development of this is given in section 3.1.2. Section 3.1.3 covers a number of parts of the model that are generic to all versions and that may also be directly usable by others as a 'plug-and-play' simulation object.

3.1.1. Lumped parameter model

The first model that was developed concerns a so called lumped parameter model. This is a model consisting of a small number of nodes that are interconnected. Each node represents a certain volume within the system with uniform properties (pressure, temperature, mass, etc.). The program links the nodes together by determining mass and energy transfer between them over a certain time interval. The in- and outflow of mass and energy is then used to determine new properties of the node at the end of the interval. The process is repeated for each next timestep. In this way the evolution of the system over time is simulated.

Comparison to Ring

A model like this is the most simple type of model that can be constructed for any type of physical system. A model specific for the pressurization of a propellant tank has actually already been described in full by Elliott Ring in his 1964 book on pressurization systems[52]. He presents a generic program flowchart for a tank pressurization simulation, followed by an overview of the physical equations used in each step. As his program is from the real days of infancy of computer simulations, his program is still very simple and straightforward. It does however include all important parameters and mass/heat transfer mechanisms that are of relevance in any lumped parameter representation of the system. Although computer capabilities have changed over the years, physics has not.

The program described by Ring is the main source of inspiration of the lumped parameter model described in this section, but the advances in computational power since his time allow for a large improvement on this part of his work. Of course a large improvement on prediction capabilities and ease of use is already achieved by the current day possibility to perform these simulations on any normal laptop within seconds at a far greater time resolution then in 1964. In that time such a simulation would "necessitate the use of a large-scale high-speed digital computer" (Ring [52]). The larger availability of software tools allows to make use of thermodynamic databases such as CoolProp to take into account real-gas effects, something which was not available to Ring. Also the lumped parameter model from this thesis has a greater degree of interconnectivity between nodes, such as the dependency of mass inflow rate on other system parameters, which is not present in the model from Ring.

Finally, something that has been attempted to keep in mind during development of this program is the modularity. The simulation by Ring is a very strict, linear, single script program that is constructed for one purpose only, without flexibility. During the development of this lumped parameter model an attempt was made to structure nodes and physical subsystems by means of Python objects and functions. This was done to improve code readability but also to hopefully easily allow future researchers to take snippets of the code which they can use in their own programs, or to replace parts of the code to improve the simulation as a whole. Examples of sections of code that could be of direct interest to other engineers are various thermodynamic or material property classes, or the pressure regulator simulation. Sections that could be replaced to provide better results are for example the functions that calculate heat transfer between sections.

Model nodes and interfaces

As introduced, the lumped parameter model consists of a number of different nodes between which mass and heat transfer is computed. The tank structure that is simulated is shown in figure 3.1. The different labelled sections of the system represent the nodes. The connections between them are

shown with arrows. Below here the different nodes are elaborated. For details on the heat and mass transfer between nodes, see section 3.2.

The nodes that are used in the program represent the following sections of the pressurant system:

1. pressurant gas within the pressurant tank

2. ullage gas section within the propellant tank

3. propellant liquid section within the propellant tank

4. pressurant tank wall

5. propellant tank top bulkhead

6. propellant tank wall in contact with ullage gas

7. propellant tank wall in contact with propellant liquid

8. propellant tank bottom bulkhead

The environment has specifically not been included as a node within the model. It has been assumed that the tanks are sufficiently insulated such that, within the short time frame that the expulsion takes place, heat transfer from the outside can be neglected.
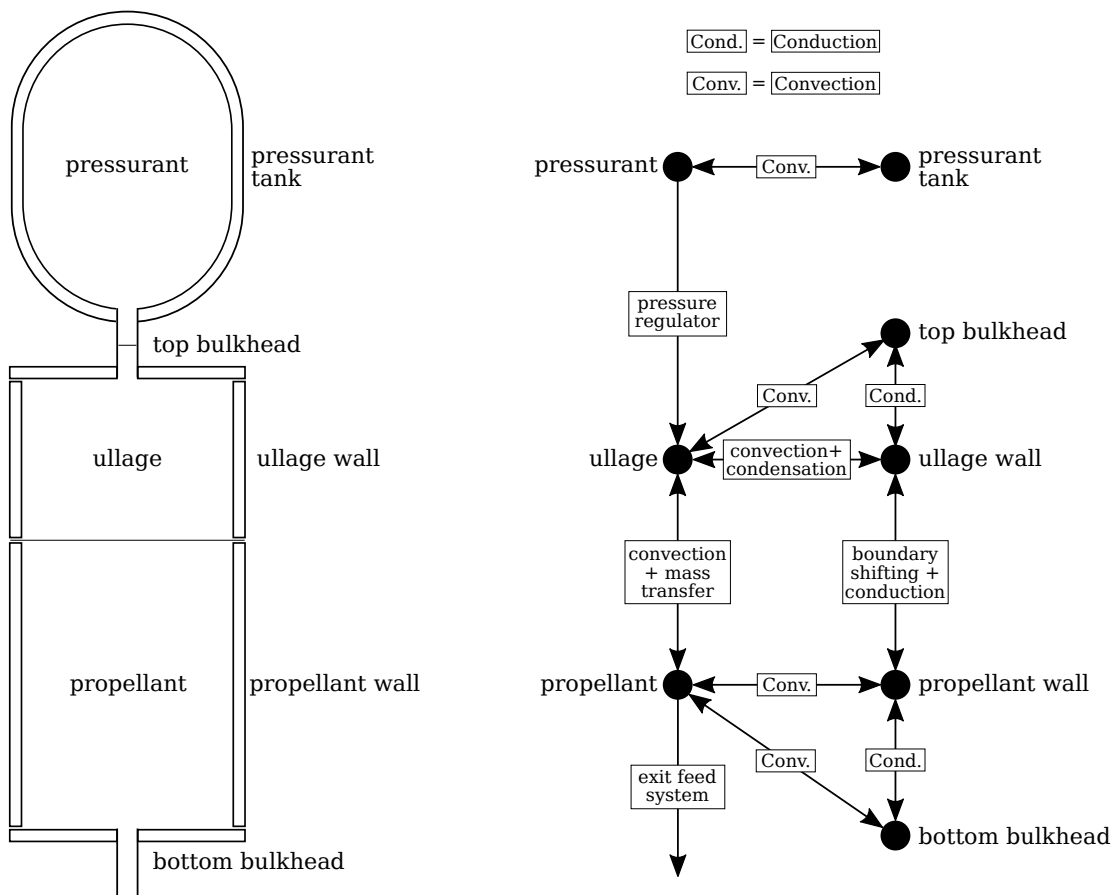
Figure 3.1: The schematic representation on the left shows the positioning of the different thermodynamic nodes within the system. The node network on the right shows how they are connected, and what kind of relations or models govern the connections between them.

The system model consists of three fluid sections and the tanks that contain them. The first fluid section is the pressurant gas. This is a section consisting of a single gas species that is modelled using an extended CoolProp HEOS model class (see section 3.1.3). During program initialization the initial gas pressure, temperature and volume need to be specified, along with the gas specie.

Gas mass and energy flow via a pressure regulator from the pressurant gas section into the ullage gas section. The pressure regulator determines the flow based on the properties of both fluid sections and the time step dt. The total energy flow is equal to the enthalpy that associated with the amount of gas mass that moves from one section to another.

The ullage gas section is the part of the simulation that merits the most attention. The ullage gas can be modelled as a single species fluid (using the same species as the pressurant gas) or as a multi-species fluid (using the pressurant gas and propellant species). Which is used can be set at program initialization by stating the mass ratio between these species. Furthermore initial temperature and pressure need to be specified. Volume is determined by the total propellant tank volume and the ullage fraction. Mass flows into the ullage section from the pressurant gas section and possibly via evaporation from the propellant section. Condensation can also occur via the interface with the propellant section or with the ullage tank wall section. Heat flows in from the pressurant section, and can also be exchanged with the tank top bulkhead, the ullage tank wall section, or the propellant. Finally, the ullage section also loses energy in the form of work via the first law of thermodynamics. The work done because the gas expands to push the propellant out of the tank.

The propellant section is a single species liquid section. It starts off at a certain pressure, temperature and volume and is assumed to be incompressible, i.e. density is constant. Mass can be gained or lost via condensation or evaporation at the ullage gas interface. Heat can be conducted to or from the tank propellant wall section or the tank bottom bulkhead. Propellant mass can flow out of the tank within the time interval that is specified at program initialization. Within this time interval the propellant flow out of the tank is calculated using a function that takes the propellant fluid section properties and determines from this the mass flow through a square-edged orifice. It is assumed that the mass flow is limited by cavitation occurring in the orifice. I.e. the pressure inside the orifice is equal to the vapour pressure of the liquid, and thus the mass flow is limited by the difference between this vapour pressure and the tank pressure.[33] The orifice discharge coefficient was chosen to be 0.6.[18] It was found using initial calculations that the tube and valve in-between tank and orifice have a negligible effect on the pressure drop compared to the orifice itself. This determination of mass flow represents the situation as seen during the validation tests conducted during this thesis (chapter 7). The structure of the program is however so, that this function can be directly replaced for some other function that takes some system parameter as input and gives a flow rate as output. This can be used to implement any mass flow relation desired (i.e. any type of feed system after the tank).

Next to the three fluid sections, there are four tank sections to simulate the propellant tank wall, and one to simulate the pressurant tank. The propellant tank is divided into two flat bulkheads and two cylindrical wall sections. The sections are all modelled as aluminium where heat capacity and conductivity are changing with temperature. They exchange energy via conduction amongst each other, and via convection, evaporation and condensation with the ullage gas and propellant. The boundary between the two wall sections is placed at the same height as the liquid level of propellant and moves down over time along with the liquid level. This creates a 'flow' of tank wall mass and energy from the bottom section to the top. The pressurant tank wall is modelled as a static cylindrical tank that only is able to exchange energy via convection with the pressurant gas.

Model logic

The model logic is shown in figure 3.2. The simulation program starts with initialization of all sections. After that the program starts into a loop that progresses over time by moving a fixed timestep into the future during each loop. The timestep is in general set to be around 10ms. During the loop the heat and mass transfers across al interfaces are calculated based on the instantaneous properties of all sections. Changes in mass, energy and volume are added or subtracted to so called 'change parameters' that are kept for each section. After all interfaces are processed, each section is updated individually. The update progress takes the values of the change parameters and evaluates what these changes in mass, energy and volume have as effect on the other state parameters such as temperature and pressure. After this the change parameters are reset to zero and the program proceeds into the next loop. This continues until a specified end time is reached, or the propellant section has been fully drained.

The updating of the individual sections does not need to be done in a specific order, except that the ullage section must be updated before the propellant section. This is needed, because the change in pressure for the propellant section is set to be equal to the change in pressure of the ullage section.

```
┌──────────────┐   ┌──────────────┐   ╱───────────╲        t + dt
│  parameter   │──▶│ initialization│──▶⟨  start of   ⟩─────────────────┐
│initialization│   │  of sections  │   ⟨ time loop  ⟩                  │
└──────────────┘   └──────────────┘   ╲───────────╱                    │
                                            │                          │
                                            ▼                          │
                   ┌───────────────────────────────────────────┐       │
                   │ determine mass transfer between:            │       │
                   │ • fluid sections (mass flow,                │       │
                   │   evaporation/condensation)                 │       │
                   │ • tank sections (mass transfer between top  │       │
                   │   and bottom wall section)                  │       │
                   └───────────────────────────────────────────┘       │
                                            │                          │
                                            ▼                          │
                   ┌───────────────────────────────────────────┐       │
                   │ determine heat transfer between:            │       │
                   │ • fluid sections (convection, evaporation/  │       │
                   │   condensation, mass flow, work done by     │       │
                   │   expansion)                                │       │
                   │ • fluid section and tank sections           │       │
                   │   (convection)                              │       │
                   │ • tank sections (conduction and mass transfer)│     │
                   └───────────────────────────────────────────┘       │
                                            │                          │
                                            ▼                          │
                          ┌────────────────────────────┐               │
                          │   update all tank sections   │               │
                          └────────────────────────────┘               │
                                            │                          │
                                            ▼                          │
                                   ╱──────────────╲         no          │
                                   ⟨  stop time     ⟩────────────────────┘
                                   ⟨ or propellant  ⟩
                                   ⟨  tank empty?  ⟩
                                   ╲──────────────╱
                                            │ yes
                                            ▼
                          ┌────────────────────────────┐
                          │   store and/or display       │
                          │          results             │
                          └────────────────────────────┘
```
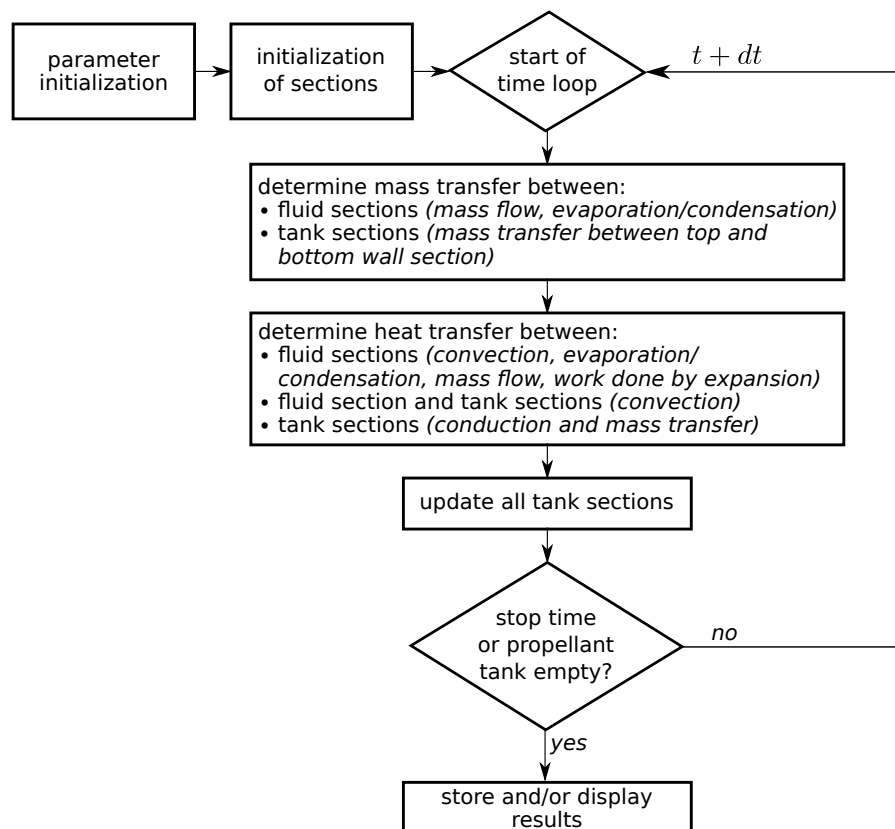
Figure 3.2: The logic of the numerical models showing the flow of the program.

This change in pressure is however only known after the update of the later. This method of direct pressure balancing has been chosen in favour of a method in which both sections would determine their changes in pressure individually based on the mass, energy and volume changes. This latter method would require an iterative procedure to equalize pressure between the sections by allowing changes in density, and thus volume. A difference in pressure would mean the high pressure section would slightly expand, which means the low pressure section would need to slightly compress as the two sections together occupy a fixed tank volume. This expansion / contraction would however result in an exchange of energy via work. This energy exchange would in turn influence the temperature and thus pressure of the sections again. Instead it was chosen to simplify this by assuming constant density for the liquid and setting its pressure based on the ullage gas pressure. All fluid properties of the propellant (specific energy, viscosity, thermal conductivity, etc.) are still evaluated on the correct pressure and temperature. Only density is fixed at the start based on a reference pressure and temperature that are given by the user.

3.1.2. Elaboration into 1D

The lumped parameter model was the first attempt to simulate the tank pressurization system. It was constructed in a simple way to try and see if it would be possible to already get realistic simulation results to estimate pressurant gas mass requirements. In general a simple simulation would be preferable because it requires less time to run and can thus be more easily implemented in an iterative design process. However, it was suspected that the simple simulation might have some specific drawbacks that would hinder its accuracy. This mostly concerns the absence of the modelling of temperature gradients or the effect of injection methods, which is thought to be of important influence on the collapse factor (section 1.2). A lumped parameter model by definition has a homogeneous temperature distribution per section. Therefore, the lumped parameter model was taken and further developed into a 1D model where the ullage is split into multiple distinct nodes.

This development progressed in two main steps. In the first step the propellant tank wall has been split up into a large number of small, static sections. This can in place of the two large, changing

sections used in the lumped parameter approach. This allows vertical temperature gradients in the wall to exists. The 'flow' of wall material from the bottom section to the top is removed and instead the liquid level and the vertical position of each wall slice determines for each slice individually whether heat transfer happens from the slice to propellant or ullage. Heat transfer inbetween the segments happens via conduction.
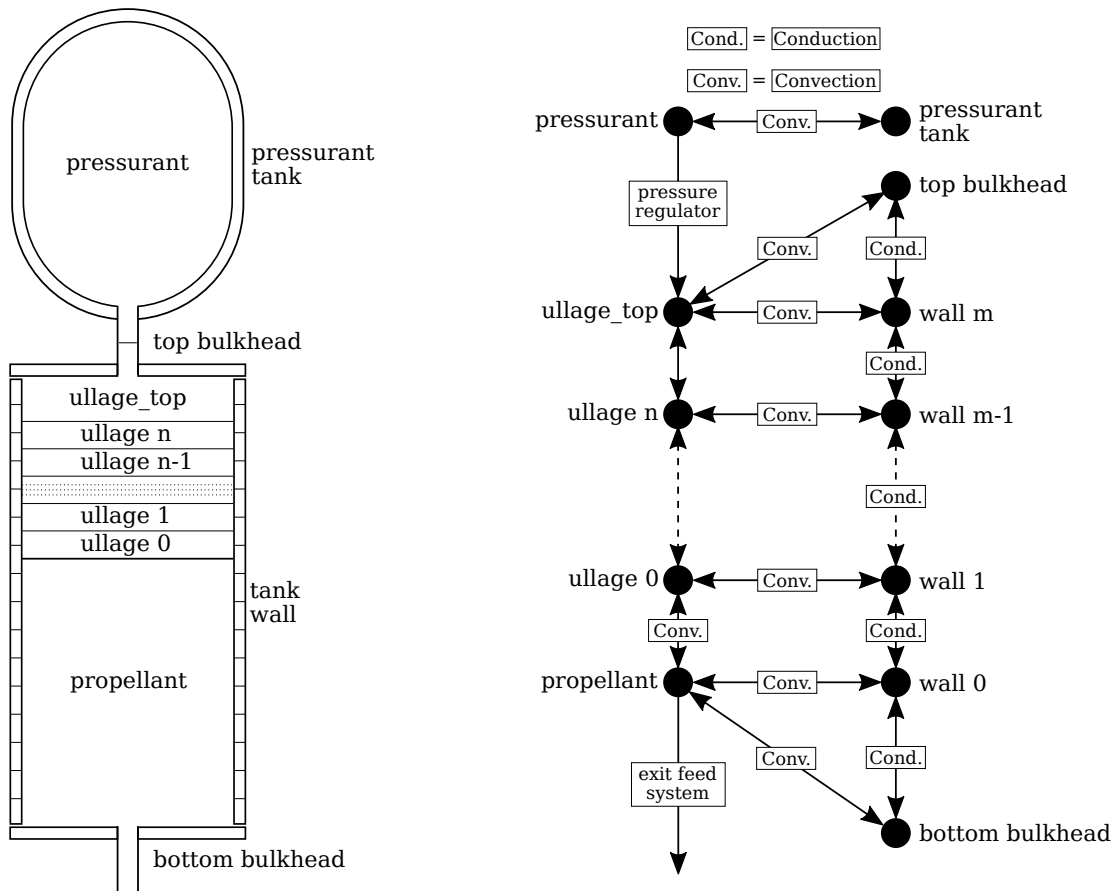

Figure 3.3: The elaboration of the LPM code into 1D means that the ullage and tank wall are split into a large number of identical sections. This is illustrated schematically on the left. The connections of the nodes on the right clearly shows how the 1D model is an evolution of the LPM model with more nodes and a more complicated way of connecting all the nodes. (Compare figure 3.1.)

The second step is to restructure the ullage section in a similar way as the wall to allow for temperature gradients to exist. This has been done in two ways again: splitting the ullage into horizontal slices or splitting it into concentric cylinders. The first allows vertical temperature gradients to build up, while the second one allows radial temperature gradients. The two models are shown schematically in figures 3.3 and 3.4. Comparing the models shows that they are similar with respect to the nodes, but only differ in the way the nodes are interconnected. It has been decided to construct both of these models as the hypothesis of this thesis is that either one of these types of gradients is more pronounced, depending on the type of injection (vertical gradient due to radial injection, radial gradient due to axial injection).

These models have been constructed such that each ullage section has a constant volume over time, with an exception for the top or core section respectively. These special sections grow over time as new pressurant gas flows in. As soon as they have reached more than two times the standard volume of one section, a new section is created as a split off from the top/core section. The constant volume requirement means that only the top/core section does pressure work. Mass (and with it, energy) transfer across section boundaries in the ullage is possible.

The split of the ullage section does however bring with it the complication that some form of pressure equalization method is needed again, just like with the ullage and propellant section in the lumped
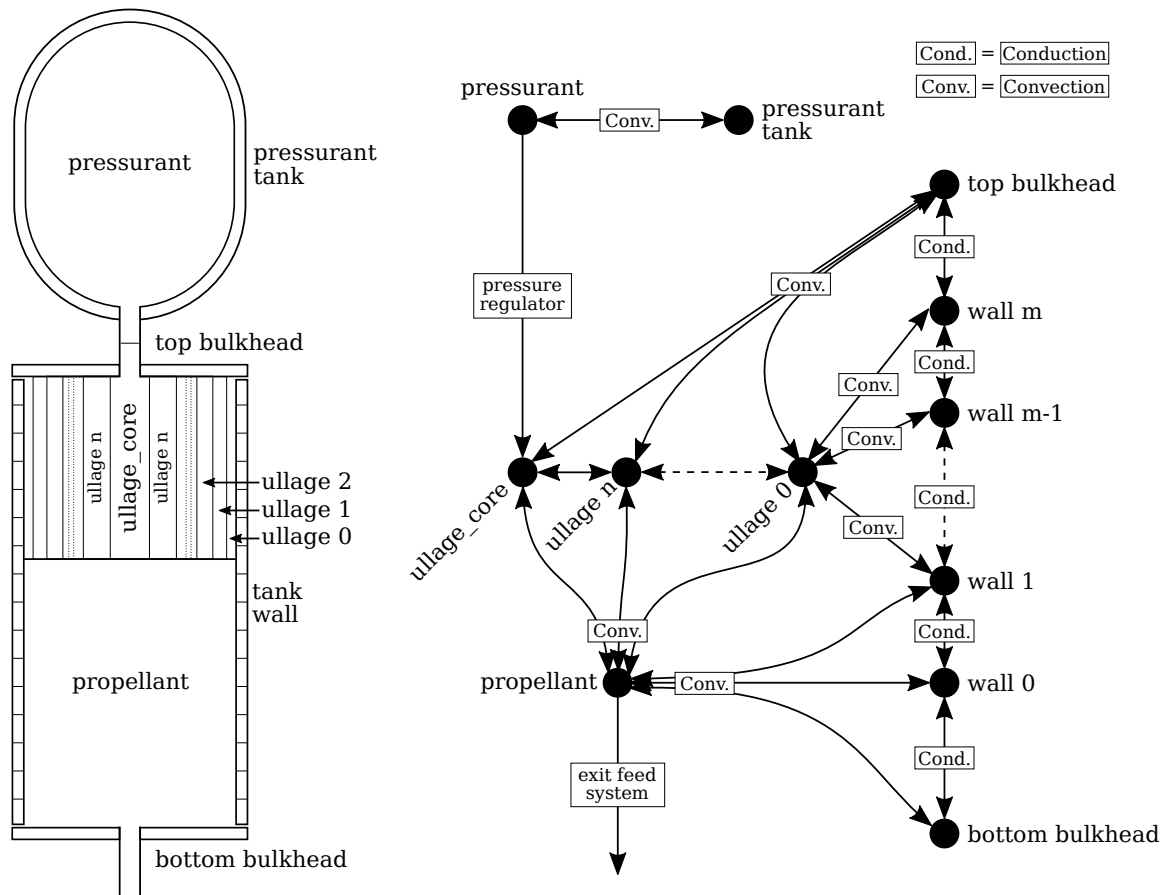
Figure 3.4: The first step in elaboration of the lumped parameter model is to split the tank wall into a large number of equal slices, allowing vertical temperature gradients to exist in the tank wall.

parameter model. Normally a 1D CFD model would accomplish this by itself by allowing mass to flow between sections, based on the pressure differential, contact area and various fluid properties such as viscosity. However if this needed to be implemented in this code, it would constitute a very large elaboration of simulation methods, optimization of solver routines, and a significant reduction of the time-step size that could be used. As code and simulation optimization in this way is not the goal of this thesis, it has been decided to instead opt for a pressure equalization routine between the ullage sections that is conducted each time-step. This routine computes a required mass and associated energy flow between two neighbouring ullage sections to equalize pressure between them. This routine then iterates a number of times over the whole ullage, shifting mass and energy between neighbouring sections, until the pressure difference within the ullage sections is below a certain threshold (usually set to 100 Pa).

The construction of these 1D models from the lumped parameter model was actually a relatively simple process when starting from the lumped parameter model. Due to the structured setup of this model, it was possible to develop it into a 1D model with relative ease as the largest part of the work was completed by simple creating more instances of the classes that represented the original ullage and wall sections. This is illustrated by figures 3.1, 3.3 and 3.4, which clearly show the similarities in the nodes used. The bulk of the work was in the creating of the pressure equalization method for the ullage sections.

3.1.3. Modelling of sections, components, and materials
The numerical models are created by linking a number of sections and components together. These sections are modelled in relatively similar ways. All are implemented as Python classes with certain properties. The pressurant gas in the pressurant tank and the propellant are both modelled by a single species CoolProp HEOS object that has been extended to include values for total mass, volume and

energy, and includes dimensions (length and diameter). The ullage gas section is either modelled by a similar gas model or by a multiple species gas model. The tank modelling objects are constructed from scratch, based on available literature data for material properties of aluminium at cryogenic temperatures. A pressure regulator has been modelled based on available flow curves for the pressure regulator used during flow tests.

CoolProp HEOS model: single species
The code developed during this thesis relies on the open-source thermodynamics library CoolProp for its analysis of the thermodynamic states of fluid properties. The CoolProp libary evaluates these properties based on certain state parameters via an Helmholtz equation of state[13]. The Python library for CoolProp offers the possibility to make use of Python class structures to facilitate the calculation of the state parameters. A CoolProp object can be initialized with a certain gas species and two state parameters (e.g. pressure and temperature). Other fluid properties, such as viscosity, specific heat, etc. can then be gotten by methods associated with this object. When desired, the state parameters of the object can be changed, after which the object methods will return the fluid properties for the new state. This type of object will in this report be called a HEOS object ("Helmholtz Equation Of State").

An HEOS object can be defined by all possible combinations of two state parameters. Which parameters are used depends on the section in the simulation which they concern. The pressurant gas section is defined by the density and specific energy, as these are also the values with which the main program does its bookkeeping. The propellant section is defined by specific energy and pressure, as its density has been defined to be constant. The ullage section is defined by density and specific energy as well, unless it consists of multiple species. See the next section for details on this.

The standard HEOS object defined by CoolProp only concerns specific fluid properties such as density and specific energy. However for the simulation it is also required that the sections have a total mass, total volume, and total energy. Next to these variables, a number of bookkeeping variables are required (such as the change variables) and also various shape parameters such as length, diameter and area. To keep track of this these variables are all combined in an extended HEOS class that is a wrapper around the basic CoolProp structure.

CoolProp HEOS model: multiple species
The HEOS object provided by CoolProp can be initialized with a single species of gas or with a mixture of species. In the later option the class also requires the specification of a molar fraction of the components. The properties it returns are an estimation of the properties of the mixture. In general the mixture handling of CoolProp is however not yet as fully developed as the single phase mixtures. This is due to the complexity of the mixture formulas in comparison to the single specie equations. Because of this, the state of the mixture can as of yet only be specified by using a combination of two parameters out of temperature, pressure, or quality.[1].

This limitation however presents a problem for the general structure of the code. As the code does bookkeeping between the sections by counting flow of mass and energy, the preferred method to set the HEOS state is by means of density and specific energy. This is however not possible for mixtures. What has been done in the model to work around this, is to retrieve the first partial derivatives of the temperature and pressure with respect to density and internal energy. These derivatives are something that can be provided by CoolProp. Using these derivatives, the changes in density and internal energy can be translated in changes in changes in temperature and pressure. E.g. $\Delta T = (\partial T/\partial \rho)\Delta \rho + (\partial T/\partial u)\Delta u$.

Working around the structure of CoolProp like this however has two main limitations. First, extra care needs to be taken concerning evaporation and condensation. Within the code it should be checked that both gasses in the mixture are actually mixed within a gaseous state. If one of the species starts to condense, this needs to be removed by mass transfer towards the propellant section instead of remaining in the ullage section. If it would remain in the ullage the modelling of interfaces would not make physical sense any more, and the HEOS object would likely start to give erroneous results (if it does not fail in computational error and is able to find a solution at all). Secondly, the calculation of changes in temperature and pressure using the partial derivatives is not ideal. When an extended HEOS object is requested to report its total internal energy content, it will look at the specific energy of the HEOS object, and multiply this with the density of the HEOS object and its own volume. This is

_____

[1]`http://www.coolprop.org/fluid_properties/Mixtures.html`

accurately enough if the specific energy and density are the parameters that has been used to define the state of the object. However if the state is instead defined by pressure and temperature, the accuracy in calculating the specific energy and density is not high and can lead to energy and mass 'leaks' in the code. This means that the energy and mass in the section are no longer what they are expected to be according to the main bookkeeping of the program. Mass and energy are 'leaking' into or away from the system and this can lead to wildly varying results produced by the code, or even an ever growing diversion leading quickly to computational errors where the HEOS model fails to converge. This problem was fixed in the code by checking the mass and energy mismatch within each update routine of the ullage section and correcting the temperature and pressure estimates proportionally to the mismatch. This seemed to fix the energy mismatch, but the author does not consider it a very well founded or robust solution. Ideally the HEOS model of CoolProp itself would be extended to accept density and specific energy as input parameters for its state.

Properties of aluminium
The thermodynamic properties of aluminium are required to model the tank wall sections and tank bulkheads, specifically the thermal conductivity and the thermal capacitance need to be known. Next to the simulation, these properties are also used to estimate tank cool-down and warm-up (section 5.2 and chapter 7). The mechanical properties of aluminium at cryogenic temperatures are treated in section 5.2.

The estimations for the specific heat of aluminium are taken from the paper by Buyco and Davis[17] Equation 11 from this paper is used. The function coefficients are taken from table III in the paper, for normal state aluminium, at the temperature range = 50.2689 K to 933.2 K. In general the specific heat of aluminium decreases with decreasing temperature, with the specific heat decreasing faster the colder it gets. The equation by Buyco and Davis gives a room temperature (293 K) value of 899 $J\,kg^{-1}\,K^{-1}$ and a cryogenic temperature (90 K) value of 422 $J\,kg^{-1}\,K^{-1}$.

The estimations for the thermal conductivity of aluminium are taken from the paper by Woodcraft[64], using method 9 from table II and the residual resistivity from table V in that paper for aluminium 6082-T6. The thermal conductivity of aluminium decreases with decreasing temperature. The equation by Woodcraft returns a thermal conductivity of 69 $W\,m\,K^{-1}$ at $T = 293$K and 30 $W\,m\,K^{-1}$ at $T = 90$K.

The density of aluminium is also slightly effected by temperature, as is evident from the equations presented by Marquardt et al.[45]. However, the change is very small. In general the density of aluminium increases with decreasing temperature. Using equation 5 and table 3A from the paper by Marquardt for aluminium 6061-T6, the density at room temperature (293 K) is predicted to be 2700 $kg\,m^{-3}$ and the density at cryogenic temperatures (90 K) is 2731 $kg\,m^{-3}$. This constitutes a difference of about 1%. As the total mass of the tank does not change or mix with other materials, a constant density is assumed for aluminium of 2700 $kg\,m^{-3}$. This also means no changes in tank volume are introduced due to expansion and/or contraction of the tank wall due to different temperatures.

These equations are all implemented in Python and grouped together in one class (`Aluminium6082`) to structure the code and facilitate future use or changes.

Exit feed system
At the bottom of the tank there is a feed system consisting of two lengths of tubing, a valve, and a square edged orifice. For the test setup case at least, the influence of the tubing and valve on the pressure drop over this feed-system is negligible. Therefore it has been chosen to determine mass flow through the feed system only by means of the exit orifice. This orifice is modelled as a square edged orifice with a diameter that can be set as a main input parameter for the model. The orifice discharge coefficient has a slight dependency on Reynolds number, but as there are more undefined parameters that could introduce larger differences on this value than the Reynolds number dependency, this influence is neglected for this simulation and the value is taken to be a constant 0.6[61]. Mass flow is determined by assuming the liquid is cavitating in the orifice, and thus that the pressure in the orifice throat is equal to the vapour pressure.

Pressure regulator
For the correct simulation of the tank system a pressure regulator needs to be modelled that accurately predicts the total mass flow of gas through it based on the gas properties and the pressure difference over it. Modelling codes by manufacturers of pressure regulators are in general proprietary and not available.

What is available are data curves that provide the regulator exit pressure versus flow rate given a certain cylinder pressure and regulator set pressure. The flow rate is usually given in standard cubic meters per hour, where "standard" means that the gas volume is taken at a set temperature and atmospheric pressure. Generally pressure regulator flow curves are available for relatively low values (<20 bar) of set pressure. Values for higher set pressures need to be specifically requested. For this thesis these curves were requested for the GCE druva FMD500-16 pressure regulator (which was the pressure regulator used during tests) for set pressures of 25 bar, cylinder pressures of 200 bar, 150 bar, 100 bar and 50 bar, for helium at 0 °C exit temperature. So this means 4 curves were available for characterization.

Based on these characteristic curves a pressure regulator model was created in the following way. First the curves are read out on each specific point indicated in the curve to give numerical values for exit pressure P_{exit} versus volume flow Q. This gave at least 7 points per cylinder pressure. The volume flow of the gas is converted into a mass flow $\dot{m}$ using the density of helium at the reference conditions (0 °C , 1 atm). It is now assumed that the flow of gas through the regulator can be modelled as a chocked gas flow through an orifice. This mass flow is defined by equation 3.1.

$$\dot{m} = C_d A \sqrt{\gamma \rho_0 P_0 \left(\frac{2}{\gamma + 1}\right)^{\frac{\gamma+1}{\gamma-1}}} \tag{3.1}$$

For each point of the curves for the pressure regulator, the values of the parameters are known, except for the discharge coefficient C_d and the orifice area A. These two are determined by the internal design of the pressure regulator and how far the pressure regulator has been opened by the gas pressure.

The orifice area A is determined by how far the regulator is opened. A gas regulator works by means of a plunger that opens or closes a flow orifice. Two forces work on the plunger to determine its position: An internal spring to push it to open and the pressure of the gas at the exit pushing it to close. Cylinder pressure has a negligible effect on it by design. When the pressure on the exit is higher then the set pressure, the exit pressure closes the regulator. When the pressure is to low, the spring opens the regulator to allow gas to flow. The spring pre-tension is set by the operator and in that way determines the exit pressure. Based on this analysis it is clear that the main parameter influencing how far the regulator is opened is the difference in the set pressure and the actual exit pressure: $\Delta P = P_{set} - P_{exit}$.

The second parameter, C_d, can depend on a variety of parameters that involve the gas properties, but also the flow speed[18]. It is assumed that these are largely determined by the pressure difference ΔP and the cylinder pressure P_{cyl}, as this influences the total mass flow but is also of influence on the gas properties. Other influences that are of importance here are the reference temperature and of course the gas species. The characteristic curves on which the regulator modelling is based were requested for the temperature and species that are of interest (helium at around 0 °C).

The modelling of the pressure regulator in this thesis is based on the assumption that the product $C_d A$ is a function of the pressure difference $\Delta P = P_{set} - P_{exit}$ and the cylinder pressure P_{cyl}. The values of this function can be gotten via the curves available from the manufacturer and using these curves to compute $C_d A$ from equation 3.1 for each point. Based on the curves for the GCE druva FMD500-16, 37 reference points were found. These are applicable to helium at around 0 °C and span the cylinder pressure range between 50 bar and 200 bar, and a range of ΔP between 0 bar and 20.3 bar.

The points were implemented in a Python class called `PressureRegulator` where they are interpolated using a surface bivariate B-spline representation from the Scipy interpolate library. When called, `PressureRegulator` takes the tank pressure, compares this to its internal set pressure and calculates the value for the $C_d A$ product from the interpolation. Using the pressurant tank pressure and gas properties (γ and ρ) it the uses equation 3.1 to calculate mass flow.

During implementation it was found that it was needed to introduce a time-to-open parameter into the modelling of the regulator to avoid oscillations in the system. These oscillations arose because without delay, the mass flow through the regulator changed instantaneously instead of gradually. These oscillations resulted in failure to converge for the HEOS models of the gas thermodynamic properties. The regulator delay was implemented by means of a time-to-90% parameter that needs to be set for the simulations. This parameter indicates how long the regulator needs to achieve 90% of the mass flow rate as determined by equation 3.1. The parameter was set to $t_{90\%} = 50\text{ms}$, which is believed to be a reasonable estimate.

3.2. Heat and mass transfer assumptions

Within the computer model heat and mass transfer are two of the main parameters that needs to be taken into account to accurately predict the amount of pressurant gas required. This section of the report will explain what methods of heat transfer (section 3.2.1) and mass transfer (section 3.2.2) correlations were used in the numeric models.

3.2.1. Heat transfer

Heat transfer can happen in three different ways: Radiation, conduction and convection. Radiation is neglected fully in the modelling. Overall, radiation is not a important parameter in gas dynamics as gasses are largely transparent. Furthermore the system is mainly at temperatures far below $0°C$ which also reduces the effect of radiation, because its magnitude drops with the 4th power. Conduction is mainly applicable to the tank wall and bulkheads. Conduction is governed by Fourier's law, and the heat conduction properties of the materials are computed by reference as was discussed in the previous section. The remaining heat transfer method is convection.

Heat transfer by convection is usually subdivided in two main mechanisms: forced convection and natural convection. The first concerns gas that is propelled by some external force, the second concerns gas movement caused by gravity and the difference in density due to the different temperatures. It is difficult to estimate which one is applicable in the situation of the ullage gas within the tank. The flow velocities are of the gas are relatively low (scale of 1 m/s) for forced convection and temperature differences (promoting natural convection) are very high (scale 100 K). The flow velocities caused by natural convection will thus likely be in the same order of magnitude as the velocities caused by the gas injection.

This is backed-up by the common criteria used to determine whether heat transfer in a certain situation is dominated by natural or forced convection. This criteria is given by equation 3.2[15]. The Grasshof number and Reynolds number need to be calculated for the situation in the tank, but it is difficult to determine the exact parameters that need to be put in. Is the characteristic length equal to the tank diameter or to the ullage volume height? (Both are of the same order or magnitude.) Are the gas properties determined at the inlet temperature, the wall temperature or some intermediate? As the difference in temperature can be nearly 200 K, this is an important parameter. And finally: What should be taken as the flow speed? Is it the speed at injection? But for radial injection, the speed drops significantly as the gas spreads radially outwards. The ratio Gr/Re^2 varies somewhere between ∼0.05 (low temperature, high speed) and ∼50 (high temperature, low speed). This means no clear distinction can be made on which type of convection is dominant within the pressurization system.

$$\frac{Gr}{Re^2} \begin{cases} \ll 1 & \text{Forced convection dominates} \\ \approx 1 & \text{Combined forced and free convection} \\ \gg 1 & \text{Free convection dominates} \end{cases} \tag{3.2}$$

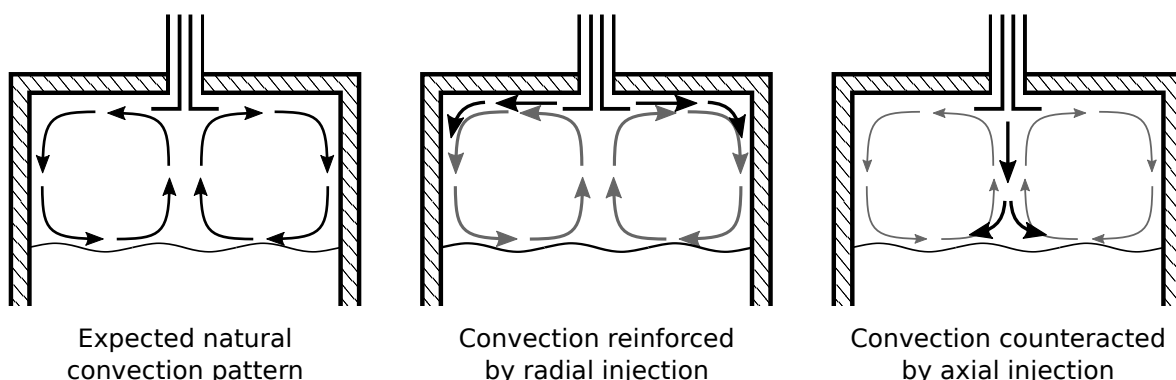|		
Expected natural convection pattern	Convection reinforced by radial injection	Convection counteracted by axial injection

Figure 3.5: A schematic representation of the expected flow patterns within the ullage volume. It is expected that radial injection will reinforce the natural convection pattern, while axial injection will counteract it.

As the two velocities from natural and forced convection are expected to be of similar magnitude,

this can already lead to an interesting conclusion, which was reached during analysis of this problem. As shown on the left in figure 3.5, the expected natural convection pattern in the tank ullage will be gas cooling down at the tank wall and thus flowing down. The gas hits the propellant surface, flows to the tank axis, and rises again there. Now if this flow pattern is compared to the flow patterns created by the radial and axial injection methods, and interesting conclusion can be reached. The radial injection, as shown in the middle drawing, will actually reinforce the natural convection pattern as the velocity vectors point in the same direction. Axial injection however, will counteract the natural convection flow, as shown on the right. The axial injection method will blow gas downward along the axis, and thus stop the natural convection updraught in the middle. Note that the actual convective pattern will likely be different, especially for the axial injection case, as it can be expected that turbulent mixing can be important here. Overall however, this observation seems to strengthen the main hypothesis of this thesis that axial injection will lead to less heat transfer from the ullage gas to the tank wall.

Returning to the problem of how to model the convective heat transfer numerically: It is decided that natural convective heat transfer equations are first implemented in the model as these will be applicable during all phases of the system operations, including the pressurization phase where the inflow of new gas is minimal.

Natural convection is most commonly modelled by means of a correlation of the Nusselt number to the Grasshof number and the Prandtl number. The Grasshof number is the ratio of buoyancy forces to viscous forces in a liquid and can be calculated based on the geometry and fluid properties. The Prandtl number is the ratio between viscous and thermal diffusion rates. It is fully a function of fluid properties, and can be directly pulled from the CoolProp HEOS model. Usually the two are combined into the Rayleigh number, which is the product of the two: $Ra = Pr \cdot Gr$. The Nusselt number is a ratio between convective and conductive heat transfer, and thus when the number itself is known, it can be used together with the fluid thermal conduction, to determine the convective heat transfer rate. Two books were used as the sources for the Nusselt number correlations. These are the "Fundamentals of heat and mass transfer" book by Incropera et al. (2011, [15]) and the "Heat transfer handbook" by Bejan and Kraus (2003, [12]).

For the tank system there are two main geometries that need to be considered. The first is that of a flat surface with a fluid above or below it. This situation is applicable to all the interfaces between the bulkheads, the propellant fluid, and the ullage gas. The second type of geometry is that of a fluid within a cylinder. This is applicable to the interface between tank wall and the propellant and ullage, and also to the pressurant gas in the pressurant tank.

For the first geometry the correlations for a warm flat plate at the bottom, and a cold flat plate at the top will be taken as given by Incropera. Bejan also lists these correlations, among others.

$$Nu = 0.54Ra^{1/4} \quad \left(10^4 \leq Ra \leq 10^7, Pr \geq 0.7\right) \tag{3.3}$$

$$Nu = 0.15Ra^{1/3} \quad \left(10^7 \leq Ra \leq 10^{11}, \text{all } Pr\right) \tag{3.4}$$

The characteristic length used for both the Nusselt number and the Grasshof number is in this case the diameter of the plate. When the situation occurs that the fluid is warmer than the plate on top of which it sits, or if it is colder than the below which it sits, the Nusselt number is assumed to be equal to one. I.e. heat transfer happens only by conduction.

For the second geometry the situation is a bit more complicated, as no Nusselt number correlations could be found that are specifically applicable to the case of a standing liquid in a cylinder. Bejan suggests that for cylinders where the radius is sufficiently large, the heat transfer coefficient can be approximated by using the correlations applicable for a flat wall instead. Bejan actually suggests this for heat convection on the outside of a cylinder, but for this model it is assumed a similar simplification can be made for the inside. A number of correlations are possible for flat plate surfaces, but the simplest (and with the largest applicability range) is the following suggested by Bejan:

$$Nu = 0.59Ra^{1/4} \quad \left(10^4 \leq Ra \leq 10^9\right) \tag{3.5}$$

$$Nu = 0.10Ra^{1/3} \quad \left(10^9 \leq Ra \leq 10^{13}\right) \tag{3.6}$$

The problem with these equations is the question if they are applicable or not. Other standard Nusselt number correlations could also be selected for the model with just as much validity to support the

choice. The heat transfer could for example also be modelled by the relations for a rectangular cavity, with a width equal to the radius of the tank. Or any of the other vertical plate correlations could be more suited. However it is not known which one is more applicable, and no well founded decision for one or the other can be made without a more extensive analysis, either via experiment or CFD analysis.

Next to the uncertainty of applicability of the correlations due to geometry, the applicability of certain correlations is also doubtful due to the conditions of the surface and the ranges of the dimensionless parameters. Heat transfer conditions are usually assumed to be be either for isothermal plates, or for constant heat flux. Neither of these two is truly applicable here. For the dimensionless parameters: During the analysis of the simulations it was found that often the Grasshof number is above the boundaries recommended by Bejan and Incropera. The Grasshof number is defined as:

$$\text{Gr} = \frac{a\beta\,(T_s - T_\infty)\,x^3}{\nu^2} \tag{3.7}$$

In this equation a is the lengthwise acceleration of the system (taken to be equal to Earth's gravity, but can of course still be around 5 times higher in an accelerating rocket). β is the coefficient of thermal expansion. T_s is the temperature of the wall surface. T_∞ is the temperature of the fluid. x is the characteristic length, equal to the height of the wall in this case. And $\nu = \mu/\rho$ is the dynamic viscosity. The specifics of the system under consideration make that this value is, within the ullage, often near the upper validity boundary of 10^{13}. This is likely because the temperature difference is often very high (~ 100 K). The absolute temperature is also relatively low, making that the value of β is generally higher. And finally the value of ν is relatively low because the system operates at high pressures and low temperatures. Density for a gas increases rapidly with increasing pressure, while viscosity is not much affected, meaning ν drops. In general it can be concluded that the situation in the tank is so out of the ordinary that, unfortunately, it is impossible to make a clear cut decision for one specific Nusselt number correlation.

In conclusion: The Nusselt number correlations that are presented in this section are the ones that are used within the simulation, however it is stressed that these equations form the largest assumption within the whole simulation. It is highly recommended that for future research more investigation is done to clarify the heat transfer mechanisms in the tank. Another option might however also be to accept a higher uncertainty in this simulation, design a system, and then perform detailed CFD or experimental analysis to determine the heat transfer coefficients. This would be the recommended approach if it turns out in future research that the heat transfer is too sensitive to design peculiarities that it is not feasible to capture it in general Nusselt number correlations.

3.2.2. Mass transfer

Mass transfer suffers from most of the same problems as does heat transfer: The system does not fall within standard reference cases, and the most comparable cases are usually not applicable due to different surface conditions, out-of-bounds dimensionless parameters or the very basic fact that they are derived for single species gas.

An attempt was however made based on equations presented by Incropera for condensation of a fluid film on a flat wall.[15] He presents equation 3.8 for the Nusselt number to calculate the heat transfer from gas to a vertical wall over a condensed fluid surface.

$$\text{Nu} = 0.943 \left[\frac{\rho_l a(\rho_l - \rho_g)h'_{fg}L^3}{\mu_l k_l(T_{sat} - T_s)} \right]^{1/4} \tag{3.8}$$

In this equation the subscript l indicates a property of the fluid, subscript s of the surface, and sat that of the vapour at saturation point. a is again system acceleration. L is the characteristic length, which is taken to be the height of the fluid column. h'_{fg} is a relation of the specific enthalpy of condensation defined by equation 3.9. In that equation h_{fg} is the enthalpy of condensation.

$$h'_{fg} = h_{fg} + 0.68c_p(T_s - T_{sat}) \tag{3.9}$$

Using the the definition of the Nusselt number, this leads to the average heat transfer coefficient over the length of the wall, which can be used to get the heat transfer to the wall (equation 3.10) and the

total condensation rate at the wall (equation 3.11). The heat transferred away from the ullage is taken to be the condensed mass times the enthalpy of the that species at the pressure of the ullage. The heat flowing into the propellant together with the condensed mass completes the energy balance. The mass transferred from the ullage is taken away from the amount of condensible vapour that was present, and the molar fractions in the ullage are recomputed.

$$\dot{Q} = h_L A(T_{sat} - T_s) \tag{3.10}$$

$$\dot{m} = \frac{h_L A(T_{sat} - T_s)}{h'_{fg}} \tag{3.11}$$

These equations are used to try and model the condensation and heat transfer rate from the ullage to the wall. They are only applied in the model when the ullage pressure is smaller than the condensible vapour's critical temperature, and when the partial pressure of the vapour is greater than the saturation pressure of the vapour at the tank wall temperature (Raoult's law, section B.1). When that is not the case, the code uses the heat transfer assumptions described in the previous sections to describe the heat transfer.

Condensation/evaporation at the propellant-ullage interface is handled in a relatively simple way, equal to the way Ring computed it[52]. It is assumed that the mass transfer takes place through a thin liquid layer at the propellant surface. The surface film has a temperature that is equal to the propellant its saturation temperature at a pressure equal to the propellant vapour's its partial pressure in the ullage. The heat transfer by natural convection from the liquid to the surface, and the natural convection by the ullage to the surface is computed as described in the previous section. The total in heat transferred is then used to evaporate/condensate an amount of propellant based on the heat of evaporation.

3.3. Verification
The code developed for the models has been verified during its development process on a number of levels. The different parts of the physical model, structured in separate classes as described in section 3.1, were isolated and tested individually. The functions that were constructed were checked against their input models. This all was greatly facilitated by the modular structure of the code. The full models were subsequently compared to the analytical approximations for temperature rise during pressurization, and to the pressurant mass equation of Ring[52] (see appendix B for these relations).

This section describes the verifications that were done on the simulation. The discussion and evaluation of the pressure, temperature, and mass curves versus time is used to further clarify the processes that are ongoing in the system and the different phases that occur during pressurization and expulsion.

3.3.1. Sections, components and materials verification
The various subsystems of the simulation were subjected to a variety of tests to check that they respond correctly. This section lists these checks.

HEOS fluid sections
The different sections of the tank modeled as HEOS fluid sections, as discussed in section 3.1.3, have been submitted to various verification tests to check that they work as expected. The processes the sections were submitted to were:

- Constant mass outflow

- Constant heat inflow

- Constant volume decrease

These processes represent the available change parameters that can be used to affect the properties of a section. For each of these processes the properties density, temperature, pressure, enthalpy and volume were observed. For each process it can be reasoned whether these properties should show a linearly decreasing or increasing trend. In this way it was checked that all sections responded correctly do different thermodynamic processes.

The pressurant tank section and the ullage gas section, both as the single gas species and the mixture version, were also subjected to a process of constant volume increase, where simultaneously an amount of heat equal to the gas pressure times the volume change was removed. This constitutes an isentropic expansion process. All these three sections have been tested by setting them with helium as gas, starting at $T = 293$ K and $P = 50$ bar. For the mixture section the second species has been set to be oxygen, at a 1 to 1 mixture ratio in molar quantity. The sections were then subjected to a constant increase in volume, which means temperature, pressure and density all drop. The process was stopped when the pressure reached 10 bar. The temperature and density at that point have then been compared to the values that can be calculated using the isentropic relations. For the pressurant gas section the deviations in temperature and density are -0.3% and 1.7% respectively. For the single species ullage section the deviations are equal: again -0.3% and 1.7%. For the mixture section the deviations are found to be 1.1% for temperature and 1.14% for density. All of the deviations are sufficiently small that the gas sections are considered to function sufficiently accurately to be used in the code. Part of the deviations mentioned here are of course also due the fact that the code takes non-ideal gas effects into account, while the isentropic relations do not.

Tank wall sections and bulkheads
The tank wall sections and bulkheads were subjected to similar tests as the fluid sections, however as their complexity is limited, the amount of possible checks is as well. The bulkhead were only tested by applying a constant inflow/outflow of energy and observing that their temperature changed accordingly. The tank wall sections were subject to that same test, and also to a test in which their mass and corresponding energy content was changed linearly. In this last case temperature and mass were observed to remain constant, respectively change linearly.

Aluminium material properties
The aluminium properties class contains two functions that relate heat capacity and thermal conductivity to temperature. These relations have been obtained from literature. (See section 3.1.3.) These functions were plotted over their full range and compared to the curves found in literature. They were compared numerically on various points within the temperature range to check that they provide the right value.

Exit feed system
The mass flow values for the feed system at the exit of the propellant tank were compared at a number of randomly selected operating points to values that were computed by hand. The system returned the exact same values as those obtained by hand calculations.

Pressure regulator
The pressure regulator class was compared to the data sheets from which the model was generated. A range of pressure differentials and regulator pressure settings was evaluated. These two values were placed on an x-y grid and the resulting mass flow prediction was plotted on the z-axis. The resulting surface was found to not contain any irregularities, unexpected trends, or discontinuities which could have resulted from the interpolation methods used. The only things noticed were that close to zero pressure differential, the model generated a minute negative mass flow that occurred due to an undershoot of the interpolation at this extreme point of the curve. This was resolved by implementing a boolean check that only allows positive mass-flow. This means the curve is forced to zero close to zero pressure differential.

3.3.2. Full model verification
The simulations were also checked as a whole. This was also done in various ways. The main check was via the collapse factor. The heat transfer in the simulation can be switched off by means of a single setting. Same goes for the mass transfer. This turns the simulations into a basically "perfect" physical process, and thus the collapse factor predicted by the codes should be (near) unity. Indeed, all simulations give a collapse factor near unity for both cases. Slight differences from unity are due to the inclusion of non-ideal gas effects in the simulation, which are not present in the analytical approximations. The LPM and 1D wall simulations both result in a collapse factor of 1.09 and both 1D ullage simulations give 1.04 as result.

The simulations including heat transfer (and mass transfer when turned on) can be inspected qualitatively by looking at the output graphs produced by the simulations over time. All simulations produce slightly different curves, but in general they produce the same results (as is shown in section 3.4). Below here are three graphs created via an analysis of the test case via the LPM (Q) code.
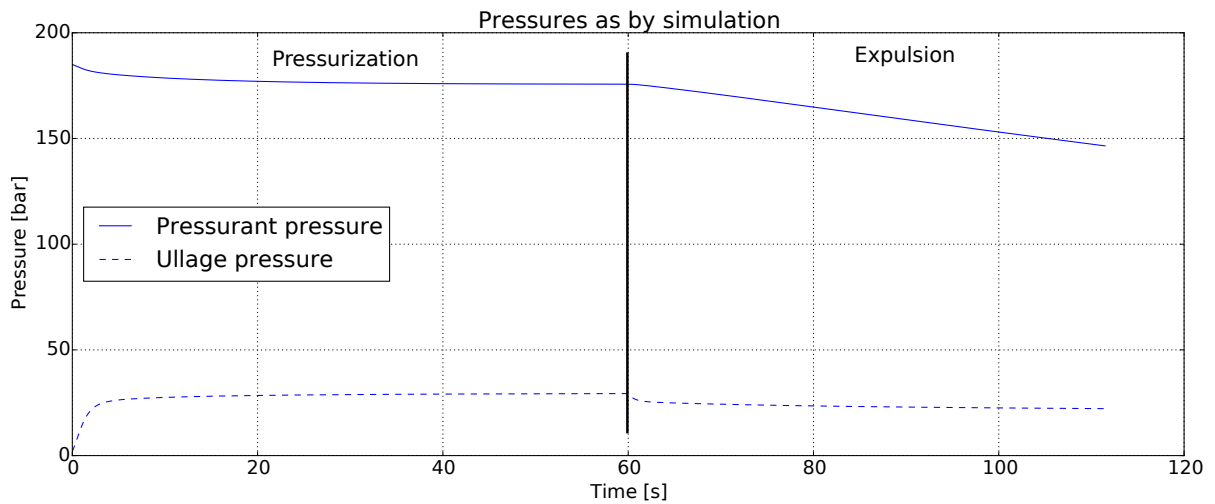

Figure 3.6: Pressure versus time in the ullage and pressurant tank for the test setup simulation using the LPM (Q) code. Before $t = 60$ s the tank is in pressurization phase, after that time the expulsion starts. Expulsion proceeds till the tank is empty.

Figure 3.6 shows the pressure over time in the pressurant tank and in the propellant tank. At t=0 s the pressurant pressure is at its maximum, while the propellant pressure is at its start level. Then gas starts flowing into the ullage, quickly rising the pressure there. After a few seconds the pressure starts to level off to reach the set pressure of the regulator. In the pressurant tank the pressure first drops quickly, and then also slowly levels off, because the gas flow stops as the propellant tank reaches pressure. The drop however never goes fully level; the gas in the ullage slowly cools down, so that new gas needs to flow from the pressurant tank to keep the pressure at the set level. At t=60 s the propellant then starts flowing from the tank. The propellant tank pressure drops as the system finds a balance between the rate at which gas can flow in, and at which propellant flows out. The pressure in the pressurant tank slowly drops but remains quite high overall, because in the test setup the gas cylinder is significantly higher than needed to empty the propellant tank.

Figure 3.7: Propellant mass versus time in the ullage and pressurant tank for the test setup simulation using the LPM (Q) code. Before $t = 60$ s the tank is in pressurization phase, after that time the expulsion starts. Expulsion proceeds till the tank is empty

Figure 3.7 shows the propellant mass left in the tank over time. The tank starts out at the initial fill level and remains constant for the pressurization phase. At t=60s the expulsion starts and the propellant

starts to flow out of the tank. The curve shown in the figure is actually slightly curved, dropping faster just after the start of pressurization. Lower in the process the tank pressure has slightly dropped, which results in a slightly lower mass flow as well. At approximately 110 s the propellant tank is empty and the simulation stops.
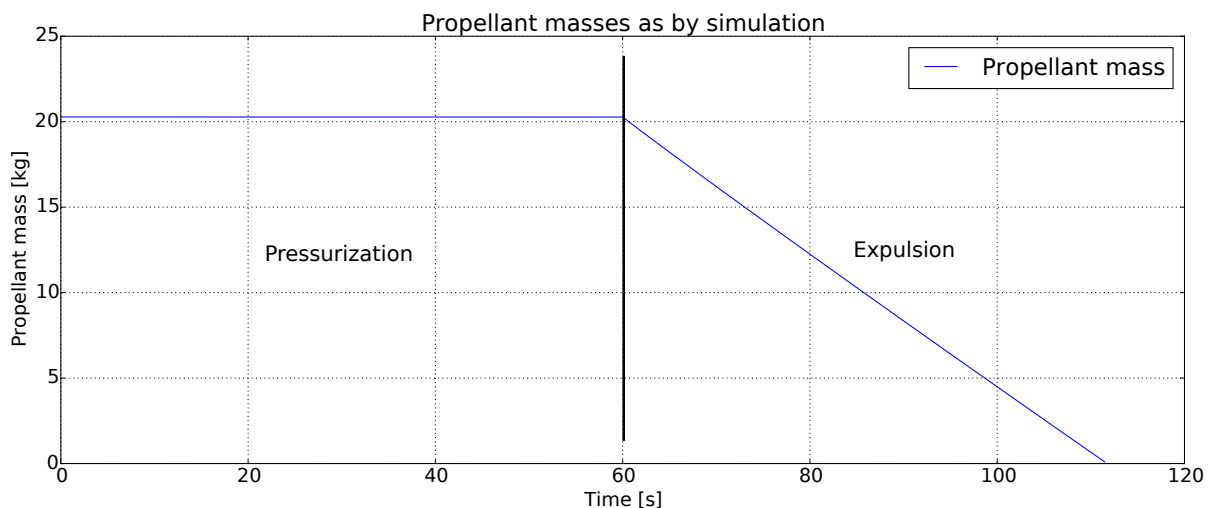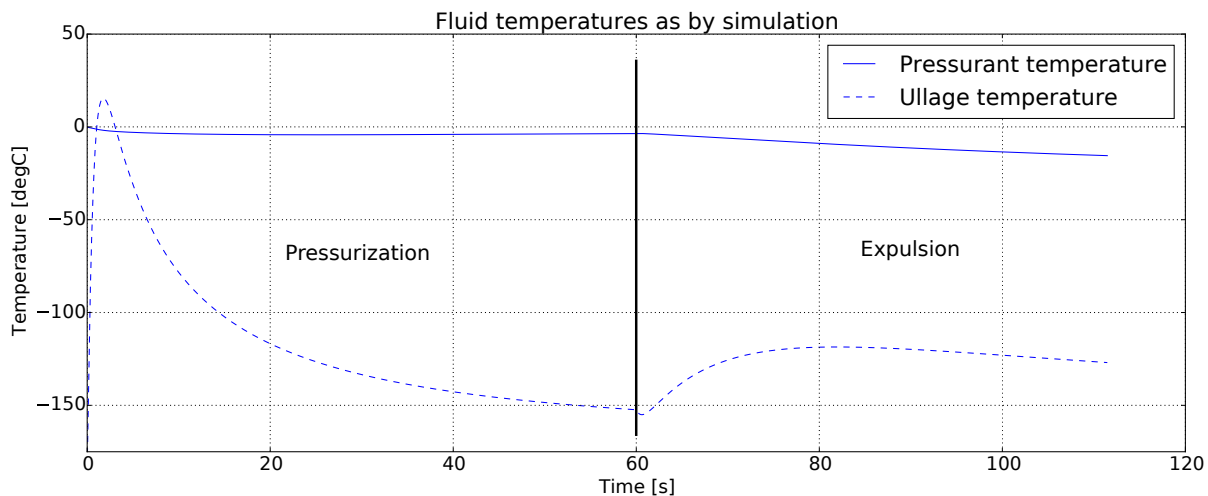

Figure 3.8: Pressure versus time in the ullage and pressurant tank for the test setup simulation using the LPM (Q) code. Before $t = 60$ s the tank is in pressurization phase, after that time the expulsion starts. Expulsion proceeds till the tank is empty

The third plot is figure 3.8. This shows the temperature of the pressurant and of the ullage over time. The pressurant temperature graph is quite similar to that of its pressure: A small quick drop at the start, followed by a level time up to 60 s, and a slow decline during expulsion. Interesting to note, although not clearly visible in the graph, is that between 0 s and 60 s the graph actually slowly starts to rise again after the initial drop. The rise is not much more than 1 °C but it does show that heat is transferred from the pressurant tank to the gas. The ullage temperature graph is more complex. At pressurization it shows a very high initial spike, which is a logical consequence of pressurization, although maybe counter intuitive at first sight. The gas initially in the volume is compressed by the inflowing pressurant gas, leading to a sharp increase in its temperature. (See appendix B.1 for the theoretical background.) After the initial pressurization, the heat transfer from the ullage towards the propellant and the tank becomes the dominant effect, and the temperature quickly drops again. At t=60 s it is however still about 30 °C above its starting temperature. Then as the propellant begins to flow out, the ullage gas temperature shortly drops a few degrees due to the initial drop in ullage pressure (figure 3.6). After that it quickly rises because the inflowing gas is more than 100 °C warmer than the ullage itself. At around t=80 s however, the ullage volume has grown so big that the heat loss towards the now exposed tank wall overcomes the energy inflow from the pressurant gas, and temperature slowly drops down again.

Looking at the graphs produced by the numerical simulations, it is clear that these show all the phenomenon that are to be expected during the process of tank pressurization and pressurized expulsion. It is therefore save to conclude that the tank code has been verified to simulate the process that it was designed to simulate.

3.4. Model outputs and comparison between models

As described in section 3.1, a number of different models have been developed over the course of this thesis. The models are different in complexity and in the effects that they take into account. It is interesting to compare the models amongst each other, so that the effect of different simulation methods, and of different simulated effects can be investigated.

Section 3.4.1 describes the simulation cases that were conducted, and the selected parameters used in these simulations. Section 3.4.2 discusses the results.

3.4.1. Simulation cases and parameters

During the analysis, six versions of the simulation have been developed that were all evaluated individually. This evaluation was conducted for 2 simulation cases, the first to simulate the hardware test setup constructed during this thesis, and the second to simulate a rocket flight tank on approximately the sizes described in chapter 2. In this section only the test setup case will be discussed. The conclusions drawn for the "students to space" case are basically the same. The results of this second case have been included in appendix C.

The different versions of the simulation are listed in table 3.1. They range in complexity from simple, to fairly complex. Because of this they also vary in required run-time. The simplest lumped parameter model can be ran nearly in real time (i.e. each second of simulation time equals one simulated second of the system), while the 1D models can require up to 1.5 hours to simulate a pressurization and expulsion process of in total 90 s (on a regular laptop). The lumped parameter model (LPM) and the models where only the wall was split into multiple sections were relatively easy and quick to evaluate. These models were evaluated with only the heat transfer simulated, and with both the heat and mass transfer taken into account. It was however found that including the mass transfer does not affect the outcome of the simulation very much, as is discussed in 3.4.2, but it does complicate the simulation, introduce extra assumptions, and increase the total run time. Therefore it was decided to not try and implement mass transfer in the 1D ullage simulations.

Table 3.1: The six different versions of the simulation that have been developed during this thesis. The development and evaluation proceeded roughly in the same order as how the versions are listed here.

Designation	Description
LPM (Q)	Lumped parameter model. Only heat transfer.
LPM (Q&m)	Lumped parameter model. Heat and mass transfer.
1D wall (Q)	Lumped parameter model, but with the wall split in a large number of equal, horizontal slices. Only heat transfer.
1D wall (Q&m)	Equal to 1D wall (Q), but also including the mass transfer.
1D ullage (H)	Lumped parameter model, but with the wall split into equal, horizontal slices and the ullage volume also split into a (variable) number of horizontal slices. Only heat transfer.
1D ullage (V)	Equal to 1D ullage (H), but with the ullage split into vertical, concentric cylinders instead.

Each of these simulations has been conducted with input parameters based on the test setup constructed during this thesis. The most relevant parameters used for the simulations are given in table 3.2. The parameters were chosen to match the setup its geometry, and to approximately match the fluid conditions during the axial and radial injection tests (chapter 7). There is one parameter that warrant some more explanation, being the boolean parameter that forces a constant temperature inflow. This parameter has been introduced to model the observed behaviour in the test setup that the inflowing helium was of relatively constant temperature. When set to true, the simulation adds or subtracts energy to or from the inflowing helium gas so that its temperature remains constant.

3.4.2. Simulation results

The simulations that have been conducted need to be compared to each other. This can be done in a number of different ways. Here it has been chosen to compare a number of parameters that are likely to be of interest to a rocket engineer that would be using the code to design his or her pressurization system. A number of parameters are evaluated as a single value, and the pressure and temperature of the ullage gas and pressurant gas are evaluated via plots over time.

The numeric parameters are: The collapse factor, the total expulsion time, the average propellant tank pressure, the amount of pressurant that flows into the propellant tank, and the pressurant tank pressure at the end. The collapse factor is important because it defines how effective the pressurization system is, and if there is room for improvement. The total expulsion time is basically equal to the possible burn time, and combined with the tank volume will give the total oxidizer mass flow into the rocket engine. The average propellant tank pressure can be used to determine the achievable com-

Table 3.2: The most important initialization parameters for the conducted simulations.

Parameter	Value	Unit
Timing		
Timestep	10	ms
Pressurization time	60	s
Propellant		
Propellant	Nitrogen	-
Initial pressure	2	bar
Initial temperature	80	K
Propellant tank		
Diameter	0.23	m
Inner length	0.74	m
Wall thickness	10	mm
Bulkhead thickness	30	mm
Ullage fraction at start	0.1	-
Number of wall segments	50	-
Top bulkhead initial temperature	90	K
Number of ullage sections (start)	5	-
Number of ullage sections (end)	50	-
Ullage initial temperature	90	K
Pressurant		
Pressurant	Helium	-
Initial pressure	200	bar
Initial temperature	273	K
Force constant temp. inflow?	True	-
Pressurant tank		
Volume	50	L
Inner length	0.74	m
System		
Exit orifice diameter	3.8	mm
Pres. regulator set pressure	30	bar

bustion chamber pressures for the engine. The amount of pressurant flowing into the tank indicates how much helium needs to be brought along. Finally, the pressurant tank pressure at the end shows if the tank pressure is not too low or too high. Too low would mean performance is lost as the propellant tank pressure would drop significantly towards the end, too high would mean the pressurant tank is to big for the system.

The collapse factor is calculated using equation 1.1, where the compressibility has been set to one, and the propellant tank pressure is set equal to the average pressure during the expulsion.

The values for the numeric parameters that are given as output by the simulations are given in table C.2. These results show that all the 6 simulations give results that are roughly the same, but there are small differences.

But first, let's look at the similarities. The two lumped parameter models produces results that are virtually the same with less than 2% deviation. This means that for the lumped parameter model it is not of relevance whether or not the mass transfer is included or not. The same can be said for the extended models where only the wall is split into a larger number of elements. The difference between including or not including the mass transfer equations is minimal. It turns out that mass transfer is likely not an issue, and thus it can be neglected. This is the reason why it has been chosen to do this for the full 1D simulations.

The differences between the simulations are those between the different types. The lumped parameter results do show a small difference with the 1D wall models, but the deviations remain below 5%. The 1D wall methods predict a slightly lower collapse factor. Likely the LPM models overestimate the heat transfer to the tank wall. In the LPM mode the average tank wall temperature in contact with

Table 3.3: The main system parameter resulting from the simulations for the test setup simulation.

		Collapse factor [-]	Expulsion time [s]	Avg. tank pressure [bar]	Inflowing gas mass [kg]	Pressurant pressure (end) [bar]
1	LPM (Q)	1.98	51.5	23.4	223	146
2	LPM (Q&m)	1.94	51.3	23.5	219	147
3	1D wall (Q)	1.93	51.3	23.6	218	147
4	1D wall (Q&m)	1.89	51.1	23.7	214	148
5	1D ullage (H)	1.79	51.1	23.8	214	149
6	1D ullage (V)	1.52	50.0	24.8	179	154

the ullage drops significantly when the expulsion starts. This is because 'new' cold wall is exposed to the ullage, lumped together with the warmer wall into the top wall section, and thus the average temperature of the whole top tank wall drops. In the 1D wall models this effect is reduced. New, cold wall sections are exposed during the expulsion, but the tank wall temperature near the top of the tank does not drop any more, resulting in less heat loss.

A similar, but stronger effect is observed when looking at the 1D ullage (Horizontal) simulation. This simulation allows for the existence of vertical temperature gradients. This allows 'hot' injected gas to stay near the relatively warmer top bulkhead and upper sections in the wall, while only the colder gas at the bottom of the ullage is subjected to the newly exposed cold tank wall and the cold propellant surface. When the ullage is not split up, the heat of the inflowing gas is averaged over the full ullage, and so can leak away to the wall and propellant.

The horizontal 1D ullage simulation predicts slightly lower collapse factors than the simpler simulations. Deviations are however less than 10% compared to the LPM (Q) model, so this effect should likely be considered to be within uncertainty bounds of the simulation. The deviation grows up to 25% when comparing the vertical 1D simulation to LPM (Q). This shows that the different geometry into which the ullage is split does show the expected effect of a different temperature distribution: less heat leakage to the tank wall results in a lower collapse factor. If this however does match with reality, is something that needs to be investigated by means of validation tests.

Figure 3.9 shows the pressure versus time for both the ullage and the pressurant tank, for all 6 simulation types. It is visible that there are no significant differences to be observed in the pressure versus time over the simulations. All follow roughly the same path. That is good news, because if it is shown through validation that any of the simulations is able to predict the pressure history of the system with a good accuracy, it is likely so that the most simple and thus least computationally intensive simulation (LPM (Q)) can be used by the rocket engineer to get a good estimate of pressure for his or her design. Small differences can be noted in the simulation. The first four simulations line up nearly exactly, and it is interesting to note that LPM (Q) and 1D wall (Q) are equal to each other, and so are LPM (Q&m) and 1D wall (Q&m). The differences between whether or not mass is included is however noticeable at the initial pressurization. This shows that only splitting the tank wall into multiple sections does not offer any significant advantage over using the LPM models here. It only results in more computational time required. Only the vertical 1D ullage simulation shows any marked difference: it is able to maintain a slightly higher and more constant tank pressure.

Figure 3.10 shows the average temperature of the ullage and pressurant tank gasses. The ullage temperatures in the 1D ullage simulations are averaged over all sections at each point. The ullage temperature does show a difference between the different simulation versions. Here it is clear that for estimating the ullage temperature spike during pressurization, including mass transfer is of importance. Both the LPM and 1D wall models including mass transfer show peak temperatures around 50 °C higher than those without. This is due to the effect that when mass transfer is included, propellant vapour initially in the ullage condenses, and gives up energy to the tank wall and ullage gas. The effect however quickly disappears when the vapour has condensed, and the ullage gas cools down due to its contact with tank wall and propellant. In the final stages of pressurization and during the full expulsion, all simulations behave nearly the same, with the exception that the temperature of the two 1D ullage
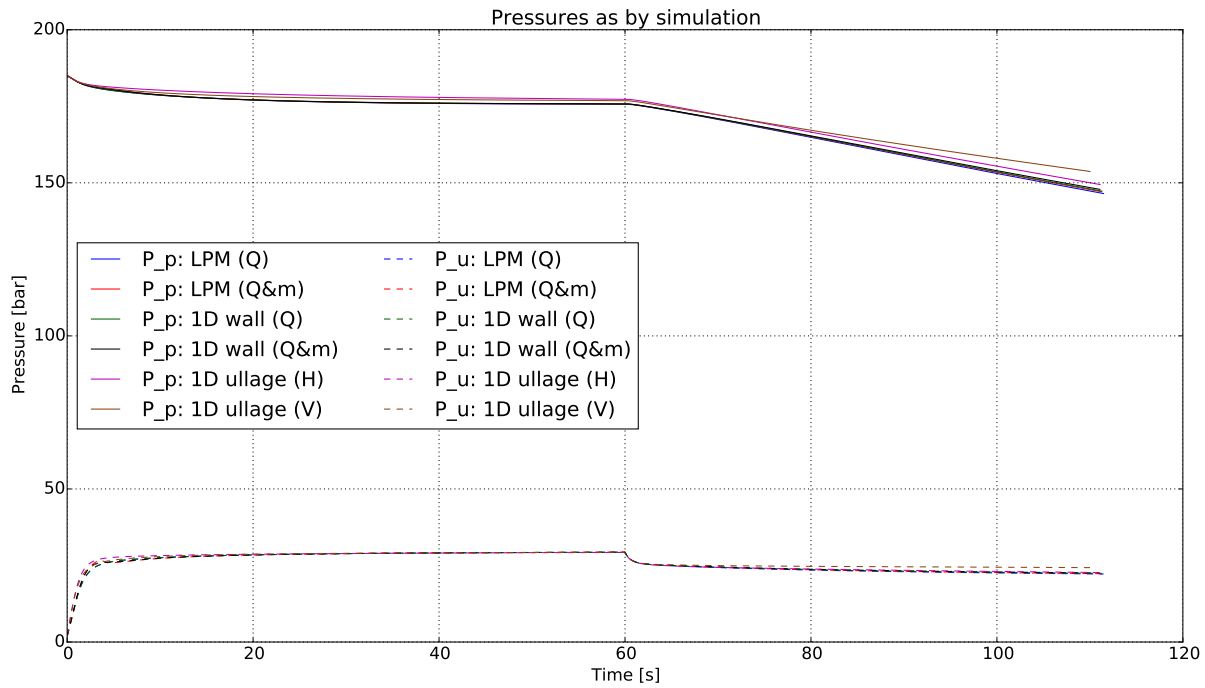
Figure 3.9: Pressure versus time in the ullage and pressurant tank for the test setup simulation.

simulations is somewhat higher. The average temperature of the horizontal simulation follows the same shape as that of the simpler simulations; first rising and then falling. The average temperature of the vertical simulation however shows a steeper increase and a levelling off of the temperature.
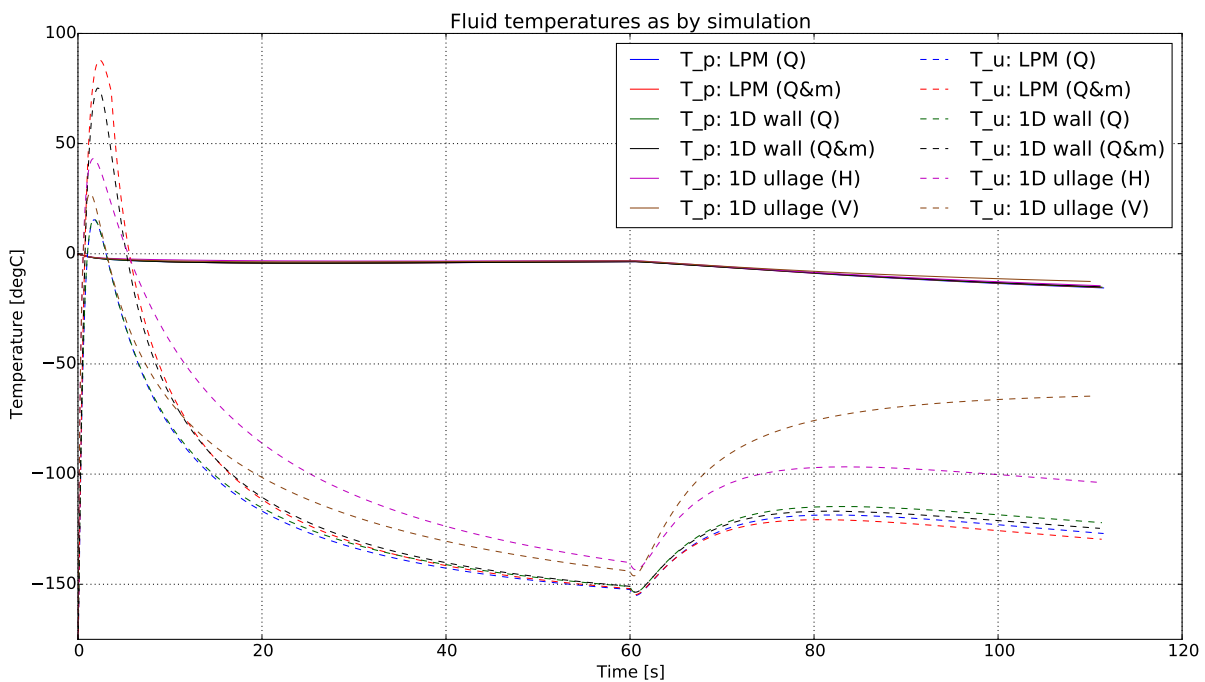

Figure 3.10: Temperature versus time in the ullage and pressurant tank for the test setup simulation.

3.5. Sensitivity analysis

Using the model it is possible to try and analyse the effect of certain design choices on the amount of pressurant gas required. An easy way of investigating all the effects is to do a sensitivity analysis. In

this type of analysis the parameters of the simulation are decreased or increased with a certain amount and the effect is noted. In this way it is possible to construct a kind of "partial derivative" of the simulation outputs for each input variable. Furthermore it allows to check that simulation parameters that have nothing to do with the physical processes, such as the simulation timestep, have negligible influence on the simulation outcome.

For this thesis it has been chosen to vary the main physical parameters of the simulation up or down by 10%. These are values such as tank dimensions and operation pressure. It has been chosen to vary them all by a similar percentage so that it is easy to judge which parameter have the largest influence on the output. Next to these parameters the timestep of the simulation has been varied by -50% (factor 2 less) and +100% (factor 2 more) to show that this value does not have a significant influence on the simulation outcome. Finally the variables of pressure regulator rise time and the convective heat transfer are also varied by -50%/+100% to reflect the large uncertainty in these parameters.

Parameters are varied individually, never in combination. I.e. for each simulation case there is only one variable that is different from the nominal case. The sensitivity analysis has only been carried out for the lumped parameter model, without mass transfer. This has been done because of time constraints, as a large number of simulations needs to be run for a sensitivity analysis. The analysis has been conducted for the test setup simulation case discussed in section (3.4). It is believed that the influence of these parameters will be roughly the same for all simulations. The values listed in table 3.2 have been used. The results are compared based on the same parameters as the previous section. For each of these the effect of the change in input parameters has been evaluated as a percentage of change compared to the nominal simulation output.

The results are listed in table 3.4. The first parameter in the table are the main simulation parameters: The timestep. Changes in this values does not affect the simulation outputs significantly. This is good, as it shows that there are no simulation artefacts that influence the results. The pressure regulator rise time can also be seen in this light. It is a parameter that needs to be present to avoid mass flow fluctuations that would cause the failure of the simulation, but its value does not influence the simulation outcome.

The influence of the heat transfer is interesting to notice. A deviation of a factor 2 in the heat transfer coefficients is not unlikely if force convection plays a larger role than taken into account now. This can lead to deviations in the tank collapse factor of more than 10%. This confirms that to improve the simulation further the uncertainty in heat transfer coefficients certainly needs to be addressed.

The output parameters that are most influenced by the result are the expulsion time and the total inflowing gas mass. The pressurant pressure at the end is not influenced very much. This is because the volume of the pressurant tank is far larger than it needs to be to empty the tank. The average tank pressure is only much influenced by the set pressure at the pressure regulator, which is how it is expected to be, due to the nature of how a pressure regulator operates. The orifice diameter also affects it, as this value couples directly to the mass flow. This in turn affects how well the regulator can 'keep up' with keeping the ullage volume at the intended pressure. The collapse factor is affected by the heat transfer and also by

From the input parameters, the most significant changes can be explained by simple geometric considerations. An increase in tank diameter leads to a significant decrease in expulsion time and amount of inflowing gas mass. This is logical, as a 10% increase in diameter, leads to an approximate 21% increase in tank volume. Similarly, tank length influences the tank volume linearly: 10% change in tank length results in approximately 10% in expulsion time and inflowing gas mass. A change in orifice diameter leads to an even higher change in orifice area, and thus a large change in mass flow, and thus in expulsion time.

More interesting are the smaller changes, or the absence of changes. Such as the overall small influence in the pressurant tank start pressure (except its logical effect on the end pressure). Related to this is the effect of pressurant tank temperature. An increase of which leads to a higher collapse factor, likely due to higher heat transfer. But it also leads to a decrease in inflowing gas mass, likely due to the decreased density. These pressure and temperature effects on the collapse factor are in line with the theory behind it as described in section 1.2. Interesting as well is the effect of the regulator set pressure on the collapse factor. A higher pressure leads to a lower collapse factor. This could indicate that in the current regime the heat transfer is more effected by the total expulsion time (which is decreased by an increase in pressure) than by the influence of the increased gas density.

Table 3.4: Results of the sensitivity analysis. Changes in the parameters are expresed as percentual change with respect to the nominal output of the simulation. Differences lower than 0.5% have been removed from the table.

		Collapse factor [-]	Expulsion time [s]	Avg. tank pressure [bar]	Inflowing gas mass [kg]	Pres. pressure (end) [bar]
Nominal result		1.98	51.5	23.4	0.223	146
Timestep	-50%	-	-2%	-	-1%	-
	+100%	-	-2%	-	-1%	-
Heat transfer	-50%	-13%	-3%	2%	-11%	1%
	+100%	12%	-	-3%	9%	-
Pres. Reg. Rise time	-50%	-	-2%	-	-1%	-
	+100%	-	-2%	-	-1%	-
Pres. Reg. Mass flow	-10%	-	-	-2%	-2%	1%
	+10%	-	-2%	2%	1%	-
Tank diameter	-10%	-1%	-19%	1%	-20%	5%
	+10%	1%	17%	-	18%	-4%
Tank length	-10%	-1%	-10%	1%	-11%	3%
	+10%	1%	10%	-	11%	-2%
Initial ullage fraction	-10%	-2%	2%	-	-	-
	+10%	2%	-2%	-	-	-
Pressurant tank volume	-10%	-	-	-	-	-2%
	+10%	-	-	-	-	2%
Pressurant tank pressure	-10%	-	1%	-1%	-1%	-11%
	+10%	-	-1%	1%	1%	12%
Pressurant tank temperature	-10%	-5%	-	-	5%	1%
	+10%	5%	-	-	-4%	-
Pres. Reg. Set pressure	-10%	3%	5%	-9%	-7%	2%
	+10%	-2%	-5%	10%	7%	-1%
Orifice diameter	-10%	4%	17%	3%	2%	-
	+10%	-3%	-16%	-3%	-6%	1%

3.6. Conclusions and recommendations

Various models to simulate the pressurization and pressurized expulsion processes in a cryogenic propellant tank have been developed. The models range in complexity from a lumped parameter model including heat transfer only to a 1D simulation where both ullage and tank wall are split into multiple sections. The models have been verified, their output has been compared and a sensitivity analysis has been conducted.

During the development of the code it was realized that the problem of modelling the heat transfer proved more difficult then expected beforehand. The situation in the tank, with low gas injection velocity and very high temperature differences, produces a situation where it is not clear whether natural or forced convection plays a dominant role. It was chosen for the development of this model to implement only the natural convection. However, even for only this, there are no Nusselt number correlations found that are directly applicable to the situation in the tank. From the sensitivity analysis it became clear that the uncertainty in heat transfer could lead to an uncertainty of 10% in the collapse factor.

On top of this it has become clear that the method of gas injection, and the flow pattern of gas in the ullage volume caused by it, either strengthens or weakens the pattern of natural convection that already occurs in the tank. Radial injection produces the same flow pattern as natural convection, thus strengthening the total heat transfer. Axial injection causes a flow pattern that is exactly opposite to the natural convection pattern, and thus weakens it. This is in line with the hypothesis put forward in this thesis that axial injection produces a lower collapse factor than radial injection for this case of tank pressurization.

The main recommendation for future research resulting from this is that the best way to model the heat transfer coefficient in the propellant tank needs to be investigated further. 2D or 3D CFD modelling

of the heat transfer might provide correlations that are applicable to the situation within the tank and so the lumped parameter models and 1D models can be improved.

The comparison of the different models showed that, except for the 1D vertical ullage model, all produces results within 10% of each other. From this it is advised to use the LPM (Q) model in a rocket system sizing simulation, as this is the model requiring the least amount of computational time.

The 1D vertical ullage model produces estimates for collapse factor that are up to 25% lower than that predicted by all the other models. This is in line with the concept of why this simulation has been setup. The 1D vertical ullage model is meant to mimic the influence of axial temperature gradients caused by axial injection. The 1D horizontal ullage model instead produces vertical temperature gradients, and thus mimics radial injection. As is in line with the hypothesis put forward about injection methods: the model simulating axial injection produces a lower collapse factor than the one simulating radial injection.

Mass transfer seems to play a marginal role in the overall behaviour of the system and can be neglected.

4

Test plan

As became clear from the literature (section 1.2) the pressurization of small cryogenic tanks is a field of research that is still lacking in the amount of available test data. However the investigation on modelling the tank pressurization and expulsion (chapter 3) shows that test data is highly desired because there are no straightforward methods to predict the tank collapse factor and to choose between pressurant injection methods.

To contribute to this research topic it has been decided to develop a practical test setup that allows filling a tank with liquid nitrogen, pressurizing it with helium, and subsequently performing a pressurized expulsion of the liquid.

This chapter of the report describes the test plan for performing these kinds of hardware tests. It describes the test goals, the requirements for the hardware and the measurements to be made in section 4.1. The test location that was found is shortly described in section 4.2, and the test procedures that were written for the test are given in section 4.3.

4.1. Test goals
The design of the hardware test setup and the conduction of the various tests with LN2 during this thesis are guided by a number of design requirements and test goals. The hardware requirements for the test setup, including requirements for the sensors, are given in section 4.1.1. Sections 4.1.2 and 4.1.3 given the detailed test goals for the hardware validation test, and the pressurized expulsion tests respectively.

4.1.1. Hardware requirements and measurement goals
The hardware that needs to be designed for conducting the tests needs to meet a number of criteria. These criteria are first of all in the form of functional requirements, related to the workings and handling of the system; If the system cannot be (safely) operated it is of no value to do tests with. Secondly there are sizing requirements; The system needs to have parameters within reasonable ranges to be in any way representable for the type of rocket that is intended to be constructed. And thirdly there are measurement requirements; The setup needs to be instrumented in such a way that sufficient information can be obtained from it to make sensible conclusions concerning the system its operational point and its efficiency.

This can all be formulated in the following requirements:

1. The system must be safe to operate

    (a) Failure modes of the system should be designed such that the hazard they form for personnel and facilities is minimized

    (b) Operation of the system during pressurized phases must be done remotely

    (c) Operation of the system during unpressurised phases involving cryogenic liquids is preferred to be done remotely

43

(d) The system must be designed so that in unpowered, uncontrolled state it will return to an unpressurised state

(e) The dumping of LN2 must be done such that it does not present any danger to personnel or facilities

2. The system must be able to perform a pressurized expulsion of LN2:

   (a) The system must be able to be filled with LN2

   (b) The system must be able to be pressurized with helium gas

   (c) The system must be able to allow the LN2 to be expelled under pressure

   (d) The system must be able to vent the pressurized gas directly, without needing to dump LN2 first

3. The system must be representable for the design parameters determined in chapter 2

4. The system must be able to measure the processes occurring in the tank during pressurization and expulsion:

   (a) The propellant tank pressure must be measured versus time

      i. A pressure sensor needs to be implemented on the tank. No oscillations or other high-speed changes are expected in the tank pressure. Measurement frequencies on the order of 10 Hz or higher are sufficient.

   (b) The amount of propellant in the tank must be measured versus time

      i. The tank mass needs to be measured with a load cell. No oscillations or other high-speed changes are expected in the propellant mass. Measurement frequencies on the order of 10 Hz or higher are sufficient.

      ii. Previous experiences with load cell measurements cause for concern on high noise levels[33]. It is therefore desired to investigate a capacitive liquid level sensor as alternative to determine the amount of propellant.

   (c) The amount of pressurant consumed during a test needs to be measured

      i. The pressurant tank mass needs to be measured with a load cell. No oscillations or other high-speed changes are expected in the pressurant mass. Measurement frequencies on the order of 10 Hz or higher are sufficient.

      ii. The pressurant tank pressure must be measured before and after each test to provide an additional way to measure the amount of pressurant consumed.

   (d) The temperature distribution in the ullage volume needs to be measured

      i. An array of thermocouples needs to be installed in the tank to measure absolute temperature values and radial and axial temperature gradients. Measurement frequencies above 1 Hz are required. Higher frequencies are desired, but it is recognized that this is limited by the nature of thermal measurements.

   (e) The temperature distribution of the tank wall needs to be measured

      i. Thermocouples need to be placed on the tank wall to measure the axial temperature distribution on the wall. Measurement frequencies above 1 Hz are required. Higher frequencies are desired, but it is recognized that this is limited by the nature of thermal measurements.

   (f) The influence of the pressurant feed line and the pressurant injector on the state of the inflowing gas needs to be measured

      i. The temperature of the inflowing gas before the injector needs to be measured. Measurement frequencies above 1 Hz are required. Higher frequencies are desired, but it is recognized that this is limited by the nature of thermal measurements.

      ii. The pressure of the inflowing gas before the injector needs to be measured. No oscillations or other high-speed changes are expected in the pressure. Measurement frequencies on the order of 10 Hz or higher are sufficient.

4.1.2. Test goals for the first exposure test

The first exposure test is planned as a single test to validate that the hardware test setup is usable for the pressurized expulsion tests. During the test the tank needs to be cooled down and partially filled with LN2. Then all lines need to be closed to seal of the tank and to allow the system to build pressure. After a specified time (15 minutes) or when reaching a specified pressure (15 bar) the main valve will be opened to eject all the LN2 from the tank.

It is not only the first experience with cryogenic liquids for the system, but also for the operators of the system. Working with cryogenic liquids is a new thing in DARE and there is little to no experience with these types of systems. Therefore the test goals for this test are more of a qualitative than a quantitative scientific nature. That is an unfortunate but unavoidable consequence of not having any experience with a system. The test goals are defined as follows:

1. Gain experience with the handling of the test setup in general

    (a) Gain experience with all tools and equipment required for setting up the test.

    (b) Gain experience with the test location.

    (c) Test run the procedures.

2. Gain experience with the handling of cryogenic liquids

    (a) Gain experience with the safety precautions taken during work with cryogenic substances.

    (b) Gain experience with the usage of cryogenic safety equipment such as gloves and oxygen concentration detectors.

    (c) Gain experience with usage of a dewar.

    (d) Test run the procedures for the handling of cryogenic liquids.

3. Test if the system is leak-free at cryogenic temperatures

    (a) The feed system piping attached to the tank should show no leaking liquid or gas. Leaking liquid will be visually directly observable. Leaking gas needs to be inferred from either sound (hissing) or frost formation blown away at the point of leakage. Frost formation on parts that should have no gas or liquid flowing past it, such as the PSRV/pressure sensor tubing, or the aluminium test bench structure itself, also indicate the presence of leaks.

    (b) There should be no leakage via the tank bulkhead sealings. (Detectable in the same method as described above.)

    (c) There should be no leakage via the custom sensor adapters. (Detectable in the same method as described above.)

    (d) There should be no noticeable leakage through the valves.

4. Test if all valves operate as desired:

    (a) Valves should actuate only when commanded to by the user via the cRIO system.

    (b) Valves should actuate without noteworthy delay when commanded to.

5. Test if all sensors give the desired output:

    (a) All thermocouples should give temperature readings in accordance with what is to be expected from the presence of liquid nitrogen. Temperatures should decrease from room temperature to a minimum of approximately -196°C. All temperature sensors should give readings in approximately the same temperature range.

    (b) The pressure sensor should give pressure readings near atmospheric pressures during filling. During hold of the liquid in the closed tank it should show increasing pressures consistent with what can be expected as nitrogen vapour pressure at the temperatures indicated by the thermocouples.

    (c) The capacitive liquid level sensor should show an continuously increasing trend in signal output during filling, a constant value during hold, and a continuously decreasing signal during expulsion. The signal should be expected to be linear with the load-cell output as they are related through the density of the liquid. The output value should start around 20 pF and rise to a maximum of around 28 pF ($\approx$85% fill level).

    (d) The load-cell should give a continuously increasing signal during filling up to a maximum of 21 kg ($\approx$85% fill level), a constant value during hold, and a continuously decreasing signal during expulsion.

4.1.3. Test goals for the pressurized expulsion tests

After the test setup has been found to work sufficiently via the first exposure test, the testing can proceed with the pressurization and expulsion tests. These consist of three test series. In each series a different injector type is tested: radial, axial and vortex. The radial and axial injection tests are considered to be of high priority, while the vortex injection tests are a 'nice-to-have'.

    The radial and axial tests both need to be conducted 3 times. This number has been chosen as a trade-off between the need to do more tests and the available resources. Three tests each is considered sufficient to determine if a test is representative for its measured operational point, or if it constitutes an outlier. Also it is estimated that it is possible to do 3 tests on one test day and with one helium gas cylinder. Doing more tests would involve scheduling of more test days and acquisition of more helium gas. Scheduling a test day is expensive man-power wise, as it involves 5 people full-time for the full duration of the test (three test operators + one DARE safety officer + the 3ME location supervisor).

    The vortex injection test needs to be conducted at least once, but if possible multiple times. This is decided based on the availability of resources and manpower.

    Tests will be numbered in the order in which they are conducted. Radial tests will be prefixed with the designation "rad", axial injection with "ax" and vortex injection with "vtx". I.e. tests will be numbered "rad1", "rad2", "rad3", "ax1", ...etc.

The test goals for each injection test can be formulated as follows:

1. Perform the full testing sequence

    (a) Cool the tank down to LN2 temperatures (if not done so already)

    (b) Fill the tank with liquid nitrogen to ~85% fill level

    (c) Pressurize the tank with helium to 30 bar for 60 s

    (d) Empty the liquid nitrogen out of the tank under pressure in ~50 s

2. Collect validation data:

    (a) Collect data of all 15 tank thermocouples to monitor thermodynamic processes in the tank during cool-down, pressurization, and expulsion

    (b) Collect temperature data of the inflowing helium

    (c) Determine tank pressure over time

    (d) Determine pressure drop over the pressurant injector by means of pressure measurements

    (e) Determine tank fill level by means of the load cell

    (f) Determine mass flow by means of the load cell

    (g) Collect data on liquid fill level by means of the capacitive liquid level sensor

    (h) Determine pressurant gas mass needed for pressurization and expulsion

4.2. Test location

For the conduction of the validation tests, a test location needed to be found that was suitable to conduct the tests. This was found at the faculty of Mechanical engineering at the TU Delft. A field behind the faculty was selected (see figure 4.1). The field is a grass field approximately 25m by 20m, and is located at 52°N, 4.371°E. Is is managed by the department of Process and Energy, who also have four storage

containers and a gas storage location at the edges of the field. Furthermore, on one corner of the field, there are three large dewars. Two contain liquid nitrogen while the third contains CO_2 stored under its vapour pressure. Next to the usage of the field itself, the department of Process and Energy was so kind to provide a 60L LN2 dewar for use during the tests, as well as the liquid nitrogen itself, cryogenic safety gloves, and personal gas detection devices. Authorization to use the field was arranged via Prof. Dr. Ir. Boersma. Ir. Van den Brink was the main contact with the department and for the arrangement of the equipment. He also supervised and helped during all tests.

The field was used during the tests but has become unavailable for further tests, as major reconstruction work of the field started at the end of February 2017.

Figure 4.1: An overview shot of the test location.

4.3. Test procedures

The application for the tests, safety review, and supervision was done according to the standard DARE guidelines. The tests were conducted under the DARE cryogenics project. For each test a test application was submitted to the DARE safety board. These applications consisted of a description of the test setup, the test plan, the expected outcomes, the safety risks, and the test procedures. These were reviewed by the safety board, after which they assigned a safety officer to supervise each test. A copy of the test procedures, as used during the radial and axial injection tests, is included in appendix D of this report.

5

Test setup design and construction

To investigate different pressurant injectors and to evaluate the predictive power of the simulations, a test setup was constructed to perform cold-flow tests of pressurized liquid nitrogen. The test setup was designed keeping in mind what the design parameters of a large DARE LOx-powered rocket would be (chapter 2) but was heavily influenced by the materials and manufacturing methods available.

This section of the report describes the design and construction of the test bench, but also covers acquisition of parts, the data acquisition & actuation system and the first exposure test, that was used to check the hardware. The work that is described in this chapter actually covers the largest single chunk of work conducted during this master thesis. Physical construction takes more time and effort than people usually think. To illustrate this, an overview of hours spent on production has been included in appendix F.

All of the construction was done at the TU Delft 'Dreamhal', at the workshop of DARE, using tools of DARE. The parts have been processed using a variety of machining methods, including lathing, milling, and sheet metal working. All construction work was done by the author of this thesis, with the exception of some help received during assembly of the system.

The whole test setup is designed to house the full feed system that allows filling a tank with liquid nitrogen, pressurizing it with helium from the top, and letting the nitrogen flow out at the bottom. Therefore the feed system is described first, in section 5.1. The whole feed system is constructed around the centrepiece of the setup: a 30L aluminium cryogenic tank (section 5.2). Within the tank, the main item of importance is the pressurant diffuser (5.3). The tank and feed system are all suspended in a sturdy test bench structure (5.4). On and in the tank a large number of sensors are placed, to measure a large set of parameters during the tests (5.5). For the development of these sensors, a special new technique has been developed where glue is sucked into an aluminium adapter by means of a vacuum, to seal sensor wires against the high tank pressures and low temperatures. All valves are actuated, all sensors are read out, and all data is collected via a cRIO system using LabView (5.6). The parts and budget acquisition is presented in section 5.7.

The first test of the system was the so called "First exposure test", in which the tank was filled with LN2 for the first time. During this test a number of important lessons were learned that have been used to improve the system. This test can thus be seen as a validation test for the system. The test and its outcome is described in section 5.8. The chapter closes with section 5.9, that summarizes all lessons learned concerning hardware and software during construction and operations.

5.1. Feed system

The test setup for the cryogenic tests consists mainly of a feed system laid out around the main run tank. The feed system design is displayed graphically in figure 5.1. A list of all components and their properties is given in table 5.1. This section of the report describes the full test setup, the functions and properties of the different lines, the valves and the orifices.

The centre piece of the feed system is the main run tank. This is a 30.7 L aluminium tank with flat bulkheads (see section 5.2). All feed system connections are screwed into the flat bulkheads. There are five feed system lines that run from the tank. On the top bulkhead, from left to right in figure 5.1,

are the bleed line, the auxiliary line, and the pressurization line. At the bottom, from left to right, are the dump line and the fill line. Next to these five line there is a low pressure nitrogen system that runs from a 10 L nitrogen bottle, via a compressed gas regulator (not displayed in the figure) to the three pneumatic actuated valves. This is a line consisting of small diameter (~5 mm inner diameter) plastic lines which is pressurized to ~7 bar and which is used to drive the valves.
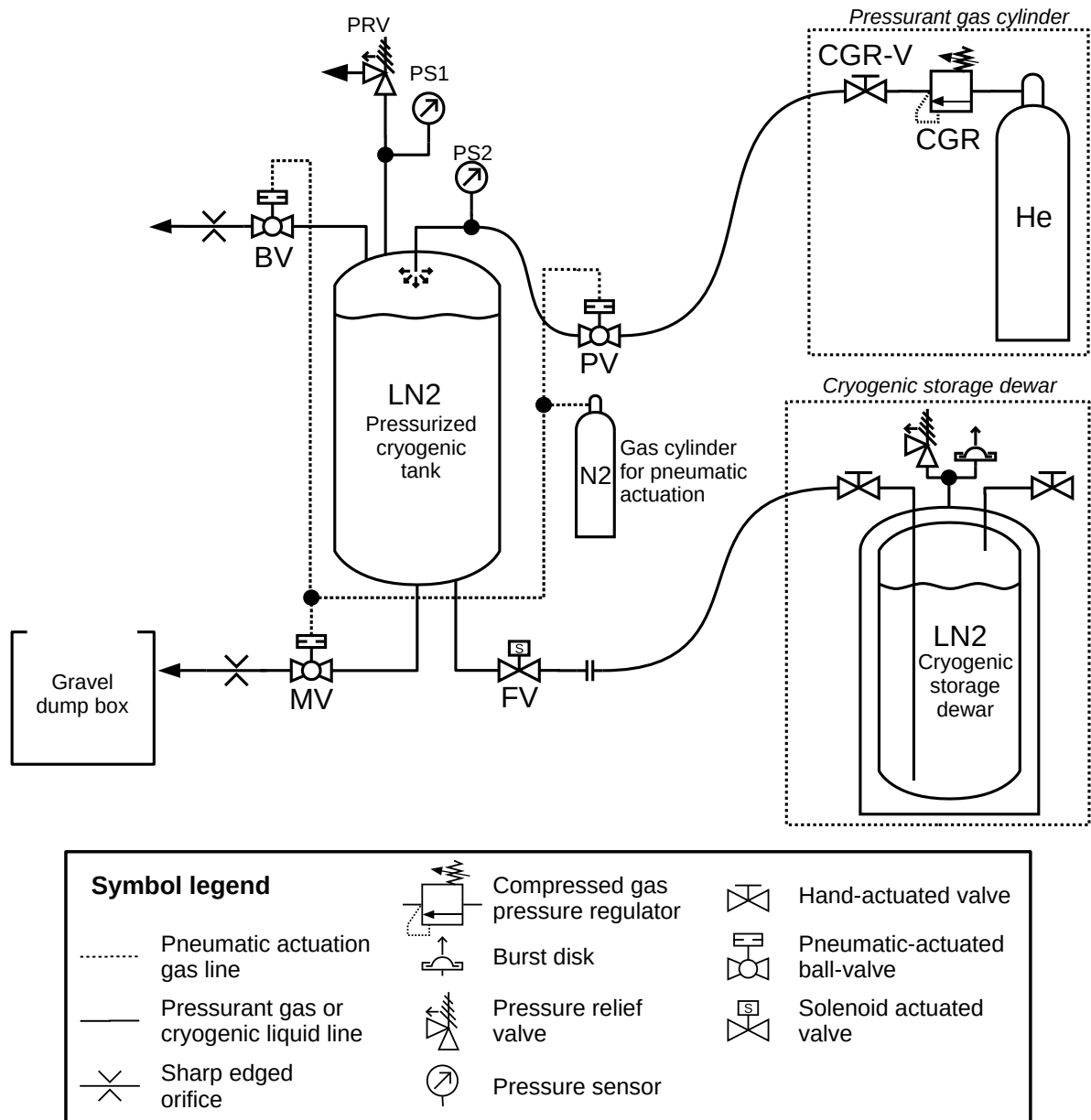
Figure 5.1: The feed system layout for the test setup.

The bleed line consists of the bleed valve (BV) and the bleed line orifice. The line starts at the top bulkhead in a 1/2" BSPP connection. The line is made of 1/2" stainless steel tube with a wall thickness of approximately 2 mm. The bleed line is used to vent evaporating nitrogen from the tank during the filling process so that the pressure in the tank remains lower than the pressure in the dewar. The line is also used for de-pressurization of the tank.

The auxiliary line is a 8 mm stainless steel line (1 mm wall thickness) that goes approximately 250 mm up from the tank bulkhead. There it branches via a T-piece to the safety pressure relief valve (PRV) and the tank pressure sensor (PS1).

The pressurization line starts at the chosen inlet for the pressurant injector as a 8 mm stainless

steel pipe that runs for about 150 mm before it branches via a T-piece to the feed line pressure sensor (PS2). After the T-piece follows the helium line temperature sensor (TC0). This is then connected to the pressurization valve (PV) via a flexible braided hose of approximately 2 m length, 7 mm inner diameter. From PV a second flexible hose (again ~2 m) runs to the compressed gas regulator assembly on the helium bottle. This assembly consists of a small hand actuated valve (CGR-V) and the regulator itself (CGR). The helium bottle is a standard 50 L, 200 bar, 4.6 purity, helium bottle. This line is used to feed the high pressure helium into the tank during pressurization.

The dump line starts in the centre of the bottom bulkhead in a 3/4" BSPP connection. The entrance of the line at the bulkhead side is slightly rounded to reduce losses at the inlet (rounding with 0.15 times the entrance radius[18]). The tube is made of 18 mm stainless steel tube with 2 mm wall thickness. The tube bends 90° with a bending radius of 54 mm and is in total approximately 400 mm long. It then connects to the main valve (MV). The tube then continues for about 250 mm and ends at the dump orifice. The dump orifice is a straight-edged round orifice of 3.8 mm diameter. It has been sized to give 400 g s^{-1} mass flow for the expected operating pressure of the tank. The orifice was sized by means of equation 5.1, which is the equation for a cavitating orifice (i.e. the pressure in the orifice is equal to the liquid vapor pressure)[33]. Its coefficient of discharge was assumed to be 0.6.[61] During expulsion the main valve is opened and LN2 can flow out of the tank via this line. The LN2 is dumped into a cubic aluminium box (400 mm on each side) that is half filled with approximately 22 kg of plain gravel. The box is half open at the top. The dump box proved effective in containing the nitrogen outflow and allowing a controlled evaporation of the LN2.

$$\dot{m} = C_D A_{orifice} \sqrt{2\rho \left(P_{tank} - P_{vapour} \right)} \tag{5.1}$$

The final line is the fill line. This line starts from the main bulkhead in a 3/4" BSPP connection. It is also stainless steel 18 mm diameter, approximately 150 mm long, with a 90° bend of 54 mm bending radius. Connected to this is the fill valve (FV). Attached to this valve is a connector to which the flexible braided hose of the LN2 dewar can be connected. The dewar itself is a small 60 L movable dewar.

Table 5.1: An overview of the feed system components, their main properties, and their type numbers.

Name (abbreviation)	Description
Bleed valve (BV)	1" cryogenic ball valve. Pneumatically actuated. Normally opened. 12V supply. Build by Armatec. Actuator type number: AT 3811. Valve type number: AT 3502C.
Pressurization valve (PV)	1/2" ball valve. Pneumatically actuated. Normally closed. 12V supply.
Main valve (MV)	3/4" cryogenic ball valve. Pneumatically actuated. Normally closed. 24V supply. Supplied by ERIKS. Actuator type number: SAF fig. 7971. Valve type number: 1380.
Fill valve (FV)	1/2" cryogenic, solenoid piloted globe valve. Normally closed. 12V supply. Supplied by ERIKS. Valve type number: 32616.
Bleed line orifice	Custom made aluminium orifice. Square edged. 1/4" BSPP attachment. Diameter: 6 mm. Orifice length: 5 mm.
Dump line orifice	Custom made aluminium orifice. 3/4" BSPP attachment. Square edged. Diameter: 3.8 mm. Orifice length: 5 mm.
Pressure relief valve (PRV)	1/4" Herose safety valve. Type number: 06002. Orifice diameter: 6.0 mm. Set pressure: 55bar (certified). Bought from Vcc bv.
Compressed gas regulator (CGR)	GCE DruVa FMD500-16 cylinder pressure regulator. Max. set pressure: 200 bar. Supplied by TU Delft Logistiek & Milieu.

5.2. Tank design and construction

This section of the report discusses the design and construction of the run tank that forms the main component of the test setup. The tank is a cylindrically shaped aluminium tank with flat bulkheads. The main dimensions, the design parameters, and the materials are discussed in section 5.2.1. The

construction of the tank is shortly shown in section 5.2.2. The pressure testing, to ensure the tank can safely hold the design pressure, is described in section 5.2.3. The sealing of the tank, and the problems that arose there, are described in section 5.2.4. The insulation that was placed around the tank is discussed in section 5.2.5. The whole section is concluded in 5.2.6 with a number of recommendations for future tank design and construction within DARE.

5.2.1. Dimensions, materials and design

The LN2 tank was designed according to the basic structure that is common within DARE. The tank consists of an cylindrical tube that is purchased off-the-shelf, sealed off with two custom machined bulk-heads that fit into the tube, and that are fixed radially with bolts. These types of tanks have been used for the hybrid rocket engine research at DARE[14], the Stratos II rocket[63], and they have been investigated in the DARE minor on cryogenic tanks[11]. A bolted type of design was chosen, as opposed to a welded tank such as was investigated during the minor[11], because of the existing experience with these types of tanks within DARE, and because it offers the possibility to remove a bulkhead when desired. This may be needed to inspect the tank itself or any of the sensors placed inside it.

Dimensions

The dimensions for the tank were influenced mainly by the work done during the DARE minor in 2015-2016. The design choices made there mainly reflected the desire of DARE to construct ever bigger rockets. The design of Stratos II+ featured a 200 mm outer diameter tank[63], but larger diameters will be required when aiming for higher altitudes. Because of this and because of availability of tubes, an aluminium tube of 250 mm outer diameter and 230 mm inner diameter was selected. The length of the tank is 800 mm, which was selected as a balance between a tank with a high L/D, a manageable size for a test setup, and again the availability of tubes. The bulkheads were designed to be 30 mm thick each (more details later in this section). This means the main outer dimensions of the tank are 250 mm diameter and 800 mm length. The inner dimensions are 230 mm diameter and 740 mm length, resulting in a total inner volume of 30.7 L. The total mass of the tank (as by measurement, including bolts) is 23.3 kg. The tank is very heavy for its size and certainly not designed for flight. The main mass is due to the 10 mm thick tank wall (16.3 kg). All the bulk dimensions have been selected to withstand the design pressure (discussed below) and to try and minimize the required machining work on the components. In hindsight it would most likely have been better to have machined the tank wall down to a smaller thickness as this also reduces the thermal mass, and thus eases the cooling procedure of the tank in cryogenic operations (section 5.8.2).

Three further sizing parameters of the tank were left open to size for the design pressures. From the calculations (presented later on) it follows that the distance from the bolt centreline to the wall edge is 11 mm, the amount of bolts in the top bulkhead is 20, and the amount of bolts in the bottom bulkhead is 24. The difference in amount is chosen to make sure the top bulkhead fails first. Furthermore the amount of bolts was chosen so that the angular spacing between them is a whole number of degrees. This was chosen to ease production as the tools used for making the holes have markings in whole degrees only.

For the simulations and analysis of the tests the inner volume of the tank is of importance. The inner diameter is designed to be 0.230 m and the length to be 0.740 m. The uncertainty on the diameter is estimated to be ± 0.5 mm, based on measurements of the inner diameter of the tube. The accuracy of the tank length is estimated to be ± 2 mm, based on measurements of the tank wall, bulkhead thickness, bolt hole locations in bulkhead and tank wall, and play of the bolts in the bolt holes. Combining these uncertainties for the nominal tank dimensions gives an inaccuracy for the tank cross-sectional area of $\sigma_A = 2R\sigma_R = 2 \cdot 0.115 \cdot 0.5 \cdot 10^{-3} = 0.115 \cdot 10^{-3} \mathrm{m}^2$, which is 2.8% of the total area. Adding in the inaccuracy in the length, gives the uncertainty in tank volume: $\sigma_V = R\sigma_L + L\sigma_R = 0.6$ L, which is about 2% of the volume. Based on the inaccuracy of other parameters, it can be decided if this production in accuracy is of relevance. Parameters that could also be considered of influence on the total tank volume are the volumes enclosed in the feed-lines ($+0.16L \approx +0.5\%$), the volume taken up by the sensors in the tank ($-0.04L \approx -0.1\%$), and the change in volume due to thermal expansion (contraction) of the tank ($-0.36L \approx -1.2\%$).

Materials

The tube that forms the tank wall has been bought from Alumeco, a Danish aluminium supply company. The company specifies the material as aluminium EN AW-6082 T6, with the mechanical properties via

EN 755-2. According to a datasheet provided by the aluminium supply company Aalco[6], the strength properties at room temperature for this material are: proof stress (0.20% deformation) of 260 MPa and ultimate stress of 310 MPa.

The bulkheads are machined from two circular slabs of aluminium (230 mm diameter, 50 mm thick) bought from the Dutch company AluminiumOpMaat. The material is specified as EN AW-6082 T6, with mechanical properties via EN 755-2 (both equal to the tank wall). Additionally the chemical composition is specified as being via EN 573-3.

A relevant paper on the influence of cryogenic temperatures on AW-6082 T6 has been published by Park et al.[48]. They performed tensile tests on bars of 6082-T6 on temperatures from 293 K (20°C, room temperature) down to 110 K (-160°C, temperature of liquid methane at 1 bar). The specific alloy composition they cite for their test samples fall within the range for the definition of AW-6082, as also specified by the Aalco datasheet[6]. The proof stress and ultimate stress at room temperature given by Park et al. are however higher at approximately 340 MPa and 370 MPa respectively (slightly dependent on the speed with which the strain was applied). The values by Aalco, as stated above, are the minimum values for the alloy specification and thus the more conservative ones. Park et al. find continuously increasing proof stress and ultimate stress for decreasing temperature. At 110 K the proof stress has risen to approximately 450 MPa and the ultimate stress to around 495 MPa. These results have been deemed sufficient to indicate that the aluminium will not weaken in strength when cooled down to cryogenic temperatures.

The bolts were selected to be from a commonly used stainless steel in cryogenic engineering. The bolts were bought from Techwinkel.nl and are specified by the supplier as stainless steel A2-70 (DIN 267), which is equivalent to the commonly used designation 304. The bolts are M10x40 with an hexagonal head. The thread extends up to 27 mm of length along the bolts. The bolts are loaded in shear on the untreated part, meaning that the effective shear area for the bolts can be based on the thread major diameter (i.e. 1 0mm).

At room temperature these types of stainless steel bolts have an ultimate tensile stress of 700 MPa (as by DIN and ISO standards for stainless steel fasteners). The proof strength (0.20% elongation) for these bolts is 450 MPa. For the yield shear strength of these types of bolts the British stainless steel association recommends a value of 311 MPa.[1] However, applying the Von Mises stress relation, the shear stress would be $\sigma_y = 450/\sqrt{3} \approx 261 MPa$. Which is a more conservative value. For ultimate stress the Von Mises relation for stainless steel is applied using a factor of 0.75, which gives $\sigma_u = 700 \cdot 0.75 = 525 MPa$.[7]

Publication number 4368 of the Nickel Development Institute lists the properties of various types of steel for cryogenic service [47]. For type 304 steel figure 1 in this publication shows that the ultimate tensile stress increases from 700 MPa at room temperature to 1600 MPa at cryogenic temperatures. Yield stress also increases, only to a slightly lower degree. The description in the publication furthermore states that for these types of steel "ductility values remain high down to the lowest temperature for which data is available" and "exposure to sub-zero temperatures has no adverse effect on the tensile properties [...] at normal temperatures". Based on this it was determined that these bolts were suited to be used in the cryogenic tank design and that they will not weaken or become brittle at the LN2 temperatures.

Based on this information the mechanical properties of the aluminium and the stainless steel are taken to be those presented in table 5.2. The values for room temperature are the conservative ones mentioned in the text above. It is difficult to obtain reliable material properties data for cryogenic temperatures for the specific alloy compositions, so these values should be considered merely indications of the expected strength of the tank. One thing that is for sure is that the yield and ultimate strengths of both the aluminum and the steel will increase significantly with the decreasing temperature, thus increasing the design margins on the tank. The values at cryogenic temperatures for aluminium are calculated by increasing the values from the Aalco datasheet with the same factor as found by Park et al.[6, 48]. The values at cryogenic temperatures for the steel have been found by taking the DIN standard strengths for stainless steel fasteners and by increasing these with the same factor as the data presented by the Nickel Development Company for stainless 304 (figure 1 in their publication)[47].

Tank failure modes
The design of the tank was evaluated based on the three possible failure modes of the tank:

---

[1]http://www.bssa.org.uk/topics.php?article=127

Table 5.2: Strength properties for aluminium EN AW-6082 T6 and stainless steel 304 at room temperature and cryogenic temperatures based on references [6, 7, 47, 48]. The values for cryogenic temperatures are rough, conservative estimations. The values for shear stress are calculated from the values for tensile stress using the Von Mises criterion.

| | Room temperature | | | | Cryogenic temperatures | | | |
| | Tensile [MPa] | | Shear [MPa] | | Tensile [MPa] | | Shear [MPa] | |
Material	σ_y	σ_u	σ_y	σ_u	σ_y	σ_u	σ_y	σ_u
Alu 6082-T6	260	310	151	233	344	415	200	311
Stainless 304	450	700	261	525	879	1600	510	1200

1. Radial burst of the tank wall

2. Shear failure of the bolts in a bulkhead

3. Wall shear out (tear-out of the bolts through edge of the tank wall)

Of these failure modes the 3rd is the preferred one. Water pressure tests with these types of tanks within DARE has shown that such a tear-out will occur relatively slowly with the aluminium wall tearing, instead of breaking, and with the bulkhead rotating away from the tank axis. This means that when the tank fails, it will release pressure without creating metal shrapnel.[14] The tank will be designed such that it is the top bulkhead that will shear out first, instead of the bottom bulkhead, which is the more common practice for DARE. It is thought for this specific application that it is better to have the top bulkhead fail instead. There are 2 main reasons for this:

1. If the bottom bulkhead would fail, it would mean that a leak or failure at this site would eject cryogenic liquid from the tank instead of pressurized gas. This has various consequences:

   (a) This ejected cryogenic liquid could cause more damage to the rest of the test structure / test location and could potentially lead to more dangerous situations still. Failure at the top would allow for a slow boil-off of the cryogenic liquid instead.

   (b) De-pressurization at the top would be faster as a small breach in the tank would allow quick release of the pressurizing gas. If the breach would occur at the bottom, liquid would be ejected first, which makes the de-pressurization occur slower.

   (c) Large amounts of liquid that are quickly ejected from the tank in uniform direction could act as a reaction mass for the tank top bulkhead and tank wall, more quickly and violently displacing these (see point 2).

2. Normally tanks at DARE are clamped along the circumference, leaving both bulkheads free. The insulation on the tank required for cryogenic operations does not allow easy circumferential clamping. Therefore the tank holder design has the tank sitting in a frame and resting on the bottom bulkhead. Failure of the bottom bulkhead would mean that the whole tank wall is displaced upwards. While failure of the top bulkhead would only displace the top bulkhead.

Design
The tank dimensions had been fixed by the requirements and the availability of materials. The maximum tank operating pressure had been determined from the initial system sizing (section 2). The maximum operating point for this master thesis research was set to be 30 bar. However, as the tank is intended to be usable for later small scale tests within DARE, the maximum operating point for the tank is set higher at 55 bar. Over this pressure a safety factor of 1.5 is applied, leading to a design pressure of 83 bar.

The first failure mode (radial burst) is expected to occur for the tank at 226 bar at room temperature (equation 5.2). This equation can be repeated for the ultimate stress and for cryogenic temperatures.

$$\sigma_y = \frac{Pr}{t} \Rightarrow P = \frac{\sigma_y t}{r} = \frac{260 \cdot 10}{115} = 226 \text{ bar (yield, room temperature)} \tag{5.2}$$

The second failure mode occurs when the bolts would fail by shear. Each bolt has a core cross-sectional area with diameter 10 mm. There are 20 bolts in the top bulkhead and 24 in the bottom.

Equating the pressure force on the bulkhead with the shear stress in the bolts leads to equation 5.3. The factor 0.58 in this equation is due to the Von Mises relation for shear. For the top bulkhead at room temperature this means this failure mode occurs at 98.7 bar tank pressure.

$$\sigma_y = \frac{PA_{\text{tank}}}{0.58nA_{\text{bolt}}} = \frac{4Pr_{\text{tank}}^2}{0.58nD_{\text{bolt}}^2} \Rightarrow P = \frac{0.58nD_{\text{bolt}}^2\sigma_y}{4r_{\text{tank}}^2} \tag{5.3}$$

$$P = \frac{0.58 \cdot 20 \cdot 10^2 \cdot 450}{4 \cdot 115^2} = 98.7 \text{ bar (yield, top bulkhead, room temperature)}$$

The calculation of tear-out of the bolts from the wall can be done by calculating how much force the shear areas in the aluminium wall above each bolt can hold combined. This leads to equation 5.4 as presented by Kulak et al. [40]. In this equation t is the wall thickness and L is the distance between the bolt centerline and the wall edge. The factor 0.58 in this equation is again due to the Von Mises relation for shear.

$$P = \frac{n \cdot (2t)\,(L - D_{\text{bolt}}/2)\,\left(0.58\sigma_y\right)}{\pi r_{\text{tank}}^2} \tag{5.4}$$

$$= \frac{20 \cdot (2 \cdot 10)\,(11 - 10/2)\,(0.58 \cdot 260)}{\pi 115^2} = 87.1 \text{ bar (yield, top bulkhead, room temperature)}$$

One thing that still needs to checked with this final calculation is if the distance between the bolt centreline and the wall edge is not too small to make the method of calculation invalid. Kulak presents equation 5.5 to check this. In this equation L is the distance between the bolt centreline and the wall edge, σ_u is the ultimate stress of the wall material and σ_b is the bearing stress, which is defined by equation 5.6.

$$\frac{L}{D_{\text{bolt}}} \geq 0.5 + 0.715\frac{\sigma_b}{\sigma_u} \tag{5.5}$$

$$\sigma_b = \frac{F_n}{D_{\text{bolt}}t_{\text{wall}}} = \frac{P\pi r_{\text{tank}}^2}{nD_{\text{bolt}}t_{\text{wall}}} \tag{5.6}$$

For the room temperature situation at the top bulkhead these equations give a bearing stress of $\sigma_b = 171.4$ MPa and a minimum bolt-wall distance of $L_{\text{min}} = 8.95$ mm. With the chosen value of $L = 11$ mm this criterion is thus satisfied and equation 5.4 is applicable in the current design.

From this it is clear that the tear-out of the bolts will be the first failure mode to occur, and it will occur only above the design pressure. Equations 5.2, 5.3 and 5.4 can be evaluated for yield strength and ultimate strength, for the top and bottom bulkhead, and for room temperature and cryogenic temperatures. Using the material properties from table 5.2 results in the tank pressures associated with the different failure modes as given in table 5.3.

5.2.2. Construction
The tank was produced via a number of machining steps. The first was the processing of the tank wall. The tank was placed horizontally on a mill and rotated around its axis by a rotating clamp. Because of the large diameter, wooden spacer blocks needed to be added to the clamp to ensure the tank could be fitted on the bench. The use of these wooden blocks also was beneficial to production as it meant there was no chance of the tools hitting the steel clamp. The wood can be safely drilled and milled with the same tools as used for the aluminium. The method of clamping allowed to first mill the outer edge of the tank to make it flat, smooth, and perpendicular to the tank axis (figure 5.2). After this the holes were drilled without removing the tank from the clamp. The milling of the outer edge and the subsequent drilling of the holes without moving the piece or changing the mill reference ensured that the 11 mm of distance between tank wall edge and bolt hole centre, as specified by the design, could be met. Subsequent inspection of the holes showed that the instance did not vary by more than 0.1 mm over all holes along the circumference of the tank. After removal from the mill the tank wall edge and all bolt holes were manually deburred and smoothened.

The tank bulkheads were produced in a number of milling and turning sessions. First the main shapes of the bulkheads were turned from the bulk aluminium blocks (figure 5.3) and the centre holes

Table 5.3: Calculated tank pressures at which certain failure modes are expected to occur. The associated safety factors are calculated as compared to the maximum operating pressure of 55 bar. The calculations are done using equations 5.2, 5.3 and 5.4 and the material properties from table 5.2.

Failure mode		Room temperature		Cryogenic temperature	
		P [bar]	Safety factor	P [bar]	Safety factor
1. Radial burst	yield	226	4.1	299	5.4
	ultimate	270	4.9	361	6.6
2. Bolt shear	top, yield	99	1.8	192	3.5
	top, ultimate	118	2.2	231	4.2
	bottom, yield	198	3.6	454	8.2
	bottom, ultimate	238	4.3	544	9.9
3. Wall tear-out	top, yield	87	1.6	115	2.1
	top, ultimate	105	1.9	138	2.5
	bottom, yield	134	2.4	180	3.3
	bottom, ultimate	161	2.9	216	3.9

Figure 5.2: Flattening the outer edge of the tank wall with a mill.

Figure 5.3: The two bulkheads after the first production step.

Figure 5.4: Top bulkhead after the final production step, with all holes drilled and threaded

were threaded. Subsequently the radial bolt holes were drilled on a mill, clamped in a similar fashion as the tank wall. The holes were threaded manually. After this the tank was first pressure tested (section 5.2.3) and only after that the off-centre holes for sensors and feed system connections were drilled and threaded on a mill, resulting in the final product (figure 5.4).

During all production steps on the mill of tank and bulkheads a reference point and reference direction was kept (visible by the red line and arrow on the bulkhead in figure 5.4). The first radial hole to be drilled was kept as starting point ('hole #1') and the direction in which the holes were drilled was made the reference direction. This facilitated inspection of the products and subsequent processing steps as it serves as a datum feature. The angular spacing of the holes turned out to have been created constant enough for both bulkheads and both sides of the tank that the reference points could be made to match (i.e. hole #1 in the tank matches up with hole #1 in the bulkhead during assembly).

An overview of the production and the amount of man-hours spend on it is provided in appendix F.

5.2.3. Pressure testing

The tank was pressure tested with water at the company Advanced Lightweight Engineering (ALE)[2] in Delft on the 13th of October 2016. The tank was assembled with rubber O-ring seals for this test. In preparation for the water pressure test the tank was first subjected to a leak test with nitrogen gas up to 10 bar at the DARE workshop on the 10th of October. During this leak testing a small leak was found at the top bulkhead. After de-pressurization the bolts were loosened and re-tightened in a different order so as to put more uniform force on the tank wall, and to try and even the distance between tank wall and bulkhead. The method proved successful as no leakage was observed during the tests at ALE.

---

[2]http://www.ale.nl/

The intended set pressure of the water pump at ALE was to be the maximum operating point of 55 bar, which was to be held for 5 minutes. Examining the pressure data later on showed however that the pump setup at the company was not properly configured. The tank pressure could only be maintained in stretches of about 90 seconds at a time and the maximum pressure that was put on the tank was 70 bar. Three tests runs of around 90s each were conducted on the tank. Subsequent inspection of the tank did not show any visible damage on the tank wall or the tank bolt holes. As metal tanks do not suffer from effects such as creep, as the number of operation cycles of the tank during its lifetime is expected to be low, and because of the large safety factors on the tank, the three tests are considered sufficient assurance that the tank can be safely operated up to pressures of 55 bar.

5.2.4. Sealing

The sealing at the tank bulkheads was intended to be achieved by making use of a single FEP spring-loaded O-ring on each bulkhead. The O-rings were supplied by the UK company Eastern Seals[3]. The grooves in the bulkheads were machined according to the specifications of the supplier. During the first test assembly of the top bulkhead it was however found that the FEP rings are very sensitive to the tolerances for the fit and that they are damaged very easily. During assembly the rings are first compressed into the groove when the bulkhead is inserted. Then as the bulkhead is slit down into position the O-ring passes over the bolt holes and slightly expands into these holes. Subsequently the O-ring needs to be compressed again into its final position. It was found that the edges of the bolt holes can severely damage the O-ring (figure 5.5). The main reason for this damage is believed to be the non-roundness of the tube itself. The tube is sold as being 250 mm outer diameter with 10 mm wall thickness. However upon inspection it was found that the tank wall on some places goes down to 9.5 mm thickness, and that the tube is actually far from round. Measurements of the inner diameter of the tube varied between 229.75 mm and 231.1 mm for the tank bottom, and between 229.5 mm to 231.45 mm at the tank top. The tank wall was not machined on its radial dimensions, and so, although the bulkheads were made according to the O-ring specifications, the deviations in the tank wall made that the O-ring was squeezed too much during assembly.
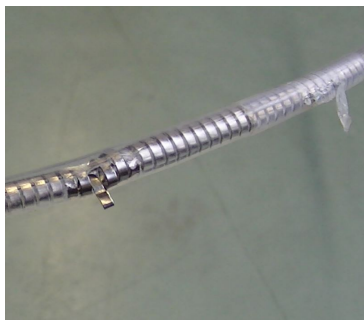

Figure 5.5: Major damage at the FEP o-ring due to the bolt holes. The FEP outer ring has broken on two places and on one spot the metal spring comes out.

Figure 5.6: Forcing the tank into shape with two clamps reduces the deviations in roundness for the tank substantially.
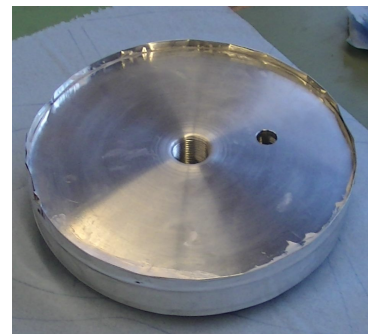
Figure 5.7: Aluminized tape was used as a protective wrap around the tank bulkhead and FEP o-ring during assembly of the tank. The tape could subsequently be pulled out of between the tank wall and bulkhead.

To solve the O-ring damage problem two methods were employed. First the tube was artificially forced into shape with two clamps (figure 5.6). In the top bulkhead this significantly reduced the diameter deviation to a minimum of 230.1 mm and a maximum of 230.7 mm. As a second method the O-ring was protected during assembly by applying an aluminized tape around the tank bulkhead. The tape was folded double to make sure no adhesive from the tape could stick to the ring, bulkhead, or tank wall. The tape protects the O-ring from sharp edges during insertion, and retains the O-ring when it passes over the bolt holes, limiting the expansion of the O-ring into these holes. Added to this the applied Krytox lubricant eased the assembly.

Visual inspection of the O-ring after the first exposure test in December 2016 (section 5.8) showed no significant damage to the O-ring, indicating that the described methods were effective in preventing

---

[3]http://easternseals.co.uk/

damage. However, the O-ring was not doing it's job of sealing the tank itself, as was observed during the first exposure test. Leak-testing of the tank with compressed air to 5 bar showed that the bottom bulkhead had small leakage that could not be solved by a new O-ring, or by different methods of tightening the bolts. Therefore it was decided that the bottom bulkhead be sealed by applying PU glue instead of a lubricant (see section 5.5.3 for information on the PU glue). This unfortunately means that the tank is no longer oxygen compatible and can only be used for LN2 tests.

The tank was subsequently leak tested with nitrogen at ambient pressures up to 25 bar in pressure on the 22nd of December 2016 and was found to be leak-tight.

5.2.5. Insulation

The insulation material applied to the tank was a roll of aerogel material, about 10 mm thick, selected during the DARE minor 2015-2016 [11]. The material is called "Insulroll" and has been provided by the company Insulcon. The material comes in a sheet that is relatively soft but not very pliable. Wrapping the material around the tank requires quite some effort and force. The processing of the material with scissors or knifes is cumbersome, making cutting of small sections for the top and bottom bulkhead difficult. The material also gives of a white powder that makes skin feel dry, akin to talc-powder. Considering the insulation material, this powder is most likely silicon-dioxide. Wearing gloves is highly recommended during the processing of the material. The cut edges of the materials are also not a clean cut and small fibres and powder are coming off of the edge when it is touched. The fibres and the power mean that tapes in general do not stick to the material.

During the first expulsion test the material was wrapped around the main tank and held in place by wires wrapped around it. A small sheet of the material was placed under the tank bottom bulkhead, but this sheet was displaced during transport or during the test (see section 5.8). The top bulkhead, and the bottom feed system connections were not insulated at all during the first exposure test. Due to a failure of the mass sensor during that test, no proper estimate of the average heat leak into the tank could be determined.

During the subsequent tests, the sheet at the bottom was replaced by a Styrofoam plate of 20 mm thickness. The tank top bulkhead partially covered by a small 1 mm thick PTFE plate. The bottom feed system connections were insulated by loosely wrapped aluminium foil around it.

5.2.6. Tank design recommendations

Based on the experiences during tank construction and operations a number of recommendations can be made for tank design within DARE.

Cryogenic tank sealing
1. Investigate more in detail the sealing methods possible with cryogenic compatible O-rings and sealants together with industry experts; Sealing of a tank in this way with O-rings is possible, we just have not properly figured out how.

2. Investigate if liquid oxygen compatible glues exist and can be acquired. This can form a sure way to achieve a seal on a tank.

3. Find a way to machine the inside sections of a tank wall so that these can be made to match the tight tolerances required for the O-rings.

4. Use a smaller diameter tank when possible: Smaller diameters are more readily available with smaller wall thickness and inaccuracies in the tank diameter are proportional to tank diameter. Smaller tank diameters will thus result in less problems with the tolerances for the O-rings.

Machining
1. Use of wooden spacer blocks at the clamps greatly facilitate drilling and milling of the tank wall as it means that the clamps do not form any obstacle to the machining tools any more.

2. Debur bolt holes and tank edges very carefully and thoroughly to make sure no sharp edges remain.

Thermal

1. The Insulroll insulation material can be used for wrapping around the tank circumference, but is not suited to use for flat bulkheads or tubes. Possibly it can be better applied by attaching the material with some form of glue to the tank. It would however be more beneficial to try and find an alternative insulation material that is easier to cut into shape, more pliable, and releases no powder or fibers.

2. Reducing the tank mass is beneficial because it reduces the thermal mass of the system and thus decreases the amount of liquid cryogen needed to cool it down, saving in operation time and in liquid cryogen.

5.3. Pressurant diffuser

The pressurant diffuser is the injector element at the top of the tank that determines how the pressurant gas is injected into the tank. For this research it is chosen to investigate simple radial and axial injection. To simplify operations a diffuser design has been made that allows to switch between these two injection methods by changing connections on the outside of the tank. The design with dimensions is shown in figure 5.8. Two inlet ports are present that allow to switch between axial and radial injection (or both, during a test with a vortex tube). The port not in use is sealed off with a blind stop. This design means that for changing the injection method a simple metal-to-metal feed system connection needs to be redone on the outside of the tank, and no PTFE crush rings need to be replaced. Also the tank does not need to be opened.
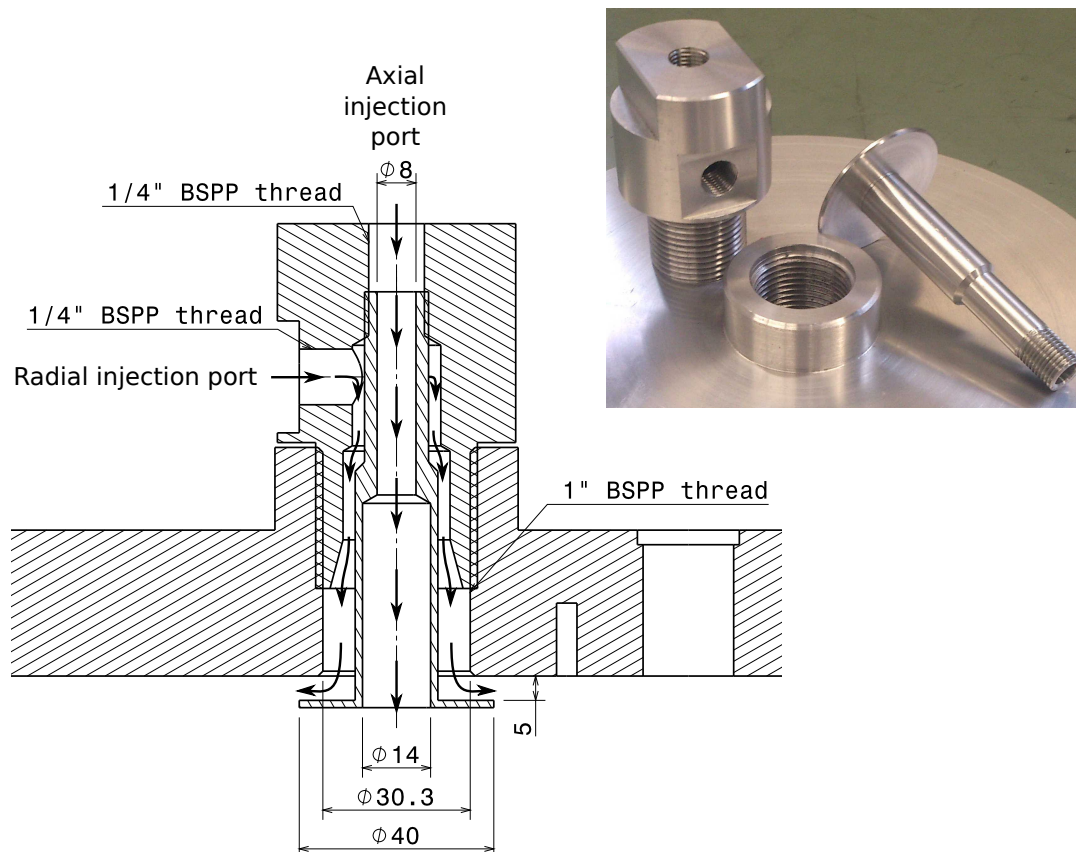

Figure 5.8: Cross-section of the assembled diffuser in the top bulkhead of the tank. Flow patterns for radial and axial injection are indicated with the thick black arrows. Dimensions are in millimetre. The injector is axisymmetric, apart from the radial injection port. *Inset picture:* The produced diffuser body and insert on top of the tank bulkhead.

The diffuser consists of a main body that is screwed into the tank top bulkhead from the outside of the tank, and an insert that is screwed into the main body from the inside of the tank. This construction does mean that the diffuser cannot be fully removed without opening the tank. The orifice sizes have

been sized to make sure the gas velocity of the injected gas is below 10 m s^{-1}, to make the injection situation comparable to those describe by DeWitt[25]. Note that the inside surface of the hole of the tank bulkhead into which the diffuser is screwed is not flat but has a 1" BSPP thread on it. The injected gas flows over this thread. The injector pieces are made of aluminium 6082-T6 and weight approximately 25 g (insert) and 220 g (main body).

5.4. Test bench structure

The main test setup to hold the tank and all feed-system components was constructed out of an inner cage structure in which the tank sits. This cage is suspended on two flex-plates and rests upon a load cell. The whole setup is hung in the main test bench structure. The front beams of the main structure and the cage can be removed so that the tank can be placed into the tank holder.

The structure was made using standard 40x40mm aluminium profiles, typically used for test setup construction in laboratories and industry. A total of approximately 12 m of profile was used. The choice for this type of structure was made because of its flexibility in usage, its ease of construction, and the possibility to disassemble it fairly easily. It was observed that test benches within DARE in the past were always bulky solid structures made of steel tubes welded together. These benches are heavy, cumbersome to adapt to design modifications, and take up a lot of space in the workshop after they have been used in a project. The connections between the beams were made using either centre screws (that screw into the central hole in each tube profile) or screw-threaded tube connector combinations (that are screwed into the groves in the profile). The centre screws were bought because they were significantly cheaper than the other type of connectors. They however turned to be way less practical, more labour intensive and less flexible to use. It is recommended for future usage of these profiles to only used the self-threading tubes + screw type of connectors.
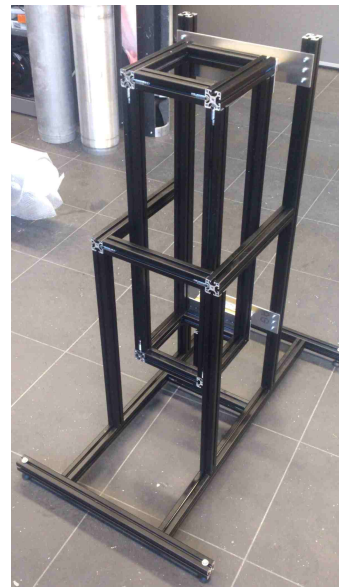

Figure 5.9: The assembled main test bench structure.

5.5. Sensors

The total test setup contains 21 sensors that measure various parameters on the test setup. These are 16 thermocouples, 2 pressure sensors, 2 load cells, and one capacitive sensor. This section of the report lists all different sensors, their type and properties, and their exact position inside the tank.

Sections 5.5.1 and 5.5.2 describe, respectively, the pressure sensors and load cells. Sections 5.5.3 and 5.5.4 elaborate on the thermocouples and capacitive sensor respectively. These last two sections are significantly more elaborated than the first two, as the thermocouples and capacitive sensor all required extensive modifications to be able to apply them in the test setup.

5.5.1. Pressure sensors

There are two pressure sensors on the test setup. The first (PS1) is connected to the tank via a 0.25 m stainless steel tube (8 mm outer diameter). This is connected on the port indicated in figure 5.10. The second sensor (PS2) is connected on a T-piece side branch in the helium feed system line, directly after thermocouple TC0. The branch is approximately 0.07 m long.

Both sensors are produced by the company Automation24 GmbH, with type number PC6708, with a measurement range of 0 to 100 bar.

5.5.2. Load cells

There are two load cells included in the test setup. The first is a 500 lb (227 kg) minature inline load cell from Futek, type number LCM300. The second is a 100 kg Scaime ZFA s-beam load cell. For the first exposure test the Scaime load cell was mounted at the bottom of the tank holding structure. However, here the sensor got exposed to temperatures below its recommended operating range, and

did not give any usable output. For subsequent tests, the Scaime sensor was replaced with the Futek sensor. The small dimensions of the Futek allowed it to be moved near the top and side of the tank holding structure (see section 5.8.2). The Scaime load cell was used as measurement load cell for the pressurant bottle during subsequent tests. For this it was equipped with stiff aluminium plates at the top and bottom to place the gas bottle upon. Aluminium struts at the corner points of the plates prevent putting high bending loads on the load cell or the plates. The whole measurement setup was encapsulated in styrofoam insulation to protect it against cold vapours coming from the tank.

During all tests the load cell at the tank is labelled LC1, and the load cell for the pressurant bottle is labelled LC2.

5.5.3. Thermocouples

There are a total of 16 thermocouples on the test setup, labelled TC0 through TC15. Of these, 1 is positioned in the helium feed line (TC0), 10 are positioned inside the tank (TC1 through TC10) and 5 are positioned on the outside tank wall (TC11 through TC15).

TC0 is a K-type thermocouple that is glued into an aluminium feed system adapter. The tip of the thermocouple is positioned in the centre of the pressurization line. During processing the tip of the thermocouple got covered in an estimated 2 or 3 gram of PU epoxy, which slightly heightens the thermal mass of the thermocouple. The adapter is positioned in the feedsystem approximately 0.20 m away from the inlet of the pressurant diffuser.

All other thermocouples are T-type thermocouples that are positioned in or on the tank. The sensors are placed in groups of 5 along three vertical lines: TC1-TC5 at 35 mm from the tank centreline, TC6-TC10 at 95 mm from the tank centerline (i.e. 15 mm from the tank wall), and TC11-TC15 on the outside tank wall. The first thermocouples are placed at 100 mm below the tank top bulkhead, and are then spaced 100 mm apart. The horizontal positioning of the three vertical lines is shown in figure 5.10. The thermocouples inside the tank are mounted on two M5 threaded stainless steel rods that are covered with a Teflon layer approximately 1 mm thick. The thermocouple tips are bent away approximately 5 mm from the rods, pointing towards the tank centre axis. The thermocouples on the outside tank wall are placed directly onto the aluminium of the tank wall by means of aluminium tape. The insulation material is wrapped over the thermocouples.
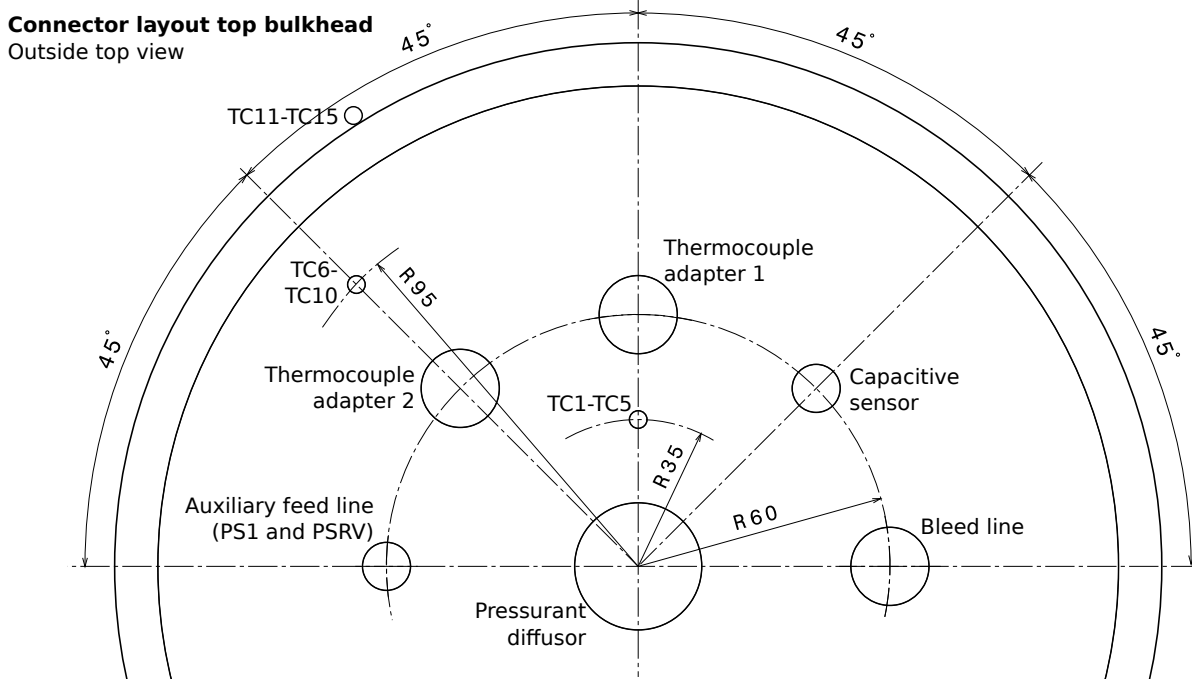

Figure 5.10: A top view of the tank top bulkhead with the various connection points for sensors and feed systems labelled. The positions of the thermocouple rods are indicated. Note that the thermocouples are on the outside of these rods, bent slightly towards the centre. The distances of the thermocouples to the centreline of the tank are 30 ± 3 mm and 90 ± 3 mm respectively. The thermocouples TC10 through TC15 are taped to the outside of the tank.

The thermocouples that are led into the tank (TC1 through TC10) need to go in via a special adapter, as the thermocouple cables need to be electrically isolated from each other and from the tank bulkhead itself. This is realized by means of a custom adapter construction in which the thermocouples are glued in and sealed with a special Polyurethane (PU) glue. The following paragraphs describe why there was no standard solution available for the thermocouple adapters, how the adapters were designed and constructed, and how they were tested before application in a cryogenic environment.

Standard thermocouple seals

Thermocouple placement into a pressurized system such as a feedline or tank is often realized by using a thermocouple that is mounted in the tip of a steel rod. The rod is fed into the tank via a regular tubing adapter. The seal can then be achieved with a double ferrule metal-to-metal seal between the rod and the tube adapter, which is exactly equivalent to a seal on a regular tube. However this method has a number of disadvantages in the intended application within this project. (1) The thermocouples in a steel rod are more expensive than loose thermocouples, plus extra adapters and sealing rings need to be acquired for each. (2) The thermocouples need to be mounted at various depths, up to 60 cm from the top bulkhead. These lengths of thermocouples within a rod are difficult to find and more expensive still. (3) Placing 10 separate adapters onto the top bulkhead would not be possible due to the restrained available area in the bulkheads. (4) Each separate adapter forms a potential leak path. (5) The volume, thermal mass, and conduction of the steel rods and their disturbance of the fluid flow all interfere with the thermodynamic processes occurring in the tank. (6) The steel rod gives the thermocouples a higher thermal mass, which reduces its response time to temperature changes.

Of these disadvantages, numbers 2 and 3 could be avoided by mounting the thermocouples through the tank wall instead of through the top bulkhead. This was however decided against because it breaks the integrity of the tank wall and because it does not alleviate any of the other disadvantages.

Thermocouple feed-through adapters that could handle multiple thermocouple cables at once were sought but could not be found suited for both the cryogenic temperatures and high pressures. Even if these would be found after a more intensive search, it is expected that the costs of these kind of adapters would be prohibitively large.

Because of these disadvantages it was decided to personally investigate the construction of a thermocouple feed-through adapter that would allow multiple thermocouple cables to be fed into the tank without a steel casing.

Design and construction

To construct the adapters it was decided to go for a so called "potting" method, in which the electric components (the thermocouple wires) are placed in an enclosure (an aluminium adapter) and are then sealed into the adapter by means of an epoxy or PU resin.

A resin needed to be found that would be suited for cryogenic temperatures. This was found with help of the company Temati[4], who recommended their product Kestopur PL2400[5]. Kestopur is a polyurethane glue that is normally used for the attachment of insulation material. They generously supplied 5 kg of this resin for this project, free of costs.

Kestopur has a high viscosity during preparation ($1.5 \cdot 10^6$ mPa s), therefore it cannot be applied by the regular potting method of simply pouring the resin into the enclosure. A force needs to be applied to force the PU into the adapter. To do this a small vacuum setup was made that allows to suck the PU into the adapter. This setup is shown in figure 5.11. It consist of an aluminium end piece (on the left) where the adapter that is to be filled with the resin can be screwed in. This end piece is attached to a plexiglas tube that allows viewing the inner end of the adapter during the potting process. After that follows another aluminium piece that holds the connection to the vacuum pump. After that follows a one metre long PVC tube with a closed PVC endcap. The setup has been constructed to be this long to make sure the thermocouple wires do not need to be forcefully coiled up in the equipment during the potting. The leaking in the equipment is minimal, allowing the pump to bring the setup down to below 20 mbar. The pressure can be somewhat controlled by means of a regulator valve in the line to the pump, that can be opened to allow outside air to be sucked in.

The adapters are all designed similar to the one shown in figure 5.12. They are cylindrical aluminium casings with an outer thread to screw the adapter into the tank. Internally there are small channels to

---

[4]http://www.temati.com/
[5]Kestopur PL2400 technical datasheet

feed the thermocouple wires through. These channels are kept as small as possible to ensure that there is relatively little pressure force acting on the hardened resin. On both the inner and outer end of the adapter there is a wider opening to allow for easy deposition of the resin on the outside, and for collection of the resin on the inner side. These wider plugs of resin that form here are also a more secure way to achieve a seal, compared to the small channels which were expected to not fill up properly (But which actually do, as it turned out. See next section.).

Figure 5.11: Thermocouple adapter potting equipment. The tube in front is pumped empty by the vacuum pump visible in the background. Adapters are mounted at the left end of the tube.
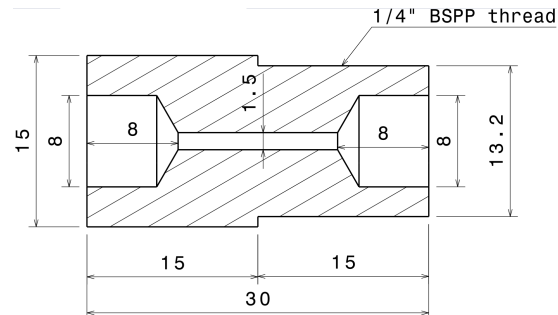
Figure 5.12: Technical drawing of the cross-section of an aluminium test adapter designed to hold one thermocouple. The dimensions are in millimetre.

During the potting process the empty aluminium adapter is placed into the aluminium end of the vacuum equipment. The thermocouple wires are placed in the adapter and fixed on the outside to ensure that the vacuum does not pull them in. Using a plastic syringe the resin is deposited in the outside cavity of the adapter. The vacuum pump is then turned on, which will slowly suck the PU resin through the small channels in the adapter. New resin is deposited continuously on the outside of the adapter to ensure that no air bubbles are introduces into the channels. On the inside the resin accumulates in the cavity present there. When it is observed that the cavity on the inside is full, the vacuum pump is turned off, and air is let back into the system. The adapter is then gently removed and the wires are then stirred sightly to evenly distribute the resin around the wires in both cavities. Extra resin is added by hand on both sides to form a smooth finish. Around 20 ml of resin eventually ends up in the adapter. A similar amount more remains on the equipment used to prepare the resin and in the syringe.

The process was conducted most smoothly if the PU had been prepared about 30 to 45 minutes before. Within this time the viscosity of the PU already increases, which actually eases the application process; If the PU is applied directly after mixing its viscosity is too low and it is sucked into the adapter too quickly for it to evenly distribute. The total potting process takes around 5 to 10 minutes per adapter.

Testing and evaluation
The first production test of an adapter was conducted with a large adapter designed to hold 5 thermocouples and which had an outer thread of 1/2" BSPP. Within this adapter four pieces of woven rope were placed, which are similar in structure to the glass fibre weave uses as isolation on the thermocouple wires. The fifth hole was taken by a small teflon isolated metal wire, intended to represent the cables that are used in the capacitive level measurement in the tank. The decision to place this wire in instead of a fifth piece of rope was made only after the holes had been drilled, which meant this hole was substantially larger than the wire going through it. During preparation it was found that this larger hole actually allowed the resin to flow through very easily. The supply of resin on the outside was not quick enough and so air bubbles were sucked in through this hole.

This adapter was leak tested with nitrogen gas but started to leak already at pressures below 5 bar. The gas appeared to leak through the weave of the rope itself. No leaks were observed through the PU, between the aluminium and the PU, or around the teflon insulated wire.

After this test the thermocouple adapter was inspected internally by step-by-step milling off 0.5 mm thick layers from the adapter, exposing the internal structure. Figure 5.13 shows such a cut through for

the first test adapter. Visible are the teflon isolated wire and one of the ropes. Clearly visible is that the rope is completely not permeated with the PU resin. The leakage can occur through these dry fibres. The teflon wire is well encapsulated. Visible at the bottom right are large air pockets, believed to have been caused by the air intake during production.
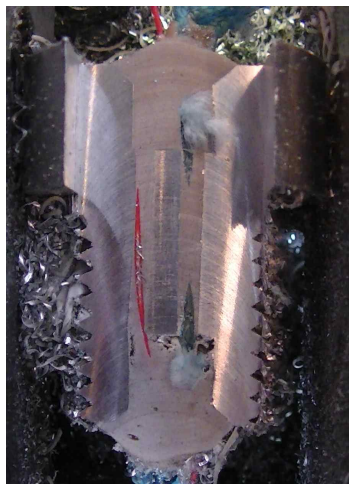

Figure 5.13: Cut through of the first test thermocouple adapter. Two channels are visible. On the left the fully encapsulated teflon isolated wire. On the right the dry weave of the rope. Parts of the rope have been pulled out by the mill. At the right bottom large air pockets in the PU are visible.

Figure 5.14: Cut through of a test thermocouple adapter. These wires had the full glass fibre isolation still present before potting. Visible in the middle is the empty channel in the PU in which the cable was embedded. Shown left are the dry fibres pulled out of the adapter by the mill.
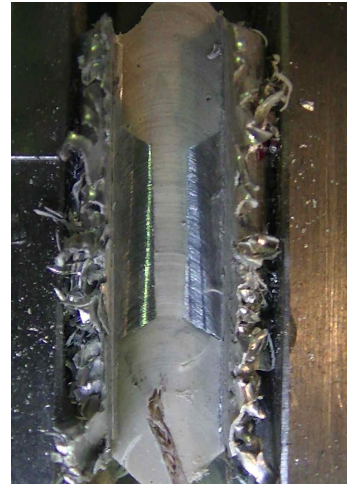
Figure 5.15: Cut through of a test thermocouple adapter. These wires were fully stripped and encapsulated in PU before the final potting. No un-covered areas nor bubbles can be spotted. The outline of the initial PU encapsulation is still faintly visible in the top cavity.

After this four small test adapters were created that had an outer thread of 1/4" BSPP and each contained one wire. These adapters were also pressure tested with nitrogen gas. Adapter one contained one actual thermocouple cable with all glass fibre isolation present. A cut through of this adapter is shown in figure 5.14. This adapter also leaked below 5 bar through the glass fibre weave as the PU did not permeate. Test adapters 2 and 3 both contained a thermocouple wire where the outer glass fibre isolation was stripped off, but the isolation around the two individual conducting cores remained in place. Still the PU did not permeate sufficiently to prevent leaking fully, although the leaks were substantially smaller compared to those of adapter one. Test adapter 4 contained a thermocouple wire that was fully stripped. To prevent electrically conductive contact between the two wires and between the wires and the metal casing, the wires had first been encapsulated in small layer of PU resin. After curing, this encapsulated section was potted into the adapter. This adapter held the nitrogen pressure without leak up to 55 bar.

Based on the results obtained with test adapter 4 the eventual thermocouple adapters used for the cryogenic tests were constructed with 5 thermocouples per adapter. The thermocouples were first stripped for about 30 mm at a location measured from the thermocouple tip, so that the distance from tip to adapter was equal to their vertical distance from the tank top bulkhead plus 50 mm margin. The completed adapter for thermocouples 1 through 5 is shown in figure 5.16. The thermocouples were screwed into the top bulkhead before tank assembly. The thermocouple wires were guided along two M5 threaded stainless steel rods, covered with a Teflon coating approximately 1 mm thick, that extend from the top bulkhead into the tank. They are attached to the rods at various positions with steel wire. The tips of the thermocouples are bent approximately 5 mm outwards away from the rod, pointing towards the tank centre axis. (See figure 5.17). See section 5.5 for the exact positioning of the thermocouples.

The 5 piece thermocouple adapters were pressure tested with gaseous nitrogen up to 25 bar during the leak testing at the 22nd of December. Using leak detection spray, it was found that very minor leakage was, unfortunately, still occurring along the thermocouple wires. The leakage was however very minor and deemed insignificant considering the total tank volume and the pressurization times involved.

Figure 5.16: The fully prepared thermocouple adapter for thermocouples 1 through 5.
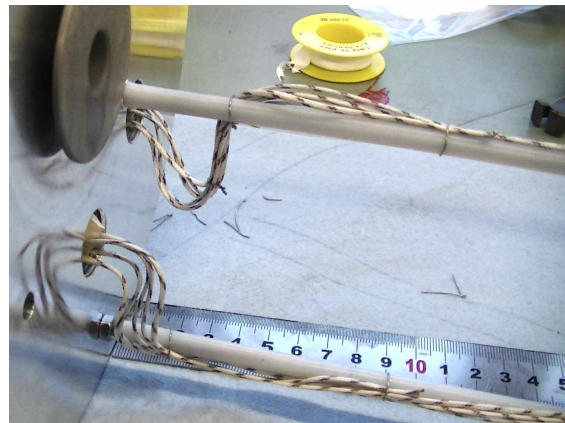

Figure 5.17: A close-up from the inside of the top bulkhead during assembly with the wires from thermocouples 1 through 10 visible. The thermocouples are attached to two rods that run parallel to the tank axis. The tips of TC1 and TC6 are visible in the bottom, respectively the top, of the figure.

5.5.4. Capacitive sensor

The capacitive sensor is a liquid level sensor that can be used to determine the amount of liquid present in the tank by making use of the difference in dielectric constants of the liquid and gas phases in the tank[31]. Up till now, the only method of measuring the amount of liquid in the tank within DARE has been via measurement of the mass. This however is usually a cumbersome and inaccurate method on ground tests, and is of even less usefulness and accuracy on rockets in a launch tower[33]. To improve on this it was decided to try out the possibilities of a capacitive sensor.

The basic setup of a capacitive liquid level sensor consists of two measurement elements that extend along the length of the inside of the tank. Liquid and gas are allowed to flow freely in between the two elements. The capacitance between the two elements is measured with an electronic measurement device. This capacitance changes when the fluid level changes because of the difference in dielectric constant between the gas and liquid.

Measurement electronics

For the measurement electronics a Texas Instruments FDC1004EVM board was selected. This board is claimed to be able to measure capacitance below 1 fF in accuracy. The measurement range is ±15 pF with a programmable offset capacitance of 100 pF. The output rate can be configured at 100 Hz, 200 Hz or 400 Hz. Four channels can be measured simultaneously. The board measures the capacitance between the channel connection point and a ground connection point. Also a shield can be connected, to block out any influence of the cable connecting the sensor to the chip.[2]

The FDC1004 could not be directly interfaced with the cRIO system via a cRIO measurement board. The connection was implemented via an Arduino Uno that communicates with the FDC1004 board. The Arduino adds a counter to the data and relays it via an TTL link to a converter board. This converter board then rewrites the data to the RS232 protocol, which is passed on to the cRIO. The code implemented on the Arduino was available via the Arduino community on GitHub[54]. For this project this code was adapted to incorporated the TTL link and to add the counter.

Electrical properties of LN2 and He

To determine the sizing of a capacitive liquid level sensor, the differences in the dielectric constant of the liquid and gas phases in the tank need to be known. In the tank of this test setup this involved liquid nitrogen, gaseous nitrogen and gaseous helium. All within a range of different pressures and temperatures, which can potentially effect the dielectric constant.

In general the value of the dielectric constant differs per substance and is influenced by the density of the substance. These are related via the Clausius-Mossotti equation, given by 5.7.[37] Via the CM coefficient, which is dependent on the substance, this relates density to dielectric constant. Overall: Higher density means higher dielectric constant. The values for CM for gaseaous nitrogen is given by Johnston[37] as $CM_{GN2} = 1.57 \cdot 10^{-4} \text{m}^3 \text{kg}^{-1}$. For liquid the value is virtually the same at $CM_{LN2} = 1.54 \cdot 10^{-4} \text{m}^3 \text{kg}^{-1}$. For helium the value is slightly lower at $CM_{He} = 1.305 \cdot 10^{-4} \text{m}^3 \text{kg}^{-1}$.[6]

$$CM = \left(\frac{\varepsilon_R - 1}{\varepsilon_R + 2} \right) \frac{1}{\rho} \Rightarrow \varepsilon_R = \frac{1 + 2\rho CM}{1 - \rho CM} \tag{5.7}$$

Using these values along with densities obtained from NIST[4] in equation 5.7 shows that for helium within the whole range of temperature and pressures that can be expected, the relative dielectric constant varies between 1.0001 (293 K, 1 bar) and 1.0076 (100 K, 30 bar). The pressure and temperature of the helium are therefore not of significance to the capacitive measurement. For liquid nitrogen at 80 K and 30 bar the value becomes $\varepsilon_R = 1.423$. This shows that the capacitive sensor can likely be used to determine the difference between liquid nitrogen and gaseous helium. It does need to be noted that, as the density of LN2 varies quite strongly with temperature (14% between 80K and 100 K at 30 bar), so does its dielectric constant. It does not vary significantly with pressure (<1% between 10 bar and 30 bar at 80 K). Making quantitative conclusions based on the measurements with a capacitive sensor should therefore always be accompanied with a statement about the temperature of the liquid. For gaseous nitrogen the pressure is of significance, and also needs to be accounted for.

Capacitive sensor version 1
During the development of the capacitive sensor, and the subsequent tests with liquid nitrogen, two different versions were developed and tried. Both sensors were screwed into the top bulkhead at the position indicated in figure 5.10. Sensor version 1 was used during the first exposure test and the axial injection test.

The first version (shown in figure 5.18) consisted of two parallel wires spanned along the length of a stainless steel, PTFE covered rod. The wires are held in position by means of aluminium spacer blocks. The wires and rod are glued into an 1/4" BSPP aluminium adapter constructed in a similar fashion as the thermocouple adapters (see section 5.5.3). The wires are insulated with PTFE. The sensor is screwed into the top bulkhead and is 710 mm long. The sensor thus starts 30 mm above the tank's bottom bulkhead inner surface.

Figure 5.18: Version 1 of the capacitive sensor. The sensor consist of two wires that are spanned along the length of an M5 stainless steel rod. The rod and the wires are all insulated by PTFE. The wires are kept in place by aluminium spacers.

Unfortunately sensor version 1 was not properly configured during any test. During original development the connections to the measurement board were not understood properly and the connections to ground and shield were mixed up. This meant that for all tests using capacitive sensor 1, the measured capacitance is actually that between one of the wires and the tank wall + steel rod, and not that between the two wires. As this capacitance to the tank is also influenced by the fill level of the tank, the measurement did however give useful results.

The spacing of wires and rods was based on an expected capacitance that would fall within the measurement range of the chip. The expected capacitance range for this sensor is however difficult to calculate, as the total capacitance is dependent on the capacitance between the two cables, but also on the capacitance of each cable individually to the tank wall and the steel rod. The capacitance between the two cables can be estimated as two parallel wires. The capacitance between a wire and the rod can be estimated as either two parallel wires, or between a wire and a flat wall. The capacitance between a wire and the tank wall can be estimated as either a coaxial cable, or as a wire to a flat wall. For the

---

[6]For completeness: Liquid oxygen: $CM_{Lox} = 1.21 \cdot 10^{-4} \text{m}^3 \text{kg}^{-1}$ and gaseous oxygen: $CM_{GOx} = 1.24 \cdot 10^{-4} \text{m}^3 \text{kg}^{-1}$[37].

capacitance between one wire and the wall + rod in an empty tank (the configuration that was actually measured), the calculation for the design showed a capacitance between ~ 13pF and ~19 pF. The filled capacitance could thus be expected to be 1.42 times this, meaning between 18 pF and 26 pF. This gives a capacitance difference between a full and empty tank of between 5 pF and 7 pF. These values are all well within the available measurement range of the sensor. Measurements during the axial tests (section 7.1.4)shows the zero level of the sensor to be around 20.7 pF. The difference between an empty tank and 85% fill level was around 3.5 pF. The calculation thus was off, but still close enough to show that simple capacitance calculations can be used to size a sensor for the FDC1004 measurement range.

Sensor version 1 has two main problems that limit the accuracy of the sensor. The first is that the design itself is not ideal. The way the wires are put up means that the distances between the wires and between the wires and the rod are slightly varying along the length of the rod. On top of this, the wires were put under tension during construction, but it was found after the first exposure test, that the wires has loosened slightly. This is likely due to some form of stress relief due to thermodynamic expansion. The wires can vibrate and thus change the distances in the sensor, which affects the measured capacitance. This makes the sensor sensitive to vibrations, and it makes it non-linear in general. The second problem is that the capacitance measured is heavily influenced by the fact that each wire on its own also has a capacitance to the steel rod, and to the tank wall. Because of this inclusion of the capacitance to the tank, the influence of waves and droplets that are expected to move around in the tank is greatly increased. Furthermore, the movement of the wires due to vibrations also couples back into this capacitance to ground, amplifying its effect.

Capacitive sensor version 2

Sensor version 2 was used during the radial injection test and the vortex tube injection. During the radial injection tests however, the same connection mistake was made as described above for version 1. This mistake meant unfortunately that the measurement of this sensor during the radial injection tests did not give any useful results.

The second version (shown in figure 5.19 during assembly) was made to eliminate the problems with version 1. This new sensor is a coaxial design that consists of an aluminium tube with a steel rod placed in its centre. The tube has holes drilled at 100 mm intervals along its length to allow fluids to freely flow in and out of the tube. The rod in the core is kept centred in the tube by a strip of PTFE that is 'woven' around the rod. The tube and rod are also glued into an aluminium adapter. The sensor is 730 mm long and thus starts 10 mm above the tank's bottom bulkhead inner surface. The tube has an outer diameter of 8 mm, and an inner diameter of 6 mm. The rod has a diameter of 1.5 mm. Both rod and tube are fully electrically isolated from the adapter and thus from the tank.

The sizing of the tank and rod was based on a capacitance calculation using the relations for a coaxial cable. The initial prediction of the capacitance was around 29 pF, with an expected difference between a full and empty tank of around 12 pF. The effect of the presence of the PTFE strip is difficult to estimate. PTFE has a relative dielectric constant of around 2.1, and the strip occupies around 15% of the inner volume between the tube and the rod. Using the relative volume to size the capacitance, this would put the empty capacitance more around 34 pF, and the expected difference around 10.5 pF. The measurements during the vortex injection tests showed that the empty-tank value was estimated too low, and was closer to 52 pF instead. For the vortex tube tests this offset was properly configured, and a difference of approximately 7.7 pF was measured for a 70% filled tank (thus 11 pF for a fully filled tank). This means that the sizing for the measurement range was very close to the eventual measured value.

Figure 5.19: Version 2 of the capacitive sensor during assembly. The sensor is made of an aluminium tube with holes drilled in it at 100mm spacing to allow fluid to flow in and out of it. The central rod is placed inside the aluminium tubed and kept centred by means of a PTFE strip that is woven around it.

The method of centring the rod in the tube with the teflon strip proved very effective in making a stiff and sturdy design, eliminating the effect of vibrations. It also fixed the distance between tube and rod quite accurately, largely eliminating non-linearities due to geometry. Overall the tube construction is also stiffer than the steel rod, making the full sensor less susceptible to bending. The coaxial construction also shields the inner rod from the tank wall, meaning the measured capacitance is only dependent on the liquid that rises inside the tube, and not to any droplets or waves moving around in the main volume of the tank. Finally, the connection between the sensor and the measurement chip was also improved. The tube connection (ground) and rod connection (channel) were both implemented as coaxial cables from the sensor directly outside the tank to the chip. The shields of these two coax cables were connected together and linked to the shield connection on the chip. This eliminates any capacitance of the connecting cable, and thus also any influence of factors outside the tank, such as ice formation.

5.6. LabView actuator control and data acquisition

The test setup contains an array of sensors that need to be read out continuously during the tests, and it contains four valves that need to be controlled from a distance. To do this an actuator control and data acquisition was needed. For this purpose a system based on a National Instruments compact RIO was selected. This system was created as a multi-purpose actuation and data acquisition tool for the Stratos II+ project in 2015 and has been available since then within DARE. This section describes the system itself and its usage within in the project (section 5.6.1), the hardware modifications made on it (section 5.6.2), and the software written for it during this thesis (section 5.6.3).

5.6.1. The cRIO box

During the Stratos II+ project the need for a standardized measurement and actuation system within DARE arose. This need was met with the construction of the system known as the 'cRIO box' (see figures 5.20 and 5.21). This is an electronics system contained within a stainless steel enclosure that contains as main component a National Instruments compact RIO. Within this cRIO there are 5 standard modules. Of these modules 4 are used during this project: The NI9375 Digital I/O module, the NI9237 strain gauges module, the NI9203 current sensor module and the NI9213 thermocouple module. The sensor modules are connected to various standard sensor connectors on the outside of the system enclosure. The digital I/O module is used to control an array of relays which switch power lines for actuators. These lines are also routed to various connectors on the outside. Various power supply units (PSU) are included in the enclosure to provide power to the cRIO and the actuators.

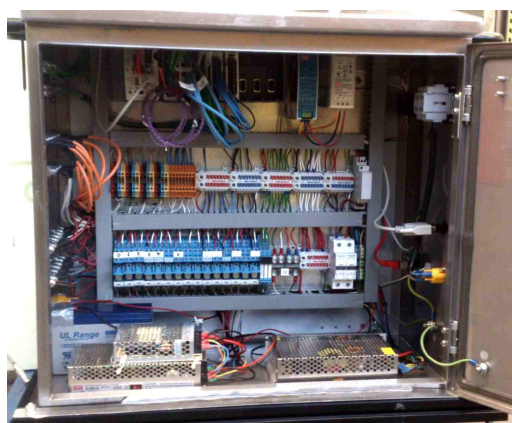Figure 5.20: The cRIO box. Visible on the outside are the sensor and actuator connectors.

Figure 5.21: The inside of the cRIO box. The cRIO itself is positioned near the top.

The cRIO box was constructed by Radu Florea, TU Delft student and member of DARE. The design project was nominated for the 2016 LabView student design competition: Northern Europe.[30]

5.6.2. Hardware modifications

The cRIO was designed and constructed for use in the Stratos II+ project and needed a number of modifications to be suited for use in the cryogenics project and within this thesis. The modifications made were the following:

General clean-up of wiring. Various wires that were hanging lose within the system were investigated and removed. A wiring 'fix' with ducktape that was created during the Stratos II+ campaign was repaired properly.

Removal of an unused power supply unit. One 12V PSU was connected to mains power but unused for any actuators or other devices and was thus removed in the clean-up.

Restructure of the load-cell cables. The cRIO supports 4 load cells via the NI9237 module. This module is wired via a number of internal connector blocks, to the outside connectors. During Stratos II+ apparently the cables between the load-cells and the cRIO box were wired wrongly. At that point the easiest way to fix this was to change the internal wiring in the cRIO box. This meant that the connectors for load-cells 1 and 2 did not match up with the intended wiring and were at this point considered "broken" by DARE. The internal wiring was redone so that load-cell connectors 1 and 2 matched those of load-cells 3 and 4, making all 4 load cell connectors operational again.

Installation of a 24V PSU. During Stratos II+ mostly 12V actuator channels were needed. One 24V channel that was used during that project was created by putting a 12V PSU in series with a 12V lead battery. More 24V channels were needed during this project as the valve pneumatic actuators supplied by ERIKS could only be delivered in a 24V configuration. To accommodate this, a 24V PSU was bought and installed in the cRIO box. Three unused outside connectors were hooked up to this supply. Two of these were connected via relays (numbered 0 and 1). For the third no available relay could be found directly and the cables were left unconnected for now. The connectors selected on the outside are physically different from the 12V connectors, so that a 12V actuator cannot not be accidentally exposed to a 24V supply.

Installation of T-type thermocouple connectors. The NI9213 thermocouple module supports 16 thermocouples. In the Stratos II+ configuration these were all wired with cables and connectors for K-type thermocouples. For measurements at cryogenic temperatures however it was desired to use T-type thermcouples for increased accuracy at low temperatures. Therefore the five last thermocouple connectors were replaced with T-type wiring and connectors (visible as the brown connectors at the top of the box in figure 5.20). The other 10 T-type thermocouples used during testing for this thesis were connected via direct wiring to the module on the inside of the cRIO box. These wires were removed at the end of the thesis test series.

5.6.3. LabView software

To control the cRIO box hardware a software program had to be created using National Instruments LabView. In this section the general structure of this program is described first followed by the main problems encountered during the program development.

Program description

The LabView control of the cRIO happens mainly via two LabView "Virtual Instruments" (VI's). These are basically computer programs created in LabView that run on the cRIO. The first is an FPGA acquisition program that is compiled to run in real-time on the FPGA chip inside the cRIO. The second program is the real-time control VI ('RT-control'). This program runs on the real-time operating system on the cRIO. The FPGA VI is a static program that is compiled once for the project. It forms the interface between the different modules of the cRIO and the RT-control VI. The FPGA VI is controlled via the RT-control VI, which is a more dynamic program and which also features the interface for the program user.

The basic structure of the whole program is shown in figure 5.22. The two main LabView VI's are visible in the center. They communicate to the outside world via an RS232 serial connection (for the capacitive sensor, see section 5.5.4) and via the cRIO's communication with the various modules.

The FPGA VI is shown in the lower part of the diagram. This VI consists of four main loops that are executed continuously and in parallel. The first is the actuator update loop (m) that communicates with the Digital I/O module (5) to actuate the relays and give back the relay outputs. This loop does not contain any time control and its exact update frequency is therefore not known. Loops n, o and p read out the three different types of sensors from the respective modules 6, 7 and 8. The frequencies with which these loops run, and thus with which they sample the sensors, are set by the RT-control VI during startup.

The RT-control VI contains the main bulk of the software. It consists of three main step that are executed in series. The first is an initialization step. Here the serial connection to the capacitive sensor is specified and opened (a). The data logging files for storing the measurement data are created (b). Various configuration variables are set and controls are initialized (c). And the connection to the FPGA is set up, and measurement frequencies are specified (d).

The second step contains six loops that are executed continuously, in parallel, until stopped by an action of the user. Two loops are dedicated to the capacitive sensor, to read out the data from the serial connection buffer (e) and to log this data to a file (f). Two more loops are used for controlling actuators. One (g) handles manual actuation by the user and updates the valve state indicators on the front panel. The other (h) contains the logic for the automated sequence. This allows to predefine a sequence of valve actuations that can be executed by the program itself. This allows for exact and repetitive operation of the valves. The final two loops concern the sensor data. The first (i) reads out the sensor data from the three FIFO buffers and writes these values to the respective datafiles. Each time it reads out the FIFO's it also reads the current state of all valves and various software state parameters and logs these to a separate data file. All FIFO buffers also contain a sample counter that is generated in the FPGA VI to allow to check if the samples are read out in the proper order and if no samples have been lost. The counter that is associated with the load cell FIFO is also taken by loop i and appended to the valve state data to allow synchronization of this data set. For the same purpose, this loop also passes the load-cell counter to the capacitive data logging loop. Finally, the second loop dealing with sensor output (j) takes data from the FIFO read-out loop and displays this on the front panel.

The final part of the LabView program that needs to be mentioned is the front panel. This is the part of the program that the user actually sees and operates upon during tests. A screenshot of the front-panel is shown in figure 5.23. In this front panel the feed system diagram is placed centrally. The control buttons for the different valves are placed next to their position in the diagram to create logical and intuitive operation of the system. Also the main parameters that are to be monitored by the user during operations (tank mass and pressure) are placed in this central location. On the left are various system state indicator lights, controls for the automated sequence and the data acquisition, and indicators for certain other sensors. Finally the right shows an array of indicators for the various thermocouples that are in the system.

Program development process

The development of this program was started as an adaptation of the code used during Stratos II+. However when implementing this code for the first cryogenic exposure test it was found out that the basic structure of this program was not suited for the amount of sensors and measurement frequencies desired. During usage the FIFO data buffer would slowly fill up, slowing down all features of the system, including front panel display and valve actuation. This happened because the Stratos II+ program ran using the cRIO's FPGA mode (with 1 FIFO buffer) and the cRIO's scan mode in parallel. Here the thermocouple readings were passed via the scan mode. This however needed to be changed for the cryo project to properly set different thermocouple types for different channels, and to log the cold junction compensation (CJC) and autozero channels of the module (required for the calculation of the temperature). Passing the thermocouple readings through the same FIFO buffer as the load-cells and pressure sensors however meant all sensors were sampled at the same frequency. This was not practical as sampling rates for the thermocouples are about one order of magnitude lower than those for load-cells and pressures sensors.

To overcome this the program structure was completely turned upside down and changed to the structure described in the previous section. This new structure only uses the FPGA mode of the cRIO, which enables the use of 3 separate FIFO buffers for the three different sensor types. These 3 buffers can be used to sample the sensors at different frequencies.

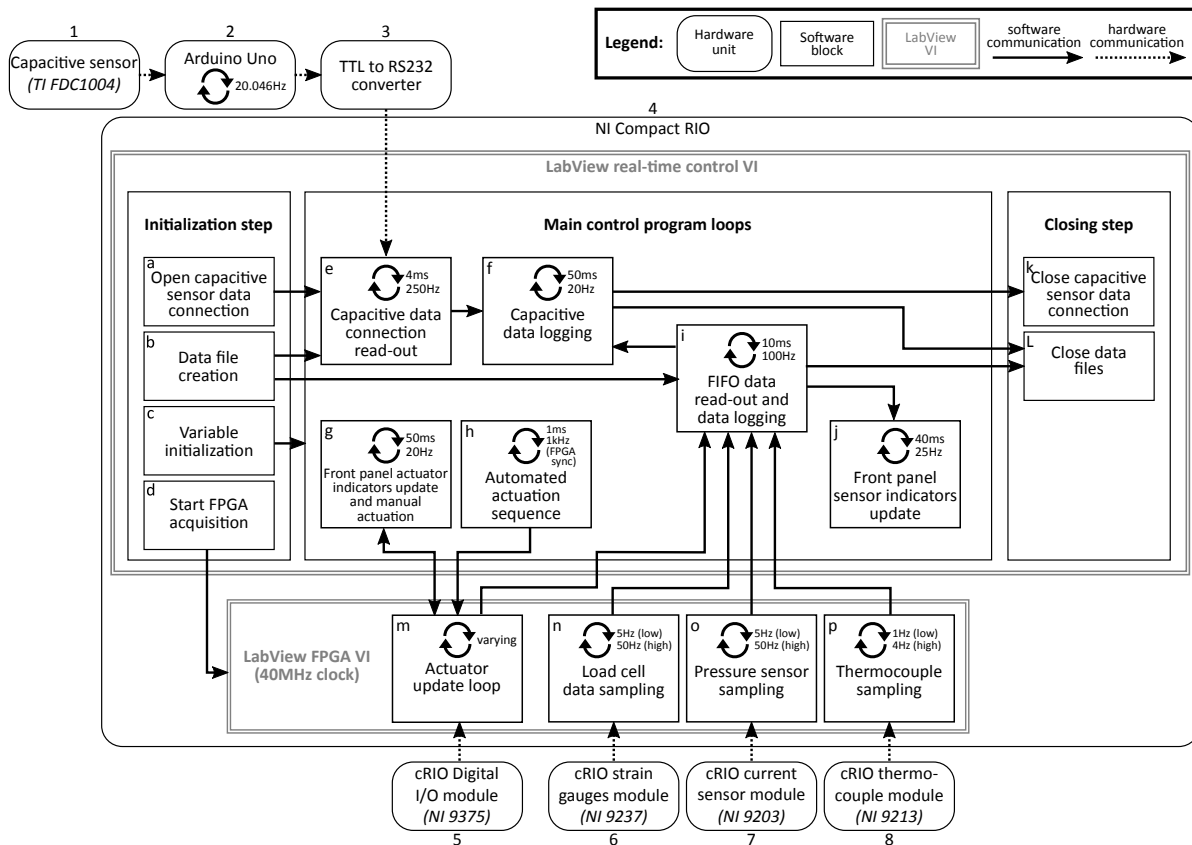This new structure was already envisioned in a general DARE cRIO program of which the devel-

Figure 5.22: The generalized structure of the cRIO measurement and actuation software and its communication with the various hardware modules.
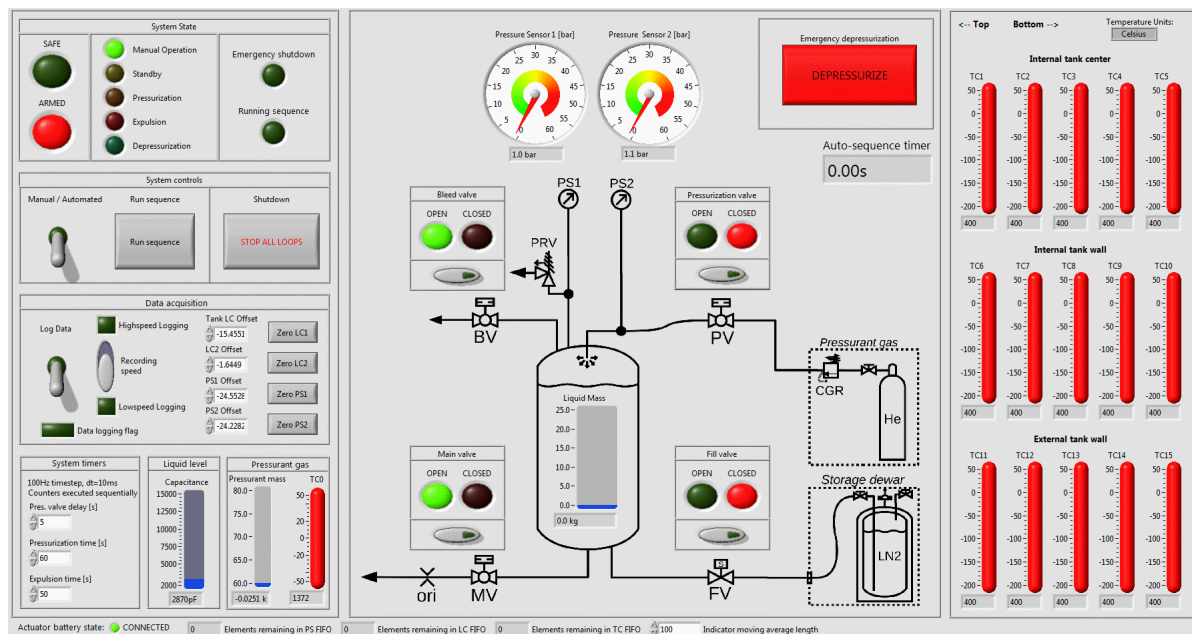

Figure 5.23: The front panel interface of the RT-control VI.

opment was started after Stratos II+. However this program was never completed and therefore it was not taken as basis for the program development during this thesis. In hindsight, development of the new program would probably have been less labour intensive if the unfinished general program was

used as starting point. However this unfinished program was very much lacking in documentation and in-code-comments to guide further development. Starting from this program would have been more of a jump into the deep and would have resulted in a less thorough understanding of the cRIO software and probably a less clean and less efficient code.

5.7. Parts and budget acquisition

For this master thesis research a whole test setup had to be constructed. Relatively little parts were available at DARE or at the faculty that were available and suited for the setup. The rest of the parts needed to be bought or acquired through sponsoring.

This section describes the different sources for funding and parts that were tried and used for this master thesis project. This section should not only be read as a summary but also as an acknowledgement of the companies that helped out.

Materials available within DARE

Various materials used in the project were already available within the society DARE, mostly because of the heritage of the Stratos II+ project. The parts used included the bleed valve (although this valve was revisited by ECONOSTO before use), the pressurization valve, the flexible hoses in the pressurization line, various small feed system components, the pressure sensors, pneumatic lines and connectors, and most importantly: the cRIO box.

Next to these available components, small amounts were spent from the DARE cryogenics budget on raw aluminium and other various components. Also the workshop of DARE in the Dreamhal was used for the construction and assembly of all parts. Virtually all tools used during the MSc thesis are property of DARE.

ERIKS/ECONOSTO

Eriks is a large supplier of industrial products within the Netherlands. They deliver fluid systems and components, as well as tools, personal safety equipment, bearings, greases, sealings, and more. The flow control department

of Eriks is called Econosto. Eriks was contacted in the first half of 2016 and a contract was signed in August 2016 for sponsorship of the society DARE. Eriks has provided various valves and feedsystem components for the cryogenics project and has helped tremendously in the overall design process by helping with the selection of valves, the sizing of valves and feedsystem sealing rings. Also they have been very helpful and insightful with technical discussions both via mail and at their office.

The contract between Eriks and DARE has been realized mostly by Jeroen Wink, with help from me (Rob Hermsen). The deal with Eriks started the usage of cryogenics within DARE via this thesis and will continue to support the cryogenic efforts within DARE for years to come.

Teesing

Teesing B.V. is a Dutch company located in Rijswijk that provides fluid systems and components for a large variety of industrial branches. The company was contracted by the organization of Stratos 3 for sponsorship of that project. The main bulk of the feed-system adapters were acquired through this sponsorship contract.

Temati

Temati is a Dutch company that provides various insulation and coating solutions to industry. They also provide insulation solutions for cryogenic applications. Because of this they were able to supply the cryogenic rated PU glue that

was used to construct the thermocouple adapters and capacitive sensors (section 5.5) and to seal the tank (section 5.2). They supplied, free of costs, a bucket of 5kg of Kestopur PL2400, along with a can

of the required harder.

TU Delft Space Systems Engineering department
The Space Systems Engineering department, under which this MSc thesis was conducted, has contributed an amount of €500 to this project. This is the amount that is made available for each practical MSc topic. This budget was mostly used to acquire thermocouples, structural parts for the aluminium profiles used in the test bench, raw aluminium and the helium bottles for testing.

TU Delft Spacecraft Engineering minor 2015-2016
The TU Delft Spacecraft Engineering minor has been organized by DARE members under the guidance of TU Delft professor Chris Verhoeven since 2009-2010. Each time the minor was held it served as a major boost to research and capabilities within DARE. In the academic year 2015-2016 the minor focussed on advanced tank design and the construction of cryogenic tanks via welding[11]. They also intended to construct a tank using a bolted design, but that was not realized due to time constraints. The materials required for the construction of this tank were however acquired. This concerned the tube that serves as tank wall. The tank bulkheads, and the FEP O-rings for sealing. (See section 5.2).

TU Delft Faculty of Applied Physics
During the summer of 2016 the Faculty of Applied Physics on the TU Delft campus moved from their old facilities into a new building. During the moving a large number of aluminium profiles had become superfluous and could be acquired from this faculty at no cost. These aluminium profiles were used for the construction of the test-bench.

TU Delft department of Process and Energy
The department of Process and Energy (part of the faculty of Mechanical Engineering) has been very helpful and providing during this master thesis research. The initial contact with them was established during the DARE minor 2015-2016 and was picked up again in June 2016. The department allowed the use of the testing location on their terrain, a storage location for helium gas bottles and the test setup, the usage of their cryogenic dewar and the usage of cryogenic safety gloves and oxygen deficiency detectors. Furthermore they provided all the LN2 used during all tests, free of costs. Also Ir. Van den Brink, employee of this department, has assisted on all four test days for the full day.

TU Delft universiteitsfonds
In August 2016 a grant application was filled in and submitted for the TU Delft Universiteitsfonds for the amount of €300. The application consisted, amongst other standard documents and forms, of a letter of motivation, a project description, a budget overview and a letter of recommendation by Ir. Zandbergen. Unfortunately the grant was denied because the application committee considered that the expenditures should be fully paid by the faculty itself. (Quote from the letter of rejection (in Dutch): "De Commissie is van mening dat de betreffende kosten volledig door de faculteit bekostigd dienen te worden.")

5.8. First exposure test

The first test using cryogenic liquids was the so called "first exposure test" conducted on the 2nd of December 2016. In this test the tank was filled for the first time with liquid nitrogen. The main goal of this test was to validate that the test hardware could be used for the planned injector tests (as described in section 4.1).

In section 5.8.1 the general setup of the test, the proceedings of the test on the day, and notes on the operations are given. The findings of the test, including data analysis are given in 5.8.2. And the conclusions and recommendations resulting from this test are written down in 5.8.3 and 5.8.4.

5.8.1. Test description

The first exposure test was conducted on Friday the 2nd of December. The test was the first time that the cryogenic test setup was exposed to a cryogenic liquid. The setup feed system was as described in section 5.1, with the exception that no pressurant gas supply was present. The connection points for the pressurization line were sealed off by dead stops. A radius of around 5 m was set off around the

test setup. The CP was positioned around 20 m away from the setup. Various oxygen level indicators were placed around the field to check for possible oxygen deficiency.

The supervisor from the department of Process and Energy was Michel van den Brink. The operational safety officer of DARE was Felix Lindemann, the test conductor was Juan Mussini, the test operator was Arthur Thiam, and the CP was manned by Rob Hermsen. Various other members of the DARE cryogenics team were present to help out with setting up and cleaning up.

The test day commenced around 8:45 when the team left the TU Delft Dreamhal and moved the test setup towards the test location. The official procedures commenced at 9:35. By that time the test setup had been set fully ready and the dewar had been filled up and connected to the test setup by Michel van den Brink. The fill level indicator on the dewar at that point indicated that the dewar was around 80% full, which corresponds to 54 L of LN2.

The weather at the day was overall good. Partially cloudy with sun breaking through. The outside temperature was around 8°C at the start of the test. Wind indications for Delft at that time showed 16 km/h winds. The test location is however quite well shielded from the wind by buildings and nothing but a light breeze could be observed on the field. A minor shower passed over around 10:40. The thermocouples in and on the tank all indicated around 17°C as starting temperature before the cooling down.

The test procedures were worked through without problems and at 10:17 the filling of the tank commenced. At suggestion by Michel van den Brink this was done not by remotely operating the fill valve on the test setup, but by him partially opening the hand actuated fill valve on the dewar. He suggested this to avoid a thermal shock to the tank setup. The fill valve on the tank cannot be opened partially, while the hand actuated ball valve on the dewar can, allowing finer flow control. Over the course of the test Michel van den Brink adjusted the valve twice after initial opening, each time opening it a little further. During filling it was already observed that the load cell did not operating as expected and was giving wrong readings and its output was not used for any operations.

From start till end of filling a vapour cloud was visible and audible coming from the bleed valve exhaust. This exhaust started off quite loud but became less strong and less noisy over time. An indication of how this vapour plume looks is visible in figure 5.24.

Figure 5.24: The vapour plume originated from the bleed valve exhaust that was visible during the whole filling procedure. This is evaporated N2 that escapes the tank to keep the pressure low. Water condensing in the air renders the plume visible. The size and speed of the exhaust plume seemed to decrease over time.

At 10:44 the bleed valve and fill valve were closed and the dewar was disconnected from the test setup. At that point the dewar fill level indicator showed around 15%, which would correspond to 9 L of LN2 still left, and thus a total of 45 L used during this first test. Nearly directly after closing the valves it was observed that LN2 was leaking from the bottom of the tank and effecting the load cell. It was decided that, although it was not good for the test results, it was no problem from a safety aspect and the test was continued.

Around 18 minutes after the start of the holding time the area was cleared and the main valve was opened. This event is visible in figures 5.25 and 5.26. Figure 5.25 is a shot taken less than a second

after sending the signal for opening of the main valve. Visible near the valve is ice flying around. This is ice that had formed on the main valve casing during filling but which flew off by the shock of opening the valve. Also visible is the stream of LN2 that is ejected from the orifice and that is blown into the gravel box. Figure 5.26 shows the setup from a bit further away about 3s after opening of the main valve. A cloud of vapour originating from the gravel box can be seen rising upwards due to the evaporating N2. Directly after this the cloud collapsed back down and spread over the ground as a large vapour blanket, rolling a few meters away from the test bench before disappearing. The expulsion took about 1.5 minutes. After this the main valve was left open. A few minutes later the bleed valve was also opened.

After this the system was turned off and all equipment was taken back to the workshop. All equipment and personnel was back at the workshop around 12:30. The tank remained at temperatures below freezing for quite some time still. Around 14:00 the thermocouples in the tank still read temperatures around -60°C. Warning labels were placed on the tank and it was left to warm in the lab over the weekend.

All actuation during this test was done manually. I.e. no use was made of the automated sequences programmed into the LabView code.

Non of the oxygen level indicators went off, showing there were no danger of oxygen deficiency during the test. Only when Michel van den Brink placed one indicator directly under the leaking LN2 on purpose did it go off.

Figure 5.25: Close-up shot from the main valve and exhaust less than a second after start of expulsion. The liquid nitrogen spray is visible from the orifice. Around the main valve ice can be seen which was thrown off of the main valve when it opened.
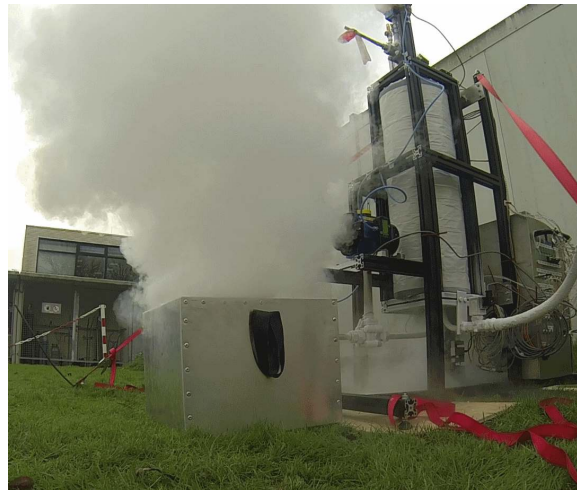

Figure 5.26: Overview shot from the test setup seconds after start of expulsion. LN2 is ejected from the exhaust and vented into the gravel box. Here it evaporates and forms the large cloud emanating from the box.

5.8.2. Test results and data analysis
During the tests four main types of sensors were active on the setup. The data coming from these sensors will be discussed in this section.

Pressure sensor data
During the first exposure test one pressure sensor was attached to the top of the tank. The graph of pressure over time is displayed in figure 5.27. Over the data a moving average filter is applied with a window size of 201 samples. Comparing the original data to this averaged value, a standard deviation of 0.175 bar is found.

A number of trends and events are visible in the graph. First the general shape of the graph: A relatively low pressure part is visible for the first half (t = 0 s till t≈1290 s). This is the filling of the tank. Data recording was commenced a few minutes after the start of filling. After this the pressure

increases up to around 5.3 bar. During this time all valves were closed and the tank pressure slowly increased due to heat flowing into the tank (t≈1290 s till t≈2410). During this time also the leaking at the bottom bulkhead occurred, which will have had a decreasing effect on the pressure. Then follows a rapid de-pressurization (t≈2410 s till t≈2500 s) where the LN2 / N2-vapour is ejected out of the tank through the main valve. Finally the pressure in the tank settles steadily around 1 bar (atmospheric pressure).

This description immediately shows that one important piece of data was not recorded during this first test: The actuation of the valves. The closing and opening of the valves gives rise to the different events and thus the different phases of the test, however the times at which their actuation took place were not recorded. The timing of the phases can thus only be inferred from the sensor data, which is rather inaccurate. This has been improved for subsequent tests (see section 5.6.3). When in the following discussion of the test the various test phases and times are mentioned, it are the phases and times mentioned in the previous paragraph, as inferred from the pressure sensor data.
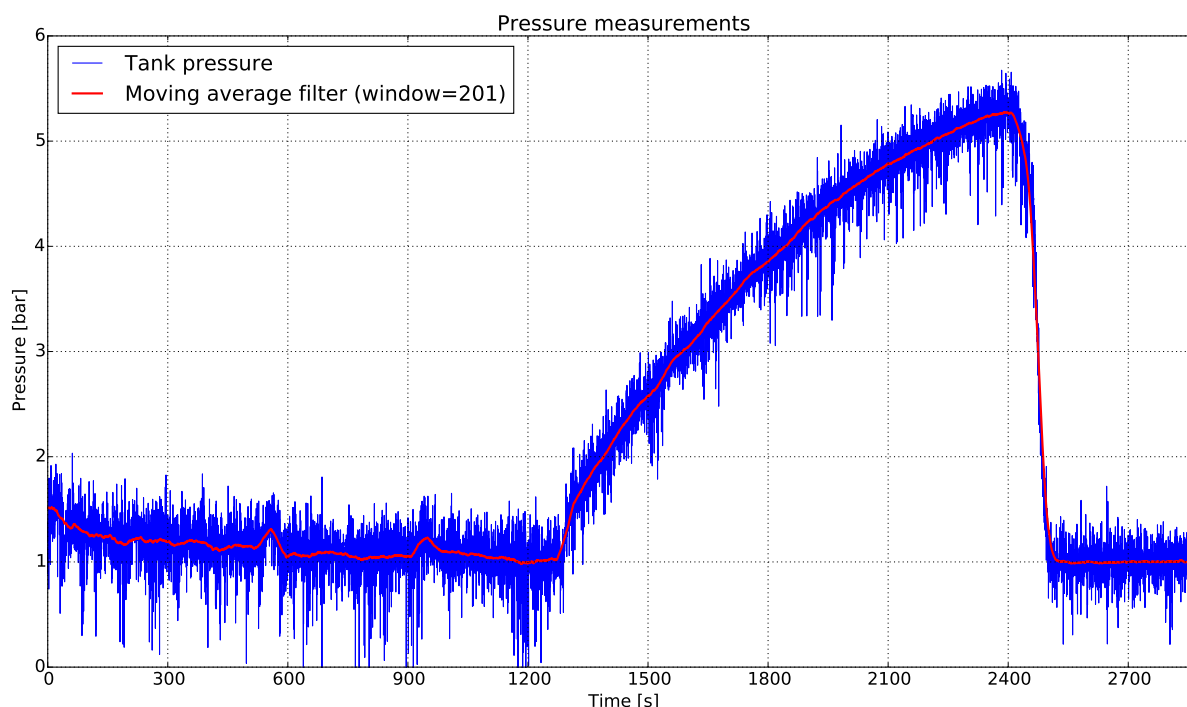

Figure 5.27: The pressure data versus time during the first exposure test. The blue curve is the originally sampled data. The red curve is a moving average filter applied over this data with a window size of 201 samples (which equals 40.2s in time). Standard deviation of the data w.r.t. the average is 0.175bar.

During the filling phase of the test the pressure data can be seen to fluctuate, but in general shows a decreasing trend. The fluctuation is due to the boiling process that is ongoing in the tank. The decreasing pressure arises because, as the tank cools down, the boiling process becomes less violent and less gaseous nitrogen is generated per second that needs to escape through the bleed valve. Two peaks can be observed during this phase at approximately t = 560 s and t = 950 s. At these points the valve on the dewar fill line was adjusted by hand to increase the flow of LN2. In both cases this lead to more LN2 flowing into the tank, and thus a momentarily increase in evaporated N2 and thus in tank pressure.

The hold phase started with the closing of the fill valve and the bleed valve. This closed the tank completely and lead to the expected increase in pressure due to the nitrogen in the tank heating up and evaporating while the tank wall cooled down further. During this time also LN2 was seen to be leaking from the bottom bulkhead. The holding phase was intended to be 15 minutes (as by procedures) but eventually lasted about 18.5 minutes, as is evident from the data.

After this the expulsion phase started by opening the main valve. This rapidly allowed all N2 to flow out of the tank till the pressure in the tank reached atmospheric pressure again.

Thermocouple data

The thermocouple data recorded during the test is shown in figure 5.28. Again the different phases in the test can be observed: First the filling procedure in which all temperatures show a decreasing trend, but with very heavy fluctuations seen at the thermocouples inside the tank. This is believed to be due to the highly turbulent inflow of LN2 from the bottom inlet which sprays up into the tank akin to a fountain. Furthermore violent boiling at the tank wall and bottom bulkhead will have occurred as it can be observed that tank wall temperatures are far above LN2 vapour temperatures during the whole process. Thermocouples are alternately exposed to liquid N2 droplets and gaseous N2 and thus experience large swings in temperature.

What can be seen though, is that various thermocouples, one by one, show a decrease in these fluctuations, presumably because they become fully soaked or submerged in LN2. This is first seen around t≈200 s on TC5, which is positioned the lowest (50 cm from the top, 24 cm from the bottom) and near the tank centreline. Followed around t≈500 s by TC4, around t≈650 s by TC3 and TC10, and finally around t≈900 s by TC9. The standard deviation of the thermocouple measurements with respect to the moving average applied to them is varying between 3°C to 12°C during the filling phase[7], but drops to between 0.2°C and 0.4°C as soon as they become fully soaked or submerged. Thermocouples at the centreline experience this submersion earlier than their neighbours at the same height at the wall. This is presumably because boiling of the N2 takes place mostly at the wall, as the wall is still high above the N2 vapour temperature.

Plotted in the figure as well is a 16th curve that shows the temperature that corresponds to that of an N2 vapour at the measured pressure in the tank at that time. The temperatures are calculated using CoolProp from the pressures sensor data (filtered by moving average, figure 5.27). Given that the tank is fully filled with an N2 vapour this should be the minimum temperature achievable at each point in time. Looking at the thermocouples in the tank that become soaked or submerged during the test it is indeed observed that they approach this vapour temperature quite closely. During the timespan t = 900 s till t = 1250 s average deviations from this vapour temperature for these thermocouples are: TC3: +1.5°C, TC4: +0.0°C, TC5: +1.3°C, TC9: -0.6°C, and TC10: +0.6°C. Negative here means that the thermocouple shows a temperature lower than that predicted by the vapour pressure. The manufacturer claimed thermocouple accuracy around ±1.5°C, which does appear to be a valid statement looking at this data.

The five thermocouples on the outside wall do not show these large fluctuations as they are not exposed to the turbulent two-phase flow inside the tank. The thermal mass of the tank wall itself acts as a damper for these kinds of fluctuations. Standard deviations of these thermocouples w.r.t. their moving average filterd data stays around 0.1°C during the entire test time. An exception to this is TC15, which shows deviations up to 0.4°C starting at t≈1200 s. The fluctuations disappear again around t≈1350 s. What causes these sudden fluctuations in temperature is unknown. A possible cause could be sought in outside influences such as evaporated LN2 from the leak at the bottom finding its way through the insulation material.

Visible in the temperature data as well are the two adjustments of the dewar fill valve at t = 560 s and t = 950 s. At these points pressure increases, which results in an increased vapour temperature for the N2 in the tank, which is observed in the thermocouples that were soaked or submerged at that point. The two adjustments are also visible in the outside tank wall temperatures, although these are not obvious from figure 5.28. They become visible when the derivative of the curves for TC11 through TC15 are calculated. These curves are shown in figure 5.29. Here the first valve adjustment at t = 560 s is visible at all 5 thermocouples as a momentary increase in cool-down rate. It is interesting to note that the cool-down rate increases here, while the thermocouples inside the tank simultaneously show an increase in temperature, meaning the temperature differential over the wall should be lower. This means that the increase in pressure at that point, combined with a momentarily different flow pattern of the N2 in the tank combine to actually increase heat transfer rate to the wall. The second adjustment around t = 950 s is also clearly visible. At this point the cool-down rate of the tank wall measured by TC15 suddenly increases by a factor of 2.5. What most likely is observed here is a transition in boiling mode. The wall is coolest at the bottom and warmer near the top. Boiling occurs in various forms along

---

[7]This high deviation indicates that applying a moving average filter to this data is not a good procedure when wanting to do quantitative analysis on the data. It was however decided to still apply it here to make the data more representable, to be able to show the general decreasing trends, and to given an indication of the turbulent boiling process and its decrease in intensity over time.
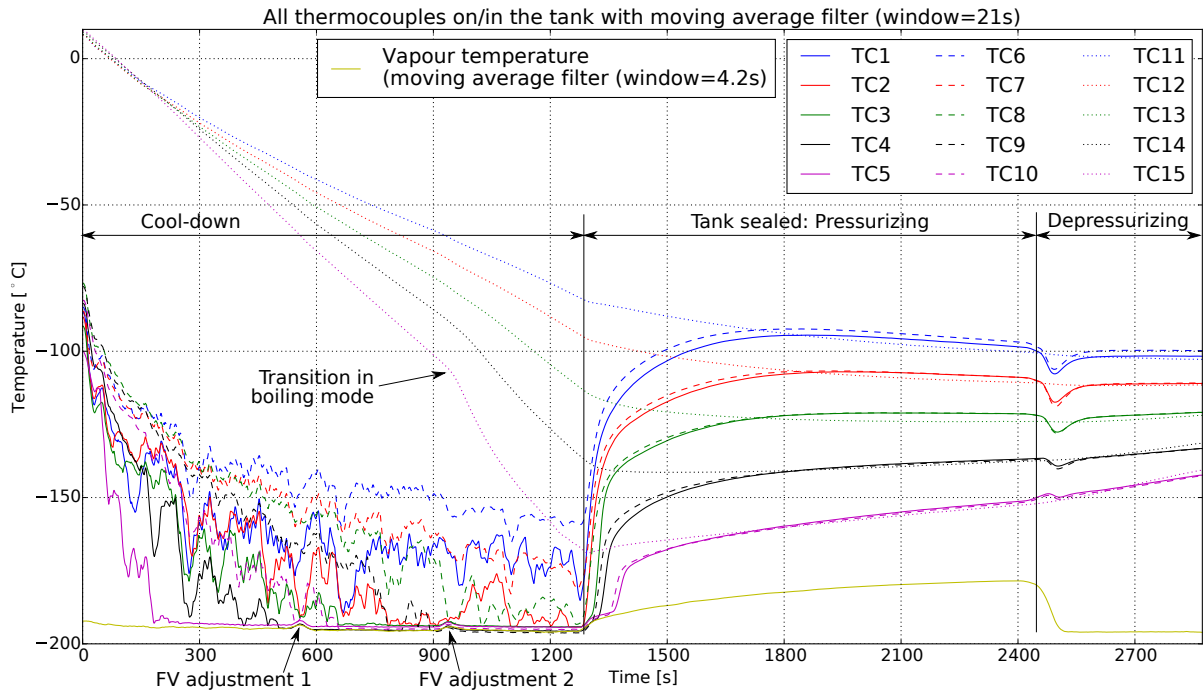
Figure 5.28: The thermocouple data versus time during the first exposure test. Thermocouples at the same horizontal position have the same line style (full line for inside tank (center), dashed line for inside tank (wall), and dotted line for outside tank wall. Thermocouples at the same vertical position have the same colour. A moving average of 41 samples is applied to all thermocouple data in the graph. Added as well is a line showing the expected vapour temperature for N2 given the pressure in the tank at that time.

the length of the wall, with nucleate boiling near the bottom bulkhead. Moving up along the wall there is a point where nucleate boiling transitions into film boiling, where a film of vapour blankets the wall (this is called "boiling crisis"). This vapour film limits the heat transfer between wall and fluid substantially.[16] What seems to happen around t = 950 s is that the transition point between film and nucleate boiling rises up past the height of TC15, leading to the substantial increase in heat transfer at that time. That this coincides with the second adjustment of the dewar fill valve may be purely coincidental but is most likely related to the increased inflow of LN2 and the changing conditions in the tank. A less sudden, and less dramatic increase in heat transfer is observed in TC14 around 1040 s, indicating that the transition point is approaching this position as well or has moved past this position. The increase here is about a factor of 1.5.

After the filling process follows the holding period, starting around t≈1290 s. From this point on the boiling process in the tank stops abruptly, as no new LN2 flows into the tank and no gas can escape through the bleed valve. All thermocouples in the tank show a quick rise in temperature, although TC3, TC4, TC5, and TC10 still follow the curve specified by the vapour temperature for a number of seconds up to 1.5 minutes (TC5 and TC10). This curve also rises as pressure in the tank increases. Having a thermocouple at the vapour temperature indicates that it was probably covered by liquid N2. However this covering was more likely due to LN2 clinging to the thermocouples and the thermocouple rod, than complete submergence by LN2 liquid level. Compete submergence seems unlikely because this would mean the liquid level dropped with tens of centimetres (past several thermocouples) within 1.5 minutes. If this was due to the leak then the tank would have been empty and de-pressurized minutes later, or if it was due to evaporating N2 within the tank itself, pressure would have risen much higher, much quicker.

Over the course of the holding time the thermocouples in the tank show that a strong vertical thermal gradient exists within the tank, with nearly 70°C of difference between TC1 and TC5 around t = 1500 s. The tank however slowly moves to equilibrium and the difference between TC1 and TC5 has decreased to around 40°C at the end of measurements. A small horizontal gradient also seems to exist at the start of the holding period, however temperature difference are in the order of only 1 to 2°C and they have virtually disappeared around t≈1700 s. Only between TC1 and TC6 a constant temperature difference
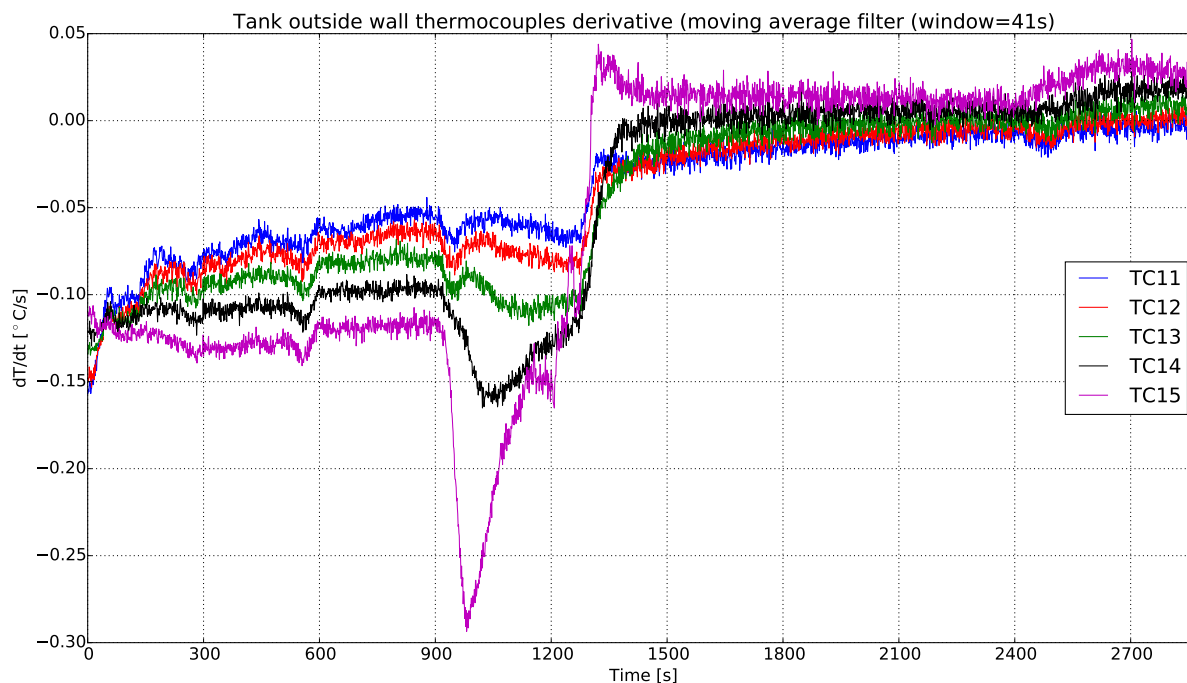
Figure 5.29: Derivatives of temperature over time for the 5 thermocouples positioned on the outside wall during the first exposure test. For generating these graphs first the derivatives were taken from the original temperature data, only after this the moving average filter was applied. Clearly visible are the first dewar fill valve adjustment around t = 560 s and a transition in boiling mode in the tank around t = 950 for thermocouple 15.

of around 2°C seems to remain until the end of measurements. However this difference is so constant and so in contrast to the other thermal measurements (where virtually no horizontal temperature gradient is observed at the end) that it can be assumed that this difference is due to systematic measurement errors in TC1 and/or TC6. At the start of the holding period all thermocouples on the outside wall directly experience a change in cool-down rate, due to the changing boiling processes in the tank. Over the course of the holding period their values change slowly till around t = 1800 s they have all five approached the same values as the thermocouples inside the tank at the same vertical positions. From this point on there are virtually no horizontal temperature gradients present in the tank.

The final step in the whole process is the expulsion, which is directly visible on all thermocouples in the tank, and via a change in gradient in the thermocouples on the outside of the tank wall. Except for the lowest two thermocouples (TC5 and TC10), all thermocouples in the tank show a decrease in temperature that starts at the start of the expulsion and reaches a minimum at the end of the expulsion. After that the temperatures quickly return to values comparable to those before the expulsion. This cooling down is due to the expansion of the gas. Only thermocouples TC5 and TC10 show a different pattern: Their temperatures start increase at the start of expulsion, reach a maximum halfway through, and at the end return to values comparable to those at the start. This is probably due to the fact that as the gas in the tank expands, the hotter gasses that were stored near the top expand to push out the cold gas near the bottom. This creates the momentary increase in temperature. After that the cooling down of the gasses again takes over and makes that the thermocouple readings drop again.

It must be noted that specifically during these kind of fast expulsion processes, it is doubtful how accurately the readings of the thermocouples reflect the temperature of the gas, as the change is fast, and the thermocouples themselves also have a thermal mass that dampens the changes.

Load cell data
As described in section 5.8.1, a leak appeared during the holding phase at the sealing of the bottom bulkhead. This leak spilled LN2 onto the field and the bottom half of the tank holding structure. This cold also reached the load cell and meant that it experienced temperatures that are outside of its recommended operating range. The calibrated range for this particular load cell goes down to a minimum of -10°C only[3]. Because of this the voltage output of the load cell can no longer be expected to be correlated quantitatively to the mass of the tank.

The voltage output of the load cell is displayed in figure 5.30. The fact that the load cell output is not strictly related to tank mass is most clearly observed in the first ~300 s and the last ~300 s. In the first ~300 s the load cell voltage indicate a decreasing tank mass, while tank mass should be increasing because tank is being filled. The last ~300 s indicate an increasing tank mass, but it should should show a constant value, as the tank is empty and at atmospheric pressure at that point.

In between the start and end at least general trends can be observed which indicate the expected behaviour: A noisy upward trend shows that tank mass is increasing till around 1400 s (around 2 minutes after end of the filling). After that the graph decreases again, which may be due to leaking. Finally, a sharp decrease in sensor output is observed around t = 2450 s, where expulsion took place.

The noise seen during the filling phase seems to show regular spikes between t≈700 s and t≈1300 s that appear at an interval of approximately 15s (0.0667 Hz). These spikes appear to be related to some type of flow phenomena happening in the tank, as the video footage of the test shows that the exhaust from the bleed valve exhibits short bursts where flow from the valve shortly peaks and decreases again. These bursts also occur at an approximately 15s interval. As the valve exhaust is mounted perpendicular to the direction of sensing for the load cell, the higher outflow cannot have been the direct cause for the load cell sensor spikes. Furthermore, the spikes are also visible in the data from the capacitive load cell. It seems more likely that some low frequency oscillation occurred in the tank which coupled to the mass flow from dewar to tank. If the mass in this line is somehow pushed back and forth by a changing rate of evaporation (and an associated pressure change) this may have coupled back into the tank mass and into the capacitive sensing. Strangely enough the peaks are not visible in the pressure sensor output. However this sensor is quite noisy at these low pressure levels, so small, short-term pressure fluctuations might not show up in that data.
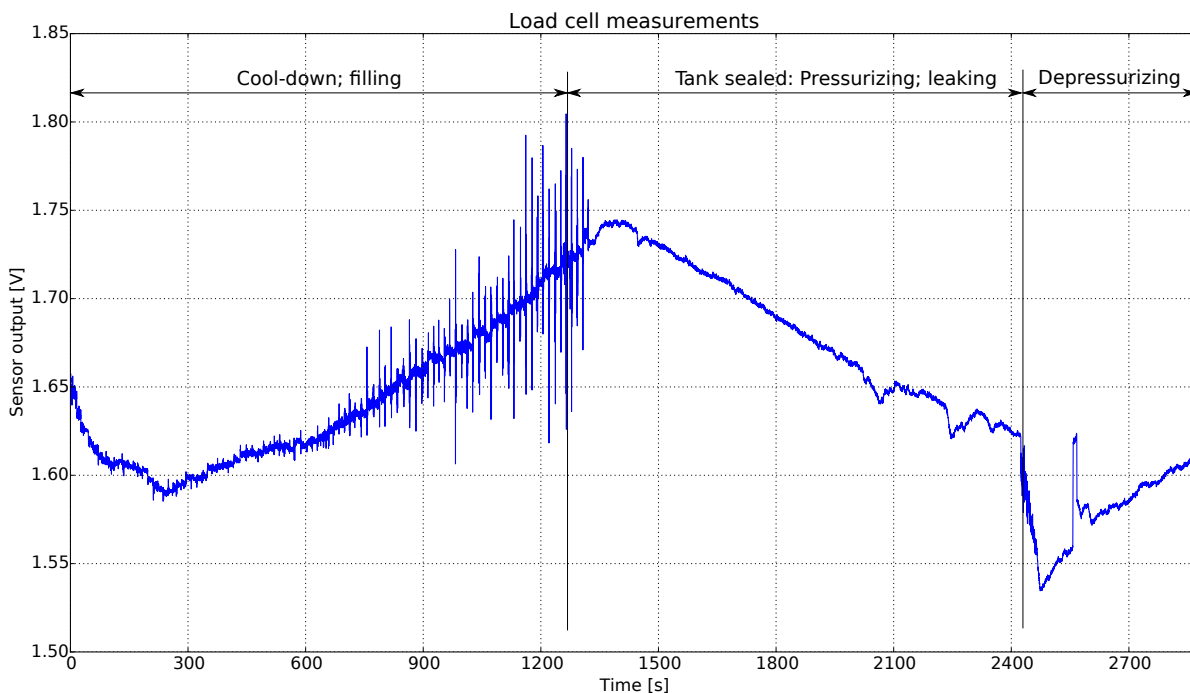

Figure 5.30: Load cell readings from the first exposure test. Due to leaking LN2 cooling the load cell to far below its rated temperature, it is not possible to link the load cell output voltage to tank mass.

Capacitive liquid level sensor data
This test was the first time a capacitive liquid level sensor was tried within DARE. The measurement output of the sensor in pF is shown in figure 5.31. It can be seen that the capacitive sensor starts at a time before zero. This is because in the software the capacitive sensing loop is implemented separately from the other sensor loops (see section 5.6.3) and for this test this loop was still implemented to start running as soon as the program started. The start and end time of this data set are thus the start and end time of when the program was running. The starting point of the data set has been set at roughly t = -1222s. This time has been determined by looking at the time of expulsion and correlating

this with the pressure sensor output, as well as by comparing the 15s spikes that are observed on the load cell output. After this test the software was updated to make sure correlation is done by means of a synchronized counter that is shared between load cell output and capacitive sensing output. (See section 5.8.3.)
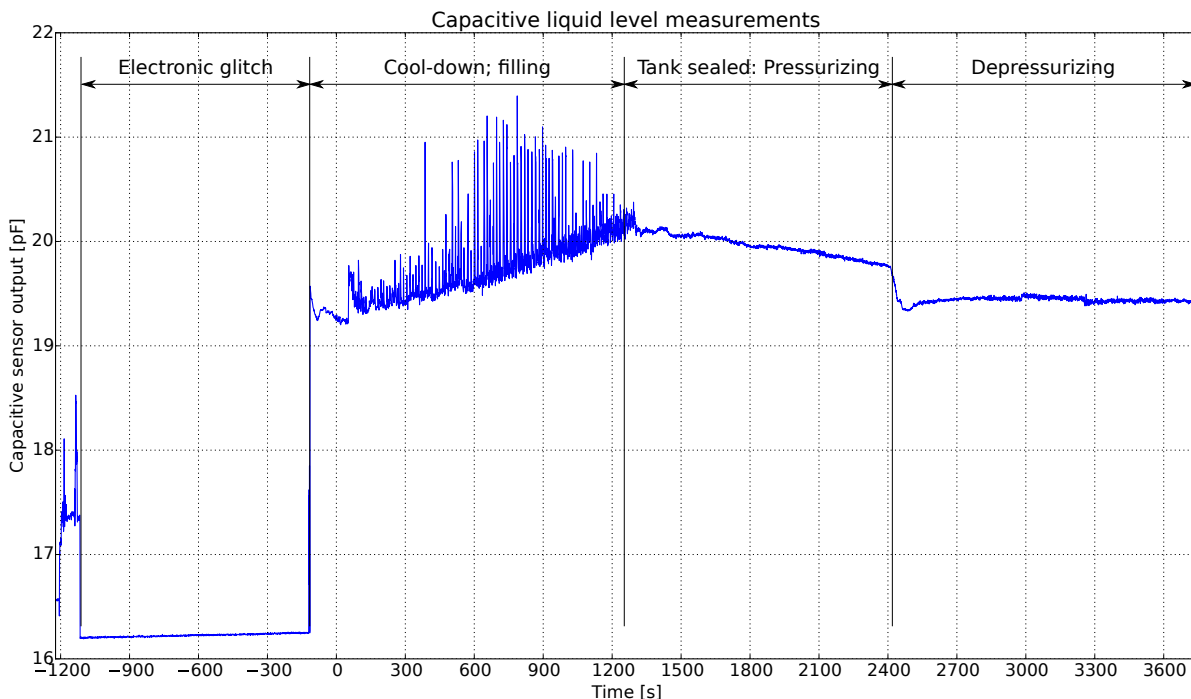

Figure 5.31: Capacitive liquid level measurements from the first exposure test. Due to the failing load cell measurements it is not possible to correlate the capacitive sensor output to liquid level or tank mass.

In figure 5.31 the output from the capacitive sensor is displayed. The first important feature to notice is the large, noiseless plateau in the data from t≈-1115s till t≈-120 s. The plateau is not flat, and not completely noiseless (but far smoother than any other part of the data). What causes this plateau in the data is not clear. Most likely it is due to some form of short-circuit somewhere in the sensor or any of its read-out parts.

From t = 0 s onwards the capacitive sensor shows the output that was expected from it beforehand: First an increase in signal, which indicates a rising liquid level. Followed by a decreasing signal, indicating liquid level drop. And ending in a relatively smooth plateau which is on similar height as the signal before filling. The rising section of the signal corresponds to the filling phase of the test. The signal is however much noisier than hoped for. This is quite likely also due to the violent boiling process in the tank which generated the noise on the thermocouples. The bubbles and droplets flying around in the tank create large spikes on the sensor output. The noise also shows the 15s spikes that were observed in the load cell output. At t≈1290 s, the start of the hold period, the noise decreases abruptly and the signal slowly starts decreasing. This is consistent with the signal from the load cell, and is most likely due to an actual decreasing liquid level due to the leak in the tank. Then at t≈2490 s a sharp drop in the signal is visible, which should indicate the expulsion process.

Unfortunately it cannot be definitively concluded from this test whether the sensor worked as expected. The sensor seems to show the correct trends, but because the intended reference sensor to check its measurements is not available (the tank load cell data) these trends cannot be quantified. Next to this the graph does show some undesired behaviour such as the large noise during filling. Furthermore the fact that the sensor output does not return to the same value at the end as where it started could indicate some thermal sensitivity of the sensor. However this might also be due to some electronic error, as observed before t = 0 s.

5.8.3. Conclusions
In this section the test goals are evaluated and an overview is given on actions that were taken to improve the test setup for subsequent tests.

Evaluation of test goals
The test goals as described in section 4.1.2 are evaluated and conclusions are drawn on if the goals of the test were met.

1. *Gain experience with the handling of the test setup in general:* **Met.**
   The DARE cryogenics team and one DARE safety officer gained experience in working with the test setup and the test location.

2. *Gain experience with the handling of cryogenic liquids:* **Largely met.**
   Experience was gained with the DARE cryogenics team and one DARE safety officer regarding operations with cryogenic substances. Only point 2c, regarding dewar operations is not fully met as most of these operations were done by the 3ME supervisor Michel van den Brink.

3. *Test if the system is leak-free at cryogenic temperatures:* **Partially met.**

   (a) *No leaks in the feed system:* **Met.**
      No leaks were observed in the feed system. One leak at the dewar hose to fill valve connection froze shut within minutes. The appearance of this leak, and its freezing shut, was beforehand predicted by Michel van den Brink. It does not pose any objection to future operations.

   (b) *No leaks in the tank bulkhead sealing system:* **Not met.**
      Leakage was observed at the bottom bulkhead sealing. Liquid nitrogen was seen to drip from out of the bottom insulation. The exact position of the leak on the tank circumference could not be found as it was obscured by the tank insulation. Furthermore the load cell at the bottom was affected by the cold temperatures and frost was observed at the whole bottom structure of the tank holder. Part of the frost at the bottom section probably originated from the structural support at the fill valve line, but most will have come from the leakage. (See figure 5.32.) This leakage is deemed the most critical problem with the setup encountered during this test. No leakage was observed at the top bulkhead.

   (c) *No leaks in the custom sensor connector:* **Met.**
      Although heavy frost formation was present at the top bulkhead and at the custom feed system adapters (see figure 5.33), no leakage was observed at the custom sensor connectors.

   (d) *No leaks in the valves:* **Met.**
      No leakage was observed through the valves.

4. *Test if all valves operate as desired:* **Met.**
   All valves functioned as expected.

5. *Test if all sensors give the desired output:* **Partially met.**
   See section 5.8.2 for the detailed data analysis.

   (a) *Thermocouple output:* **Met.**
      All thermocouples gave acceptable data output.

   (b) *Pressure sensor output:* **Met.**
      The pressure sensor gave the expected output, although the noise on the sensor was rather higher than expected.

   (c) *Capacitive sensor output:* **Met.**
      The capacitive sensor gave the expected data output, although a quantitative analysis of its output was not possible because of lack of a reference value from the load-cell.

   (d) *Load cell output:* **Not met.**
      Due to the leakage of the tank at the bottom O-ring sealing, the load-cell cooled down below its recommended operating temperatures. This meant the output of the sensor became heavily affected by this. As the exact temperature of the load cell was not known, the data output of the load cell cannot be correlated to tank mass.

Based on the evaluation of the test goals it can be concluded that the test was largely successful, although the leakage at the bottom bulkhead and the associated loss of data from the load-cell are an important point to improve.
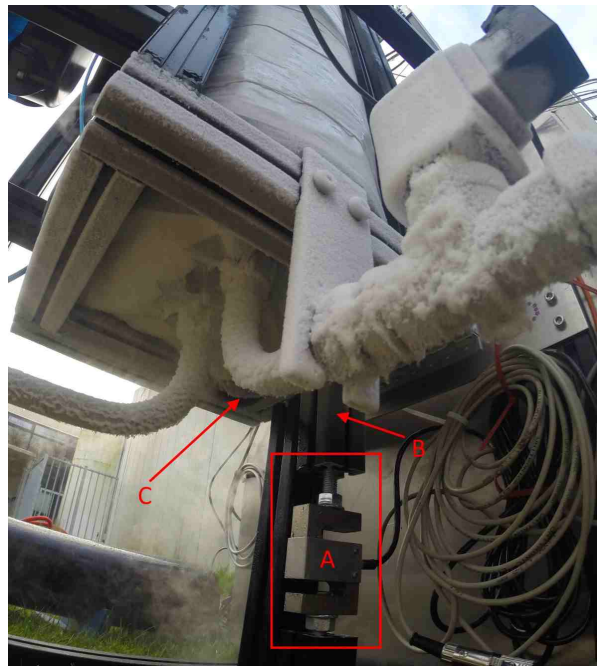

Figure 5.32: The bottom section of the test setup directly after the conclusion of the first exposure test. Severe frost formation is visible on the feed system parts and the bottom part of the tank holder structure. Part of the heat leak through this structure will have happened through the structural support at the fill valve line (visible in the center). At (A) the tank load cell is visible. At (B) frost formation is visible at the connection to this load cell. The location marked with (C) is where liquid nitrogen was observed to drip from the structure. Here the insulation material was found to be sticking out from under the tank.

Resulting actions

The first main action that needed to be taken was to resolve the leakage at the bottom bulkhead. After the tank had heated back up to room temperatures it was taken out of the test setup and pressurized with a compressor to 1 bar above atmospheric. With leak detection spray small leaks were indeed observed at the bottom bulkhead. To resolve this the bottom bulkhead was removed and inspected. It was found that at one location the sealing ring was indeed damaged. The O-ring was removed and replaced with a new one. This ring was inserted in the same manner as before (described in section 5.2.4) but now also clamps on the outside of the tube were used. After replacement the bulkhead still showed minor leaks, however now at different locations. Again the bulkhead was removed, however now no damage was observed at the sealing ring and the conclusion was drawn that the leakage was due to tight tolerances required for the sealing rings which just could not be met given the non-roundness of the tube.

It was resolved with the DARE cryogenics team that the method of sealing used is not ideal and needs to be thought through more carefully in the future. The state of the tank with the leak did not make it suited for usage in any tests at all. To still get tests done it was resolved to use the PU glue that was also used for the adapters as a permanent seal. This renders the tank useless for tests with liquid oxygen (due to chemical compatibility) but will allow continuation of the tests with liquid nitrogen.

The tank bulkhead was replaced with the undamaged O-ring and using PU glue instead of the previously used lubricant. After hardening the tank was found to be leak-tight up to at least 25 bar absolute pressure using compressed nitrogen gas.

To avoid possible future problems with a load cell that is cooled below its recommended operating temperature, the load-cell at the bottom of the structure was removed and replaced with a smaller load cell near the top of the test bench structure. The load cell and mounting are visible in figure 5.34. It is now placed to the side of the tank instead of directly below it, minimizing the chance that it will
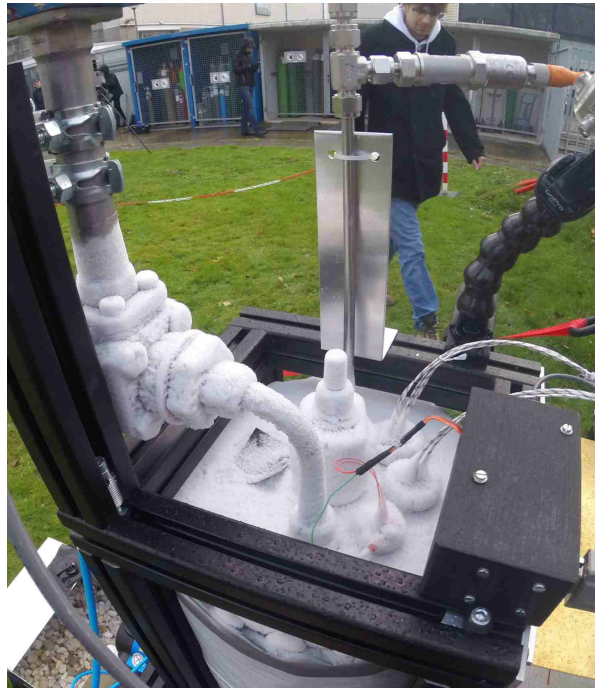
Figure 5.33: Severe frost formation occurred at the top bulkhead. No insulation was in place at this bulkhead to make sure all connectors were properly observable. No leakage was detectable at the top bulkhead. As can be observed, the PSRV/pressure sensor line at the back is free of frost. No flow is going through this line.

be exposed to any cold gasses. Furthermore it is fully encapsulated in a plastic cylinder, which also shields it. It is not connected to the tank holder structure via any metal parts, which limits possible cooling by conduction. Its only metal conduction part is via its bottom mounting screw to the main test bench structure.

A further hardware change was made to improve the cooling process of the tank by adding the bleed line orifice to the test setup. This orifice was not present during the first exposure test but was sized to increase tank pressure during the filling operations and to so promote the transition to nucleate boiling mode during the filling.

Finally some changes were made to the LabView program to control the system. These were changes that were made based on experiences during the exposure test and after analysis of the data of this test. Mostly it are corrections that were made to make sure more data is recorded. The changes made were:

- A fifth data file was added in which the system records the states of all valves and various LabView internal state parameters. This allows to determine exactly when certain valves were opened or closed, or when certain procedures were started.

- The capacitive data logging loop was also attached to the data recording control so that it was not recording data all the time, but only when asked to (just like the other sensors).

- The data counter from the load-cell FIFO was also passed on to the capacitive data file so that proper synchronization of the data is possible.

- A moving average filter was added to the front panel sensor indicators. As can be seen from the data for the pressure sensor, the noise present is quite high. The pressure sensor indicator viewed by the operator also showed this noise which means it is difficult (if not impossible) to read it out during operations. To stop this, a moving average filter was added to the indicators so that the last n values given off by a certain sensor are averaged together before being displayed. n being any positive integer value that can be set by the user. This cancels the noise on the indicator. The filter is not applied to the data logged in the files.

Figure 5.34: After the first exposure test the load cell was moved to the top of the test bench structure and placed in a plastic frame to shield it further from any cold gasses.

- Sampling rates of the sensors were adjusted based on experiences during the test and based on the data analysis afterwards. During this test the sampling rates were limited by the layout of the software on the cRIO. After the test the frequencies were set to those indicated in section 5.6. Note that after this test, it was also made possible to change measurement frequencies (between low-frequency and high-frequency) during the test itself.

5.8.4. Recommendations

Based on the experiences during the first exposure test, the following recommendations can be made for testing with cryogenic test setups within DARE and for tests in general.

1. Sealing methods for tank bulkheads for cryogenic applications need to be more thoroughly investigated. The problems with sealing the bottom bulkhead, even with a fully intact O-ring, show that sealing at cryogenic temperatures is more difficult than was expected. To make the current sealing method work either tubes with tighter tolerances need to be found or tubes like the current one need to be machined to achieve the proper tolerances. Other sealing options might be possible as well. A different tank design, possibly using welding, could be a solution. But if, for example, a liquid oxygen compatible glue can be found, the sealing problem would also be solved. How to properly seal these tanks is a perfect question that DARE can pose to industry experts.

2. Although a 'battleship-design', such as the current tank is, is often a very good choice because of the wide safety margin it gives, it also brings with it a large thermal mass. For cryogenic tests this means a lot of liquid nitrogen or liquid oxygen is needed to actually chill the tank down to operating temperatures. The increased amount of liquid needed may be sufficiently detrimental to operations that it is more beneficial to work with a less bulky tank design during ground tests. For liquid oxygen tests it is recommended that the cryogenics team of DARE constructs a more light-weight tank.

3. For the cooling down of the tank system, it is recommended to try and do the filling by intermittently allowing nitrogen flow, and stopping it. During the stop the tank can be closed off fully to allow better head transfer to the tank itself. This will aid in the cooling down process and reduce the amount of LN2 needed for cool-down.

4. For all teams in DARE, and for anyone doing tests with fluid systems at all: Always log the state of your system versus time. You will want to know at which time certain processes started and ended, and these processes are usually stated or terminated by valve actuation.

5.9. Conclusion and recommendations

A hardware test setup has been constructed for the conduction of pressurization and expulsion tests. The setup consists of an insulated aluminium tank with an attached feed system, suspended in an aluminium test bench. The tank is equipped with a suite of sensors containing pressure sensors, load cells, thermocouples, and an experimental capacitive sensor. The sensor data is recorded, and the feed system is actuated via a remote controlled system using a National Instruments cRIO system and a custom made LabView program. The system parts have been financed partially by the Department of Space Engineering, but largely by means of sponsoring and acquisition. The test setup has been validated by means of a hardware test in which the tank was filled with liquid nitrogen.

During the construction the advice of external experts from ERIKS/ECONOSTO was found to be very useful, and closer cooperation with industry in this form is highly recommended for DARE in the future. The tank design proved more difficult then expected, specifically the sealing was troublesome. Important design conclusions were reached that will assist tank design and construction in the future. (See section 5.2.6 for the detailed recommendation on tank design.) The test bench structure was constructed out of standard aluminium profiles, which proved to be a large improvement in ease of manufacturing and flexibility in design in comparison to previous test benches made by DARE. A large number of sensors was placed on and in the tank, including thermocouples that are placed in the tank. To achieve the cryogenic compatible sealing of these wires with the tank, a special method of preparing the adapters was developed that proved to be a very functional design. Finally, two versions of a capacitive sensor were developed to measure liquid level within the tank.

The whole setup was tested in the first exposure test. This was the first real experience for DARE in cryogenic rocket engine systems and has brought a lot of experience on how to conduct such a test. The test showed that more attention needed to be paid to the sealing of the tank. The detailed conclusions and recommendations resulting from this test can be found in sections 5.8.3 and 5.8.4.

Finally it also needs to be stressed again that the development and construction of hardware as presented in this chapter is a major piece of work, both in amount of man-hours needed and (financial) resources required. It is something that certainly does not need to be underestimated by anyone planning to do a practical investigation for his or her own research.

6

Vortex tube

The secondary hypothesis of this thesis concerns the injection of pressurant gas via a so called vortex tube. This is a device without moving parts that splits an incoming gas stream into a cold stream and a warm stream. The cold stream is injected radially, and the warm gas is injected axially. The idea is that this will create an even larger radial temperature gradient in the tank ullage volume.

To attempt to use such a device on the tank system, it needs to be investigated how a vortex tube is to be sized, how efficient it works, and how it can be constructed. The main goal for the design is to get a working vortex tube with a temperature separation that is as large as feasible. This chapter deals with the investigation on a vortex tube that was conducted for this thesis. The first section (6.1) discusses literature in relation to the vortex tube and various sizing rules that can be used to construct one. Section 6.2 discusses the first trial versions of a 3D printed vortex tube, which have been constructed to investigate if the lessons learned during the literature study proved useful in practice. The metal version of the vortex tube, constructed for use with high pressure helium in the actual injection tests, is discussed in section 6.3. The conclusions on the vortex tube are given in section 6.4.

For working with vortex tubes one general advice for future investigators: Do wear ear protection during the tests. The escaping air produces a loud, continuous noise that is very annoying to the ear.

6.1. Vortex tube literature

A vortex tube is a simple device without moving parts that splits an incoming gas stream into a cold and a warm stream. The device is often called a Ranque-Hilsch tube, after the two persons who discovered and investigated the device[35, 50]. A schematic representation of the device is given in in figure 6.1. Compressed gas is injected into a round chamber parallel to the chamber wall. This steers the gas into a vortex motion that progresses inwards and into the tube. The gas flows in a helical motion towards the end of the tube. There it hits a conical plug that allows gas near the tube wall to escape. This is the hot end of the tube. The remainder of the gas flows inwards to the core and travels back up, towards the central hole at the chamber side, where it escapes as a cold flow.
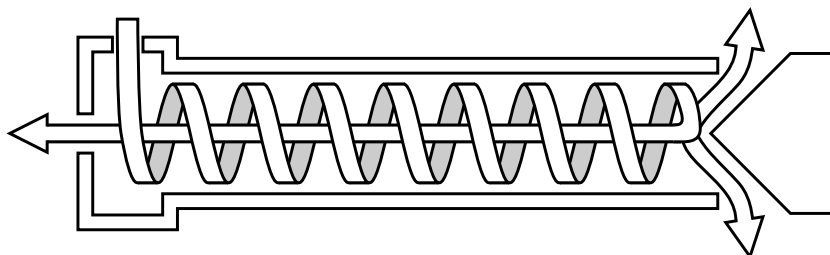
Figure 6.1: A schematic representation of the cross section of a vortex tube showing the internal flow pattern. Compressed gas is injected into the chamber on the right. The injection is such that the gas starts flowing in a spiral. The gas flows in a helical motion through the tube and splits in a warm outer gas flow, and a cold gas flow at the core. The warm gas can leave the vortex tube on the right. The cold gas is ejected at the left.

To use such a tube in a practical setup it needs to be understood how the temperature separation works, how efficient it works and on what parameters it depends. This can then be used to size a vortex tube to be used for pressurant injection. Section 6.1.1 discusses the most common theory behind the working of the vortex tube. Section 6.1.2 discusses a number of design rules. And section 6.1.3 shortly elaborates on a commercially available vortex tube.

6.1.1. Vortex tube theory

The main theory on how the vortex tube works has been originally described by Ranque in his patent on the vortex tube in 1934[51]. He suggests heating and cooling of the gas takes place because of expansion and compression of the gas by the centrifugal force the gas experiences while travelling through the tube. Over the years various authors have expanded upon this notion. An important contribution to this theory has been done by Ahlborn et al. in 1998[8]. He proposes a theory that states that there is a secondary flow present in the tube that functions as a heat pump. The secondary flow moves from the chamber, along the wall of the tube towards the hot end. Here it expands and flows inwards towards the core. The flow returns to the chamber along the core of the tube and is again compressed towards the circumference of the tube. The compression and expansion is across a pressure differential that is caused by the centrifugal force experienced by the gas. The travel paths up and down the length of the tube allow for heat exchange with the injected gas. Ahlborn backs-up his theory with experiments on a vortex tube and presents equation 6.1 for the temperature separation. In this equation γ is the ratio of specific heats of the gas, P_r is the reservoir pressure of the incomming gas, P_a is the exit pressure, and μ is the mass fraction of the cold gas flow with respect to the total massflow into the tube. The hot and cold end temperatures can then be related to the inlet temperature T_{in} by setting up a mass and energy balance, stating that the enthalpy flowing into the tube must equal the enthalpy flowing out. This results in relation 6.2.

$$\frac{T_h}{T_c} = 1 + \frac{\gamma - 1}{\gamma} \frac{P_r - P_a}{P_r + 2P_a} (1 + \mu) \tag{6.1}$$

$$T_{in} = T_C \mu + T_H (1 - \mu) \tag{6.2}$$

Further development along this same theory has been investigated at Eindhoven University of technology, by Liew[41] (amongst others). He refines the model from Ahlborn by stating that there are actually a large number of small heat pumps present along the length of the tube, instead of one large heat pump. He proposes equations 6.3 and 6.4 for the temperature separation, where P_h and P_c are the pressures at the hot and cold end respectively, and M is the Mach number at the chamber entrance.

$$\frac{T_h}{T_c} = \left(\frac{P_h}{P_c}\right)^{\gamma - 1/\gamma} \left(1 + \frac{\gamma - 1}{2} M^2\right)^{\gamma - 1/\gamma} \tag{6.3}$$

$$\frac{P_r}{P_c} = \exp\left(\frac{\gamma}{2} M^2\right) \left(\frac{D_{\text{chamber}}}{D_t}\right)^{\gamma - 1/\gamma} \left(1 + \frac{\gamma - 1}{2} M^2\right)^{\gamma/(\gamma - 1)} \tag{6.4}$$

The equations proposed by Ahlborn and Liew are quite different in structure, but it is important to note that they share two similar trends: (1) The ratio of temperature separation goes up with increasing pressure ratio between the reservoir pressure and the exit pressure. And (2) the temperature separation goes up with a higher specific heat ratio γ.

In the case of a pressurant gas system, the value for γ of course remains constant, as the gas is not changing during the expulsion. The pressure ratio is however changing. The pressure ratio term in equation 6.1 starts at 0.61 given a reservoir pressure of 200bar and an exit pressure of 35bar. This same ratio however drops to 0.45 halfway through an expulsion (120bar reservoir pressure) and to 0.05, or only 7.5% of the start value, at the end of expulsion (40bar). This shows that in a propellant tank pressurization system the temperature separation created by a vortex tube will be most strong at the start, but will strongly decrease over the course of the expulsion as pressurant tank pressure drops.

It must be noted that the theory described here is the most adhered to theory explaining vortex tube phenomena, but it is not a complete or fully accepted theory. Other alternative explanations exist, most notably the theory by Polihronov and Straatman[49] that tries to explain the split in temperature by arguing that velocity, and thus temperature, is observed differently by rotating or stationary observers.

6.1.2. Vortex tube design rules

As the theory explaining the temperature separation in vortex tubes is unfortunately not complete, it is not possible to draw general design rules from that other than those related to pressure ratio and the γ parameter of the gas. Fortunately there are a large number of studies that have investigated specific shape parameters of the system. An overview of many studies on the vortex tube is given by Subudhi and Sen[57].

The length to diameter ratio of the tube is often investigated. Ahlborn reports that typical values that produce the highest temperature separation are around $L/D \approx 30$ [8]. Other authors such as Aydin[10] find slightly lower ratios around $L/D \approx 20$.

The cold mass fraction of the tube μ, meaning the fraction of cold gas mass flow versus total mass flow, is also often investigated. Researches in general agree that the total temperature separation increases with increasing μ, up to values close to unity. The minimum cold temperature is to be found around $\mu = 0.3$.[10, 35, 41].

The size of the vortex chamber is often reported, but hardly every varied as design parameter. In most cases the chamber diameter is about 1.5 to 3 times the tube diameter.[57]

The diameter of the cold end orifice is most commonly designed as between 0.3 to 0.5 times the diameter of the tube itself[57]. This gives area ratios of 0.1 to 0.25.

The size of the hot end orifice is not often reported, but focus on this part of the tube has mostly been on the shape of the conical plug. Aydin[10] and Devade[23] report on the full-cone angle of the plug. Aydin found a 50° angle to be optimal, while Devade found that both a 45° angle and a 90° angle perform very well. Both authors reported 60° to give the worst performance.

Finally the effect of different gasses. This is not often investigated, and almost all tests that are reported are done with compressed air or pure nitrogen. One of the only ones that investigated multiple gasses is Khazaei et al.[39]. They investigated a vortex tube using air, nitrogen, oxygen, helium, CO_2, NH_3 and water vapour. They concluded that a larger temperature separation can be achieved with gasses with a high specific heat capacity ratio (γ) and a low molecular mass. Helium produced nearly three times as large a temperature separation as any of the other gasses tested by them.

6.1.3. Commercially available vortex tubes

During the thesis investigation on the vortex tube it was found out that a commercially available vortex tube is used in a Mechanical Engineering practical for second year students at Delft University of technology (course code WB2540, practical nr. 15). The vortex tube in use at this practical is produced by the company EXAIR, model number 3204. These types of vortex tubes are advertised by the company for specific spot cooling applications. The company claims that the model can produce temperature separations between 80°C (at $\mu = 0.2$) to 130°C (at $\mu = 0.8$) for inlet pressures of 6 bar. However, as by reference of the supervising professor of the practical, during the experiments conducted with the tube it is not found to be possible to achieve any temperature separations higher than 60 to 70°C at those pressures. The data provided by the company on this vortex tube is thus not reliable.

6.2. 3D printed vortex tube

The first version of the vortex tube is visible in figure 6.2. The hot end is constructed as a small chamber into which a metal nut is fastened. An aluminium conical plug (full cone angle 45°) can be moved in and out of the end of the tube by adjusting the screw. In this way the mass fraction flowing out of the cold and hot ends can be adjusted. An aluminium tube of 12 mm outer diameter, 10 mm inner diameter and 300 mm is used. Furthermore tubes of PVC were tried, with the same diamters but with lengths varied between 100, 200, 300 and 400 mm.

Four different versions of the vortex chamber + cold end were printed and tried. Each consisted of an inlet into which a pressurized gas spray could be pressed. The gas flowed into a toroidal shaped plenum and from there into the vortex chamber. Three versions tried are as showed in figure 6.2. Each had a cold end orifice of 4 mm diameter, a height of the chamber of 5 mm, and 6 inlet nozzles into the chamber, each of 1.3 mm diameter[1]. Only chamber diameter was varied between 10 mm, 14 mm, and 20 mm (which is respectively 1, 1.4 and 2 times the tube inner diameter). The fourth version is a more 'exotic' design and includes a large settling chamber at the cold end, plus a rounded, upstanding

---

[1]The accuracy of the inlet hole diameters is however questionable. The parts were printed using a Makerbot Ultimaker set to 0.1 mm layer thickness. The holes are thus not perfectly round or smooth.

Figure 6.2: The first constructed version of the vortex tube using 3D printed hot and cold end. Compressed gas is blow into the opening at the left. Hot air comes out of an opening at the right. On the right an aluminium cone serves as valve to control the cold mass fraction.

edge of 3.5 mm protruding from the cold end into the chamber, with the idea to prevent air from leaking directly from the inlets out through the cold end. This version has a chamber diameter of 10 mm (i.e. no chamber at all).

All vortex chambers were tested using compressed air from a supply line in the workshop (approx. 7 bar). Temperatures at hot and cold end were sampled using a single thermocouple. By adjusting the position of the hot end cone the points of minimal cold end temperature and maximum hot end temperature were sought out. At these points the hot and cold end temperature was recorded.

The 'exotic' chamber design was quickly dropped during testing as it produced a very small temperature separations in comparison to the other chambers. The presence of the upstanding edge in the chamber apparently seems to fully destroy the vortex tube effect.

During setting of the minimum operating point it was noticed now and then that the hot end cone started vibrating in some form of resonance with the escaping air. The vibration was possible as the fit of the bolt in the nut was rather loose. In such cases the cone was held in place either by holding it still or by fixing the bolt with a small piece of tape.

The three remaining chamber designs were combined with all 5 different tubes, and all 15 combinations were tested on the two operating points. Overall the 20 mm chamber gave the least temperature separation, and the least extreme temperatures (both hot and cold). The 14 mm chamber performed best, both in temperature separation and temperature extremes. Tube length variation (all with PVC tubes) showed maxima at 300 mm length in temperature separation at the maximum hot end temperature operating point for 10 mm and 14 mm chamber diameters. The overall maximum temperature separation was achieved at the cold operating point, 400 mm tube length, 14 mm chamber diameter. There cold end temperature was -23°C and hot end temperature was 54°C , giving a total temperature separation of 77°C . The same chamber, but with 300 mm tube length at the maximum temperature point gave values of -10°C and 66°C respectively, thus 76°C separation. The aluminium tube on average gave less separation at the maximum temperature point, but more at the minimum temperature point, when compared to the 300 mm PVC tube. These measurements should be taken with a grain of salt, as the placement of the thermocouple during measurements, and the setting of the hot end cone were not very well controlled.

Although these measurements are certainly not the most accurate every conducted on a vortex tube, they do form a sufficient indication that the design rules as distilled from literature are very useful and can be used to construct a working vortex tube. A chamber diameter of ∼1.4 times the tube inner diameter and a tube length between 30 and 40 times the tube diameter seem to provide the largest temperature separation.

6.3. Metal vortex tube

After the investigation with the 3D printed vortex tube, enough confidence was build up on the design rules for such a device to attempt to construct one from metal for high pressures.

The design created is a bulky 'battleship' design consisting of a number of pieces, as shown in figure 6.3. It consists of a cylindrical aluminium hot end (1) that contains a conical insert (2). The actual tube (3) is compressed between the hot and cold side. The ends of the tube are machined with a 5° taper so that they form tight metal-to-metal seals when compressed into the sharp edged holes of the hot and cold end. The plenum chamber with the main inlet is formed by a second aluminium cylinder (4). An aluminium insert (5) forms the vortex chamber wall with the inlet nozzles. A third aluminium cylinder (6) closes the plenum. Part 5 is squeezed between parts 4 and 6 by means of 4 bolts (7). Part 5 is
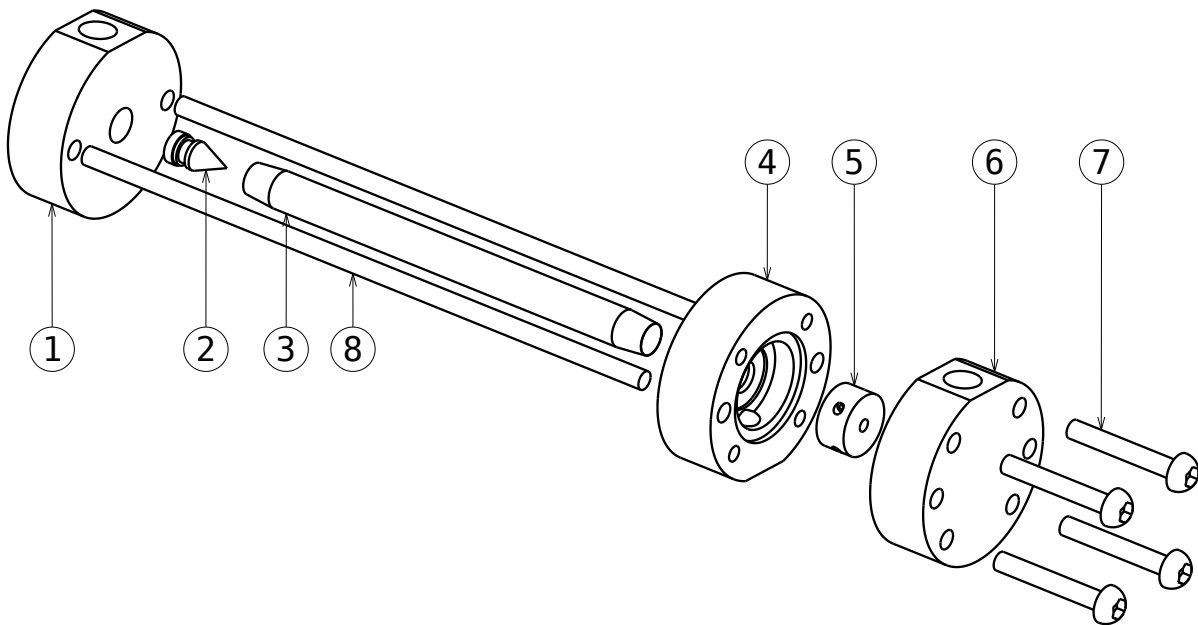
Figure 6.3: An exploded drawing of the vortex tube assembly designed for high pressure helium. The numbers are referred to in the text.

covered in teflon tape to ensure adequate sealing between plenum and vortex chamber. The sealing between parts 4 and 6 is achieved by a rubber o-ring (not shown). The compression of the vortex tube and the fixing of the hot end to the chamber is achieved by two steel threaded rods (8).

The vortex chamber is 15 mm in diameter, 7.2 mm high, and has 4 inlet nozzles of 1.5 mm diameter each. The cold orifice diameter is 4 mm. The aluminium tube has 12 mm outer diameter and 10 mm inner diameter. Varying lengths of 250 mm, 300 mm, 350 mm and 400 mm were tested. For the hot end insert, two types were tested: One with a 90°, and one with 45° full cone angle. It must be noted that due to the design, it is not possible to vary the position of the cone and thus the cold mass fraction. Both the 45° and 90° cone were designed such that the hot end annulus would have the same dimension with either of them, however it is suspected that due to production errors the orifice size, and with it the cold mass fraction, between the two inserts varied. As this is an important design parameter for vortex tubes, this effect might hide the real effect of the cone angle during testing.

Overall the design has a safety factor of at least 4 on all failure modes for 30 bar of internal pressure. It was successfully leak-tested with nitrogen up to 30 bar.

Figure 6.4: The assembled metal version of the vortex tube during compressed gas testing. (No insulation on the tube is present in this picture.)

The metal vortex tube was subjected to a more rigorous testing than the plastic vortex tube. A small feed system was constructed on the inflow side of the tube to sample inlet pressure and inlet temperature. The outlets were equipped with identical nozzles of 6 mm diameter. In the plenum chambers before these nozzles thermocouples were fixed to measure cold and hot temperatures. The inlet thermocouple was a K-type thermocouple, the outlet thermocouples were T-type. The pressure sensor is a similar one as described in section 5.5.1. The test setup is shown in figure 6.4.

A total of 12 tests were conducted. Of these tests, 8 cover all variations of tube length and hot end insert. Based on these 8 tests, the 300 mm, 90° configuration was selected, and this was used for the remaining 4 tests. This configuration was selected based on its total temperature separation, which was the third best of all configurations tested. Only the 400 mm configurations functioned slightly better, but these were eventually discarded because the difference in performance was minimal, and their length hinders easy instalment on the test setup. In tests 9 through 12 the tube was insulated in an effort to reduce the heat loss of the tube to the atmosphere, as it was noticed that the tube outside reached high temperatures during testing. This insulated configuration was tested twice with compressed air, and twice with helium.

Table 6.1: Measurement results from the metal vortex tube tests. The presented numbers were obtained from an average filter over at least 20 measurement samples. *=Tube was insulated

#	Tube length [m]	Cone angle [°]	Gas	P_{in} [bar]	T_{in} [°C]	T_C [°C]	T_H [°C]	ΔT [K]	$\Delta T/P_{in}$ [K/bar]
1	250	45	air	5.20	18.7	−11.2	39.5	50.8	9.77
2	300	45	”	5.42	18.7	−11.4	43.7	55.1	10.17
3	350	45	”	5.52	18.7	−13.8	40.2	54.0	9.78
4	400	45	”	5.62	18.9	−15.7	47.5	63.2	11.25
5	250	90	”	5.52	18.7	−13.9	41.1	54.9	9.95
6	300	90	”	5.51	19.0	−9.3	51.7	61.0	11.07
7	350	90	”	5.52	19.3	−16.7	38.5	55.3	10.01
8	400	90	”	5.37	18.7	−18.3	41.8	60.1	11.19
9 *	300	90	”	5.53	19.1	−9.2	52.7	61.8	11.18
10 *	300	90	”	5.66	16.8	−12.4	50.7	63.1	11.16
11 *	300	90	He	5.56 (0.14)	13.3 (0.36)	−21.4 (0.17)	65.8 (0.13)	87.2	15.69
12 *	300	90	”	4.21 (0.24)	14.9 (0.44)	−15.7 (0.15)	58.6 (0.26)	74.3	17.63

The results of the tests are shown in table 6.1. Tests with air were conducted by first operating the tube for 2-3 minutes to achieve stable operating conditions, after which measurements were recorded using the cRIO system for at least 1 minute. For the helium tests, the tube was first warmed/cooled by means of compressed air to get close to the operating condition. After that the helium was connected and data was sampled for more than 1 minute. Standard deviations for all tests using compressed air are $\sigma_P < 0.09$bar, $\sigma_{T_{in}} < 0.1$°C , $\sigma_{TC} < 0.25$°C and $\sigma_{TH} < 0.4$°C . For the tests with helium these deviations were slightly larger, as these tests were conducted with a supply from a gas bottle that was nearly empty, meaning cylinder pressure and temperature varied during the course of the test. Sigma values for these tests are indicated in brackets below the values in the table. Tests 1 through 9 were conducted on the 10th of January 2017. Tests 10 through 12 on the 27th of January 2017. To easily compare tests, a figure of merit for the tube $\Delta T/P_{in}$ is also shown in the table.

The test results show that, overall, temperature separation increases with increasing L/D ratio, as was expected from literature. The ΔT value seems to get to a local maximum at $L/D = 30$, then decreases at $L/D = 35$, but increases again at $L/D = 40$. This increase at longer tube lengths however may also be due to a shifting cold mass fraction. A longer tube might mean more friction losses towards the hot end, and thus a larger cold mass fraction, which according to theory also increases temperature separation. This effect cannot be confirmed or disproved as no mass flow measurements were done. Overall the 90°cone seems to perform slightly better than the 45°cone. Insulating the tube (test 6 vs tests 9 and 10) seems to shows a small increase in temperature separation, but nothing significant. Comparison of tests 9 and 10 shows consistency over multiple test days, as they were conducted

17 days appart. Also the inlet temperature changed a few degrees between these tests, but total temperature separation was not largely affected. The effect of a different gas is very clearly visible. Tests 11, using helium, shows nearly 40% more temperature separation than tests 9 and 10. Test 12 is more difficult to compare, as at this point the pressure from the helium cylinder ran very low, and the pressure at the tube was thus difficult to set and keep constant. The figure of merit $\Delta T/P_{in}$ however shows that the temperature separation is indeed very much higher than it was for air.

Finally, the data from these tests can also be compared to theory. Using equations 6.1 and 6.2, the expected hot and cold outlet temperatures can be calculated given the measured inlet conditions, and assuming a value for μ. The value assumed for μ is 0.5, as this is what the tube was designed for. Calculating the hot and cold temperatures for all tests with air (1 through 10), shows that the equations from Ahlborn predicts the cold end temperature correct within $\pm$2% and the hot end temperatures within -0.4% to +4.5% (temperatures in kelvin). For the helium tests the prediction for the cold end is off by -3.6% and -3.1%, and for the hot end by -2.6% to -1.6% respectively. Taking a value of $\mu = 0.4$ brings all predicted values for all tests down by about 2.5% less, and taking $\mu = 0.6$ brings all predicted values up by about 2.5% more. This means that the equations are not very sensitive to the value of μ, and that $\mu = 0.5$ is a good estimate for the air tests. For helium $\mu = 0.6$ seems to be a better estimate.

6.4. Conclusions and recommendations

During this the literature survey conducted before and during this thesis research a number of important papers have been found that explain the functioning of a vortex tube. Although there is no fully compleet and accepted explanation for the functioning of a vortex tube, the theory presented by Ahlborn et al. [8] is the most widely accepted one. From a selection of other papers it has proven to be possible to deduce a number of design rules that allow for a good design of a vortex tube. Research into the system is conducted on various locations in the world, including the faculty of Mechanical Engineering at TU Delft. Here it was possible to take a look at a commercial model of a vortex tube that they have in use for an educational practical.

Using the 3D printer that is available at the department of Space Systems Engineering of the TU Delft, a number of vortex tube configurations were investigated. From this it was concluded that the sizing rules resulting from literature can indeed be used to construct a functioning vortex tube. Various models were tested with pressurized air and were able to provide temperature difference in the order of 60 to 70 K. This is also comparable to what is reported by the department of Mechanical Engineering for the commercial model, indicating as well that the understanding of the tube design parameters is up to standards.

Based on this experience a metal version of the vortex tube was constructed that is suited for usage with high pressure helium in the actual injection tests. The tube was successfully leak tested up to 30 bar. Its temperature separation was measured using different tube lengths, hot end inserts, and different gasses (air/helium). The tube performs very well and produces around 60 K temperature separation with air. The measured results also match up very well to the equations presented by Ahlborn[8], strengthening the belief that his theory on the vortex tube is correct.

Future research on the vortex tube within the Space Department should mostly focus on the relation of the different mass flows to the temperature separation: The total mass flow and the cold mass fraction μ. Also the relations of tube size and total/relative pressure drop to temperature separation and total mass flow needs to be investigated if it is ever to be optimally applied in pressurant gas injection. Currently no authors present clear data on the mass flow to pressure drop relation. Structural design of the tube should focus on making the tube lightweight, which is believed to be very well possible due to the simplicity of the design. Construction of the tube could benefit from 3D printing the plenum and vortex chamber in metal. Finally, optimal implementation of the vortex tube in a pressurant injection system would mean maximizing the pressure drop over the tube by removing the pressure regulator, and instead regulating the tank pressure by means of valves at the hot and cold end of the vortex tube. This would mean the tube needs to be designed such that it can safely take the full pressurant tank pressure ($\sim$ 200 bar). It would however also allow for direct control of the cold mass fraction during operations, which might be beneficial as well. For such advanced control however, it would also be needed to very clearly understand the internal gas (thermo)dynamics inside the tank.

7

Pressurization and expulsion tests

The main bulk of work within this thesis has been in the preparation for, and conduction off, a number of validation tests to determine how much pressurant gas is needed to empty a cryogenic tank, and which method of gas injection is most efficient. This chapter in the report details the practical pressurization and expulsion tests in which three different types of injections have been tested.

The radial and axial injection tests are the most important two. These have been conducted on Monday the 15th and Tuesday the 16th of January 2017 respectively. Section 7.1 discusses these two test days side by side; How the tests proceeded and what the test results were. For each injection method three tests were conducted successfully.

Section 7.2 discusses the vortex tube injection test. This test was conducted on the 21st of February. Unfortunately a small piece of aluminium blocked the exit orifice, and the test data cannot be directly compared to the test data of the radial and axial injection tests. Important lessons on the functioning of the capacitive sensor are however still possible.

Finally in section 7.3 the three injection methods are compared and it is shown that axial injection is, as was hypothesized, indeed more efficient in terms of collapse factor than radial injection. The comparison between these two methods is the main focus of this section, but some notes are also given on the performance of the vortex tube injection.

7.1. Radial and axial injection tests

The main validation tests were conducted on Monday the 16th and Tuesday the 17th of Januari 2017. On the Monday three tests were conducted investigating the radial injection method. These tests are labelled "rad1", "rad2", and "rad3" respectively. On the Tuesday three axial injection tests were done, labelled "ax1", "ax2" and "ax3". This part of the report discusses the proceedings on both test days and the discussion of the test results.

7.1.1. Radial injection: Test description

The radial injection tests were conducted on Monday the 16th of January 2017. The tests were originally scheduled for Wednesday the 11th, but were rescheduled because of rain on that day. The weather on the Monday was fine with slight cloud cover. Temperatures were a little above the freezing point. The night before temperatures were below freezing. The sun broke through the clouds later in the morning and temperatures reached around 4°C. Apart from a very mild breeze there was no wind.

Thermocouples in the tank started around 18°C in the morning in the lab, but slowly dropped towards outside temperatures. The thermocouples were at around 12°C when tank filling commenced. The helium line thermocouple, which has virtually no shielding to the outside temperature, showed values between 2.5°C and 5.5°C from the start of data recording till the start of pressurization.

Most of the equipment was already transported to the test location the Friday preceding the test. The test-bench was transported on Monday morning. The helium bottle used for pressurization was present at the test site. The storage location of the bottle is open to the outside atmosphere, and thus the bottle was at outside air temperatures.

The test setup itself and the setup of the test location was in general the same as during the first exposure test (see section 5.8.1). However during this test the pressurization line was added. Furthermore the tank had been sealed, and the insulation on the tank and feed-lines had been improved.

Again Michel van den Brink was the supervisor from the department of Process and Energy. The operational safety officer from DARE was Felix Lindemann. For the filling operations and the first test, Juan Mussini was the test conductor and Mathijs van de Poel was test operator. For the second and third test Mathijs was test conductor and Rolf Wubben was test operator. Also Rano Veder was present and helped during the day. CP was manned by Rob Hermsen.

The test day commenced at 8:45 with the transport of the test bench from the TU Delft Dreamhal. The setup was completed around 9:55 and official procedures commenced at 10:27. No problems were encountered during the initial procedures and filling of the tank from the dewar commenced at 11:20.

After the dewar fill hose was connected, the hand operated valve at the dewar was opened, with the intention to start regulating the nitrogen flow by means of the fill valve. However, at this point liquid nitrogen was already heard flowing from the dewar into the run tank and gaseous nitrogen was venting from the bleed line. After some trail-and-error with the dewar hand valve and the controls for the fill valve it was decided that it was possible to continue the test without any safety risk by carefully evaluating the valve logic at each point. An overview of the anomalous behaviour of the valve and the proposed explanation for it is given in section 7.1.3.

The capacitive liquid level sensor (version 2) did not give any usable signal and gave the maximum value in its signal range continuously. It was concluded that the measurement range for the sensor was not configured correctly. The sensor was not used during the tests. LC2, the load cell below the pressurant gas mass, gave erroneous signals that also turned out to be useless during post-processing of the data. It is believed this was due to a faulty electrical connection.

Apart from this the valve and capacitive sensor, test operations proceeded smoothly, and the pressurization and expulsion was started on 13:34 (part G of the procedures, see appendix D). The pressurization and expulsion proceeded nominally. Thin vapour clouds were observed near the top bulkhead, with billowing vapour clouds instead of a jet. No leaking of gas could be heard. The clouds can well have formed by outside air flowing past cold system parts via natural convection.

Test rad1 was conducted around 13:40. Test rad2 around 14:45, and test rad3 around 15:50. The turn-around time between tests thus took around 65min.

The test day was concluded around 16:30. All equipment was stored on the test location for the night, to be used the following day for the axial injection tests.

7.1.2. Axial injection: Test description

The axial injection tests were conducted on the Tuesday following the radial injection test day. The test setup was stored near the test location for the night, which saved time during setup in the morning. The weather on the day started fully overcast with no sun visible. The weather report indicated temperatures of around -3°C in the morning. In the morning the sun shortly broke through, but then quickly disappeared again. There was hardly any wind present.

The storage location for the setup was shielded from the weather, but not from the outside temperatures. The ice that was formed on the tank the day before was still present on the tank on Tuesday morning. Thermocouple readings at the start of the filling were around -3°C . The helium line thermocouple started out at -3°C at the start of filling, warmed up to around 4°C halfway through filling (because the sun came out), but cooled down again to around -1°C before the first test.

In the morning the pressurization line was switched from the radial to the axial injection port on the injector. The capacitive sensor version 2 was switched back for version 1, as it was not possible to determine the new range of the sensor in the short time available. The electrical connection for LC2 was taken apart and repaired the evening before.

During the day again Michel van den Brink was the supervisor from Process and Energy and Felix Lindemann was the operational safety officer from DARE. During the whole day Krijn de Kievit was the test conductor and Eoghan Gilleran was the test operator. CP was manned by Rob Hermsen.

The test procedures were started at 10:48. Again some valves were not functioning properly, specifically PV did not actuated during the initial systems check-out. After several attempts at closing and opening the valve, changing the pneumatic supply pressure, and 'helping' the valve with a pair of pliers, the valve eventually responded again. The fill valve worked via the same 'inverted control' operations as the day before, however this day the valve stuttering was far greater then the day before. Several

attempts were made to stop the stuttering by trying different operating pressures for the dewar, but this unfortunately did not help. Eventually the stuttering was just accepted and the test continued.

The cooling down started at 11:51 and continued for slightly more than one hour. The first test took place just after 14:00. The two subsequent tests then followed in around 1h intervals. Cleaning up started around 16:30, after which the test bench and equipment was returned to the workshop.

Test ax1 was conducted using the same helium bottle as the day before, and thus started out at relatively low pressure. After test ax1 the helium bottle was exchanged for a second one that was used for both ax2 and ax3 tests. At the end of ax2 it was noticed that, less than a second before the end of expulsion, the LN2 had run out and as was venting through the orifice. This change was clearly observable by change in sound and the structure of the vapour cloud produced. This was an unforeseen situation and it was decided on the spot that it would be better, for the next test, to terminate the expulsion 5s earlier, so at t = 105s. Expulsion for test ax3 thus lasted only 45s, instead of the regular 50 s.

During the tests, again thin vapour clouds were observed near the tank. Pressurization and expulsion proceeded nominally for all tests.

7.1.3. Anomalous valve behaviour
During the tests the following observations were made in relation to the behaviour of the fill valve:

- When the dewar was connected to the setup, and the hand operated valve on the dewar was opened, the flow of nitrogen into the run tank started automatically. The solenoid valve did not need to be powered to start the LN2 flow.

- During the filling operation, when the valve was powered, it appeared to close. I.e. the controls of the valve seemed to have inverted and it now behaved as a normally opened valve. The "closing" of the valve was observed by the decrease of gaseous nitrogen escaping from the bleed valve (BV).

- When the dewar was disconnected, the valve behaviour returned to normal again: When powered it opened and LN2 was observed to flow out of the tank. When closed, it sealed the tank, even when the tank was pressurized to ~28 bar.

- During the filling operations the valve seemed to stutter: The valve could be heard clicking open and close repeatedly while LN2 was flowing from the dewar to the tank. The stuttering stopped when the valve was powered. This however also closed the valve, and thus stopped the filling. The stuttering also ceased if the dewar pressure was lowered to just under 2 bar. This however also seemed to close the valve.

Based on the observations a possible explanation for this behaviour of the valve is proposed. This explanation is illustrated in figure 7.1. The valve cross-section in these figures is not the exact cross-section of the valve used as FV, but is of a comparable valve that functions in a similar way (same manufacturer and product family).

Within the figure the normal behaviour of the valve is indicated with A and B. Figure A shows a high pressure applied to the entrance of the valve, and a low pressure applied to the exit. The valve is unpowered and no flow is possible. This is because, via the flow passage indicated by 1, the high pressure presses down on the main piston and thus closes it. The valve can be opened when it is powered (as shown in figure B). When it is powered the solenoid lifts a small plunger, that opens flow passage 2. Because flow passage 2 is bigger than flow passage 1, the pressure above the piston quickly drops, and the high pressure on the inlet can lift the piston. This opens up the main flow passage.

The atypical behavior of the valve is explained as shown in figures C and D. First in figure C, the solenoid is unpowered. The high pressure applied on the outlet side now directly pushes against the piston and the plunger. No counter force is applied because there is no flow passage towards the top of the piston. The high pressure pushes open the piston. Liquid can now flow relatively unhindered without the solenoid being powered. When the solenoid is powered, it lifts the plunger away from the piston, again opening flow passage 2. The high pressure liquid flows towards the top of the piston, thus balancing the forces on both sides of the piston. Because on the inlet side the liquid can flow out, the pressure drops here and thus the piston now closes. As flow passage 1 is smaller than flow

Normal operations | Atypical operations

A unpowered
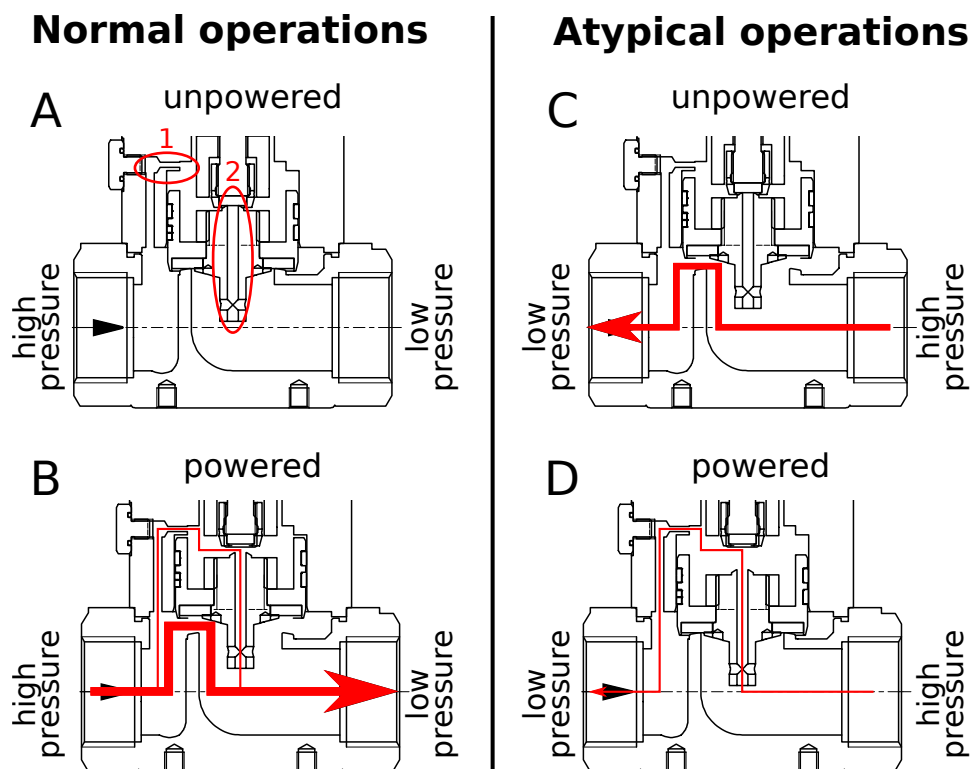
C unpowered

B powered

D powered

Figure 7.1: Fill valve states with the pressure differential across the valve in the intended direction (A and B) and in the reversed direction (C and D), as during filling operations. The red arrows indicate flow of liquid through the valve. The two internal flow passages in the valve are indicated a A by numbers 1 and 2.

passage 2, it means the pressure above the piston remains higher than the pressure at the inlet side. This explanation results in a situation where the valve is powered, but the main piston is closed. A small path still remains open for the liquid via flow passages 2 and 1. This flow can quite well have gone unnoticed during the test as the amount of liquid flowing through such a passage will have been undetectable in the sensor output or in the outflow of evaporated N2 through the bleed valve.

Overall this explanation shows why the valve can have behaved as a normally opened valve (that is leaking slightly when it is closed) when the pressure across it is applied in the wrong direction. The valve stuttering can likely be explained by the presence of a spring in the valve, pressing down on the main piston. This made that the situation shown in figure C could actually result in a resonating mode where the piston moves up and down alternately by the fluid pressure and the spring force.

This anomalous behaviour of the valve shows that solenoid valves (and possibly globe valves in general) are not suited for usage as fill valve in a system due to the pressure differential being applied in different directions over time. During these tests the behaviour likely resulted in slower filling times due to the stuttering hindering mass flow. It does not have any influence on the pressurization and expulsion process as there the fill valve is not operated.

7.1.4. Test results and data analysis

During the injection tests the various sensors on the test setup produced a large bulk of data that has been distilled into a number of graphs and numbers which give insight into the various physical processes that are ongoing within the setup. In the followin sections the data produced by the different sensors for the radial and axial injection tests is presented. First the process of tank cool-down is discussed, after which the process of pressurization and expulsion is looked at in detail. The measurement data is discussed in the following order: The load cell data (page 100), the capacitive sensor data (page 103), the pressure sensor data (page 104), the thermocouple data (page 107) and finally the helium cylinder pressure readings (page 112).

For the exact description of how the data was processed, calibrated and zeroed, please refer to appendix E.

Tank cool-down

At the start of the test day the tank needs to be cooled down to cryogenic temperatures to be able to fill it with liquid nitrogen. In contrast to the first exposure test (section 5.8) the cool-down was done by a stepwise process where LN2 was allowed to flow for 5 minutes, and then stopped for 5 minutes. During the 5 minutes stop the bleed valve was closed to allow pressure to rise and to stop venting. After that the bleed valve was opened to release pressure, and filling was resumed through the fill valve. This process was timed by a stopwatch and was not exact.

For the radial injection test the tank cooling down commenced around 11:20 in the morning. The tank was cooled down from temperatures around 12°C to -196°C by filling LN2 through the fill valve. The total cool-down time took about 1 hour and 15 minutes. After this all thermocouples, with the exception of TC14 and TC15, had reached temperatures at or below -175°C.
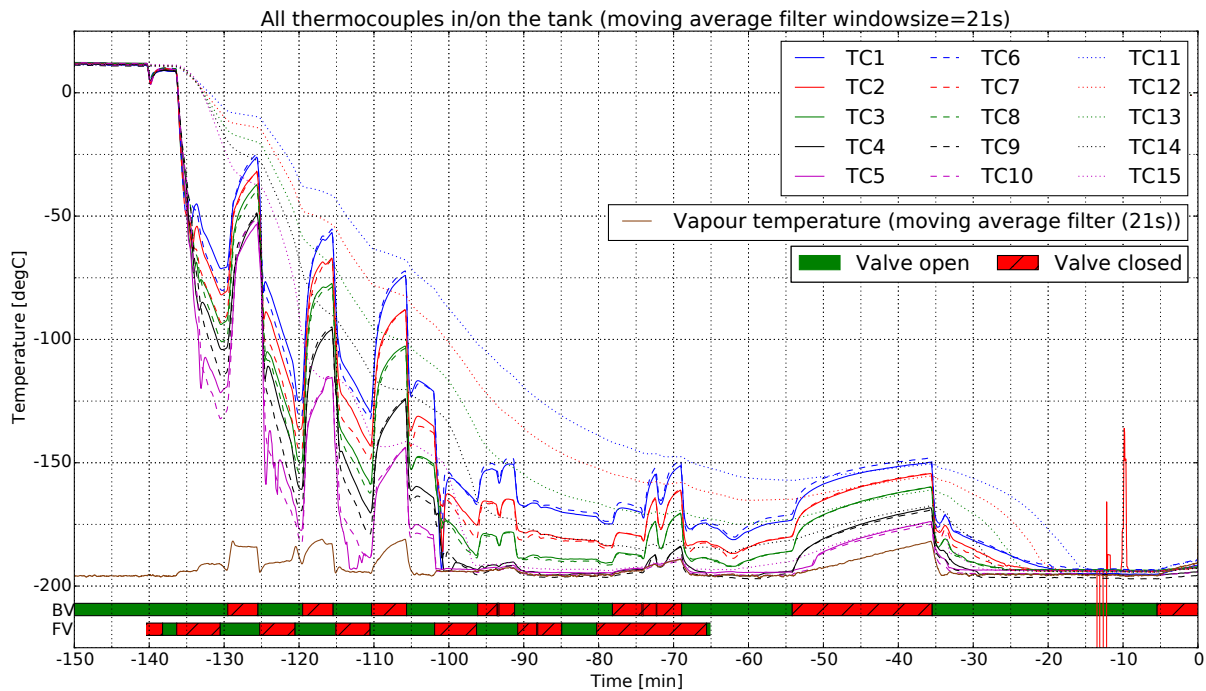

Figure 7.2: Temperature graphs of all thermocouples during the filling procedure in advance of test rad1. Displayed as well is a N2 vapour temperature curve that is generated from the pressure measured by PS1 in the tank during the filling. At the bottom of the graph are the state parameters for the bleed valve and the fill valve. Note that the fill valve state is cropped to the time where the dewar was connected and the dewar fill valve was opened.

Figure 7.2 shows the temperatures as measured by all thermocouples on and in the tank during the filling operations of the radial injection test. Added to it is a vapour temperature curve for LN2 based on the pressure measurements of PS1 done during the filling. This can be viewed as the minimum temperature possible within the tank during the process. Also displayed are bars indicating the states of the bleed valve and fill valve. The states of the valves shown in the figure are their actual physical states. The bar for the fill valve has been intentionally cropped to the approximate time frame in which the dewar was connected and the dewar fill valve was opened. This was done because of the 'control inversion' that took place in the fill valve during operations. An exact reproduction of the physical state of the fill valve is not possible without knowledge of the state of the dewar connection, dewar fill valve, and dewar pressure (all of which are not known exactly). Within the time-frame shown it is however quite certain that the state of the fill valve was as indicated.

The actual filling commences approximately at t = -140min. The first 5 minutes were spend figuring out the control inversion of the fill valve and how to work with this. After this, three fill-stop cycles were conducted. Temperature in the tank drops rapidly during filling but quickly shoots back up as soon as the bleed valve is closed. They just as rapidly drop again when the bleed valve is opened. The tank wall temperatures drop steadily and keep on dropping during the time when the fill valve is closed. This is the advantage of the cyclic fill procedure: heat transfer from the tank wall continues cooling down the tank even though no extra LN2 needs to be filled. During the filling the bleed line orifice,

which was added only after the first exposure test, also shows its benefit: Pressures within the tank are approximately 1.7 bar (first cycle), 1.8 bar (second cycle) and 1.2 bar (third cycle), while they were at a fairly continues 1.2 bar during the first exposure tests. Overall this higher pressure leads to a higher heat transfer rate. Near the end of the second filling cycle (t≈-120min) TC15 has already reached a temperature of -100°C and is cooling down at a rate of -0.27°C s^{-1}. These are values comparable to those 15 minutes into filling during the first exposure test, however now they are reached with the LN2 flowing in only during two-thirds of that time period.

Around t = -102min the fill valve is opened again and the four lowest thermocouples in the tank (TCs 4, 5, 9 and 10) all have reached the LN2 vapour temperature line. The lower end of the tank wall (TC15) also reaches this temperature 5 minutes later at t = -97min. All these thermocouples now stay to the vapour line till around t = -60min. The dewar was near empty around t = -65min and was disconnected at this point. Overall the cooling procedure has been much improved as compared to the first exposure test. With the same amount of LN2 (roughly 45 to 50L) all thermocouples in the tank showed temperatures below -150°C while during the first exposure test the maximum temperature was still near -80°C. During the waiting time, in which de dewar was filled, it was decided to keep the bleed valve closed to prevent LN2 evaporation and to allow pressure to rise.

The dewar was refilled during approximately t = -60min till t = -40min. After this the dewar was reconnected to the setup and filling took place between roughly t = -35min till t = -5min.

For the axial injection testing the next day, the cool-down process needed to be repeated. Over night the tank had warmed up again to environmental temperatures, which were around -3°C in the morning. The tank cooling started at 11:51 and the whole process took about two hours again, just like the day before. Again the stepwise cool-down process was applied. The total number of steps iterated through was larger during this test day compared to the day before. Cool-down went steady, but less quickly. This slow cool-down might be attributed to the increased stuttering of the fill valve on this second test day, which hindered the mass flow of LN2 into the tank.

Load cell data
The load cell data recorded by LC1 during the pressurization and expulsion of all three radial injection tests is shown in figure 7.3. The data for the axial injection tests is shown in figure 7.4. All the data shown in the graph is unfiltered data recorded at 50Hz.

As by the automated sequence, the pressurization process takes place between t = 0 s and t = 60 s. The expulsion than takes place from t = 60 s till t = 110 s. Only for test ax3 the timing is from t = 60 s till t = 105s. After that the tank is depressurised. All graphs show the exact same behaviour. They display virtually constant mass before pressurization and during pressurization. The mass then decreases linearly during the expulsion, and settles again near a constant value at the end of expulsion. After the expulsion the bleed valve is also opened for depressurisation, so the mass keeps on decreasing still due to evaporating LN2 from the tank.

On each of the transitions between the different phases the graphs display a classical damped vibration pattern resulting from an impulse excitation. These excitations are, respectively, the closing of PV at t = 0 s, the opening of MV at t = 60 s, and the closing of MV, closing of PV, and opening of BV at t = 110 s. It is interesting to note that the opening of PV still has such a noticeable result on the mass measurement of the tank, because PV is actually not mounted on the tank holding structure. The vibration from its actuation travels through the main test bench structure and the flex plates, and via the flexible hose that forms the pressurization line.

For each of the phases in the graph a number of parameters can be estimated regarding masses of the LN2, the helium, and the mass flow. These are all gathered in table 7.1. From the section before $t = 0$s the initial mass of LN2 can be retrieved, and this can be converted in a fill level for the tank. Accuracies on all measurements are in general very good and are limited by the accuracy of the test setup and the calibration of LC1. For determination of values like start mass the electronic noise during the measurement is in the order of one gram and thus considered not of importance.

During the pressurization, helium mass flows into the tank. The amount of gas that flows into the tank is really small, but a noticeable differences is present in the load cell measurements. The helium mass for pressurization quoted in the table is the difference between the start mass and the average tank mass over the given time span. The difference is in the order of 30 g for the radial tests, but more spread out for the axial tests. These are however values that fall within the range of uncertainty that
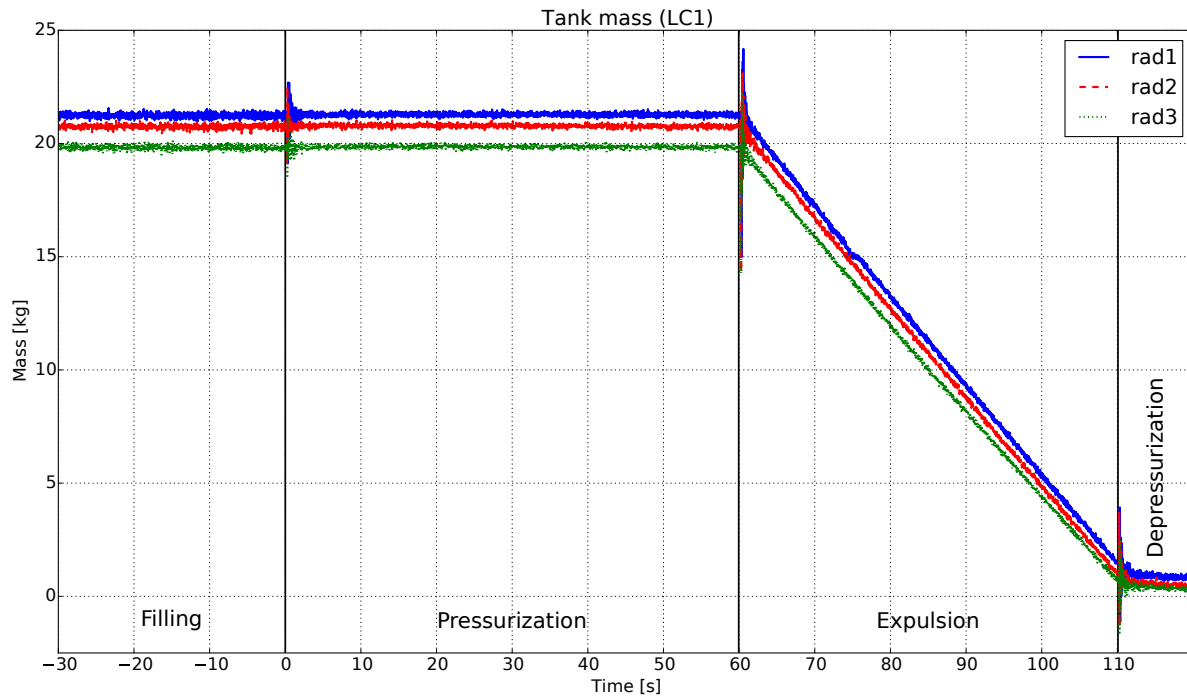
Figure 7.3: Tank mass measurements with LC1 during the pressurization and expulsion phase of the three radial injection tests.
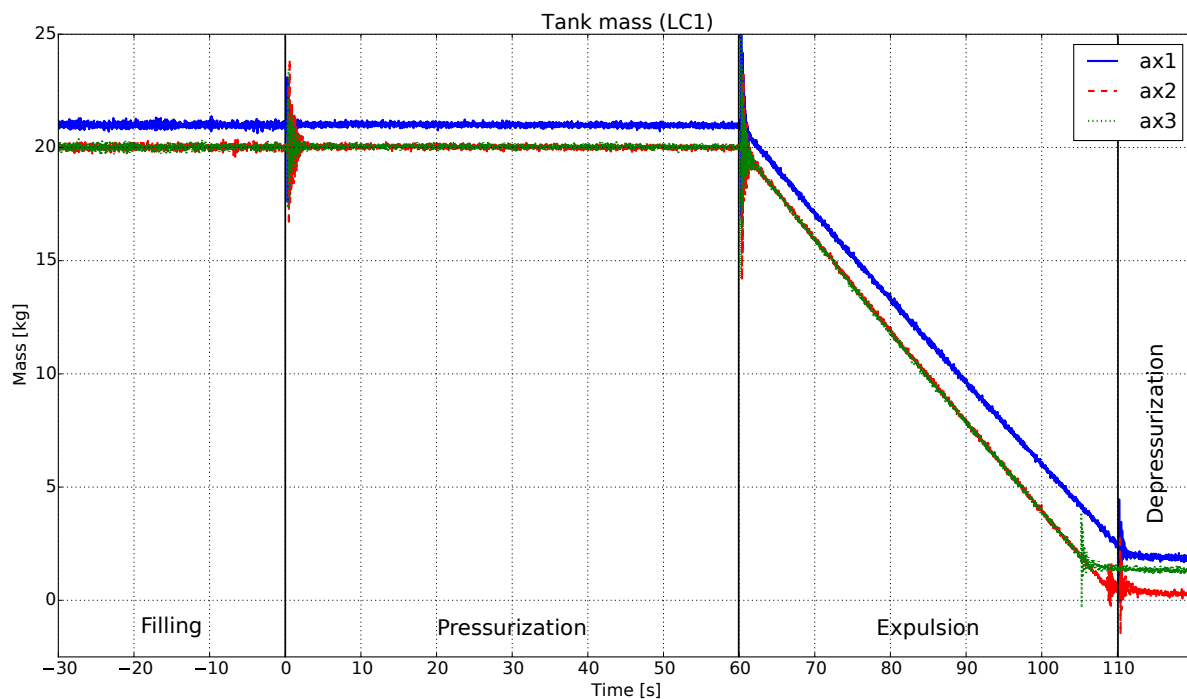
Figure 7.4: Tank mass measurements with LC1 during the pressurization and expulsion phase of the three axial injection tests.

is estimated for the test setup, the load cell, and the load cell calibration. Also here, inaccuracies due to measurement noise are not of importance. Large spreads in the value such as seen with the axial injection tests can be due to some form of physical hysteresis in the measurement setup. For example the shock when opening the pressurization valve could cause the measured load cell value to shift slightly, easily giving a few grams of offset in value.

During expulsion the mass flow out of the tank can be determined by making a linear estimate over the expulsion time. The mass flow out of the tank is consistently around or just below 400 g s^{-1}. The

Table 7.1: Mass, mass flow and liquid level estimates for the radial injection tests based on data from LC1. The liquid level indication is based on a constant density assumption for the LN2 of $\rho = 800$ kg m^{-3}. The liquid level in percent is given with respect to the total (inner) tank height of 740 mm. At test ax2 the tank was empty just before the end of the test at t = 50 s. The final mass for test ax3 is calculated for t = 45s, as this test was terminated early.

Test			rad1	rad2	rad3	ax1	ax2	ax3
Start mass ($\sigma < 0.09$kg)	m_{LN2}	[kg]	21.25	20.76	19.83	20.99	20.01	20.01
Liquid level	h_{LN2}	[mm]	639.3	624.4	596.5	631.6	602.0	602.1
(start; $\sigma < 2.7$mm)		[%]	86.4	84.3	80.5	85.3	81.3	81.4
Helium mass pressurization	m_{He}	[g]	31	24	30	6	13	25
($\sigma < 0.09$kg)								
Mass flow	$\dot{m}_{LN2}$	[kg s^{-1}]	−0.396	−0.395	−0.382	−0.371	−0.402	−0.401
($t = [63\text{s} : 103\text{s}]$)	RSE	[-]	0.0109	0.0134	0.0168	0.0095	0.0118	0.0129
Liquid level rate of change	$\dot{h}_{LN2}$	[mm s^{-1}]	−11.9	−11.9	−11.5	−11.2	−12.1	−12.1
(from mass flow estimate)								
Final mass	m_{LN2}	[kg]	1.45	1.00	0.73	2.43	0.00	1.95
(from mass flow estimate)	σ	[kg]	0.22	0.27	0.32	0.18	-	0.26
Liquid level (final)	h_{LN2}	[mm]	44	30	22	73	0	58
(from mass flow estimate)	σ	[mm]	6.5	8.0	9.7	5.4	-	7.9
	h_{LN2}	[%]	5.9	4.1	3.0	9.9	0	7.9

standard error of estimate shows that these values are within 1.68% of the actual mass flow out of the tank, meaning a deviation of maximally 6.2 g/s is possible (for rad3, which is the maximum deviation).

Mass flow for test ax1 is the lowest of all tests. The outflow of LN2 is about 7.5% slower than that at ax2 and ax3. This is also visible in the graphs in figure 7.4; the slope at ax1 is clearly lower. This is due to the lower overall tank pressure during this test, which is in turn due to the lower cylinder pressure for test ax1. The measurements show that ax2 and ax3 started of with the same start mass, and progress through expulsion with virtually the same LN2 mass flow. The tests are therefore identical for all practical purposes with regard to liquid level and LN2 mass during the tests, with the exception that test ax3 cuts of 5s earlier. The data indicates that during test ax2 all LN2 was expelled from the tank at 0.25s before the end of expulsion.

The end mass at the end of each expulsion process has been determined by means of the mass flow estimation and the total expulsion time. Therefore the uncertainty in this value is larger than in the start mass. The end mass cannot be directly determined from the measurements after the end of expulsion, because at that time also the bleed valve opens, meaning the pressurant gas mass and evaporated N2 can escape from the tank, meaning another few hundreds of grams of mass loss occurs at this point.

During the tests also a direct measurement of the mass of the pressurant gas bottle was attempted. This measurement data however proved to be unreliable. The helium gas bottle is standing on a small platform that measures the load on top of it, but the bottle is also leaning slightly against the test bench, is secured with a chain, and has a hose from the pressurization line hanging from it. This setup makes it very sensitive to any movement of the test bench and to wind. Added to this is an expected faulty electrical connection in the load cell connection line during the tests on Monday, that made the value jump to extreme minima and maxima which cannot be related to a physical phenomenon affecting the measured mass. For the tests on Tuesday the electrical connection had been repaired, but still the measurement was not deemed reliable. For the axial tests the measurements were ax1: $m_{pres} = -60$ g, ax2: $m_{pres} = 276$ g and ax3: $m_{pres} = 406$ g. This is quite a large spread, and the measurement for test ax1 even shows an increase of mass in the pressurant bottle. The change in mass that was expected should have been in the range of a few hundreds of grams. This measurement was always considered to be a long shot, as this change in mass needed to be measured with respect to a total tank mass of approximately 70 kg. Overall the accuracy of these measurements was insufficient to make any judgement on the change of mass of the helium bottle.

Capacitive sensor data

During the radial injection tests test the capacitive sensor version 2 (coaxial, see section 5.5.4) was used. Unfortunately the FDC1004 chip that performs the measurements was not configured to the proper measurement range. The sensor thus clipped to a maximum value and gave no useful data at all. To get usefull data out of this sensor version the software needed to be reconfigured. This could not be properly done overnight between the two test days, and so instead it was decided to replace the sensor with capacitive sensor version 1 for the axial tests, to at least try and get some form of measurement, even though it might not be a very good measurement due to various properties of the sensor. (See section 5.5.4.)
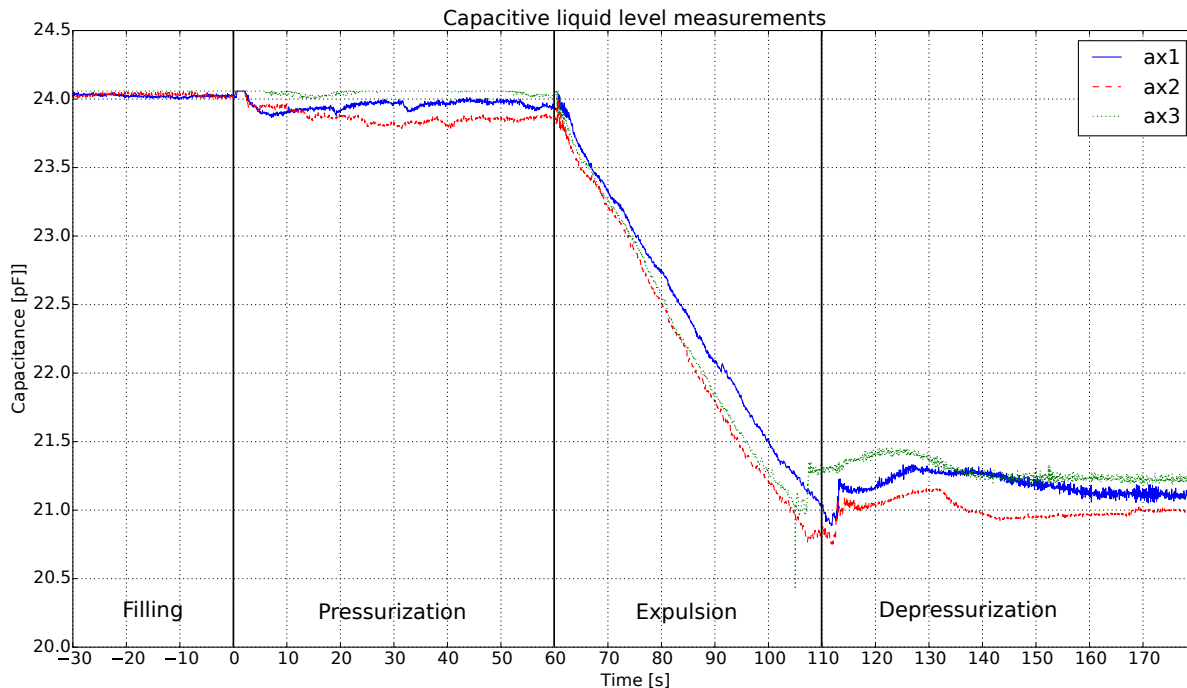

Figure 7.5: The capacitive sensor measurement during the pressurization and expulsion with the axial injection method. The sensor output range is capped at 24.058 pF.

The measurements obtained during the pressurization and expulsion in the axial tests are shown in figure 7.5. The graph is unfortunately capped at C=24.058 pF because it turned out that also for sensor version 1, the measurement range was not to properly configured. This maximum capacitance seems to approximately coincide with the maximum reading the sensor gives for a full tank, so just the top section of some measurements is missing. The most interesting thing to note is that at t = 0 s, the start of pressurization, the output by the sensors actually drops slightly, when compared to the unpressurised state before. At depressurization, around t = 110 s, the signal then again shows a sudden increase in the data. This all seems contradictory to the theory on the dielectric constant of materials (section 5.5.4), which says that the dielectric constant of fluids, and thus the measured capacitance, should increase with increasing pressure, because density increases. The capacity however decreases with increasing pressure, and increases again with decreasing pressure. Likely this is due to the fact that the type of gas in the ullage changes. During pressurization helium gas is injected into the tank, while before it was only nitrogen gas. Nitrogen does have a slightly higher dielectric constant than helium, but the difference in output signal this generates is not expected to be this big. Likely the effect of the nitrogen was underestimated, or the signal of the sensor is highly effected by effects such as droplets condensing onto the surface of the sensor. This could lead to a false high-output signal.

During the expulsion itself the capacitive sensor does give the expected linearly decreasing curve, which correlates to the mass in the tank. In figure 7.6 the load cell output is plotted versus the capacitive sensor output for the expulsion time (t = 60 s till t = 110 s). The correlation between capacitive sensor output and LN2 mass is clearly linear and can be modelled very well with a linear fit. The parameters for such fitted curves are given in table 7.2. It shows that the fits are very linear, with R^2 values very close to unity. The repeatability is decent, but not very good, as the slopes of the correlations vary. The
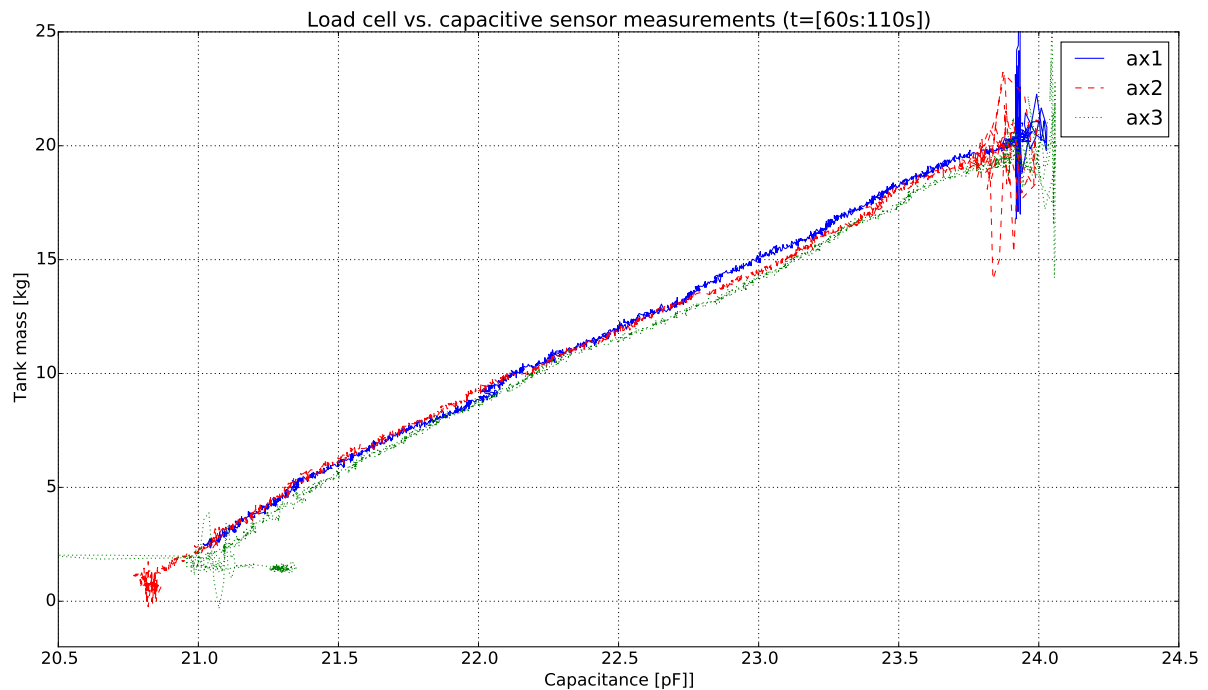
Figure 7.6: The load cell measurements plotted versus the capacitive sensors measurements for the expulsion time (t = 60 s till t = 110 s). Over time, as the tank empties, the graph proceeds from the top right to the bottom left.

Table 7.2: Linear fits for the tank mass versus the capacitive sensor output. These parameters are generated by fitting curves to the time interval of t = 65s till t = 103s during expulsion. The functions are of the form $m = a \cdot C + b$ where m is the LN2 mass in kg and C the capacitance in pF. Uncertainties are based on the deviation of the actual mass measurement with respect to the fitted curve.

Test		ax1	ax2	ax3
Slope (a)	[kg pF^{-1}]	6.05	5.85	5.94
Offset (b)	[kg]	−124.0	−119.7	−122.1
Standard deviation (σ)	[kg]	0.144	0.256	0.258
RSE	[-]	0.014	0.046	0.046
R^2	[-]	0.999	0.997	0.997

resulting RSE values for tests ax2 and ax3 show this. According to the RSE value and slope of test ax3, the slope could vary between 6.21 and 5.67 kg pF^{-1}. The standard deviation of the fits w.r.t. the actual data is about two to three times that what is achieved using load cell measurements (see table 7.1). The performance is however not bad for the first attempt at a capacitive sensor within DARE, and likely the the performance can be improved significantly still by fixing known issues with capacitive sensor version 1. If that is accomplished, such a sensor can be well used to replace the tank mass measurement within DARE. The only practical issue that still needs to be overcome there however, is proper calibration of the sensor.

Pressure data

Pressure data was collected via two pressure sensors, PS1 at the tank and PS2 at the pressurization line. The pressure data from PS1 for all three radial injection tests is shown in figure 7.7, and those for the axial injection tests are shown in figure 7.8. In this graph the three phases of each test are very clear: first pressure rises during the pressurization, pressure drops but levels during expulsion, and finally the whole system is depressurised.

All graphs lie fairly close to one another, but they do have marked differences. These are best observed using the data from table 7.3, which is derived from the pressure curves. For each of the three main sections of the curve a rise time is given, in which the pressure rises to 90% of its final value during that phase. For the pressurization phase this is the maximum pressure, for the expulsion this is
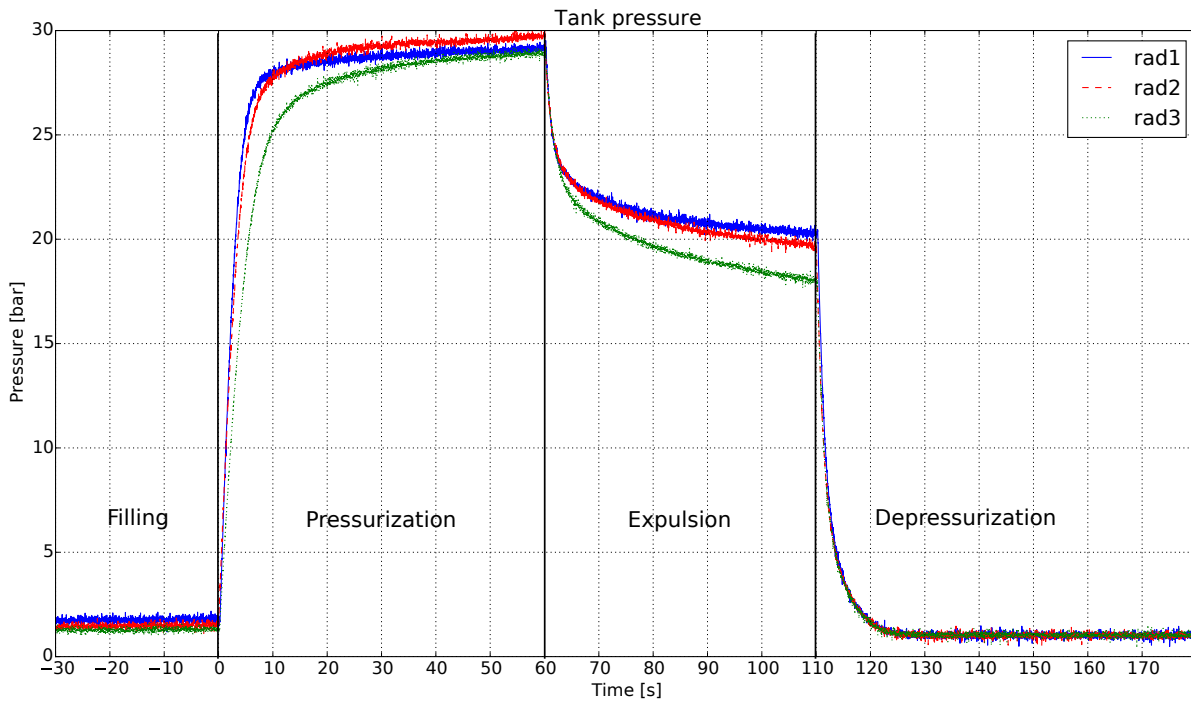
Figure 7.7: Pressure measurements from the tank (PS1) during pressurization and expulsion. Displayed is unfiltered data recorded at 50 Hz.
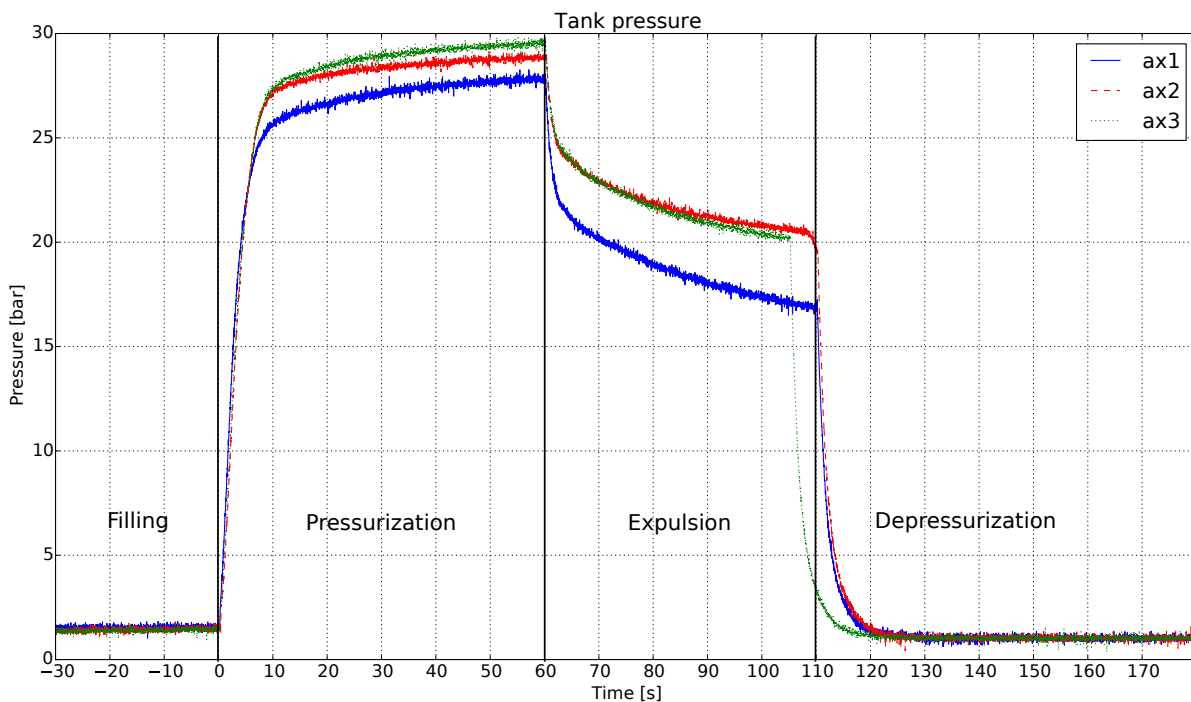
Figure 7.8: Tank pressure as measured by PS1 during pressurization and expulsion of the axial injection tests. Displayed is unfiltered data recorded at 50 Hz.

equal to $P_{final} + 10\% \cdot \left(P_{max} - P_{final}\right)$, and for the depressurization this is atmospheric pressure.

The graphs all start off at low pressures just above atmospheric. The pressures are different because at this point in the test the bleed valve is already closed and pressure is rising in the tank because it naturally warms up. Depending on how long the bleed valve was closed, the pressure differs slightly.

When the pressurization valve opens all tests show a rapid increase in pressure, however test rad1

rises faster than rad2, which in turn rises faster than rad3. Likewise pressure during ax1 rises slowly, but faster again in tests ax2 and ax3. This is due to the fact that the radial tests and test ax1 were all conducted using the same pressurant cylinder. The test pressure in this cylinder becomes lower for each subsequent test, and because in this situation the pressure regulator can be assumed to be fully opened due to the high pressure difference, the mass flow is limited by the cylinder pressure instead. For tests ax2 and ax3 a new pressurant cylinder was used. The pressures all settle near a value around 29 bar. The differences are likely due to slightly different settings of the pressure regulator during each test. For the radial tests the rise time during pressurization also decrease with each subsequent test. For the axial tests however, the rise time is quite the same during all tests. This is surprising for test ax1, because there the helium cylinder pressure was significantly lower than for ax2 and ax3.

Table 7.3: Pressure readings and rise times for the different phases of the test. All readings in this table are obtained from the data of PS1 using a moving average filter of 51 samples (=1.02 s). The fall times for the expulsion are given with respect to t = 60 s (start of expulsion). The fall times for the depressurization are given with respect to t = 110 s (start of depressurization), except for test ax3, where this is given with respect to t = 105 s.

Test			rad1	rad2	rad3	ax1	ax2	ax3
Start pressure	P_{start}	[bar]	1.75	1.47	1.28	1.52	1.42	1.40
($t = [-30s : -5s]$)	σ	[bar]	0.100	0.096	0.089	0.091	0.092	0.091
Pressurization								
Maximum pressure	P_{max}	[bar]	29.16	29.74	28.92	27.82	28.87	29.56
	σ	[bar]	0.100	0.088	0.098	0.110	0.095	0.124
Rise time (90%)	t_{rise}	[s]	5.70	7.62	12.0	8.14	7.68	8.34
Expulsion								
Average pressure	P_{avg}	[bar]	21.4	21.09	19.88	18.96	21.98	21.98
	σ	[bar]	1.38	1.52	1.89	1.84	1.48	1.65
Final pressure	P_{final}	[bar]	20.29	19.72	18.03	16.93	20.28	20.22
	σ	[bar]	0.116	0.099	0.136	0.100	0.082	0.100
Fall time (90%)	t_{fall}	[s]	20.0	23.31	27.7	30.1	31.6	26.5
Depressurization								
Fall time (90%)	t_{fall}	[s]	7.60	7.72	8.28	6.84	6.68	6.68
Fall time (2bar)	t_{fall}	[s]	7.70	7.62	7.50	5.80	6.78	6.72

After the pressurization the expulsion starts at t = 60 s. Again the pressure of test rad2 is lacking behind compared to that of test rad1, and that of rad3 is lacking behind further still. Also the pressure drop observed in test ax1 is significantly larger than for the other tests. This all is likely again due to the lower pressure in the gas cylinder for each consecutive test. Also the final pressures achieved during each consecutive test are lower, again due to the lower pressure in the cylinder.

At t = 110 s the pressurization valve and main valve are closed, and the tank is depressurized via the bleed valve. For each test this proceeds in roughly the same way and with the same speed. The fall time to 90% seems to show that test rad3 is actually quite a bit slower, but this is an artifact from the calculation, as the lower final pressure of rad3 means its pressure needs to fall further to get to the 90% level. If instead the fall times towards 2 bar are compared, then these can be see to be virtually equal. This is to be expected, as for depressurization all tests are exactly the same, with virtually the same starting conditions and exactly the same feed system geometry. The fall times for the axial tests are slightly shorter than for the radial tests. This can be due to a slightly different pressure setting for the pneumatic actuation lines. Likely the pressure was set slightly higher during the axial tests, meaning the pneumatic gas could close PV and open BV faster.

During each test two pressure measurements were done: PS1 at the tank and PS2 on the pressurization line. The intention of this placement was to see if there would be any significant pressure drop over the pressurant injector. The answer is that there is none at all. The standard deviation between the values of PS1 and PS2 (after a moving average filter of 51 samples (= 1.02 s)) is below 0.02 bar for all tests. All of these are virtually equal to the uncertainty of the pressure sensors, and are certainly not significant values. The only noteworthy difference between the two sensors is an initial spike in the PS2 measurement at the start of pressurization which is not observed in the PS1 measurement, as visible for all radial tests in figure 7.9. That this spike is present is not very surprising or noteworthy in
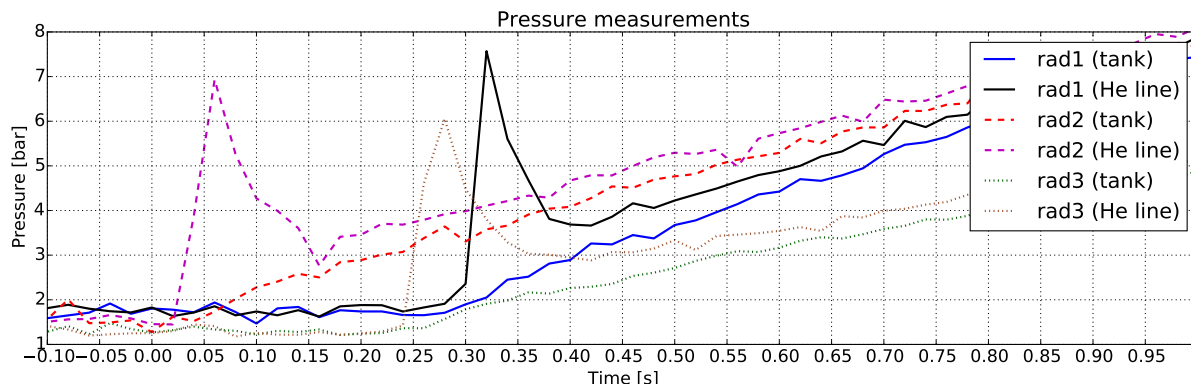
Figure 7.9: A close-up of the pressure measurements during the radial tests showing both pressure sensors. This close-up is around t = 0 s, i.e. start of pressurization. The initial pressure spike observable in the helium line pressure sensors is the only significant difference between the measurements of PS1 and PS2.

itself, the interesting thing is the timing of the spikes. The spike for rad1 occurs at t = 0.32 s, for rad2 at 0.06 s and for rad3 at 0.28 s. The accuracy in the timing parameter is 0.02 s (as the sensor is sampled at 50 Hz). The difference in timing for the spikes is quite large, even though the system that generates the spike is quite simple (one valve with one hose attached). The cause for the difference must be found in inconsistency in the opening and closing times and speed of the valve and/or the timing of the actuation of the cRIO. This is something that must be investigated if DARE every wants to use similar valves for actuation of liquid rocket engines. Exact timing of the valves is of major importance during the ignition phase of such engines and 0.26 s of variance between valve openings is very significant.

Thermocouple data
TC0 (Pressurization line thermocouple)
The helium line thermocouple (TC0) is placed in the helium feed line, about 20 cm before the entrance to the pressurant injector, and next to the PS2 branch in the line. The thermocouple is positioned in the middle of the tube and is thus fully exposed to the helium flow. The plots of the temperature measured are shown in figure 7.10 for the radial tests, and in figure 7.11 for the axial tests. The main conclusion that can be drawn from these graphs is that the helium inlet temperature can be considered constant during the tests. The variation is, with the exception of a very short minimum at the start of pressurization, always within ±2°C of an average value. Both the axial and radial tests follow the same pattern. The only difference is that for the axial tests the temperature is about 1°C lower than the day before. The graphs do however show a number of interesting phenomena that are important to understand the processes in the helium cylinder and in the feed lines.

The different phases visible in figure 7.10 can be reasoned if one main assumption is made: The expansion process in the helium cylinder is virtually isothermal. This is a reasonable assumption, as the maximum amount of helium in a cylinder of 50 L at 200 bar is around 1.62 kg. A gas cylinder however weights in around 70 kg, and although the heat capacity of helium per kilogram is about ten times as high as that of steel, the thermal mass of the tank is thus still more than 4 times bigger. When expansion takes place from a full bottle, the gas will cool down relatively little (around 25°C for 200 bar to 160 bar over the course of a 110 s test) and can remain at relatively constant temperature due to the thermal mass of the bottle. When expansion takes place from a nearly empty bottle, the gas will indeed cool down more (around 50°C from 100 bar to 60 bar) but the amount of gas in the bottle is of course also lower, again lowering the thermal mass of the gas with respect to that of the bottle.

The different phases indicated in figures 7.10 and 7.11 can be explained as follows:

A The thermocouple is at the environmental temperature.

B PV opens. The helium that was in the line between PV and the CGR rapidly expands and cools down. It is pushed at high speed past the thermocouple and cools it down rapidly. The temperature recovers just as quickly because "fresh" helium from the bottle flows past. The temperature shoots on to higher levels then before because the large amount of helium moving past is heated due to the Joule-Thompson effect. Helium that is expanded through an orifice will actually heat
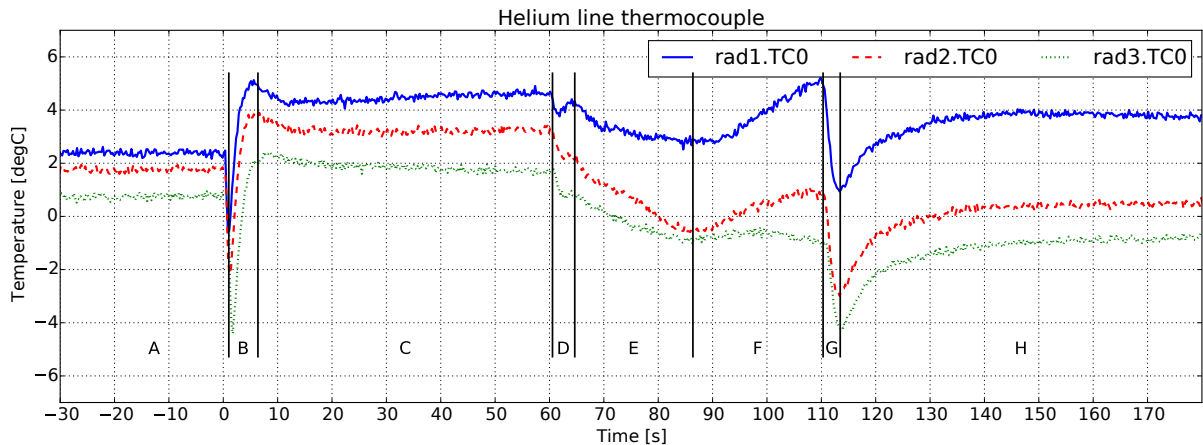
Figure 7.10: Plot of the pressurization line thermocouple during the three radial injection tests. The different phases identifiable in the graph are labelled. These phases are explained in the text.
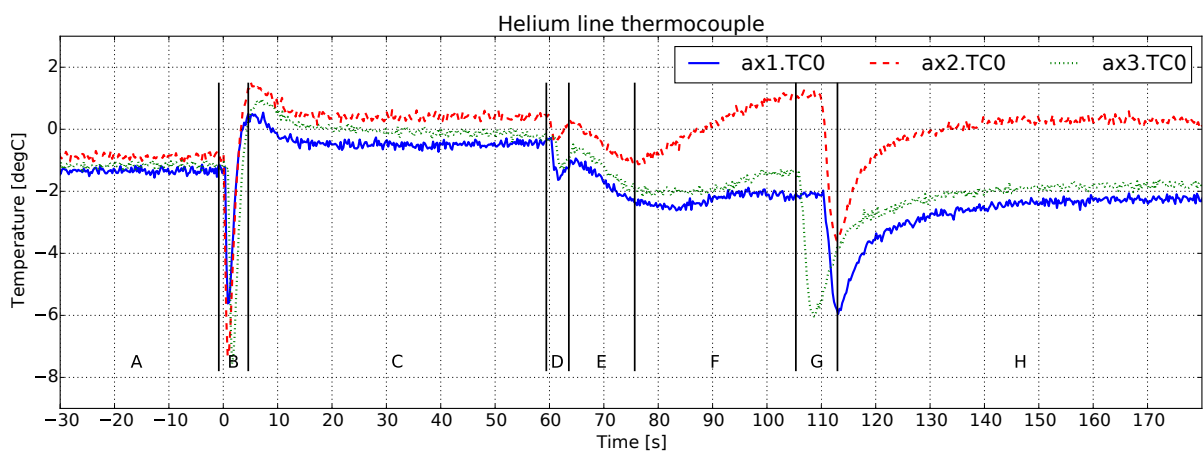
Figure 7.11: Plot of the pressurization line thermocouple during the three axial injection tests. The different phases visible in the graph are equal to those elaborated in section 7.1.4.

up at around 0.065 K/bar [4]. The effect is stronger when the pressure difference is greater, thus the heating is the largest at tests rad1 and ax2, as there new cylinders are used.

C Temperature remains relatively constant as there is hardly any helium flow coming past. The helium that does flow is either slightly warmer due to the Joule-Thompson effect (test rad1) or is slightly cooler due to heat lost via the hoses.

D The expulsion starts and a similar process as at B occures: The gas in the hoses expands due to the pressure drop and cools down the thermocouple. However temperature soon recovers as new gas flows in from the cylinder.

E The gas flowing through the hoses is cooled down because the hoses are at lower temperatures, and because flow speed of the gas is low enough so that the heat transfer has time to take place (as opposed to the high speed flow in phase B). The low minima for tests rad2 and rad3 are likely due to the cooling of the test bench structure, the hoses and PV during the LN2 expulsion that occurred at test rad1. The minimum in test rad1 does not drop below the environmental temperature.

F About halfway through the expulsion, the temperature in all tests either starts to increase again, or levels off at a constant value. This is likely because over the course of phase E, the gas has been heating the insides of the tube and by now the gas arriving at TC0 is still heated because of the Joule-Thompson effect. The heating is therefore also stronger at test rad1.

G Depressurization starts. The gas in the hoses quickly expands and drops in temperature.

H The pressure in the hoses is back to atmospheric and the thermocouple slowly starts returning to environmental temperatures.

TC1-TC10 (Thermocouples in the tank)
Figure 7.12 displays the plots of thermocouples TC1 through TC5, which are the thermocouples placed along the rod at 30 mm from the tank centreline. Figure 7.16 shows these plots for the thermocouples TC6 through TC10, which are placed in the tank at 90 mm from the tank centreline (and thus 25 mm from the tank wall). Figures 7.14 and 7.15 give the same data for the axial tests. Below here follows a largely qualitative description of the thermocouple data, a more detailed quantitative analysis is given in section 7.3 when the data of the radial and axial injection tests are compared in detail.

Before the start of pressurization, the thermocouples near the wall seem to show a larger spread in temperatures then those at the tank centre. The thermocouples near the wall show a vertical temperature gradient in the order of $8°C\,m^{-1}$, while those at the centre show only $\sim2°C\,m^{-1}$. The difference is however quite small and these gradients are only a very rough estimate. The uncertainty in the thermocouples is too high to make definitive statements on the temperature gradient here. Specifically the absolute value of TC6 is likely 2 degrees too high (see section 5.8.2).

At t = 0 s the pressurization starts, which can be directly observed in the temperature readings from the top most thermocouples (TC1 and TC6). For test rad1 and ax1 the temperatures of these thermocouples rise a few degrees but stay relatively low. For tests rad2, rad3, ax2 and ax3 the values however shoot upwards. This can be explained by the fill level at the start of pressurization (table 7.1). At tests rad1 and ax1 the fill levels are at 639 mm and 632 mm, while TC1 and TC6 are also positioned around this height (640 mm). They are thus likely submerged just below the liquid surface. Their increase in temperature does show that the top layer of LN2 gets heated relatively quickly during pressurization already. For test rad2 the fill level was 624 mm, and thus TC1 and TC6 were just above the fluid surface. At tests rad3, ax2 and ax3 the fill level was only around 600 mm and thus the thermocouples were well out of the fluid and heated by the inflowing helium. After the initial quick rise, the temperatures measured by TC1 and TC6 drop again, indicating that the helium in the ullage volume is cooling down by its contact with the tank wall and the LN2.

The start of expulsion at t = 60 s is noticeable in all graphs for TC1 and TC6 by an increase in temperature. During the radial tests this rise starts slow for the first ~5 s. After that the temperatures start to rise quickly for around 10 s, after which the heating rate seems to slow down again. The thermocouples in each subsequent row below start around 8.5 s later with an increase in temperature, as is expected with the drop in liquid level of around 12 mm/s. Thermocouples TC2 and TC7 also show a decrease in heating rate after around 10 s of steep increase in temperature. This change is less observable in the thermocouples lower in the tank, and also less noticeable near the tank wall, than near the tank centre. For the axial tests the rise in temperature starts more abrupt. Also the temperatures rise more steadily till they achieve a maximum value that is virtually the same for all thermocouples. The temperature slope is less steep the lower in the tank the thermocouple is placed. The thermocouples at the centre of the tank experience a steeper increase than those near the wall.

During the radial tests, the bottom four thermocouples, and to a lesser extend the middle thermocouples, all show a 'hump' in temperature when their temperature first starts to rise. Temperature first rises slowly, gets to a maximum, drops slightly, and then starts to rise towards its maximum at the end of expulsion again. The initial slow rise in temperature is likely due to the LN2 fluid surface that is approaching the thermocouple; the fluid surface is of a higher temperature than the bulk liquid. The subsequent slight drop is more difficult to explain. It might be due to evaporation of LN2 from the surface of the thermocouple, cooling it, when the fluid surface drops below it. For the axial tests the temperature 'hump' is only really observable at thermocouple TC10, and to a lesser extend at TC5.

For the radial tests the thermocouples all arrive at a maximum temperature just before the end of expulsion at t = 110 s. The lower in the tank, the lower this maximum is. For the axial tests the maximum temperature is reached quite soon after the thermocouple emerges from the LN2. For test ax1, the temperatures are lagging behind significantly when compared to tests ax2 and ax3, specifically TCs 4, 5, 9 and 10 only see half the temperature increase at maximum. This is likely due to the lower pressure and lower helium mass flow for ax1 due to the lower helium cylinder pressure.

At the end of the expulsion at t = 110 s the tank is depressurized and the helium is vented out of the tank via the bleed valve. This is an adiabatic expansion and thus the gas remaining in the tank cools down significantly. The thermocouples all rapidly cool down and some reach temperatures as low as -216°C. The minimal values are reached approximately 10 s after depressurization. After that temperatures start to increase again. For some of the thermocouples near the bottom this means initially a return to -196°C , the vapour temperature of N_2 at 1 bar. Thermocouples TC5 and TC10
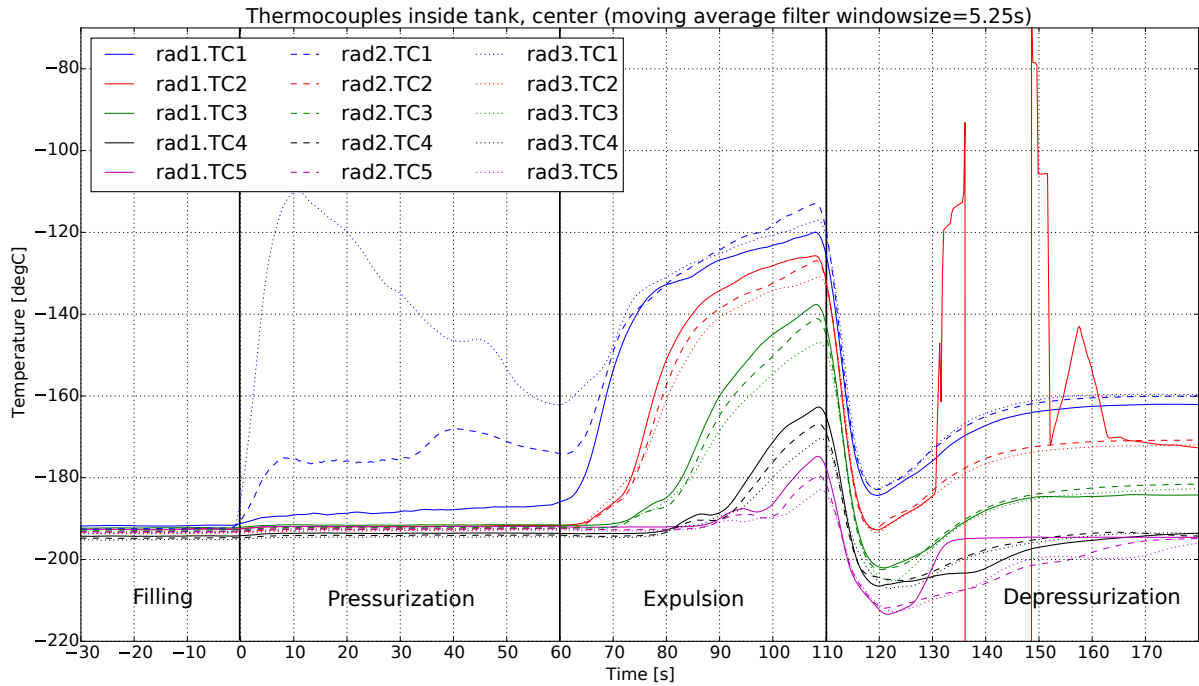
Figure 7.12: Plots of all thermocouples near the centreline of the tank for all three radial injection tests. Same colours indicate the measurement is done with the same thermocouple. Each test has a different line style for the plots. TC2 during test rad1 has various glitches due to faulty electrical connections between t = 130 s and t = 160 s. The distortion on the graph because of these glitches is increased due to the moving average filter.
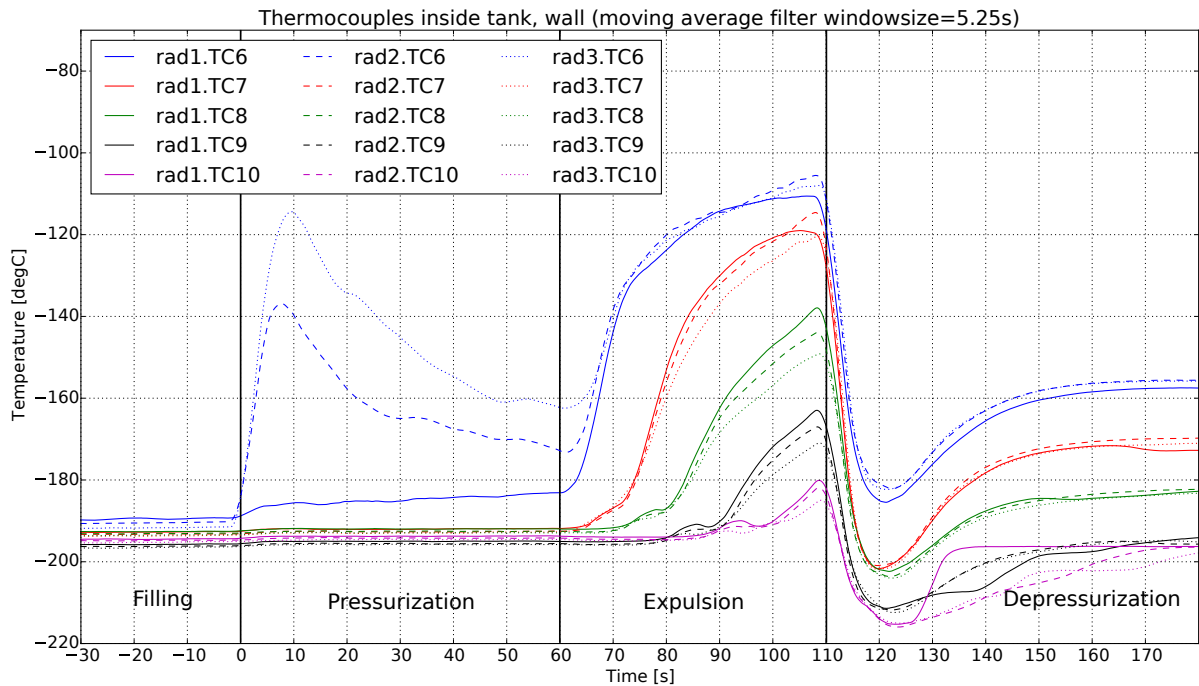
Figure 7.13: Plots of all thermocouples near the tank wall (TC6-TC10) for all three radial injection tests.

during tests rad1, ax1 and ax2 show a very abrupt return to this vapour temperature, likely because evaporated N2 condenses onto the sensor. This hypothesis is strengthened by the fact that this abrupt return is not visible in test ax2; here all the LN2 was expelled from the tank and so no condensation of N_2 could take place after depressurization.

Figure 7.16 shows the thermocouple readings for TC11 through TC15 on the outside tank wall
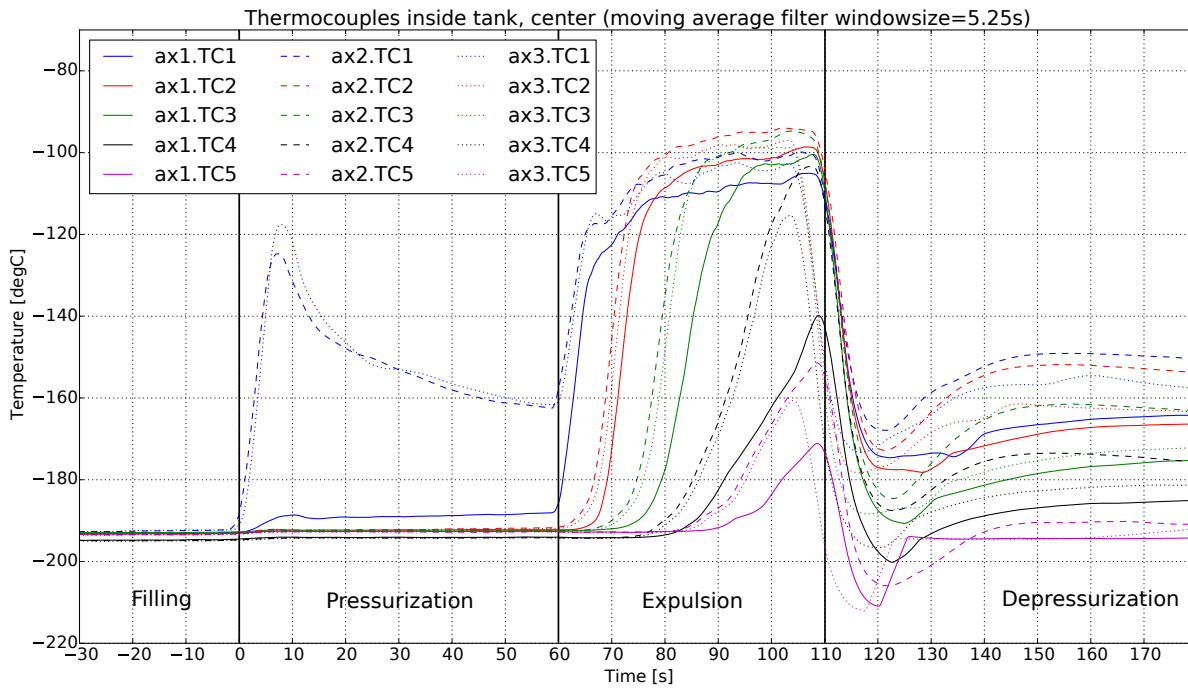
Figure 7.14: The plots for TC1 through TC5 near the centreline of the tank for all three axial injection tests. Same colours indicate the measurement is done with the same thermocouple. Each test has a different line style for the plots.
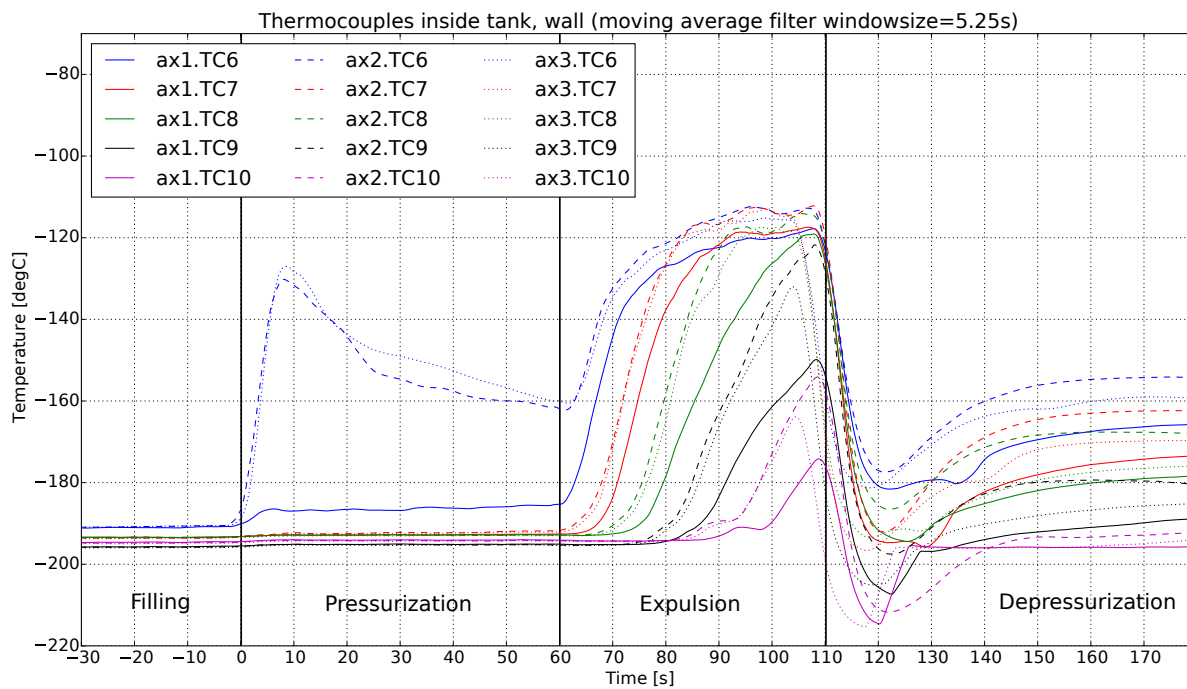
Figure 7.15: Plots of all thermocouples near the tank wall (TC6-TC10) for all three axial injection tests.

for the radial tests. Figure 7.17 shows these for the axial tests. These graphs show relatively little variation, as the thermal mass of the tank wall filters out any rapid changes in temperature. All thermocouples show graphs slowly increasing in temperature, due to heat from the incoming gas raising the temperature of the tank wall. For the top most thermocouple (TC11) temperature already slowly rises during pressurization, when the ullage volume is heated by the incoming gas. The thermocouple directly below (TC12) show this behaviour to a lesser extend. Here heat is conducted towards TC12 from the top down via the aluminium wall. During expulsion temperatures start to rise as soon as the
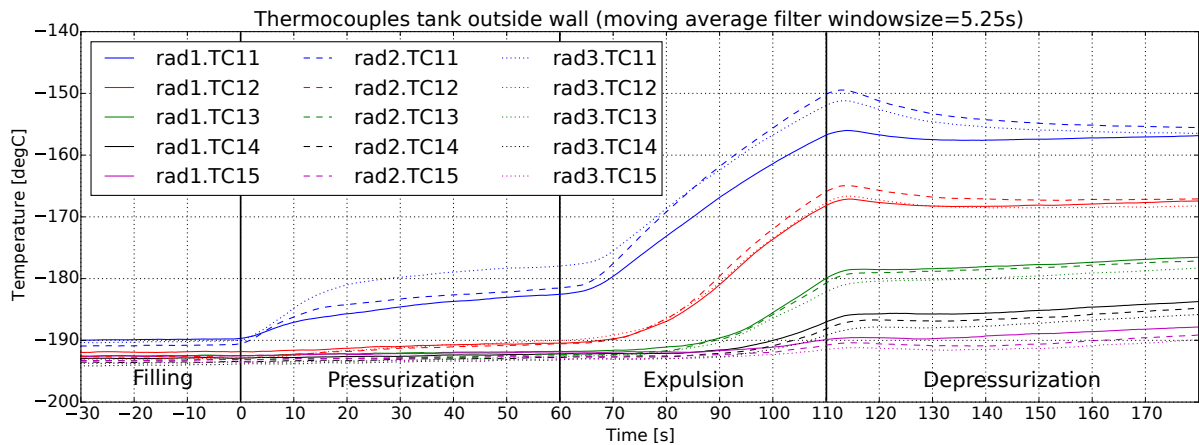
Figure 7.16: Plots of the thermocouple readings on the outside tank wall (TC11-TC15) for all radial injection tests.
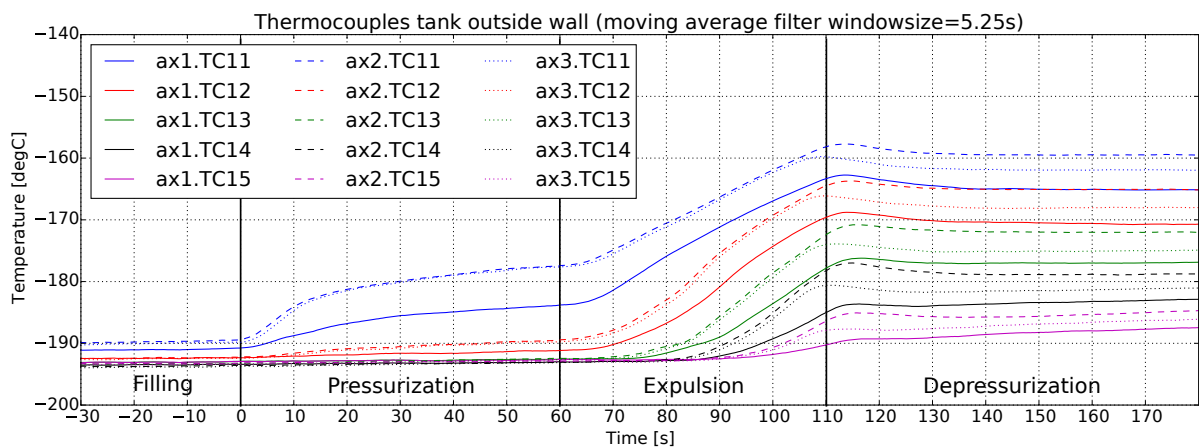
Figure 7.17: Plots of the thermocouple readings on the outside tank wall (TC11-TC15) for all axial injection tests.

liquid level drops below the height at which the thermocouple is placed. In general the thermocouples show a larger vertical temperature gradient building up in the wall during the radial tests than during the axial tests. In tests rad2 and rad3 the value of TC11 rises to -160°C , while during tests ax2 and ax3 it does not get much further than -150°C . For the bottom thermocouple (TC15) the reverse is true, it barely rises 3°C during the radial tests, but does rise 5 to 10 degrees during the axial tests. As with the thermocouples inside the tank, test ax1 shows significantly lower values for temperature than the other two axial tests. Likely again due to the lower pressures.

For tests ax2 and ax3 the similarity between all the thermocouple readings of the two tests is very noticeable. The temperature curves for ax2 and ax3 overlap with only very small differences. Between the timespan t = -10 s till t = 100 s the standard deviation between the measurements of the tests is always below 1.1K. For half of the thermocouples inside the tank the deviation is even below 0.7K (TCs 1, 3, 5, 6 and 7) and all thermocouples on the outside tank wall have standard deviations between the two tests of less than 0.21K. The equivalence however stops after t = 105s, because then the depressurization of ax3 starts, while expulsion continues for 5 more seconds at ax2. Test ax3 is, except for the early cut-off, a perfect reproduction of test ax2.

Helium cylinder pressure readings
The amount of helium used during the testing is the main value that is to be recovered from the testing. This value can be determined by measuring the tank pressure and temperature before and after a test. A direct measurement of the helium mass via a load cell was also attempted, but, as explained before, it was unfortunately not possible to do this measurement accurately enough, mostly due to the small amount of helium mass change compared to the total mass of the helium gas cylinder.

Measurements of the gas bottle pressure were done directly before and directly after each pressur-

ization test. The measurements were done visually from the pressure dial on the CGR. They were read by two persons separately, to double check the read-out for each measurement. The pressure dial has markings spaced at 10 bar intervals, covering a total span of 300 bar. The pressure dial itself has an accuracy class of 2.5 as defined according to standard EN837, which means it is accurate to within $\pm 2.5\%$ of the span, which is in this case equal to 7.5 bar. For this calculation it is however assumed that this offset is constant and that it is equal before and after the test. Therefore this inaccuracy in the absolute value of the measurement is ignored. From experience during the tests is it estimated that the dial can be read out with an accuracy of $\sigma_P = 2.5$ bar. This is taken to be the inaccuracy for the pressure measurement.

Measurement of the gas bottle temperature is done indirectly by means of the atmospheric temperature measurements. These temperatures are taken from thermocouple TC0, as the average before the start of the test at the interval t = -80 s till t = -5 s. The inaccuracies on the the temperature measurement are considered to be large, but are expected to be within $\sigma_T = 5$ K. The temperature is assumed to be equal during the measurements at the start and end of the test. This is reasonable because of the isothermal assumption made for the helium tank (see the discussion of the data of TC0 on page 107) and because the pressure measurement at the end of the test was done more than 40 minutes after each test. Environmental temperature changes within this time frame are not considered to be of influence. Changes in temperature measured by TC0 over the course of 40 minutes before each test are always within a total range of 1.2 K.

Tests rad1, rad2, rad3 and ax1 were done with the same helium cylinder. This cylinder was marked as has having an internal volume of 50.9 L. The second helium cylinder, used for tests ax2 and ax3, has an internal volume of 50.7 L. Inaccuracies on the internal volume are not specified, but are expected to be less than ~0.05 L, due to the accuracy of the volume as stated on the bottle. As total mass of pressurant used is calculated as the difference of mass before and after the test, any inaccuracy in volume will be the same before and after the test, and is thus of little influence. The inaccuracy in the volume is considered to be insignificant w.r.t. the inaccuracies in pressure and temperature.

The measurements of the helium cylinder pressures before and after each test, the temperature from TC0 for each test, the calculated pressurant mass used, the corresponding uncertainty for the pressurant mass, and the collapse factor are shown in table 7.4. The pressurant mass is calculated by making use of equation 7.1, where subscript 0 indicates the value before each test, and subscript e the value at the end of each test. The density was calculated using the CoolProp library for Python. The inaccuracy was calculated using equation 7.2 [38]. The partial derivatives for this equation were calculated using the CoolProp library, using $T = T_0$ for each calculation. The values $\sigma_P = 2.5$ bar and $\sigma_T = 5$ K were used, as discussed above. The pressure reading for the final pressure of test ax3 was done the Wednesday morning after the test day. The temperature for this measurement is estimated at -5°C (268 K) due to the colder temperatures during the night and subsequent morning.

$$m_{pres} = V_{cyl} \left[\rho \left(P_0, T_0 \right) - \rho \left(P_e, T_0 \right) \right] \tag{7.1}$$

$$\sigma_m = \sqrt{\left(\left. \frac{\partial \rho}{\partial P} \right|_{P=P_0}^2 + \left. \frac{\partial \rho}{\partial P} \right|_{P=P_e}^2 \right) \sigma_P^2 + \left(\left. \frac{\partial \rho}{\partial T} \right|_{P=P_0}^2 + \left. \frac{\partial \rho}{\partial T} \right|_{P=P_e}^2 \right) \sigma_T^2} \tag{7.2}$$

The collapse factor has been calculated by equation 7.3. In this equation m_{pres} is the pressurant mass as determined by equation 7.1. $P_{u,avg}$ is the average ullage pressure in the tank during expulsion, as listed in table 7.3. V_{prop} is the volume of the amount of pressurant that is expelled from the tank, as obtained from the data as shown in table 7.1. T_0 and P_0 are the pressurant temperature and start pressure, as given in table 7.4. γ is the ratio of specific heats for helium at the average pressure and T_0 for helium, as determined by CoolProp (≈ 1.65). P_{pres} is the pressurant end pressure, that has been determined from the isentropic flow relations that related pressure to density, as shown in equation 7.4. In that equation, m_0 is the start mass of pressurant gas in the tank. The inaccuracies on the collapse factor in percent are exactly the same as those for the pressurant mass. For more details on the analytical relations, please consult appendix B.

$$K = \frac{m_{pres}}{m_{ideal}} = \frac{m_{pres}}{\frac{P_{u,avg} V_{prop}}{R T_0} \left(\frac{\gamma}{1 - P_{pres}/P_0} \right)} \tag{7.3}$$

$$P_{pres} = P_0 * \left(\frac{\rho_e}{\rho_0}\right)^{\gamma} = P_0 * \left(\frac{m_0 - m_{pres}}{m_0}\right)^{\gamma} \tag{7.4}$$

Table 7.4: The measured pressurant cylinder pressures and temperatures, from which the pressurant masses are calculated. Calculation of the pressurant mass was done via equation 7.1, calculation of the pressurant mass uncertainty via equation 7.2[38]. Calculation of the tank collapse factor has been done via equation 7.3.

Test	P_0 [bar]	P_e [bar]	T_0 [K]	m_{pres} [g]	σ_m [g]	σ_m/m_{pres} [%]	K [-]
rad1	185	148	275.5	280	41.7	14.9	2.65
rad2	148	112	274.9	282	38.1	13.5	2.72
rad3	112	80	273.9	260	35.1	13.5	2.73
ax1	80	52	271.8	236	33.2	14.1	2.37
ax2	178	148	272.3	229	41.9	18.3	2.24
ax3	140	109	272.0	233	38.3	16.5	2.23

7.1.5. Evaluation of test goals
The test series for radial and axial injection are concluded by looking back at the test goals, and seeing if these have been met or not.

Evaluation of the test goals
The test goals were described in section 4.1.3. The test goals are discussed here to see if they were met or not.

1. *Perform the full testing sequence:* **Met.**
   The tank was successfully filled, pressurized and emptied during each test.

   (a) *Cool the tank down to LN2 temperatures:* **Met.**
   The tank was successfully cooled down to LN2 temperatures on each test day.

   (b) *Fill the tank with liquid nitrogen to ~85% fill level:* **Met.**
   The tank was filled, but only to fill levels between 80% and 87%.

   (c) *Pressurize the tank with helium to 30 bar for 60 s:* **Met.**
   Tank pressures were just under 30 bar.

   (d) *Empty the liquid nitrogen out of the tank under pressure in ~50 s:* **Met (with sidenote).**
   Test ax2 was fully empty just before the 50 s mark. Because of this, test ax3 was cut short at 45 s.

2. *Collect validation data:* **Met.**
   A large dataset was collected for 3 radial injection tests.

   (a) *Collect data of all 15 tank thermocouples to monitor thermodynamic processes in the tank:* **Met.**
   All tank thermocouples showed clear data and provide good insight into the processes on-going.

   (b) *Collect temperature data of the inflowing helium:* **Met.**
   The temperature of the inflowing helium is virtually constant.

   (c) *Determine tank pressure over time:* **Met.**
   Tank pressure versus time was successfully measured.

   (d) *Determine pressure drop over the pressurant injector:* **Met.**
   Pressure drop over these versions of a radial and axial injector are insignificant.

   (e) *Determine tank fill level by means of the load cell:* **Met.**
   Estimations of tank fill level could be made with the load cell data.

   (f) *Determine mass flow by means of the load cell:* **Met.**
   Load cell data was very clear and indicated a mass flow consisted over the tests.

(g) *Collect data on liquid fill level by means of the capacitive liquid level:* **Partially met.**
During the radial tests the capacitive sensor did not give any useful result as the measurement range of the FDC1004 was not configured correctly. During the axial tests it was shown that it is possible to accurately measure fill level. Improvements can however still be made.

(h) *Determine pressurant gas mass using for pressurization and expulsion:* **Met (with sidenote).**
The pressurant gas mass could be determined based on the pressurant gas bottle pressure before and after, but the accuracy with which it could be determined was unfortunately not very high. The determination of gas mass by means of the pressurant load cell did not give any useful data.

Based on the evaluation of the test goals, it can be concluded that the radial and axial test series were in general successful.

7.2. Vortex tube injection tests

The third and final test day for validation tests was conducted one month after the axial injection tests. On Tuesday the 21st of February one pressurization and expulsion test was conducted with a vortex tube injection system. Next to this, the test day was used to perform an injector cold-flow test for the DARE cryogenics propulsion team. The vortex tube test, referred to as "vtx", was unfortunately not as successful as the first two test series. A sliver of aluminium cuttings blocked part of the exhaust orifice, which meant the mass flow was only one fourth of what was desired. The test, plus some parts of the cold-flow injection test, will be discussed in this section as there are still important lessons to be learned from it.

The structure followed is equal to that of the previous section. The test day itself is described in 7.2.1, and the test data is discussed in section 7.2.2. Finally the test goals are evaluated, and conclusions are drawn in section 7.2.3.

7.2.1. Test description

The vortex tube injection test was carried out on Tuesday the 21 of February 2017. The test was planned together with the cold-flow injection test of the DARE cryogenic propulsion team. The DARE team tested a pintle type injector designed for LOx - ethanol, using LN2 and water as the substitutes for the propellants.

For the vortex tube test, thermocouples TC14 and TC15 were removed from their original location at the lower portion of the tank wall, and were repositioned on top of the tank bulkhead. This was done because analysis of the data from the first two test series suggested that heat transfer to the tank top bulkhead may have been quite significant. TC14 was placed at 30 mm from the inner tank wall edge. TC15 was placed 25 mm from the tank centreline, in the edge between the bulkhead's central rise and its main surface.

Auxiliary material and tools were brought to the test location the day before. The test bench itself was brought to the field in the morning. The preparations started at 9:00. The weather was relatively sunny, with a small amount of cloud cover. The outside temperature was around 9 to 10°C in the morning, but rose to 14-15°C in the afternoon. There was a small amount of wind.

Michel van den Brink was again the supervisor from the university. Felix Lindemann was operational safety officer in the morning, and Angelos Karagiannis in the afternoon. During the whole day Daniel Schwerig, Simon van Overeem, Rolf Wubben, Juan Mussini, Rano Veder and Rob Hermsen were present to conduct the test.

The test procedures were started at 9:45. Procedures went very smoothly and cool-down of the tank started at 10:30. The cool-down took significantly longer than during the other two test series, presumably due to the warmer weather conditions (nearly 20 K higher temperature). Cool-down and filling was completed at 12:30.

The vortex injection test was conducted around 12:50. During the 60 s pressurization it was already noticed that there appeared to be leakage near the top bulkhead as there was significantly more vapour formation above and below the tank than during the radial or axial injection tests. Otherwise pressurization proceeded normally and expulsion was started at t = 0 s. During the expulsion it was already clear that something was not going as planned as the vapour cloud forming at the exhaust was

significantly smaller than during previous tests. Also the noise level was very much lower. Subsequent data analysis showed that the mass flow out of the tank was about one fourth of what was expected. The tank was de-pressurized and the remaining LN2 was allowed to flow out of the tank by gravity.

After the tank had emptied, the exhaust orifice was removed so that the pintle injector could be placed for the subsequent tests. The orifice was placed in a bucket of water to allow it to warm up. After that it was taped shut on both sides, trapping any particles in it.

The cold-flow injector tests were conducted in the afternoon. The tank was filled with approximately 17 kg of liquid nitrogen. The water for the injector was supplied from a garden hose. The tank was pressurized to 28 bar tank pressure and the liquid nitrogen was ejected in a total of 6 bursts. The first 5 consisted of bursts each 3 s long, the last burst was until the tank was empty. The tank was re-pressurized for 2 s before each expulsion. The data from this test will be shortly described in the next section, as it is useful for showing the pressure drop of the vortex tube in injection, and for calibrating the capacitance sensor.

Orifice clogging

The day after the test, the orifice was examined in the lab. Within it a number of small aluminium slivers were found that presumably were responsible for blocking the orifice during the test. The slivers that were recovered are shown in picture 7.18. Possible more slivers were present, but these could have been lost on the field during the detaching of the orifice or its heating in water. The biggest sliver has been placed on top of the orifice hole in figure 7.19, clearly showing the size of the sliver and its effect on the available flow area.

Figure 7.18: The exhaust orifice and the slivers of aluminium that were recovered from it.

Figure 7.19: The largest sliver of aluminium placed on top of the orifice.

Regrettably, the slivers in the tank likely originated from the thread in the hole in the top bulkhead that accommodated the capacitive sensor. During replacement of capacitive sensor version 1 after the axial injection tests, it was noted that the thread on the sensor adapter was damaged severely. The thread in the top bulkhead was also slightly damaged. Likely this was due to a cross-threading on the morning of the axial injection test, when the sensors were also swapped out. To make sure the sensor version 2 could be placed back in the tank for the vortex test, it was decided to use a thread cutter to renew the thread in the bulkhead again. The aluminium slivers must have come from either loosening the capacitive sensor version 1, or rethreading the hole for placing sensor version 2.

7.2.2. Test results and data analysis

The test data for the vortex tube test is presented in this section via a number of graphs, just as was done with the axial and radial tests. Unfortunately the description here will be more qualitative instead of quantitative, as the test was not conducted anywhere near the desired operating point. However, valuable lessons can still be drawn from it.

In this section first some of the results from the water injector tests will be discussed. These are not strictly part of this thesis, but are however very useful in analysing the behaviour of the vortex tube

injection, and for calibrating the capacitive sensor.[1] After this the results from the vortex tube test itself will be discussed.

Cold-flow test test data

The cold-flow injector tests were conducted at the end of the day, however it is more convenient to discuss them first because the pressure measurements during the test, as well as the capacitive liquid level measurements are useful in the further analysis.
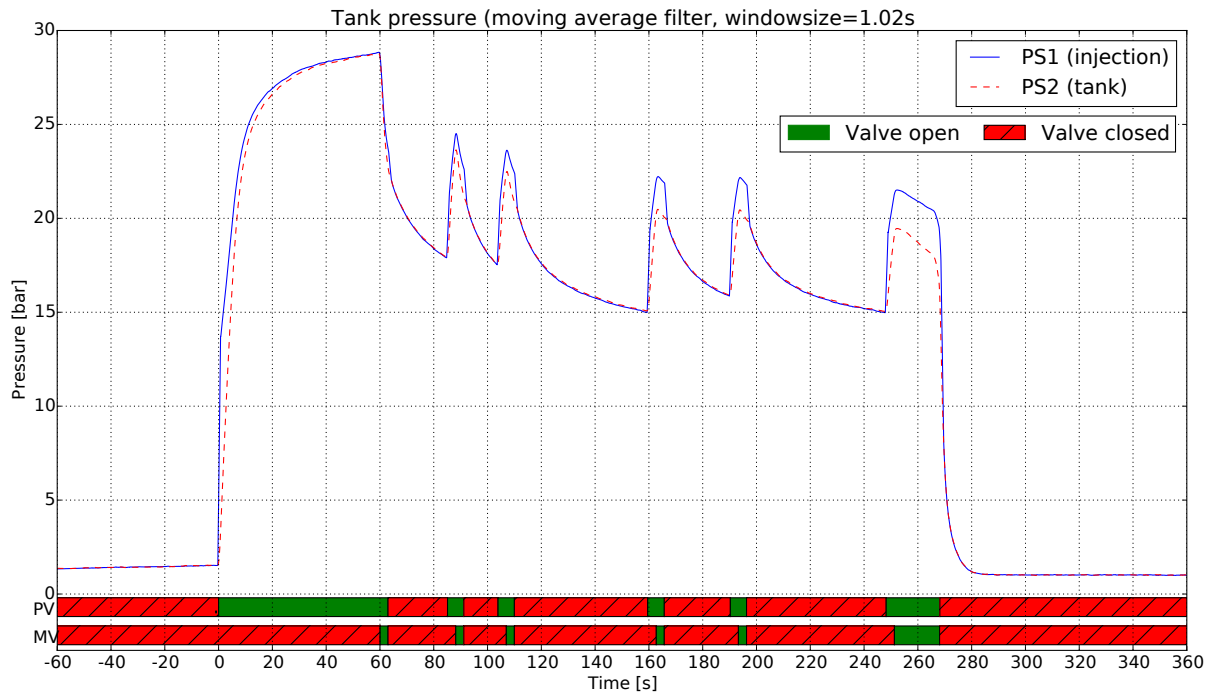
Figure 7.20: Pressure sensor data from the cold-flow injection test. Visible are the six expulsion tests conducted. The first five were 3 s each. The last lasted approximately 15 s. In contrast to the radial and axial pressurant diffusers on their own, here a pressure drop is clearly visible.

Figure 7.20 shows the pressure versus time for the injector tests. The test started with 60 s of pressurization, directly followed by 3 s of expulsion. After that follow four more 3 s bursts, each proceeded by 2 s of pressurization. The final burst was to empty the tank fully and was terminated manually. In between pressurizations the pressure can be seen to drop due to cooling of the helium in the ullage volume. The most important observation from this series of tests is that with the vortex tube in place there is actually a significant pressure drop over the pressurant injection system. In contrast to the direct radial and axial injection, where this was not the case. At the start of each pressurization, the pressure just before the vortex tube (PS1) can be seen to shoot upwards, within 20 ms, i.e. one sample. After that the tank pressure follows. During expulsion the pressure drop over the tube was between 1 and 3 bar. Mass flow of LN2 during these tests was higher then during the other tests, on average around 530 g/s. Fill level at the start was also lower, with around 17.5 kg of LN2 in the tank.

Figure 7.21 shows the tank mass plotted versus the output of the capacitance sensor (version 2). The sensor output is in general less noisy then that acquired from sensor version 1, it covers a wider range of capacitance (i.e. more sensor output per unit liquid level rise) and in general a more linear behaviour. The linear estimate that has been plotted to match the sensor output shows an output of 2.31 pF kg^{-1}, with a zero offset value of -121.7 kg. This linear fit has, with respect to the sensor output, an RSE value of 0.0308, and an R^2 value of 0.997.

Load cell and capacitance data

Using the capacitance sensor calibration curve acquired at the injector test, it is possible to look back at the first test of the day, and analyse the tank mass and capacitance output during the cool-down and the vortex tube test.

---

[1]The data files for this test are also included in the data package for this thesis.
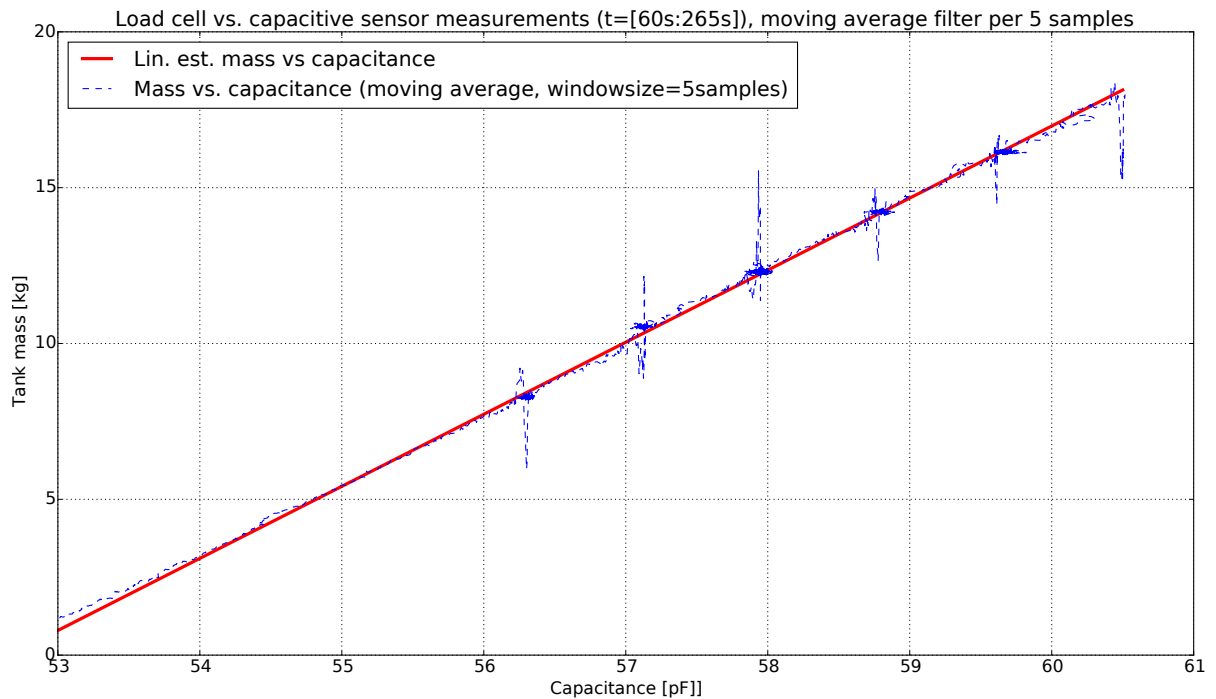
Figure 7.21: The load cell data plotted versus the capacitance sensor output. The data is averaged by a moving average filter of 21 samples wide, which equals about 0.4 s for the load cell data, and 1 s for the capacitive sensor. The straight line is the linear estimate derived from the data using least squares method.
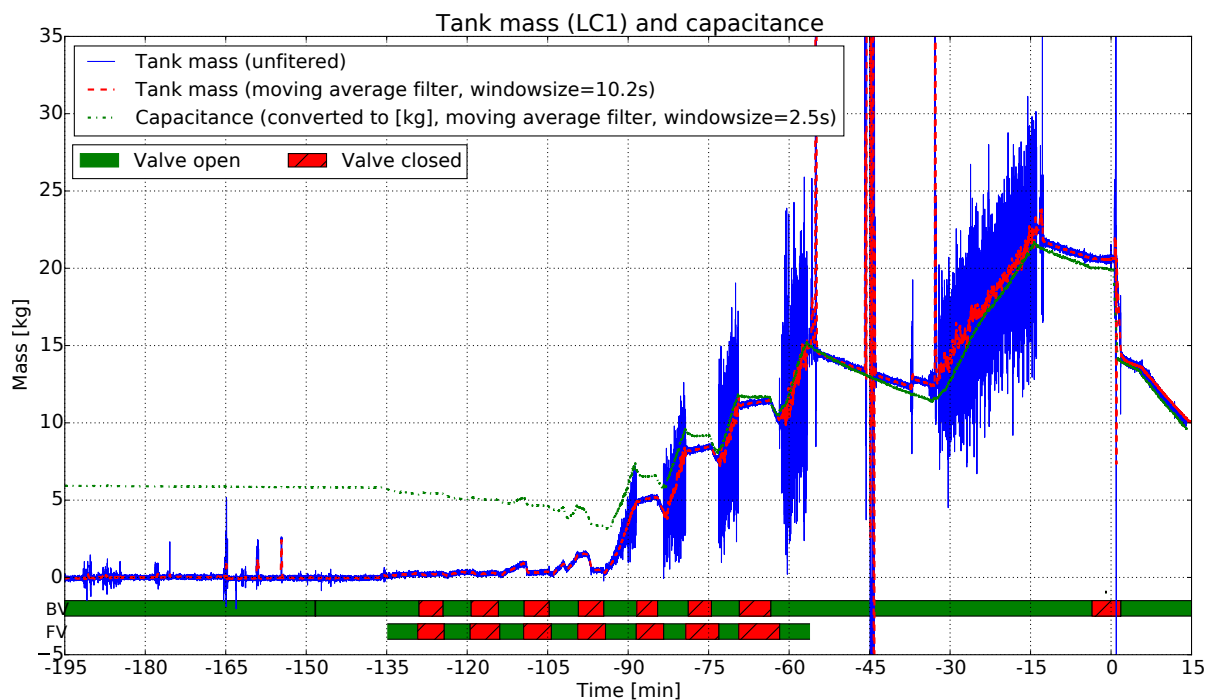
Figure 7.22: The load cell and capacitance data during cool-down, filling and expulsion. The load cell data is shown both with and without moving average filter. The capacitance data clearly shows some form of temperature dependency. The capacitance data has been converted to [kg] using the linear estimated gotten from the data in figure 7.21. The fill valve state bar shows the physical state of the valve, not that of the electrical signal.

Figure 7.22 shows the load cell output (both raw and smoothed) and the capacitance sensor output versus time during the full test duration. This largely covers the preparations and cool-down. The load cell data clearly shows the problem encountered before during load cell measurements: extreme

amounts of noise. In this case the noise is however not caused by a roaring rocket engine, but by the stuttering of the fill valve (section 7.1.3). This stuttering was actually so violent that it induced large amounts of noise during the filling process. This noise is largely taken care of by means of filtering, but the noise level still remains fairly high. Furthermore the tank load cells actually shows various glitches, such as near the -45 min mark.

The capacitance sensor does not show the oscillations caused by the fill valve, as was expected. In this way the capacitive sensor shows its advantage over the load cell measurements. However, the graphs also shows an unexpected and undesired property of the capacitive sensor: It seems to be temperature dependent. The capacitive sensor has been calibrated with the tank mass observed during the injector test (figure 7.21) where the sensor was fully at cryogenic temperatures. In the plotted data of the cool-down and filling it can be seen that the capacitance graph slowly approximates the load cell curve when the liquid level rises, and the full sensor cools down. The dependency is already visible in the section before the first opening of the dewar, from -195 min till approximately -135 min. Within this timespan the inner tank was slowly cooling down from the warm lab temperatures it came from, to the colder outside air temperatures. From this section of the curve a temperature dependency of approximately $0.025\,\mathrm{pF\,K^{-1}}$ can be determined. This would mean a drift of near 5.5 pF over the full temperature drop of more than 200 K, or about 2.4 kg offset when using the linear correlation with mass. However, checking the starting capacitance before cool-down, and the capacitance measured in the empty tank after the injector tests, the difference is only in the order of 2.5 pF. This indicates the temperature drift is also non-linear. What caused the temperature dependency is unknown. Possibly it has to do with the PTFE spacer material used within the sensor (section 5.5.4). The dielectric constant of PTFE is known to be somewhat dependent on temperature[32]. If this is however large enough an influence to fully explain the temperature drift is not known.
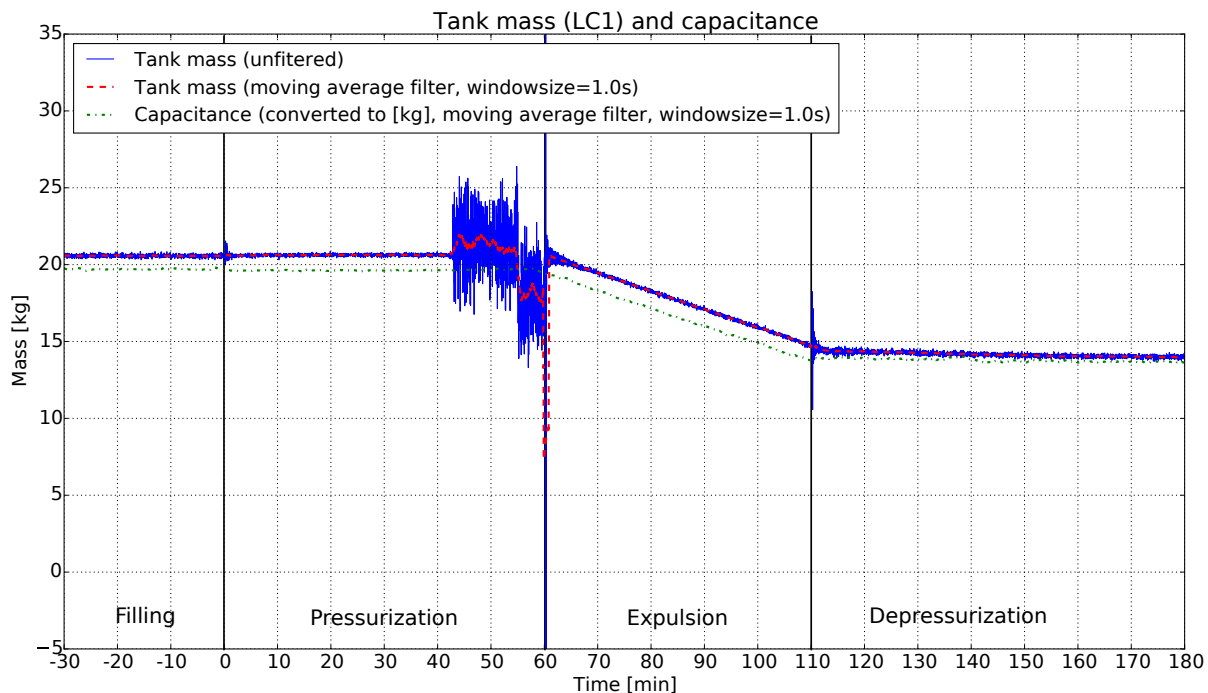
Figure 7.23: The same data as in figure 7.22, but now zoomed in at the pressurization and expulsion time. The mass flow out of the tank is far lower than was desired.

Figure 7.23 shows a close-up of the load cell and capacitive sensor data at the pressurization and expulsion times. The tank starts with 20.58 kg of LN2 ($\sigma = 0.09$ kg; liquid level at 0.62 m; 83.6% fill level). Around t = 43 s the tank mass starts showing strange behaviour. Large amounts of noise suddenly appear making the tank mass go up a kilogram on average, and several kilograms down a few seconds later. The output seems to return to normal conditions at the start of expulsion. Likely this is some form of electronic error. Possibly a loose connection. Observations on the test day itself, nor camera footage, nor any other sensor indicated any abnormalities at this point in time. Also the capacitive sensor, shown in the figure as well, does not show any deviation, indicating the error is with

the load cell or its connection to the cRIO. At t = 60 s the expulsion starts, but, as indicated, with a lower than desired mass-flow. The mass flow is on average 118 g s^{-1} (SEE = 0.0054, R^2 = 0.996). This resulted in 14.7 kg of LN2 left in the tank at the end of expulsion.

Pressure sensor data

The pressure sensor measurements are shown in figure 7.24. As indicated before, the pressure drop over the vortex tube is clearly visible and actually significant. During the expulsion process, the pressure difference is on average 0.46 bar. This is however likely not representative for the vortex tube, as the flow of helium through it was relatively low, due to the low LN2 mass flow. The maximum pressure attained during the pressurization is higher than during the axial and radial tests, because the pressure regulator was set slightly higher. This was done anticipating a higher pressure drop over the vortex tube. During expulsion this resulted in an average pressure of 30.6 bar.
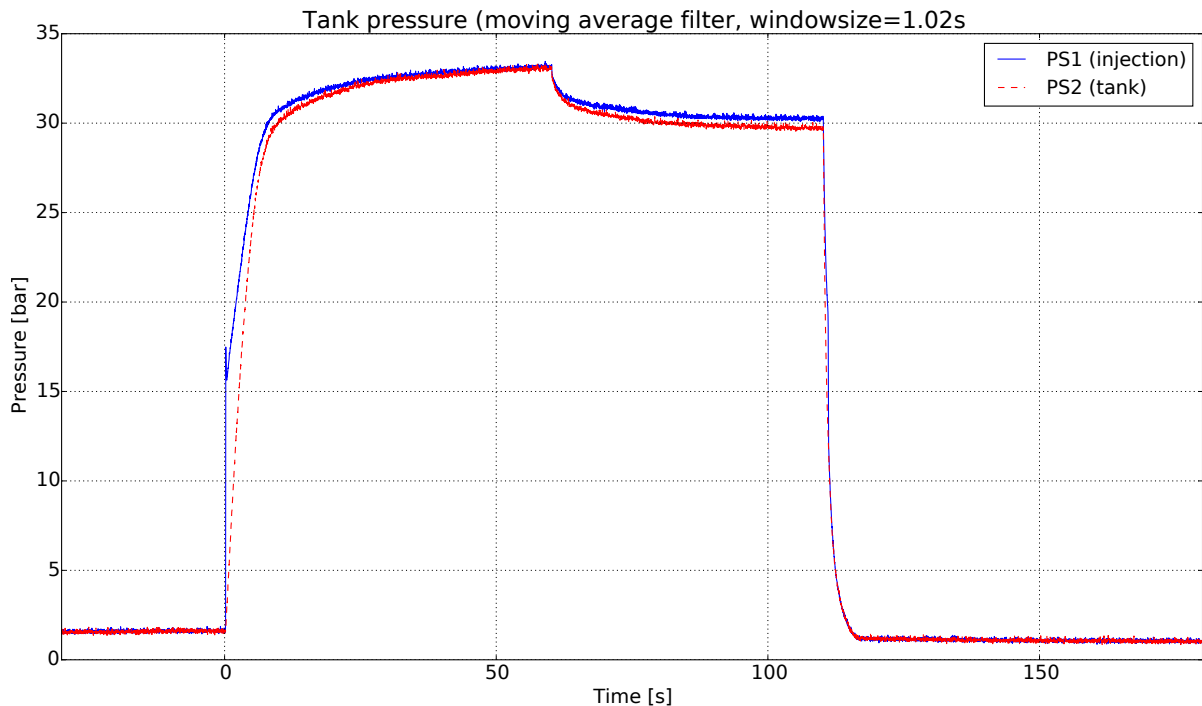
Figure 7.24: The pressure sensor data from the vortex injection tests. Clearly visible is the pressure drop due to the vortex tube. Pressure decay during the expulsion is lower than during the radial and axial tests, mainly due to the lower volume flow of LN2 out of the tank.

Thermocouple data

The thermocouple data has been plotted in two graphs. Figure 7.25 shows the measurements from all thermocouples within the tank. Figure 7.26 shows all thermocouples on the outside. The top thermocouples in the tank (TC1 and TC6) show the expected rise in temperature during initial pressurization, as was also seen during the other tests. When expulsion starts, the temperature of these thermocouples increases again, however with what seems like a small delay. The lower thermocouples follow when they appear out of the liquid level. This happens relatively late, again due to the lower LN2 mass flow. The temperature rise profile of the thermocouples seems most similar to those observed in the radial injection tests (figures 7.12 and 7.13). The temperature rises continuously and reaches a maximum at the start of depressurization. This is in contrast to the axial injection tests, where the temperature quickly seemed to reach some plateau.

Figure 7.26 shows the temperature of the thermocouples placed on the outside of the tank. Thermocouples TC15 and TC14 were relocated to the top bulkhead for this test. This turned out to have been a good decision. The temperature profiles from thermocouples TC11, TC12 and TC13 are relatively standard and comparable to those obtained in the radial and axial injection tests. The data from TC15 and TC14 is however completely new, and shows that the tank top bulkhead actually never fully cools
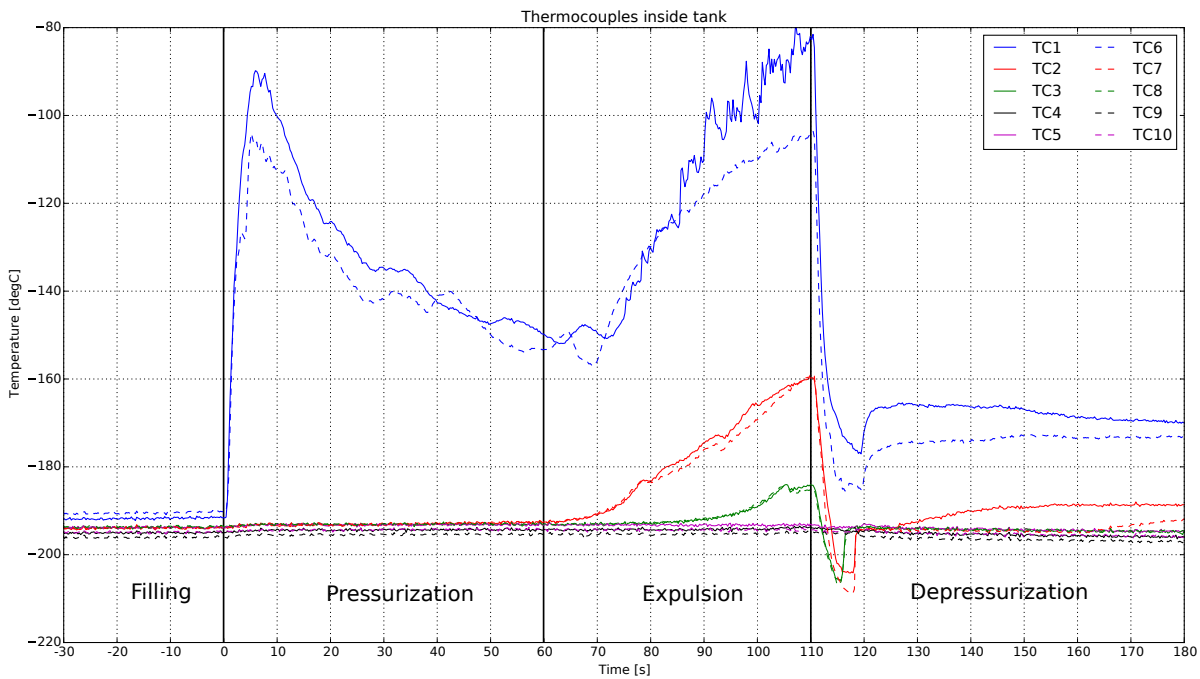
Figure 7.25: The temperature readings of all thermocouples placed within the tank during the vortex tube injection test.

down to LN2 temperatures. Instead it stays about 10 to 15 degrees higher than the bulk of the tank. Also during the pressurization and expulsion the tank bulkhead heats up considerably. Also it indicates that there is also a radial temperature gradient in the top bulkhead itself. TC15, near the centre, is consistently warmer than TC14, near the edge.

Thermocouple TC0 at the helium feed line (before the vortex tube) showed similar patterns as those found during the radial and axial injection tests. Temperature remained fairly constant, with inlet temperatures in general remaining within a 5 K range.
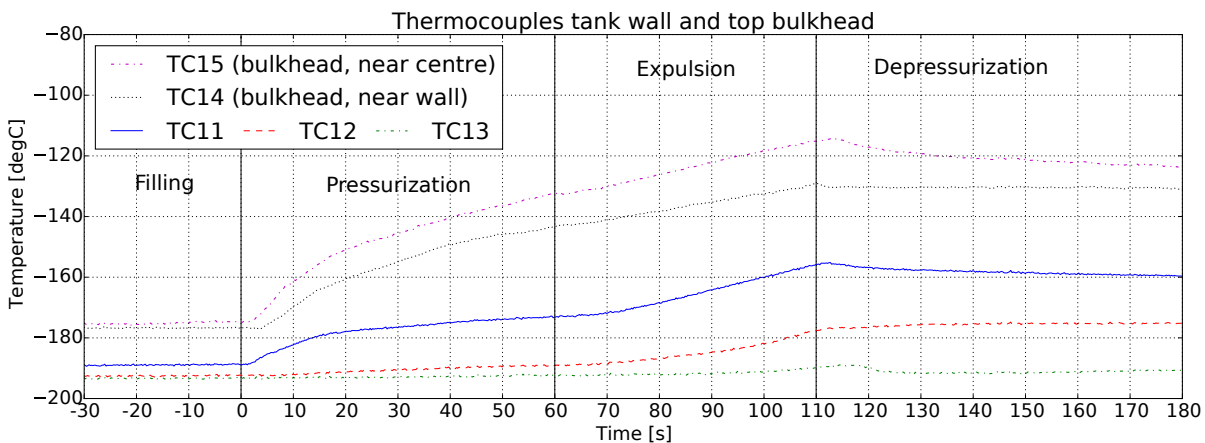
Figure 7.26: The temperature readings of all thermocouples placed on the outside of the tank during the vortex tube injection test. Note that TC14 and TC15 were placed on the top bulkhead for this test. TC15 was placed closest to the tank centre-line.

Helium cylinder pressure readings
Because the vortex tube test had a significantly lower mass flow of LN2, and because it was done at a much higher average pressure, the amount of helium used for this test cannot be directly compared to those for the axial and radial injection tests. The values measured are however given here for completeness sake. The cylinder used during the test has an indicated volume of 50.3 L and was at 198 bar pressure at the start of the test. This dropped to 163 bar at the end of the test. On average its temperature was around 16°C . This leads to an estimated pressurant mass usage of 248 g, with an uncertainty of 40.0 g (16.1%).

7.2.3. Conclusions

As conclusion of the vortex tube injection test, the test goals, as given in section 4.1.3 are evaluated. Also the collected test data is summarized.

Evaluation of the test goals

The test goals were described in section 4.1.3, and were largely similar to those of the radial injection tests.

1. *Perform the full testing sequence:* **Partially met.**
   The tank was successfully cooled-downfilled, pressurized and (partially) emptied under pressure, however the pressure was to high and the mass flow far to low.

   (a) *Cool the tank down to LN2 temperatures:* **Met.**
   The tank was successfully cooled down to LN2 temperatures.

   (b) *Fill the tank with liquid nitrogen to ∼85% fill level:* **Met.**
   The tank was filled to 83.6% fill level.

   (c) *Pressurize the tank with helium to 30 bar for 60 s:* **Not met.**
   Tank pressure was higher than 30 bar due to the LN2 mass flow being far lower than expected.

   (d) *Empty the liquid nitrogen out of the tank under pressure in ∼50 s:* **Not met.**
   Only approximately a quarter of the LN2 was ejected out of the tank during the 50 s expulsion time.

2. *Collect validation data:* **Partially met.**
   A complete dataset was recorded for 1 vortex tube test (plus the cold-flow injector test) however the data from the test is not directly comparable to that from the radial or axial injection tests due to the far lower than expected LN2 mass flow.

   (a) *Collect data of all 15 tank thermocouples to monitor thermodynamic processes in the tank:* **Met.**
   All tank thermocouples showed clear data.

   (b) *Collect temperature data of the inflowing helium:* **Met.**
   The thermocouple data in the helium line showed little temperature variation.

   (c) *Determine tank pressure over time:* **Met.**
   Tank pressure versus time was successfully measured.

   (d) *Determine pressure drop over the pressurant injector:* **Met.**
   It was determined that pressure drop over the vortex tube is significant, certainly more so than just for the radial or axial injection methods.

   (e) *Determine tank fill level by means of the load cell:* **Met (with sidenote).**
   Tank load cell data was collected and a start mass and end mass could be determined from it. However the data was in general very noisy, and showed some weird behaviour that is likely due to faulty electronic connections.

   (f) *Determine mass flow by means of the load cell:* **Met.**
   Mass flow could be clearly determined from the data.

   (g) *Collect data on liquid fill level by means of the capacitive liquid level:* **Partially met.**
   The capacitive sensor showed in general accurate, noise-free behaviour. However the data also showed a temperature dependency within the sensor that needs to be fixed for it to be useful.

   (h) *Determine pressurant gas mass using for pressurization and expulsion:* **Met (with sidenote).**
   The pressurant gas mass could be determined, even though its value cannot be directly compared to the values found for radial and axial injection. As before, the measurement does also not show a fully satisfactory measurement accuracy.

Looking at the evaluated test goals, it needs to be concluded that the vortex tube injection test was not a success, however it might also be going too far to call it a failure. The data gathered still teaches something about the way the system works, and possible it can be used to validate the code. However it does not allow for direct comparison with the radial and axial injection methods due to the different mass flows and pressures, and so it does not allow to strongly conclude if the use of a vortex tube is beneficial or not. The measurements from the capacitive sensor version 2 indeed show the expected improvements with respect to version 1, but unfortunately the data also shows that the current construction of the sensor is temperature dependent.

Data analysis

The data recorded on the vortex tube injection test cannot be directly compared to that of other tests, as the mass flow of LN2 was too low and the pressure in the tank was too high. The most important observations that can be made concerning this type of pressurant injection is that it has a significant pressure drop, and that the ullage temperature profile versus time is a slowly increasing slope, similar to the radial injection, instead of a plateau, like the axial injection.

Concerning the sensors it is observed that the load cell was not behaving as desired all the time. It showed significant glitches in the data and inexplicable noise at the end of the pressurization phase. Likely this was due to a faulty electrical connection, and it is recommended that the load cell connections in the RIO are thoroughly checked. The capacitive sensor on the other hand was behaving quite fine, and design version 2 showed improvements on the noise level, as the design intended. Unfortunately the capacitive sensor also showed a large temperature dependency that needs to be solved for the sensor to be useful.

7.3. Comparing the injection methods

In the previous sections all test results gathered during the various test campaigns have been presented. Now with this data it is possible to compare the radial and axial injection methods to each other. That is the topic of this section of the report. The pressurant mass used and the collapse factor for all tests are compared.

For the detailed comparison it is convenient to only select the data sets from two tests, instead of comparing the data from all 6 conducted tests. Trying to compare them all at once would result in a highly cluttered set of tables and graphs and would not contribute to the analysis. Instead of this it has been decided to compare tests rad2 and ax2. These two tests form the two most representable tests from their respective test series. Rad2 is basically the average of all the radial injection tests. For the axial tests it would have actually been preferred to use ax3, as this was, just like rad2, the second test conducted from a helium bottle. Unfortunately ax3 was cut short at 45s during the test campaign. It was therefore decided to instead use ax2, as the data showed this one to be virtually equal in all aspects to ax3.

Table 7.5: Overview of all important measured parameters of the tests rad2 and ax2 and the percentual difference between the two values.

Test			rad2	ax2	Difference [%] (=(ax-rad)/rad)
Collapse factor	K	[-]	2.72	2.24	−17.6
Pressurant mass used	m_{pres}	[g]	282	229	−18.8
Pressurant pressure start	P_0	[bar]	148	178	20.3
Pressurant pressure end	P_e	[bar]	112	148	32.1
Pressurant start temperature	T_0	[K]	274.9	272.3	−0.9
Propellant start mass	m_{LN2}	[kg]	20.76	20.01	−3.6
Liquid level (start)	h_{LN2}	[mm]	624	602	
	h_{LN2}	[%]	84.3	81.3	
Mass flow	$\dot{m}_{LN2}$	[kg s^{-1}]	−0.395	−0.402	1.8
Liquid level rate of change	$\dot{h}_{LN2}$	[mm s^{-1}]	−11.9	−12.1	
Final mass	m_{LN2}	[kg]	1.00	0.00	
Liquid level (final)	h_{LN2}	[mm]	30	0	
	h_{LN2}	[%]	4.1	0	
Start pressure	P_{start}	[bar]	1.47	1.42	−3.4
Maximum pressure	P_{max}	[bar]	29.74	28.87	−2.9
Rise time (90%) (pressurization)	t_{rise}	[s]	7.62	7.68	0.8
Average pressure (expulsion)	P_{avg}	[bar]	21.09	21.98	4.2
Final pressure (expulsion)	P_{final}	[bar]	19.72	20.28	2.8
Fall time (90%) (expulsion)	t_{fall}	[s]	23.31	31.6	35.6
Fall time (90%) (depressurization)	t_{fall}	[s]	7.72	6.68	−13.5

Table 7.5 lists the most important parameters of both tests and the relative difference between them. All parameters concerning LN2 mass, and most concerning pressure history match up quite nicely. Test ax2 saw a slightly higher pressure, along with a longer fall time during expulsion. The pressurant start and end pressures differ significantly, but this was to be expected, as test rad2 used a helium bottle that was used once before (for rad1) while ax2 started with a fully filled bottle. The collapse factor and pressurant masses are however the most interesting values. The collapse factor for the axial test is 17.6% lower than that for the radial test. Similarly, the pressurant gas mass used is 20% lower. This is a result that is in line with the thesis its main hypothesis: the axial injection method is more effect than the radial one. The remaining parameters strengthen the result, as the average pressure and the final pressure for the axial test are actually higher than those of the radial one. Increased pressure means increased density in the gas, which in turn increases heat transfer and thus higher collapse factor. However still the collapsed value for axial injection is lower.

Figure 7.27 shows the pressurant usage for all six tests. It is clear from the figures that the error bars on the pressurant mass values are larger than would have been desirable, but the trend is clear:

The axial injection tests show a significant decrease in pressurant mass required. The average for the radial tests is 274 g of helium, while that for the axial tests is 232 g. That is a decrease of 15%. The error bars on the average are ± 27 g for both injection methods. These errors have been determined as the standard error of the mean over three samples (see appendix E.1). All axial injection tests centre quite nicely around the average, while in the radial injection tests rad3 could be considered an outlier with respect to tests rad1 and rad2. Test rad3 did have a larger initial ullage volume and ran at significantly lower pressures than the other radial tests. Its pressure was however still lower than that of ax1, and its initial ullage volume was comparable to tests ax2 and ax3.

From these results, it is concluded that indeed, the axial injection method uses less helium than the radial injection method. This confirms the main hypothesis of this thesis.

The difference between the radial and axial injection, and the support for the initial hypothesis is also clearly visible in the graphs of the various thermocouples in and on the tank. Figures 7.28, 7.29 and 7.30 show the thermocouples values of tests rad2 and ax2 versus time. The measurements along the centreline (figure 7.28) show the most interesting difference. The shapes of the curves over time and the absolute temperatures at each position vary distinctively. The TCs from ax2 all show a very quick increase in temperature as soon as the LN2 level drops below them. After this they all shoot up to values around -100°C and remain reasonably stable around there. Even TC4, quite down in the tank, reaches this level just before de-pressurization. This shows that there is relatively little vertical temperature gradient within the tank. On the other hand, all thermocouples in test rad2 show different behaviour: first a quick rise, followed by a slow increase. Or even just the slow increase for the lower thermocouples. The values also don't reach a common plateau, instead they show a strong vertical temperature gradient, with between 1 to 2 K/cm. Overall the temperatures for rad2 fall very much short of those achieved during ax2; Even TC4 during ax2 reaches temperatures above that of TC1 during rad2.

Figure 7.27: The helium pressurant mass used for all the radial and axial injection tests. Error bars show the uncertainty on each value. The dotted horizontal lines indicate the averages for each injection method.

The differences in figure 7.29 are less pronounced. The graphs for TC6 show roughly the same profile over time. The others however again tend to a quick rise for axial injection, and a slow rise with a kink for radial injection. Also, at ax2 the graphs seem to skip the little 'bump' in temperature that is visible in those of rad2. Overall, also here the temperature profiles for ax2 rise higher than those of rad2 and on average the temperature is far higher. Again rad2 shows a stronger vertical gradient than ax2.

Finally, the temperature graphs of the thermocouples on the outside of the tank (figure 7.30) compare slightly different. Here the temperature measured by TC11 during test rad1 actually shoots up past the temperature measured during ax2. Going further down along the tank wall, the situation turns around and here TC13 and TC14 show quite higher temperature at axial injection then at radial injec-

Figure 7.28: The temperature measurements for the tests rad2 and ax2. Measured by TC1 through TC5.
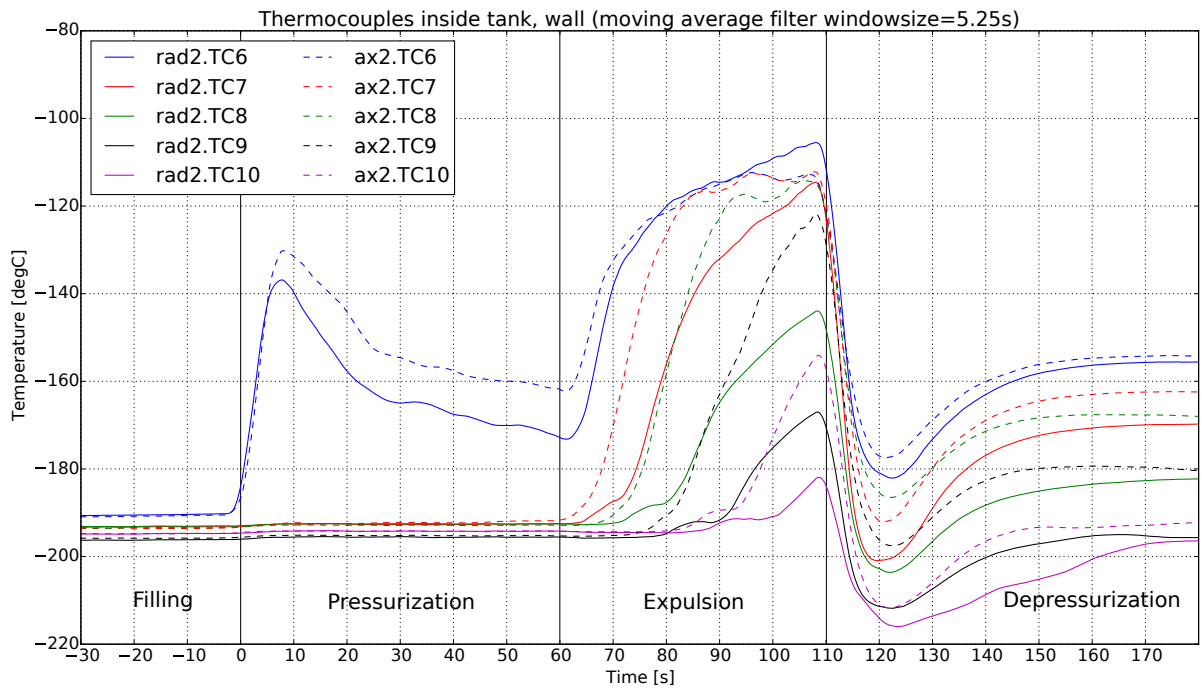
Figure 7.29: The temperature measurements from TC6 through TC10 for tests rad2 and ax2.

tion. However, again the temperature gradient at radial injection is far higher than that at axial injection. This indicates that likely the top 10 cm of the tank wall, and the massive tank top bulkhead, are at a far higher temperature as well. Because of this notion the thermocouples TC14 and TC15 were repositioned to the top bulkhead during the vortex tube test (see section 7.2.2). These measurements did show that the top bulkhead actually experiences a large temperature increase during the whole test. Likely this was also the case during the radial tests, and it is thought that the inflowing helium is actually cooled down significantly when injected parallel to the tank bulkhead during injection.

To clearly show the temperature distributions in the tank, a time instance near the end of the expulsion has been chosen for both tests rad2 and ax2. The times are chosen around t = 105 s such
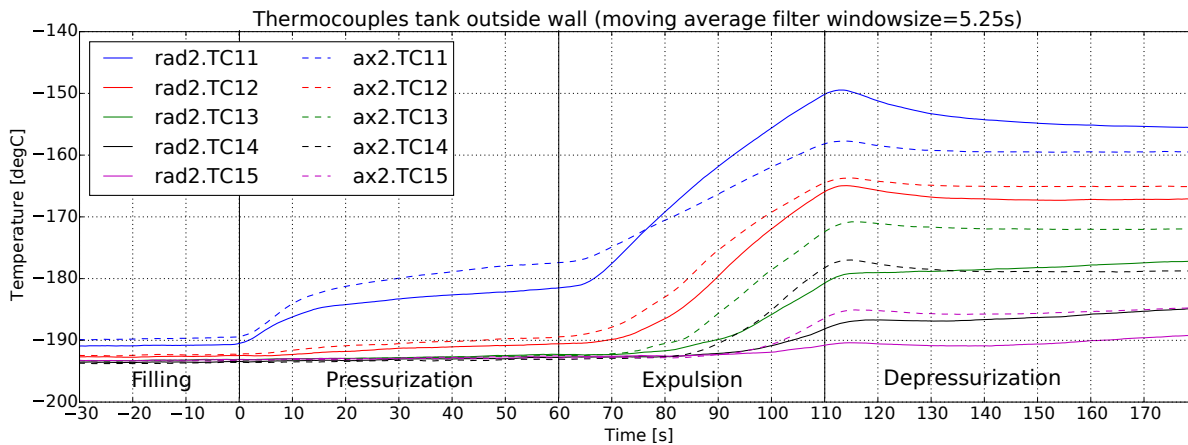
Figure 7.30: The temperature measurements along the outside tank wall (TC11 through TC15) for tests rad2 and ax2.

that at those instances the liquid level in the tank is equal for both tests. At these times the tank plots shown in figure 7.31 can be drawn. In these plots the tank cross-section is drawn to scale, with the thermocouple positions indicated as black dots. Upon each thermocouple, the temperature measured at that time, at that position is shown by a black bar. The thermocouples and their values are mirrored over the tank axis to better show the radial distribution of temperature. On the right of each tank the temperature distributions along the three vertical lines are shown. Using this figure the differences in temperature distribution, both horizontally and vertically, can be clearly shown. The radial injection shows a concave horizontal distribution, with higher temperatures near the wall, and lower temperatures near the centre. Axial injection shows the exact opposite: a convex distribution of temperature with high temperature in the centre, and low temperature near the wall. These concave and convex distributions are most pronounced near the top and weaken further towards the bottom of the tank. The graphs next to the tanks show the vertical distribution that was already found in the temperature vs. time plots before. Here the difference between the injection methods is more clearly appreciated: The radial injection shows a fairly constant vertical gradient. The axial injection has relatively constant temperatures in the top of the tank, and shows a sharper drop in temperature near the bottom. The vertical gradient at the outside of the tank is also noticeably stronger during radial injection than in axial injection. As mentioned before, this trend likely continues up towards the top bulkhead, meaning that during radial injection the top bulkhead absorbed a large amount of heat from the incoming gas.

Based on this result it is concluded that the measurement data confirms the reasoning behind the main hypothesis of this thesis: The axial injection method is more effective than the radial injection because of the difference in temperature distributions the injection methods create.

Vortex tube injection
As discussed in section 7.2, the vortex tube injection test did unfortunately not go as planned. Due to the clogging of the exit orifice, the test proceeded in a very different way than the other tests, and so it is not possible to directly compare the vortex tube to the radial and axial injection. Some conclusions can however be drawn to address the second hypothesis of this thesis: can a vortex tube be used to increase the temperature separation further and to so reduce the amount of pressurant gas needed?

Based on the experience gained during this thesis, and looking at the scarce test results, the answer is likely: no, it cannot. A vortex tube might possibly increase the radial temperature gradient, but it will not lead to a lower pressurant usage. This can be argued for with two reasons:

1. The gas that is injected radially will indeed be colder than during injection without a vortex tube, but will still be at a 'warm' -20°C to -30°C . When this is blown in parallel to the tank top bulkhead, which is at roughly -170°C , the gas will still lose significant amounts of heat. In general the lesson that should be learned from the radial tests is that it should be avoided to blow the gas along the tank wall because it leads to high heat transfer. The temperature plots of the vortex tube injection show a profile over time similar to those for radial injection. Along with the temperature measurements done on the top bulkhead this indicates that in vortex injection still a lot of heat is lost to the top bulkhead.
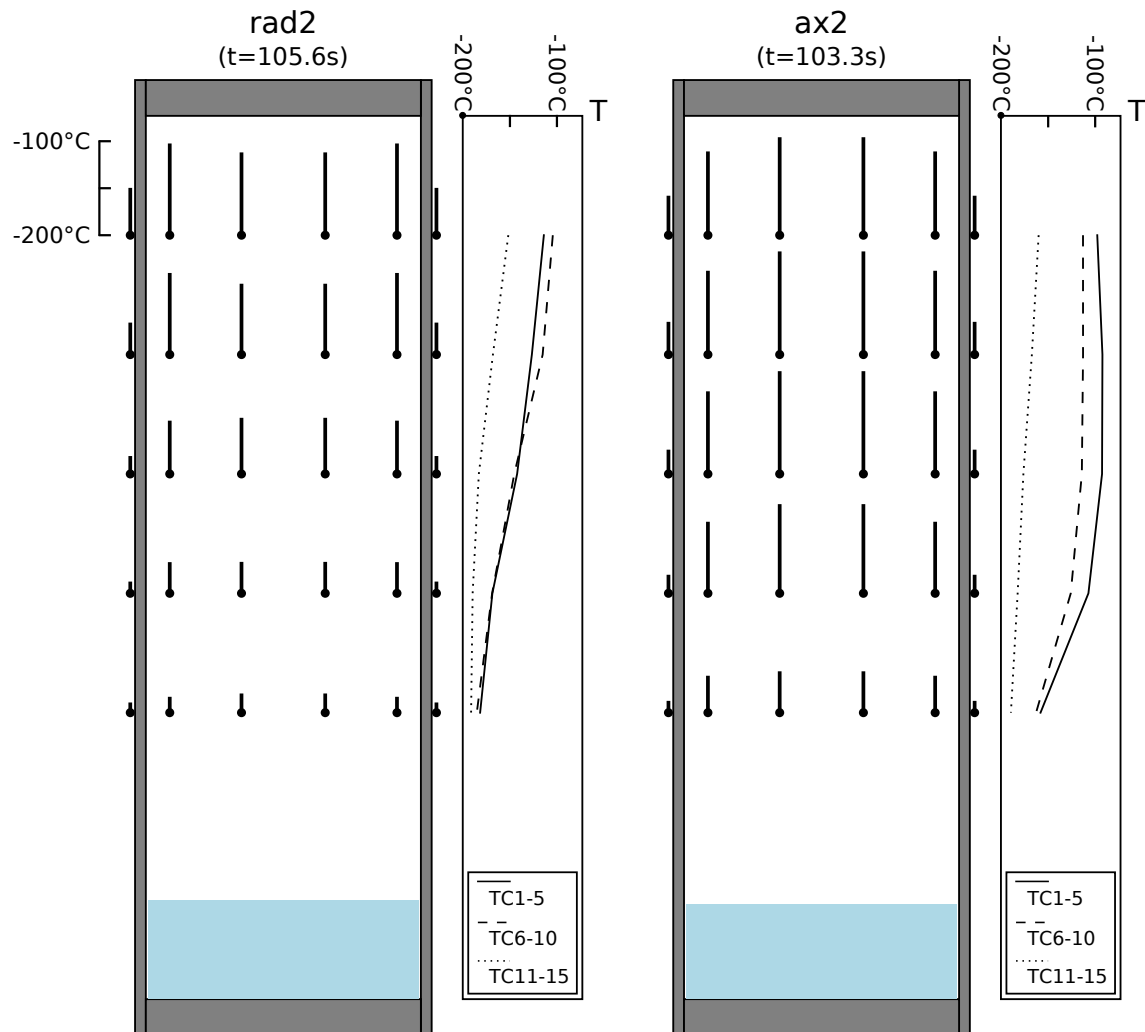
Figure 7.31: A representation of the test tank cross-section, the thermocouple positions, and the temperatures measured by them. The thermocouples and their measurements are mirrored over the z-axis to better show the radial temperature distribution. All dimensions, positions and temperature plots are to scale.

2. The theory on vortex tubes found in literature, supported by the conducted laboratory tests (chapter 6), showed that the temperature difference caused by the vortex tube is determined by the ratio of pressures between inlet and outlets, and not the absolute difference. In the case of pressurant injection, the absolute pressure difference is very high, but the pressure ratio is not. With 30 bar of propellant tank pressure, and 200 bar of pressurant pressure, the ratio is not much better than those seen during the laboratory tests (section 6.3). The temperature difference can thus not be expected to be much higher than that seen there. The pressure ratio will furthermore decrease to unity over the course of the pressurization and expulsion process, also reducing the temperature separation over the course of the expulsion.

Overall, it is reasoned that the vortex tube cannot perform better than axial injection in terms of collapse factor because too much head is lost to the tank top bulkhead.

If anyone would ever want to actually use the vortex tube for pressurant injection, a lot of research would still have to be conducted. As mentioned in section 6.4, a lot of work would need to be put into understanding the relation between total flow, pressure drop, and temperature separation in the vortex tube. Also the thermodynamics within the tank are bound to become even more complicated than they are now, with not one, but two different gas streams injected into the tank. Sorting out what the heat transfer coefficients of the gas to the tank are will be very complicated. And on top of all this would be a systems study: A vortex tube is an extra device on board the rocket that adds mass and complexity. Will a vortex tube bring enough advantage to merit its place on the rocket? Overall it is felt that the effort of optimization is better put in a different area.[2]

---

[2] The author very much recommends to investigate a pump system for the rocket instead.
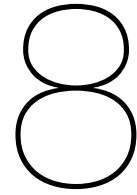
Comparison of simulations and tests

With the test results available for radial and axial injection tests it is possible to evaluate how accurately the simulation tools developed for the tank pressurization and emptying are able to predict the mass-flows, pressures and temperatures during the process, and most importantly, if the collapse factor can be determined within 10% (section 1.3).

In this chapter the simulations are validated by comparing them to the test data. This will be done by comparing the data of all radial and axial injection tests with the simulations based on a number of performance parameters in section 8.1. After that the representative tests rad2 and ax2 will also be compared to the simulations by looking at the ullage temperature and pressure versus time. This is done in section 8.2. Section 8.3 gives a short summary of the chapter and shows what the implications of the simulations are by revisiting the rocket system sizing from chapter 2.

8.1. System performance parameters

Comparison of the simulation results with the tests is done in a similar manner as the comparison between different simulation methods in section 3.4. The five main performance parameters of the system have been extracted from the test data and from the simulations and these are compared. One change is made to the parameter selection. Instead of comparing the expulsion time, the propellant mass flow is listed. This is because for both the tests and the simulations, the expulsion time was an input parameter, and so for both this value is exactly 50 s (for ax3: 45 s), and there is no use in comparing those.

Based on the comparison between the models in section 3.4, it is decided to only compare the performance parameters of the tests with those of the Lumped Parameter Model including heat transfer, but without mass transfer (i.e. model LPM (Q)). All other models produced results very comparable to this most simple model. Only the 1D ullage simulation with concentric cylinder sections (i.e. 1D ullage (vertical)) produces different results. However, its predictions deviate even further from the test results than the LPM(Q) model, as will be shown. Some more attention to this is paid in section 8.2.

The simulations have been run for each test using the same parameters as those described in table 3.2. Only the initial ullage fraction, the pressure regulator set pressure, and the tank starting pressure have been changed. The initial ullage fraction has been taken directly from the test data. The pressure regulator set pressure has been taken to be the maximum pressure achieved in the test during the pressurization period, and the tank starting pressure is the pressure measured just before t = 0 s. The values of these simulation input parameters are listed in table 8.1.

Table 8.2 shows the parameters for the simulations and tests. The collapse factor listed in this table is calculated via the method explained in section 7.1.4 (equation (7.3)). The pressurant bottle end pressure for the simulation as given in this table, is the value of the pressure after the bottle has reached thermal equilibrium with its environment again.

The results in table 8.2 show that the predictive power of the simulation is quite decent when it comes to the fluid flows within the system. The propellant mass flow is slightly under-predicted for all simulations, between 2% and 4% too low. The average tank pressure on the other hand is lightly over-predicted, with values 7% to 9% too high for the radial tests, and 3% to 6% too high for the axial

Table 8.1: Test specific simulation input parameters. These parameters are used to reproduce the test results from the radial and axial injection tests in the LPM (Q) and 1D ullage (vertical) codes. All simulation parameters not listed here are equal to the standard values mentioned in table 3.2.

Parameter	Unit	rad1	rad2	rad3	ax1	ax2	ax3
Initial ullage fraction	[-]	0.136	0.157	0.195	0.147	0.187	0.186
Pressure regulator set pressure	[bar]	29.16	29.74	28.92	27.82	28.87	29.56
Tank starting pressure	[bar]	1.75	1.47	1.28	1.52	1.42	1.40

Table 8.2: Comparison of the main performance parameters as observed during all radial and axial injection tests, and as simulated with the LPM (Q) code. The deviations in percent are calculated as the difference between simulation and test, divided by the test value ((s-t)/t).

		Collapse factor [-]	Propellant mass flow [g/s]	Avg. tank pressure [bar]	Inflowing gas mass [g]	Pres. pressure (end) [bar]
rad1	Test	2.65	393	21.4	280	148
	Sim.	1.97	387	22.9	205	158
	(s-t)/t [%]	-26%	-2%	7%	-27%	7%
rad2	Test	2.72	395	21.1	282	112
	Sim.	2.02	386	22.7	210	121
	(s-t)/t [%]	-26%	-2%	8%	-26%	8%
rad3	Test	2.73	382	19.9	260	80
	Sim.	2.13	376	21.6	208	86
	(s-t)/t [%]	-22%	-2%	9%	-20%	8%
ax1	Test	2.37	371	19.0	236	52
	Sim.	2.01	361	20.1	178	58
	(s-t)/t [%]	-15%	-3%	6%	-25%	11%
ax2	Test	2.24	402	22.0	229	148
	Sim.	2.11	384	22.6	216	148
	(s-t)/t [%]	-6%	-4%	3%	-6%	0%
ax3	Test	2.23	401	22.0	232	109
	Sim.	2.13	384	22.6	197	114
	(s-t)/t [%]	-4%	-4%	3%	-15%	4%

tests. The combination of too high a pressure, but still too low a mass flow can mean that the density of the fluid is over-predicted by the simulation, or that the discharge coefficient for the orifice is estimated too low. Specifically this too-low estimate for the discharge coefficient seems likely, as a few percent inaccuracy in this number is easily possible[61]. In these simulations it is set at $C_D = 0.6$ (see section 3.1.3.).

Also the prediction of the pressurant tank pressure at the end is quite good. All values, except that for ax1 are within 10%. They also all over-estimate the pressure. Note that the pressures listed here for the simulations are for when the gas in the bottle has warmed up again to environment after the expulsion process. Pressures predicted by the simulations directly at the end of the expulsion are slightly lower, and more in line with the measurements.

The predictions of the collapse factor and the total inflowing gas mass are unfortunately not very accurate, at least not for the radial injection tests. In general the values are significantly under-predicted. For the radial injection the collapse factor is predicted between 22% and 26% too low. For the axial tests however it is only 15%, 6% and 4% too low. For these tests the prediction is thus far better.

8.2. Pressure and temperature versus time

Next to the comparison of the simulations and tests based on the performance parameters, it is also possible to compare the temperature and pressure of the ullage versus time. This gives an indication on how well the simulations are able to predict flow phenomena (mass flow, pressures) and the thermodynamics of the system (temperature, and thus heat transfer). This can show where the simulation

performs well, and where there may be room for improvement.

A similar comparison was done among the different simulation methods in section 3.4. From that comparison it was found that all models give very similar temperature and pressure profiles compared to the most simple simulation (LPM (Q)). Only the 1D ullage, vertical, gave significantly different results. For the comparison of tests and simulations it is chosen here to compare the LPM(Q) and 1D ullage vertical simulations to the test results of rad2 and ax2. These two tests are chosen because they are considered representable for their injection methods (see section 7.3). Both temperature and pressure in the tank will be compared.

8.2.1. Pressure versus time

Figures 8.1 and 8.2 give the tank pressure versus time for tests rad2 and ax2 respectively. The graphs show in general the same deviations from the test data. During pressurization the simulations show a shorter rise time and it settles at a pressure approximately 1 bar below the maximum pressure. During expulsion the simulated pressures fall less far than test data. Here the 1D simulation flattens off to a nearly constant pressure, while the LPM simulation behaves more like the actual test data and keeps on dropping during the expulsion. The LPM data remains around 2 bar above the measured pressure at the radial test, and 1 bar at the axial test.
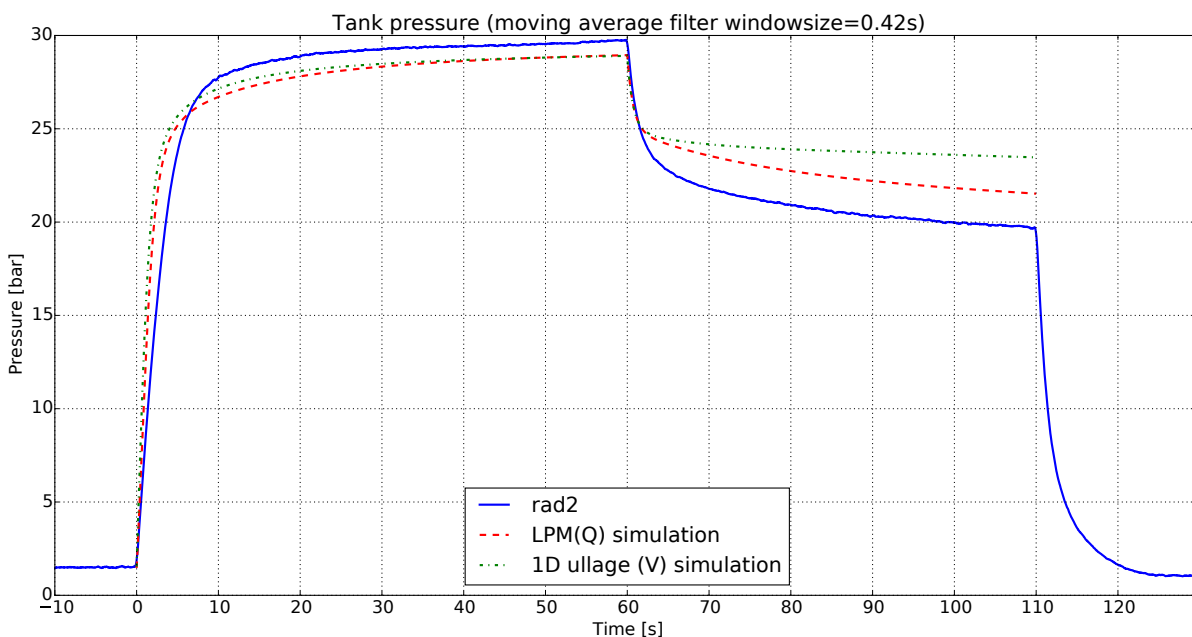
Figure 8.1: Tank pressure versus time as obtained from the test data from rad2, and from the simulations.

The differences could be explained in multiple ways. One of these is that the pressure regulator is behaving differently than what is specified in its datasheet. The results from the sensitivity analysis on the simulation (section 3.5) however seems to exclude that. The difference in behaviour of the regulator is not expected to deviate by more than the 10% that was evaluated in the analysis, and so its influence on the total simulation is limited.

A different explanation would be an underestimation of the heat transfer coefficients dictating the transfer of heat from the ullage gas to the tank and propellant. If this heat transfer is higher in reality than in the simulation, it will account for a slower pressure rise during pressurization. During pressurization the first gas flowing in will collapse significantly due to it cooling down. After that the tank pressure will however quickly settle, just as the simulation currently shows. During expulsion, a higher heat transfer will change nothing on the initial pressure drop, except that it will drop to a lower level because the pressure regulator needs to feed in more gas per second. This is the more likely explanation for the difference in the curves, as it is also supported by the sensitivity analysis. The uncertainty in the heat transfer is quite large (section 3.2.1), and so the effect on the simulation can also be significant (table 3.4).

A difference in heat transfer coefficient would also explain some of the differences between the
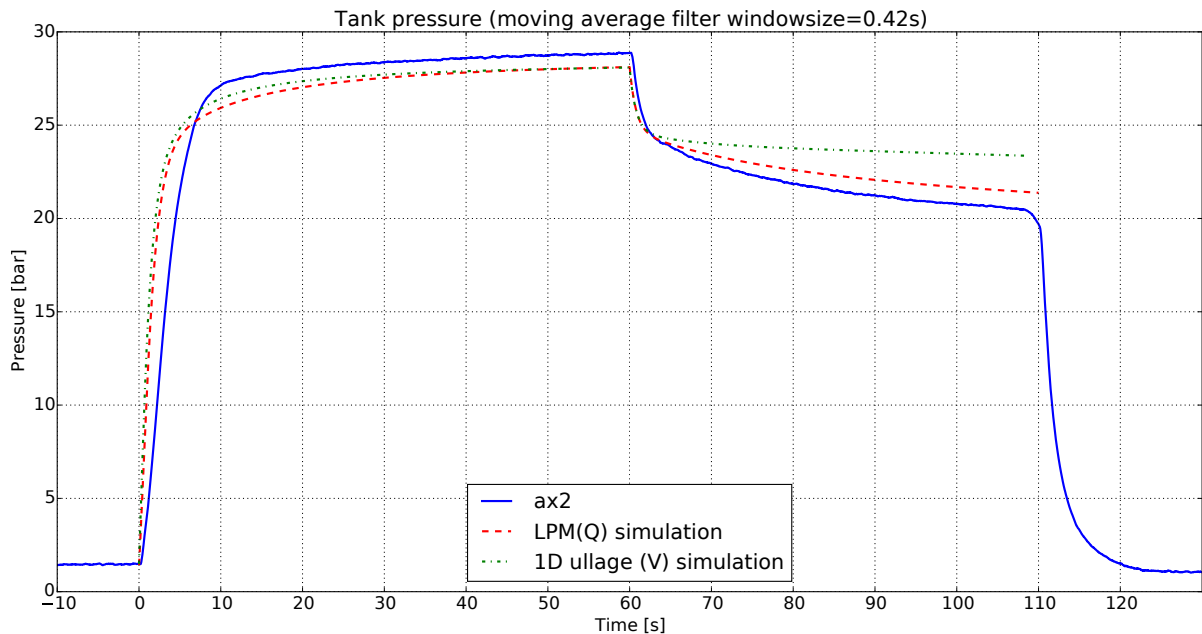
Figure 8.2: Tank pressure versus time as obtained from the test data from ax2, and from the simulations.

graphs for rad2 and ax2. The main hypothesis of this research, which is supported by the test results, is that the axial injection method leads to less heat transfer than the radial method. Indeed the graph with a lower heat transfer (ax2), and which is thus closer to the simulated case, shows a lower offset in pressure during the expulsion phase.

Overall, the pressure curves generated by the simulation match up quite well with the test data. Again, just like with the main performance parameters, the simulation complies more closely with the axial injection test data than with the radial.

8.2.2. Temperature versus time

Figures 8.3 and 8.4 show the thermocouple plots for TC6 through TC10 for the tests rad2 and ax2 respectively. Along with these is plotted the average temperature over the ullage volume for these tests as predicted by the LPM and 1D ullage (vertical) simulations.

Preferable, a comparison would be made between the average temperatures predicted by the simulation, and the average temperature measured during the test. The average temperature during the test is however difficult to determine from the data. With the temperature samples at the locations of the thermocouples, it is possible to try and determine an overall temperature distribution in the tank. This can be done (and has been tried by the author) in various ways. It is for example possible to try a linear interpolation over the volume via all thermocouples and towards the liquid surface. Or to try and fit a smooth polynomial curve through all the points. The average temperature values resulting from these kinds of interpolations can be quite dependent on the method applied. The averaging thus needs to be practised with care. It can be said however, that for the radial injection method the average temperature starts near -150°C and slowly drops towards -155°C . For the axial injection it also starts near -150°C at the start of expulsion, but then rises slowly towards -145°C .

Figures 8.3 and 8.4 show that the simulations vastly over-predict the pressurization temperature spike at the start of pressurization. Both do however show in general the correct shape of the graph, as the temperatures decrease over the course of the pressurization. After that both again show increasing temperatures when expulsion starts at t=60s. The 1D simulation after this predicts a far higher temperature than anything measured during the tests. Clearly this cannot be anything near the real average temperature in the ullage. The LPM simulation shows temperatures which are in the range of the maximum values measured during the tests, but which are still quite higher than the ~-150°C estimated as the average temperature during the test.
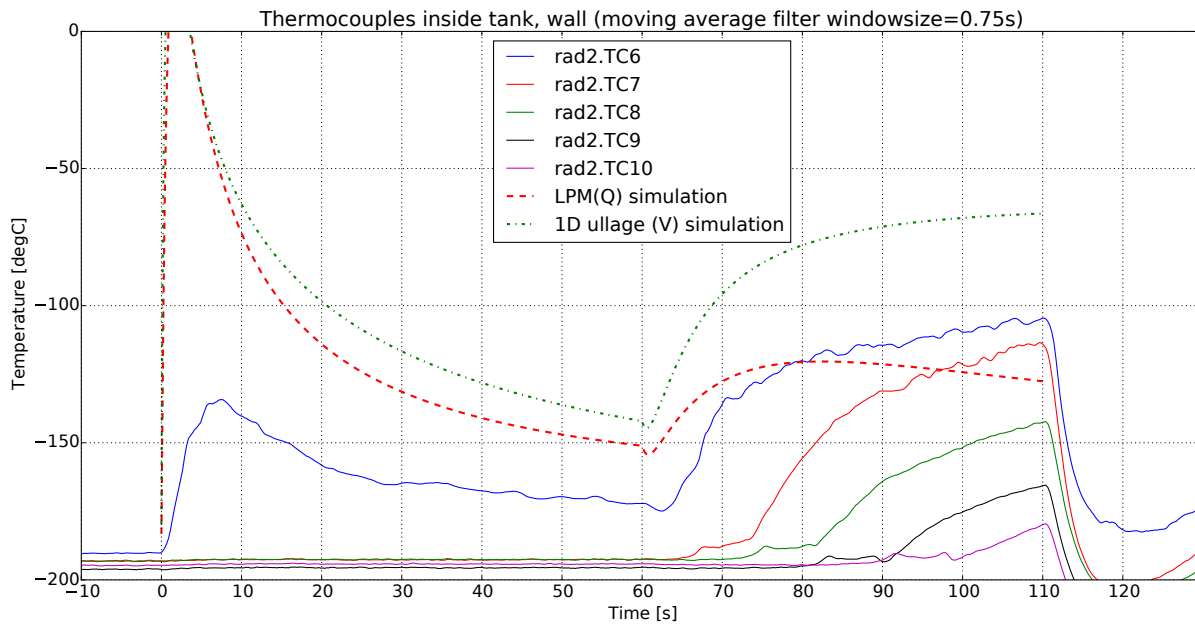
Figure 8.3: Temperature versus time for thermocouples TC6 throuh TC10 for the radial injection method (rad2), and the LPM(Q) and 1D ullage (v) simulations for this test case.
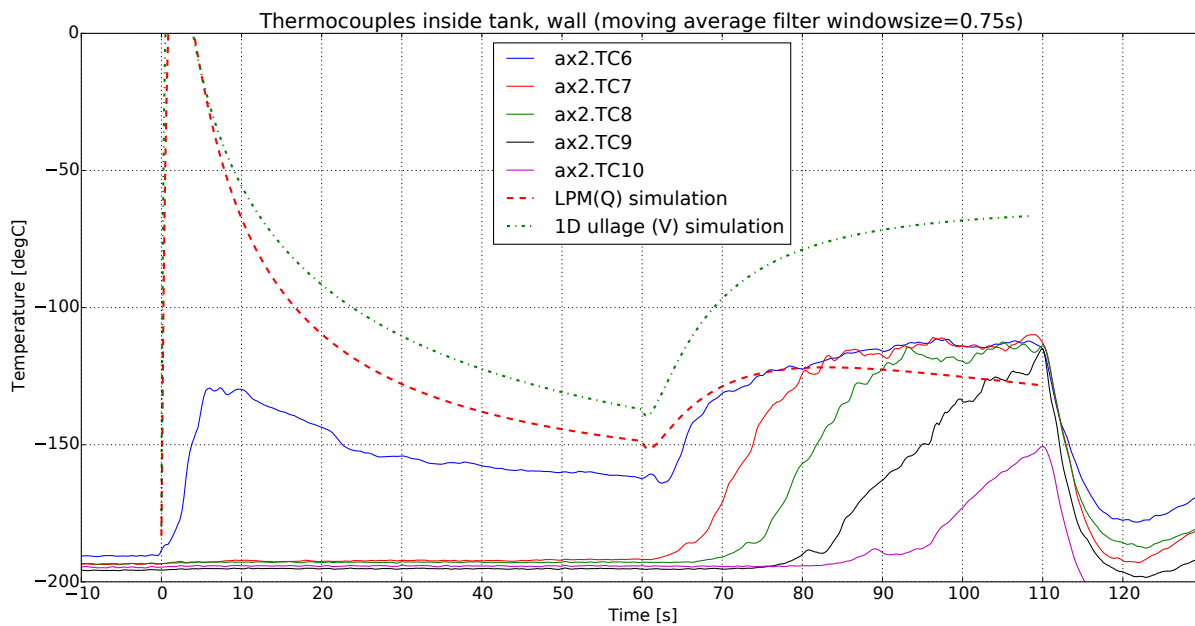
Figure 8.4: Temperature versus time for thermocouples TC6 throuh TC10 for the axial injection method (ax2), and the LPM(Q) and 1D ullage (v) simulations for this test case.

In summary, it can be concluded that the simulations are not very good in predicting the temperature distributions in the ullage. Overall the temperatures predicted are far too high. This again indicates that it is likely that the heat transfer rates in the simulation are estimated too low.

8.3. Conclusions and recommendations

From the comparison between the main system performance parameters in section 8.1 it can be concluded that the simulation is able to predict the pressurant collapse factor near the desired 10% accuracy range for at least axial injection. The accuracy will be near this 10% mark, but it cannot be said with certainty that it will be met on all configurations. It can be concluded, although with some caution, that the main goal of thesis research thesis has been completed (section 1.3). Overall the LPM(Q)

simulation is a good method to predict propellant mass flow, average tank pressure, and pressurant tank pressure. Its accuracy is however not good when looking at average ullage temperatures.

The accuracy of the simulation can likely still be improved further. All simulations currently under-predict the collapse factor, which could indicate that the heat transfer coefficients are under-predicted. This under-prediction in heat transfer is also supported by the pressure and temperature versus time measurements. Future research into this specific aspect of the simulation could heighten the accuracy of the simulation further.

Revisiting the "students to space" rocket design

As it stands now, the simulation can be used to predict the collapse factor within 10% accuracy. This is a significant improvement with respect to the uncertainty in this factor when the research was started (section 1.2), when it was assumed the collapse factor would be somewhere between 1.0 and 2.0. This large uncertainty lead to a large spread in designs for a rocket that is aimed for space (section 2.3, figure 2.3). With the simulation the design cases for the "students to space" rocket in the second chapter has been revisited. The collapse factor can now be reduces to within a range of $1.22 < K < 1.49$, where the nominal value is $K = 1.35$. This reduces the design options to those shown in figure 8.5, and whose values are given in table 8.3. When comparing these to the results from chapter 2, it is clear that the current simulation and validation have lead to a significant reduction in the uncertainty of the overall rocket design.
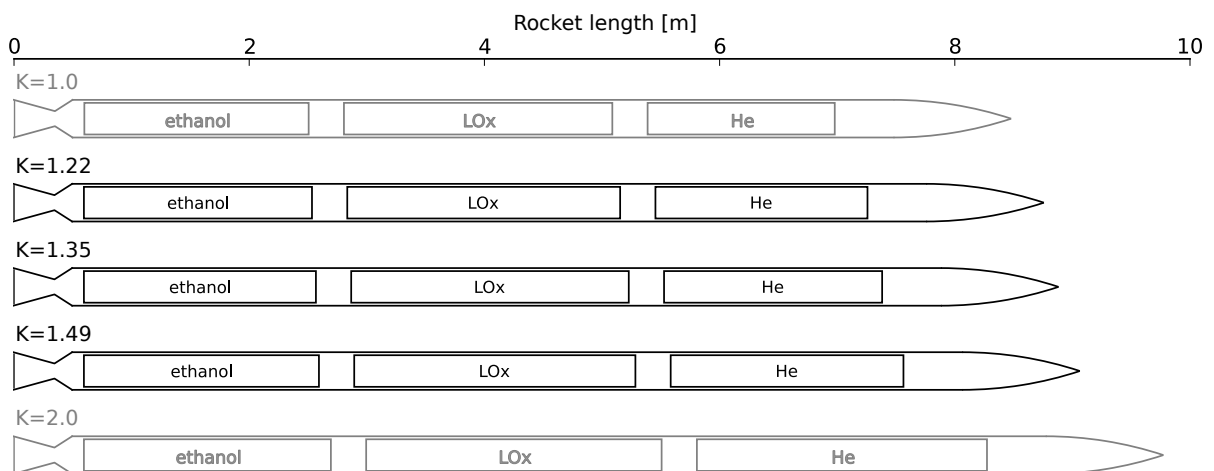
Figure 8.5: Rocket design cases for a pressure-fed rocket aimed to go to 120km. The more accurate simulations of the pressurant collapse factor allow for more focus in the design options for a student rocket going to space. (Compare to figure 2.3.)

Table 8.3: Sizing parameters resulting from the design evaluation script for rockets designed to achieve 120km altitude, using a new reduced range on the collapse factor. Compare to table 2.2.

	Unit	1		2		3	
Collapse factor	-	1.22		1.35		1.49	
Diameter	m	0.32		0.32		0.32	
Thrust	kN	27450		27600		27900	
Burn time	s	23.7		23.7		23.7	
L/D	-	27.4		27.8		28.3	
T/W	-	6.5		6.4		6.4	
Pressures							
Combustion	bar	25.2		24		23.8	
LOx tank	bar	32.9		31.6		31.4	
Fuel tank	bar	32.1		30.8		30.6	
Masses							
Rocket full	kg	431.5		436.5		442.1	
Propellant	kg	283.4	*(65.7%)*	288.6	*(66.1%)*	292.4	*(66.2%)*
Helium	kg	4	*(0.9%)*	4.1	*(0.9%)*	4.4	*(1%)*
LOx tank	kg	28	*(7.0%)*	27.6	*(6.3%)*	28	*(6.0%)*
Fuel tank	kg	24.4	*(6.0%)*	24	*(5.5%)*	24.1	*(5.5%)*
Helium tank	kg	27	*(6.0%)*	27.2	*(6.2%)*	28.4	*(6.4%)*
Lenghts							
Rocket	m	8.8		8.9		9.1	
LOx tank	m	2.3	*(26.5%)*	2.4	*(26.6%)*	2	*(26.0%)*
Fuel tank	m	2	*(22.0%)*	2	*(22.2%)*	2	*(22.0%)*
Helium tank	m	2	*(20.6%)*	1.9	*(20.9%)*	2	*(21.8%)*
Volumes							
LOx tank	l	174		181		181	
Fuel tank	l	143		151		151	
Helium tank	l	133.6		137.6		147.4	

9

Conclusion and recommendations

This final chapter presents an overview of the conclusions and recommendations that have been arrived at with the research presented in this report. It summarizes the conclusions that are presented in the various chapters and puts them in perspective with respect to each other. The research goal and research questions are used to structure the discussion.

The conclusions are given in section 9.1. The recommendations, mostly aimed at suggestions for further research, are given in section 9.2.

9.1. Conclusions

The problem of a tank pressurization system for pressure-fed cryogenic rocket propellant tanks lies in the determination of the tank collapse factor. This factor is a measure of how close to the ideal thermodynamic situation the tank system operates. The higher the collapse factor, the lower the efficiency, and thus the more pressurant gas is required. Due to the high pressures, extreme temperatures, and large area-over-volume ratio the collapse factor is mainly determined by the heat transfer from the pressurant gas to the cold propellant and tank wall.

Literature research showed that investigations on this factor have usually been concentrated on large-scale, low-pressure tanks, instead of the small-scale, high-pressure tanks of interest for a pressure-fed rocket. Furthermore there were indications in literature that the influence of the method of pressurant injection on the collapse factor may be quite high, but hardly any studies have been done to investigate this. Based on the literature it has been proposed that the common method of radial injection is actually of less efficiency than axial injection, for pressure-fed rockets. Furthermore it was hypothesized that the collapse factor could even be further reduced by using a vortex tube to split the pressurant gas flow into a cold and a warm stream.

From the literature investigation it became clear that it would be desirable to try and reduce the uncertainty in the collapse factor estimate. The main research goal of the thesis evolved from this. The goal of the thesis is to develop a method to predict the tank collapse factor within 10% accuracy and to investigate the effect of the method of pressurant injection on this factor.

9.1.1. Simulations

The first research question was aimed to figure out what the influence of the collapse factor and its uncertainty is on the total rocket design. This question was answered with the investigation in chapter 2. With a variation of the collapse factor between 1.0 and 2.0 (as gotten from literature), the total mass for a rocket aimed to reach the edge of space can vary with 10%. The length of the rocket even can vary with 15%. From the investigation it also becomes clear that the mass of the pressurant gas (helium) itself is less than a percent of the total rocket mass, but the tank in which the helium is contained is of far more importance, as it makes up around 20% of the mass.

The second research question worked towards modelling the tank pressurization system in more detail to try and predict the tank collapse factor. This lead to a lumped parameter model, and two 1D models. The models have been verified and a sensitivity analysis on them has been performed. Comparison of the models showed that mass transfer does not seem to be of importance and can easily

be neglected. The simplest lumped parameter model overall performs similar to the 1D simulation which splits the ullage into horizontal slices. The second 1D model, which splits the ullage volume into vertical sections, showed distinct differences compared to the other simulations because of the lower heat transfer resulting from this configuration. As the 1D horizontal simulation represents a radial injection method, while the vertical model represents axial injection, this result is in line with the hypothesis that axial injection is more efficient.

During investigation of the simulation it was found out that the problem of modelling the heat transfer is more difficult than expected. The regime in the tank is so extreme in temperature and pressure that there are no standard correlations available to properly model it. A deviation in heat transfer coefficient of a factor 2 would not be unlikely. This can lead to over 10% inaccuracy in the prediction of the tank collapse factor. Investigation of the heat transfer also showed that the gas flow pattern caused by radial injection seems to strengthen the natural convection pattern in the tank, while axial injection seems to weaken it. This again is in line with the hypothesis that axial injection causes less heat transfer.

9.1.2. Test setup hardware

From the start of the thesis it was already clear that the numerical simulation of the process would be difficult, and that validation data would be required. To do this a test plan has been set-up and a test setup has been construction (chapters 4 and 5). The test setup consists of a 30L cryogenic pressure vessel that has been equipped with a large array of sensors, including an array of 16 thermocouples placed in and on the tank. The materials and parts have been sourced, and the full setup has been designed and constructed from scratch. The various subsystems of the setup, such as the main tank, have been subjected to various subsystem test. The full hardware has been validated by means of the "first exposure test" (section 5.8) in which a large amount of practical and technical data was gathered on the operations of cryogenic systems. Specifically the sealing of the tank turned out to be problematic, but it was eventually possible to overcome this. The system and tests conducted with it represent the first practical experience for DARE and, to the best of the author's knowledge, for the TU delft, with the design, construction, and operation of high-pressure cryogenic systems.

One of the sensors used during the test is a capacitive sensor that has been developed from scratch during the research. It is the first of its kind within DARE and has been developed to address the problems experienced in the past with measurement of the propellant liquid level and mass flow by means of measuring the tank mass. The sensor worked, but unfortunately the current design still has a temperature dependency.

For the conduction of the injection tests with a vortex tube it was also required to look more into detail into the design of these types of systems. There is no generally accepted physical theory behind the functioning of this device yet. To be able to make a functioning design with it, a number of configurations of a vortex tube were made and tested, including tests with helium gas. These tests let to more insight into the design of the vortex tube and the test results, certainly those using helium, will be of value to future researchers.

9.1.3. Pressurization and expulsion tests

The third and fourth research question for this thesis deal with understanding the physical processes ongoing in the tank, and the direct effect of the method of injection on the tank collapse factor. These cannot be sufficiently addressed with the simulations, but can be with the pressurized expulsion tests that have been conducted. A total of 7 tests have been conducted, 3 using radial injection, 3 using axial injection, and 1 using vortex tube injection. From the collected test data, especially the temperature profile recorded by the thermocouples within the tank and on the tank outer wall are useful in understanding the processes within the tank. The data clearly shows the difference in radial and axial injection, visible in the different horizontal and vertical temperature gradients that build up in the ullage and the tank wall. It shows that conduction of heat from the ullage gas to the tank wall, and specifically to the tank top bulkhead, is of major importance. The radial injection method injects gas parallel to the tank bulkhead, and directed towards the tank wall. This leads to a significantly higher heat transfer from the gas to the wall. This all results in a reduction of 15% in the collapse factor for axial injection as compared to radial injection. This confirms the main hypothesis of this thesis, that axial injection is more effective than radial injection when it comes to the pressurization of cryogenic, pressure-fed rocket engine tanks.

The test conducted with the vortex tube was unfortunately not successful due to a blockage of the

exhaust orifice. Examination of the pressure data and the temperature profiles however indicated that the temperature split achieved in the gas stream was likely small. Thermocouple measurements on the tank top bulkhead also showed that the "cold" gas stream, which was injected radially, still lost a lot of heat to the tank bulkhead. Likely the vortex tube injection will still be less efficient than the axial injection.

9.1.4. Comparison of tests and simulations

The simulations and the test results have been compared in chapter 9. The simulated pressures and mass-flows over time match up very nicely with the test data and so the simulations certainly form a useful tool for engineers to design and size a tank pressurization system. The comparison however also shows that the prediction of the temperature profiles is still lacking, and that improvements can certainly be made by looking in more detail into the heat transfer coefficients.

The simulation is able to predict the tank collapse factor within an accuracy of 10% for the axial injection methods. Therefore it can be said that the simulation matches up with the main goal of this thesis and thus that this goal has been achieved. The predictions for the simulation are within bounds for the axial tests, but still each time under-predict the tank collapse factor. This indicates that likely the heat transfer within the tank is still higher than expected.

9.2. Recommendation

This final section of the report lists a number of recommendations that have resulted from this thesis. These recommendations are mostly listed as short, to-the-point recommendations on which aspects of this thesis could be deepened out more, and which should best be left to rest. Also a number of recommendations are of highly practical orientation, having been formulated with their usability for DARE in mind. (Note that appendix A also contains a number of less relevant recommendations still.)

On usage of the simulation
The simulations developed during this thesis should be of good value for an engineer designing a pressure-fed sounding rocket using a cryogenic propellant. For sake of speed and accuracy the LPM (Q) model should be most suited (when using axial injection), but keep in mind that the simulation consistently under-predicts the pressurant mass required, with possibly up to 10%.

Heat transfer correlations
The main uncertainty of the simulations is expected to be in the heat transfer correlations used. Likely the heat transfer is estimated too low. The situation within the tank is however so out of the ordinary that no standard reverence situations were to be found to find better correlations. It is recommended for future research that someone looks into 2D or 3D CFD simulations to try and determine the heat transfer more accurately. The test data gathered during this thesis, specifically the temperature measurements within the tank, offer a very good verification point for such simulations.

Pressurant gas mass measurements
The accuracy of the pressurant gas mass measurements during this thesis were not as accurate as what was hoped for. To improve this accuracy in the future, it is likely better to see if a pressure sensor (suited for helium up to 200 bar) can be installed in the cylinder pressure port of the pressure regulator to continuously observe the cylinder pressure.

Pressure regulator
The analysis and simulation of a pressure regulator as conducted within this thesis proved to work fine, and this process can be followed by other engineers in the future to model a pressure regulator, starting from only the data available in data-sheets. In practical considerations however, it will likely be hard to find a pressure regulator that is able to deliver enough flow to maintain constant tank pressure. Therefore an electrical or pneumatically actuated valve with a feedback loop via a tank pressure sensor should be investigated.

Fill valve
A globe valve, and specifically a solenoid operated one, is not suited for uses as a fill valve because the pressure applied on it changes direction during the whole operation process.

Data acquisition (specifically via the DARE cRIO box)
> Users of this measurement system should always make sure that they have a proper way build into the system to synchronize their measurements and to register the state of the system (e.g. the state of the valves). The code developed during this thesis should be a good base to start for the development of LabView code for a new measurement setup.

Capacitive liquid level sensor
> The coaxial version of the capacitive liquid level sensor (i.e. version 2) seems to work fine, with only its temperature dependency being a problem. It is recommended to try and construct the sensor without using a PTFE spacer strip to see if this may be the cause of the temperature dependency. Even with this dependency however, the sensor should already be useful on tank systems that operate near room temperature, such as ethanol or kerosene tanks. It is advised to certainly install this sensor in these type of tanks.

Cryogenic tank sealing
> The sealing of the cryogenic tank proved to be the most difficult aspect to realize on the test hardware. DARE should seek out help from industry professionals to develop a better way of creating cryogenic seals on a propellant tank.

Vortex tube injection
> The vortex tube on itself is a very interesting device, and certainly interesting to investigate further for fundamental research purposes. For use as a pressurant injector however, too little is known about it to design an effective system with it, and the gains that might be achievable with it are not promising enough to merit further research.

Finally, lets conclude this thesis with one recommendation that might seem at odds with the whole research topic on itself: TU Delft and DARE should develop a (cryogenic) propellant pump. The advantages of a pump-fed system as compared to a pressure-fed system start paying off very quickly, even with a student rocket aimed for the edge of space. This as much became clear from the research in chapter 2. Certainly with the possibilities in 3D printing of metal and the advancements of electrical motors and batteries within the recent years, a small electrical pump should be within the capabilities of TU Delft and DARE. As the author of this thesis I do hope that some aspects of it might still be useful, even if DARE fully switches to pump systems, but the main thing I would like to advice is this: get rid of pressure-fed systems, and start development of a propellant pump.

Bibliography

[1] URL `http://www.dare.tudelft.nl/`.

[2] FDC1004 4-Channel Capacitance-to-Digital Converter for Capacitive Sensing Solutions (Revision B). SNOSCY5B - August 2014 - Revised April 2015.

[3] SCAIME ZFA S-beam load cell datasheet.

[4] NIST online chemistry reference webbook. URL `http://webbook.nist.gov/chemistry/form-ser.html`. Date accessed: 1st of April, 2016.

[5] European student rocket altitude record: Mission successfully completed!, November 2016. URL `http://www.hybrid-triebwerk.de/`.

[6] Aalco Metals Ltd. Aluminium alloy 6082-t6 extrusions, January 2016. URL `http://www.aalco.co.uk/datasheets/Aalco-Metals-Ltd_Aluminium-Alloy-6082-T6-Extrusions_338.pdf.ashx`.

[7] A.D.Deutschman, W.A Michels, and C.E. Wilson. *Machine design Theory and Practice, Machinery's Handbook 27*. MacMillan Publishing, 27 edition, 1975.

[8] B. K. Ahlborn, J. U. Keller, and E. Rebhan. The heat pump in a vortex tube. *Journal of Non-Equilibrium Thermodynamics*, 23(2):159–165, 1998. doi: 10.1515/jnet.1998.23.2.159.

[9] Vineet Ahuja, Ashvin Hosangadi, Stephen Mattick, Chun P. Lee, Robert E. Field, and Harry Ryan. Computational analyses of pressurization in cryogenic tanks. In *44th AIAA Joint Propulsion Conference*, July 2008.

[10] Orhan Aydin and Muzaffer Baki. An experimental study on the design parameters of a counterflow vortex tube. *Energy*, 31:2763–2772, November 2006. doi: 10.1016/j.energy.2005.11.017. Issue: 14.

[11] Barreiro, Okkerman, Rijn, Pütz, and Hikspoors. Dare minor 2015-2016 - cryogenic fuel tank. Technical report, Delft University of Technology, 2016.

[12] Adrian Bejan and Allan D. Kraus, editors. *Heat transfer handbook*. Wiley, July 2003.

[13] Ian H. Bell, Jorrit Wronski, Sylvain Quoilin, and Vincent Lemort. Pure and pseudo-pure fluid thermophysical property evaluation and the open-source thermophysical property library coolprop. *Industrial & Engineering Chemistry Research*, 53(6):2498–2508, 2014. doi: 10.1021/ie4033999. URL `http://pubs.acs.org/doi/abs/10.1021/ie4033999`.

[14] Bentla, Van Boxtel, Eiche, Hermsen, Huijsman, Tri, KNop, Mkhoyan, Powell, Van Straten, Takeda, Tang, Ullrich, and Wink. Spacecraft engineering minor 2011-2012 et3054tu - hardware implementation project definintion: The design, modeling, production and testing of a hybrid rocket engine. Technical report, Delft University of Technology, 2011.

[15] T. L. Bergman, A. S. Lavine, F. P. Incropera, and D. P. Dewitt. *Fundamentals of Heat and Mass Transfer*. John Wiley & Sons, seventh edition, 2011. ISBN 13: 978-0470-50197-9.

[16] Christopher E. Brennen. *Fundamentals of Multiphase Flows*. Number ISBN 0521 848040. Cambridge University Press, 2005.

[17] Edgar H. Buyco and Fred E. Davis. Specific heat of aluminum from zero to its melting temperature and beyond. *Journal of Chemical and Engineering Data*, 15(4):518–523, 1970.

[18] *Flow of Fluids through Valves, Fittings and Pipe*. Crane Co., 2010. Technical Paper No. 410.

[19] M. Carroll Croarkin, William F. Guthrie, George W. Burns, Margaret Kaeser, and Gregory F. Strouse. Temperature-Electromotive Force Reference Functions and Tables for the Letter-Designated Thermocouple Types Based on the ITS-90. *NIST Monograph 175*, 1993.

[20] Laurence de Quay. *Validated prediction of pressurant gas requirements in cryogenic run tanks at subcritical and supercritical pressures*. PhD thesis, Mississippi State University, Department of Mechanical Engineering, December 2009.

[21] Laurence de Quay and B. Keith Hodge. A history of collapse factor modeling and empirical data for cryogenic propellant tanks. In *46st AIAA Joint Propulsion Conference*, July 2010.

[22] L. Denies. Regenerative cooling analysis of oxygen/methane rocket engines. Msc. thesis, Delft University of Technology, December 2015.

[23] Kiran Devade and Ashok Pise. Effect of cold orifice diameter and geometry of hot end valves on performance of converging type ranque hilsch vortex tube. In *Energy Procedia*, volume 54, pages 642–653, 2014. doi: 10.1016/j.egypro.2014.07.306.

[24] Richard L. DeWitt and Thomas O. McIntire. Pressurant requirements for discharge of liquid methane from a 1.52-meter (5-ft.) diameter spherical tank under both static and slosh conditions. *NASA technical note*, (NASA TN-D7638), May 1974.

[25] Richard L. DeWitt, Robert J. Stochl, and William R. Johnson. Experimental evaluation of pressurant gas injectors during the pressurized discharge of liquid hydrogen. Technical Note NASA TN D-3458, NASA Lewis Research Center, June 1966.

[26] Neil T. Van Dresar and Robert J. Stochl. Pressurization and expulsion of cryogenic liquids: Generic requirements for a low-gravity experiment. Technical Memorandum NASA 104417, NASA Lewis Research Center, June 1991.

[27] N.T. Van Dresar and Gregory A. Zimmerli. Correlation of helium solubility in liquid nitrogen. *NASA Technical Memorandum*, (NASA/TM - 2012-217716), October 2012. Document ID: 20120016683.

[28] J.R. Elliott and C.T. Lira. *Introductory Chemical Engineering Thermodynamics*. International Series in the Physical and Chemical Engineering Sciences. Prentice Hall PTR, 2nd edition, 2012.

[29] F. M. Engelen. Quantitative risk analysis of unguided rocket trajectories. Master's thesis, Delft University of Technology, May 2012.

[30] Radu Florea. The stratos ii+ ground control system - using the compactrio and labview to reach 21.5 km, August 2016. URL http://forums.ni.com/t5/LabVIEW-Student-Design/ THE-STRATOS-II-GROUND-CONTROL-SYSTEM-Using-the-CompactRIO-and/ta-p/ 3537858. Submission for the LabView student design competition: Northern Europe.

[31] Thomas M. Flynn. *Cryogenic Engineering*. Marcel Dekker, 2005. Second Edition Revised and Expanded.

[32] A.N. Hammoud, E.D. Baumann, E. Overton, I.T.Myers, J.L. Suthar, W. Khachen, and J.R. Laghari. High temperature dielectric properties of apical, kapton, peek, teflon af, and upilex polymers. *Conference on Electrical Insulation and Dielectric Phenomena*, 1992. NASA Technical Memorandum 105753.

[33] R.J.G. Hermsen. Feed system design for an oxygen/methane liquid rocket engine, March 2016. Literature study. Delft University of Technology.

[34] Rob Hermsen. Investigation of pressurization methods for a cryogenic propellant tank. MSc thesis research proposal, March 2016. Delft University of Technology.

[35] R. Hilsch. The use of the expansion of gases in a centrifugal field as cooling process. *The review of scientific instruments*, 18(2):108–113, February 1947. doi: 10.1063/1.1740893. Translation by I. Estermann.

[36] Huzel and Huang. *Design of liquid propellant rocket engines*. NASA, 1967.

[37] D. R. Johnston, G. J. Oudemans, and R. H. Cole. Dielectric constants of imperfect gases. i. helium, argon, nitrogen, and methane. *The Journal of Chemical Physics*, 33(5):1310–1317, November 1960. doi: 10.1063/1.1731405.

[38] Joint Committee for Guides in Metrology - Working group 1. Evaluation of measurement data - Guide to the expression of uncertainty in measurement. (JCGM 100:2008), September 2008. First edition.

[39] H. Khazaei, A.R. Teymourtash, and M. Malek-Jafarian. Effects of gas properties and geometrical parameters on performance of a vortex tube. *Scientia Iranica*, 19:454–462, June 2012. doi: 10.1016/j.scient.2012.03.003. Issue 3.

[40] Geoffrey L. Kulak, John W. Fisher, and John H. A. Struik. *Guide to Design Criteria for Bolted and Riveted Joints*. American Institute of Steel Construction, Inc., 2 edition, 2001.

[41] R. Liew, J.C.H. Zeegers, J.G.M. Kuerten, and W.R. Michalek. Maxwell's demon in the ranque-hilsch vortex tube. *Physical Review Letters*, 109(054503), August 2012. doi: 10.1103/PhysRevLett.109.054503.

[42] Logistiek & Milieu TU Delft. Prijslijst gassen 2015-2016.

[43] Carina Ludwig and Michael Dreyer. Analyses of cryogenic propellant tank pressurization based upon experiments and numerical simulations. In *5th European Conference for Aeronautics and Space Sciences (EUCASS)*, July 2013.

[44] Alok Majumdar and Todd Steadman. Numerical modeling of pressurization of a propellant tank. *Journal of Propulsion and Power*, 17(2):385–390, March-April 2001.

[45] E.D. Marquardt, J.P. Le, and Ray Radebaugh. Cryogenic materials properties database. In *11th International Cryocooler Conference*. National Institute of Standards and Technology, June 2000.

[46] M.E. Nein and J.F. Thompson. Experimental and analytical studies of cryogenic propellant tank pressurant requirements. Technical Memorandum NASA TM X-53165, NASA George C. Marshall Space Flight Center, February 1965.

[47] Nickel Development Institute. Publication nr. 4368. materials for cryogenic service: Engineering properties of austenitic stainless steel, 1974.

[48] Park, Kim, Choi, and Lee. Study on cryogenic mechanical behavior of 6000 series aluminum alloys. *Journal of Ocean Engineering and Technology 29*, 1:92–100, February 2015. doi: 10.5574/KSOE.2015.29.1.085.

[49] Jeliazko G. Polihronov and Anthony G. Straatman. Thermodynamics of angular propulsion in fluids. *Physics Review Letters*, 109(054504), August 2012. doi: 10.1103/PhysRevLett.109.054504. Issue 5.

[50] G.J. Ranque. Expériences sur la détente giratoire avec productions simultanées d'un echappement d'air chaud et d'un echappement d'air froid. *Le Journal De Physique et le Radium*, 4:112–115, June 1933. Supplement.

[51] G.J. Ranque. Method and apparatus for obtaining from a fluid under pressure two currents of fluids at different temperatures, March 1934. US Patent US1952281. Year filed: 1932.

[52] Elliot Ring, editor. *Rocket propellant and pressurization systems*. International series in space technology. Prentice-Hall, Inc., Englewood Cliffs, NJ, 1964.

[53] J.H. Robson, W.A. Cannon, and W.D. English. Pressurization systems design guide vol. iii. Technical Report DAC-60510-F1, NASA, 1968. NASA contract NAS7-548.

[54] Benjamin Shaya. FDC1004, 2016. URL `https://github.com/beshaya/FDC1004`.

[55] Steven W. Smith. *Digital Signal Processing: A Practical Guide for Engineers and Scientists*. 2002. URL `http://www.dspguide.com/`.

[56] Robert J. Stochl and Richard L. DeWitt. Pressurant gas requiremenys for the pressurized discharge of liquid hydrogen from propellant tanks. In *5th AIAA Joint Propulsion Conference*, number 69-526, June 1969.

[57] S. Subudhi and M. Sen. Review of ranque-hilsch vortex tube experiments using air. *Renewable and Sustainable Energy Review*, 52:172–178, 2015. doi: 10.1016/j.rser.2015.07.103.

[58] George P. Sutton and Oscar Biblarz. *Rocket propulsion elements*. Wiley, 7 edition, 2001.

[59] Lei Wang, Yanzhong Li, Yonghua Jin, and Yuan Ma. Experimental investigation on pressurization performance of cryogenic tank during high-temperature helium pressurization process. *Cryogenics*, (66):43–45, 2015.

[60] Lei Wang, Yanzhong LI, Kang Zhu, and Yonghua Jin. Comparison of three computational models for predicting pressurization characteristics of cryogenic tank during discharge. *Cryogenics*, (65): 16–25, 2015.

[61] Frank M. White. *Fluid Mechanics*. Mechanical Engineering. McGraw-Hill, seventh edition, 2011.

[62] J. Wink. Project cryogenic; development of a 10 kn liquid oxygen/ liquid methane rocket engine. DARE project proposal, April 2015.

[63] J. Wink, T.R. Knop, R. Huijsman, S. Powell, K. Samarawickrama, A. Fraters, R. Werner, C. Becker, F. Lindemann, J. Ehlen, A. Cervone, , and B.T.C. Zandbergen. Test campaign on a 10kn class sorbitol-based hybrid rocket motor for the stratos ii sounding rocket. In *Space propulsion conference*, number SP2014-2969362, 2014.

[64] Adam L. Woodcraft. Predicting the thermal conductivity of aluminium alloys in the cryogenic to room temperature range. *Cryogenics*, 45(6):421–431, June 2005. doi: 10.1016/j.cryogenics. 2005.02.003.

[65] B.T.C. Zandbergen, editor. *Thermal Rocket Propulsion reader*. Delft University of Technology, 2016. Associated course code: AE4-S01. Version 2.05.

$$A$$
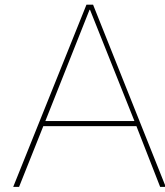
General recommendations for a pressure-fed rocket system

This appendix contains various subjects that were (briefly) looked into this thesis. They are related to the thesis topic but are not that relevant that they made it into the main report. It has however been decided to include them here, specifically for the benefit of DARE. The questions answered in this appendix are those often asked by anyone who starts working on cryogenic rocket engine systems (such as anyone starting new in DARE). Its hard to find clear, concise answers to these questions so it was decided to collec them here.

A.1. Propellant selection and usage of liquid methane

The main consideration for rocket engine design is the selection of the propellants. The main criteria for propellants to be used within DARE is its safety in usage. Safety in usage is in this case understood as that the substance is not toxic, not highly corrosive, not carcinogenic or in any other way known to be of direct harm to humans. This directly excludes substance like monomethylhydrazine or dinitrogen-tetroxide. Also mono-propellants are usually excluded based on their risk of explosion. Of the oxidizers it is usually only liquid oxygen, nitrogen-dioxide and hydrogen-peroxide that are considered 'safe', although they of course still carry certain risks in usage.

The second main consideration is availability. DARE is a low-budget operation that cannot spent thousands upon thousands of euros for the propellants and therefore some propellants are not directly in reach. Availability can also depend on regulations. It may be that a desired substance cannot be bought or sponsored because DARE is not permitted to store or use it.

For oxidizers liquid oxygen has been selected by the DARE team because it is more potent than the other two available options. Liquid oxygen is considered to be the next step that needs to be taken to enable DARE to go to space.[62]

For fuel the situation is more complicated as there are more substance to choose from. The DARE cryogenics project conducted an investigation into different fuels in the first half of 2015 and selected three fuels that were of specific interest. These were liquid methane, kerosene and ethanol. Other fuels were discarded because of their complexity in usage (e.g. hydrogen) or their lower performance (e.g. methanol). Substances like ethane, propane, and butane were discarded as they would require the same handling difficulties as methane (they need to be cooled down to be liquefied) but offer less performance.

Liquid methane was considered very interesting at the start of the cryogenics project as a potential fuel, mostly because of the high interest in it in the space community at this time. Some research into its usage had been done within DARE and at the TU Delft.[22] However during this thesis research an evaluation of its performance, its availability, and its handling characteristics, revealed a number of important disadvantages that make it undesirable for use as rocket propellant within DARE. These are, in order of importance (most important first):

1. Methane has a density of around 430 $kg\,m^{-3}$ when stored at 30 bar of pressure. This is around half that of ethanol or kerosene. This means that the tank for the fuel needs to be around twice as

large. As for pressure fed rockets the tanks need to hold large pressures, they are relatively heavy and contribute significantly to the total mass (as discussed in section 2.1). For methane the near doubling in tank mass because of its low density negates any positive chemical properties it has compared to kerosene or alcohol. On top of this, a larger fuel tank puts larger requirements on the pressurization system, requiring this to be larger as well. In other words: Methane's specific-impulse may be greater, but for pressure-fed rockets, its system-specific-impulse is lower.

2. No supplier for liquid methane could be found within the Netherlands. Various possible suppliers were contacted by the cryogenics team, including Linde gas, Praxair and Shell. None of these indicated it was possible to supply LNG (let alone pure liquid methane), specifically not at such a small scale as what we would need.[1] The only alternative would be to buy the methane in gaseous form, and let it condense in a cooled tank. This would however be quite expensive. The methane itself would already cost around €9 per kilogram if all methane in the supply bottles would be usable.[2] On top of that would be the costs and efforts for liquefaction of the methane.

3. Linked to the supply of the fuel is the storage. If a supplier of methane is found, either a deal needs to be made that the supplier also delivers a large storage vessels from which a run tank can be filled, or DARE needs to acquire a storage vessel that the supplier is willing to connect to and fill. Liquid methane is also stored at cryogenic temperatures, and thus will slowly boil off when stored, meaning more methane will be required during a test campaign.

4. Venting of methane (or dumping in emergency situations) requires some form of gas flare to burn of the methane instead of releasing it into the atmosphere. Venting methane might result in an explosive atmosphere if it is done is some form of closed test location. Furthermore, methane is a very potent greenhouse gas, so release of it into the atmosphere is undesirable/forbidden.

5. Methane will always need to be pressurized with helium, increasing its costs. Pressurization with nitrogen is something that could be acceptable for liquid oxygen when doing ground tests. However, nitrogen also dissolves fairly well into liquid methane and as methane is actually significantly lighter than nitrogen, instead of forming a saturated layer in the top of the tank, the dissolved nitrogen will sink tot the bottom of the tank and bring fresh methane to the top, accelerating the dissolving process.[24]

Taking all these considerations into account, liquid methane is a bad choice for pressure-fed rocket engine systems and should involve very careful consideration in pump-fed systems as well.

The remaining options are kerosene and ethanol. Kerosene offers a slightly higher specific impulse than ethanol ($\sim$317 s v.s. $\sim$307 s [3]) while having comparable densities. Ethanol however has a lower oxidizer to fuel ratio than kerosene ($\sim$2.45 for kerosene, $\sim$1.65 for ethanol), which effectively decreases the system specific I_{sp}. Ethanol is hardly ever sold in a pure form and always comes with a certain fraction of water mixed in. This reduces its specific impulse slightly, but increases density. The added water however also has as benefit that the heat capacity of the fuel rises significantly, making its usage as a coolant more likely. Finally the added water reduces the combustion temperature, which could also be beneficial for the combustion chamber design. The same cooling benefit is gotten from ethanol as it has a lower OF-ratio than kerosene.

   Both kerosene and ethanol were looked at by the DARE team, however no direct supplier for kerosene could be found. For ethanol however there are a large number of suppliers, mostly owning to the popularity of bio-ethanol in recent years. Because of this the team decided to go for ethanol as the fuel of the rocket. This is also the fuel that is used during the system sizing described in this section of the report. More specifically: A mixture of 95% ethanol and 5% water by mass is used.

---

[1]A possible alternative would of course be to buy methane in gas form in pressurized cylinders and liquefy this in some way. This would however likely be a cumbersome and very expensive procedure. One 50 L cylinder at 200 bar contains only around 8 kg of methane, and comes at a cost of around €160.[42]

[2]As comparison, the N_2O used as oxidizer for Stratos II+ costed approximately €5.20 per kilogram,[42] however a large amount was lost because not everything from the storage cylinders could be filled into the run tank. Taking this into account, four 50L cylinders per test at $\sim$€200 per cylinder, for 80 kg of usable N_2O per test, means the costs were effectively around €10 per kilogram. All bottles used during the tests were sponsored to DARE by various companies.

[3]Both for 20 bar chamber pressure expanding through a nozzle of expansion ratio 8 to vacuum. Data via RPA Lite.

A.2. Pressurant gas selection

The pressurant gasses that can be used in a pressure fed rocket need to be selected based on the propellant type used and the desired properties of the gas. Ring[52] gives a good overview of the desired properties of a pressurant gas when it is desired to minimize pressurant weight. Added to these should be requirements on the safety of storage and handling, availability of the gas, and the price. Overall the gasses that are most commonly used in pressurization are helium and nitrogen[36]. Nitrogen is often used in ground system tests as it is cheaper then helium.

There are hardly any gasses that do not condense at the low temperature and high pressures in cryogenic systems under consideration in this thesis. The vapour pressure curves of nitrogen, oxygen and argon are all very close together and they will thus readily condense when used as a pressurant gas for LN2 or LOx. (Same goes for fluorine, but that is more dangerous to works with than oxygen, and not readily available in large quantities.) Nitrogen and oxygen actually form a completely miscible solution[53]. Other gasses in general condense at higher temperatures still and are thus certainly not suited. Only hydrogen, helium, and neon do not condense. Of these neon is not readily available in large quantities, and is in general more expensive then helium. Hydrogen is cheaper then helium (by about a factor of three for a 50 L, 200 bar gas cylinder[42]) but is of course flammable, and thus certainly not suited for use with LOx. Its usage with LN2 should also be carefully considered, as during venting it could react with oxygen from the atmosphere. Helium remains as the only realistic option for pressurant gas. Its higher price is its only downside, but for a small system, the price of all other subsystems (mainly valves) is actually far more significant than the price of the gas.

For this thesis, the price of helium gas was shortly investigated to ensure the cheapest supplier could be found. Quotes were requested at different suppliers for 50L, 200bar helium bottles at a purity level of 4.6 ($=$ 99.996%). Prices for helium have a significant spread, between ~€230 (WestFalen), ~€180 (Praxair), ~€165 (Airproducts), down to ~€120 for Linde Gas. The supplier for the Delft Logistiek & Milieu department is also Linde gas, and the price from this department is equal to that requested by Linde Gas. the helium was thus acquired via the TU Delft.

A.3. Initial pressurization of the propellant tank

When considering a rocket system in flight configuration the system will involve at least two reservoirs of all involved fluids: One storage vessel on ground and one flight tank on-board the rocket. During filling of the rocket from the storage vessels, the transfer of the liquid oxygen and the high-pressure helium will likely only happen when the rocket is in the tower.[4] The transfer will happen via some umbilical system and will be remotely actuated.

The main recommendation here is the realization that initial pressurization of the LOx tank can best happen via the LOx umbilical. It only requires one extra branch in the feed system, just before the umbilical connection at the ground, towards a helium supply. This has multiple advantages:

1. The helium required for initial pressurization does not need to come from the tank on-board the rocket. This could save something in the order of 5 to 10% of helium mass, and thus helium tank volume. (Depending on initial ullage size.)

2. The time between initial pressurization and launch can be longer. When pressurizing, the inflowing helium starts cooling down to the LOx temperatures. If this initial helium is supplied from a ground vessel, this is no problem as the vessel on ground likely contains more than sufficient helium to compensate this.

3. The helium injection via the umbilical also acts as a inert gas purge of the umbilical before disconnect. Making the disconnect safer, as there is no chance of LOx being spilled.

4. This initial pressurization means that effectively there really is only one gas present in the ullage during expulsion. This means the assumptions made in the model will be more valid. This improves the predictive capability of the code.

---

[4]Although for helium this may need to be reconsidered. To fill the on-board tank with high pressure helium you will need some kind of pump like a gas-booster that will pump the helium from a bottle at lower pressure to 200 bar or more in the flight tank. This pumping is likely going to be a slow process.

A consideration should be the speed at which to pressurize. To avoid excessive pressure and temperature fluctuation due to LOx boiling off because of its contact with the warm helium bubbling through, it is recommended to do this pressurization rather slowly.

A.4. Effect of gravity on tank pressurization

Does gravity have any effect on the tank pressure? For large, pump-fed rockets the answer is usually yes. The effect of gravity on the tank pressure can be quite significant because the pressure in the tank is so low to start with. For pressure-fed rockets however, the answer is no. Pressure-fed rocket engine tanks operate at a far higher tank pressure (usuall in the order of 30 bar at the least), and the tanks are relatively small and short because of the high pressure.

As an example for the test setup constructed in this thesis: The tank here contained a column of approximately 0.65 m of LN2 at maximum under normal gravity conditions. As LN2 weighs about $800 \, \mathrm{kg \, m^{-3}}$ at atmospheric pressures, this leads to a pressure differences of $\rho g h = 800 \cdot 9.81 \cdot 0.65 = 5 \cdot 10^3$ Pa = 0.05 bar. This is an amount that is 0.2% of 30 bar, and it is decreasing rapidly as soon as the tank empties. It is completely negligible.

For another example: Consider a tank like that for the "students to space" rocket (see appendix C) of 2.5 m long, filled with LOx ($\rho = 1100 \, \mathrm{kg \, m^{-3}}$) and accelerating upwards at 5 g. The pressure caused by the liquid column in this case becomes $\rho a h = 1100 \cdot 5 \cdot 9.81 \cdot 2.5 = 1.35$ bar. This is just under 4.5% of 30 bar. So in this case the pressure caused by the liquid column could be considered as an influence on design, but still the effect is marginal.

B

Analytical relations for tank pressurization

This appendix to the pressurization thesis report goes into depth on a number of analytical relations with respect to tank pressurization and pressurized expulsion.

Section B.1 discusses tank pressurization and the effects that come into play here. Specifically related to the increase in gas temperature that is observed when a tank is pressurized. This is something that may seem counter-intuitive at first, but is actually a logical result of the thermodynamics involved.

Section B.2 is used for the full derivation and discussion of the standard tank pressurization formula as given by Sutton[58] and Ring[52].

Section B.3 concludes with various nodes on the tank collapse factor.

B.1. Analytical approach to tank pressurization

Starting from a rocket engine system that has just been loaded with the propellants and the pressurants, the first step that will take place is the propellant tank pressurization. Pressurant gas (assumed to be helium for this section) is allowed to flow from the pressurant tank into the ullage volume to bring it to the desired pressure. How much helium is required for this can be calculated analytically.

First the analytical ideal situation is discussed, when only one gas species is considered, in section B.1.1. Section B.1.2 then discusses a number of considerations when dealing with multiple gas species in the system.

B.1.1. Tank pressurization formula

The calculation of how much gas is required to pressurize a certain volume while the gas is in equilibrium is very straightforward: Just use the ideal gas law at start and end to find the amount of extra gas required for pressurization:

$$m_{in} = m_F - m_i = \frac{P_{prop} V_u}{R T_{prop}} - \frac{P_i V_u}{R T_i}$$

That is the equation when the gas in the ullage volume has been allowed to fully come to thermodynamic equilibrium with the propellant in the tank. However, usually pressurization is only done a limited time before the propellant needs to be pushed out of the tank. Which means the ullage gas does not achieve thermal equilibrium. Furthermore, the gas in the ullage volume is actually very much heated during pressurization, because it is being compressed. This needs to be kept in mind if any heat sensitive materials are used in the tank.

The pressurization of the ullage volume can be considered as a standard textbook example. Gas is allowed to flow from a high pressure reservoir into a small container that is initially at lower pressure or evacuated. Elliot and Lira present such and example in their textbook as well[28]. The assumptions in the calculation are that the reservoir is at a constant temperature and pressure, and that the container is thermally insulated. For the specific case of the pressurization of a propellant tank, this means firstly

that the pressurant tank must be sufficiently big so that the pressurization process does not require a significant amount of the pressurant in the tank, and secondly that no heat transfer takes place between the ullage volume and the tank wall and propellant surface. As a third point it also means that no mass transfer can take place between ullage volume and propellant. So no condensation, evaporation or dissolving can take place. The first assumption is usually a valid one, but the second and third assumption are likely not true. Nonetheless, the result for the fully insulated case together with the ideal gas law for thermal equilibrium form the lower and upper bound respectively of the amount of pressurant needed.

The start situation assumes that the ullage volume V is already filled with a mass m_i of pressurant gas at temperature T_{ini} and pressure P_{ini}. The pressure that needs to be achieved through pressurization is P_F. This is achieved by a letting an amount of pressurant gas m_{in} flow into the tank with constant enthalpy h_{in}. The energy balance for the system is written as follows:

$$E_{start} = E_{end} \tag{B.1}$$
$$m_i u_i + m_{in} h_{in} = m_F u_F \tag{B.2}$$

On the left in equation B.2 the energy in the ullage volume at the start plus the total enthalpy of the pressurant flowing in is placed. On the right is the final situation with a mass m_F and internal energy u_F. To rewrite the right side $u_F = C_v T_F$ and the ideal gas law on the final situation can be used.

$$m_i u_i + m_{in} h_{in} = m_F C_v \frac{P_F V}{R m_F} \tag{B.3}$$
$$m_i u_i + m_{in} h_{in} = P_F V \frac{C_v}{R} \tag{B.4}$$
$$m_{in} = \frac{1}{h_{in}} \left(P_F V \frac{C_v}{R} - m_i u_i \right) \tag{B.5}$$
$$m_{in} = m_i \left(\frac{P_F}{P_i} - 1 \right) \frac{u_i}{h_{in}} \tag{B.6}$$

Note that in all the equations in this section, R is the specific gas constant, and the values of u and h are per mass unit. The final simplification step involves the ideal gas law for the start situation. Equation B.6 gives the amount of pressurant needed for initial pressurization without heat transfer. The total mass in the ullage volume at the end can easily be calculated using $m_F = m_i + m_{in}$. Using this and the ideal gas law, the equation for the final temperature can be derived, which results in equation B.7.

$$T_F = \frac{P_F V}{R m_F} = \frac{P_F}{P_i} T_i \left[\left(\frac{P_F}{P_i} - 1 \right) \frac{u_i}{h_{in}} + 1 \right]^{-1} \tag{B.7}$$

As an example of how high this temperature can rise: For a ullage volume initially filled with helium at 1 bar and 100 K, that is pressurized to 35 bar by helium from a 200 bar, 293 K tank, the temperature in the ullage volume can rise to 451 K. An increase of 350 K. A gas at high temperature like this in a cryogenic will of course quickly dissipate that heat to tank walls and propellant.

B.1.2. Multiple species: condensation and gas mixtures

Equations B.6 and B.7 represent the situation when the gas initially in the ullage volume and the pressurant gas are the same species. However this is usually not the case. The ullage volume is initially often filled with propellant vapour and is pressurized by an inert gas like helium.

Even without taking into account condensation and evaporation, this already complicates the situation quite significantly. A full analytical expression is no longer possible, mostly because the relation between temperature and internal energy for mixtures is no longer a simple linear formula with a factor C_v, specifically not when it concerns a combination of non-similar gasses like helium and oxygen. It is however possible to achieve a result that is very easily solvable if a look-up table or computer program (like CoolProp) is available to relate temperature to internal energy. This can be done by doing the

same analysis as in section B.1.1, but now using the only the ideal gas law. It is also more convenient to write the amounts of gas in molar quantities instead of in masses. In the following equations R_u is the universal gas constant, and values of u and h are per mole. The species initially in the ullage volume is indicated with subscript A, while the pressurant gas species is indicated with subscript B.

$$E_{start} = E_{end} \tag{B.8}$$
$$n_A u_A + n_B h_B = n_F u_F \tag{B.9}$$
$$\tag{B.10}$$

Now the molar balance $n_F = n_A + n_B$ and the ideal gas law can be used.

$$n_A u_A + (n_F - n_A) h_B = n_F u_F \tag{B.11}$$
$$\frac{P_A V}{R T_A} u_A + \left(\frac{P_F V}{R T_F} - \frac{P_A V}{R T_A} \right) h_B = \frac{P_F V}{R T_F} u_F \tag{B.12}$$
$$\frac{P_A}{T_A} u_A + \left(\frac{P_F}{T_F} - \frac{P_A}{T_A} \right) h_B = \frac{P_F}{T_F} u_F \tag{B.13}$$
$$\frac{P_A}{P_F} \frac{1}{T_A} T_F u_A + \left(1 - \frac{P_A}{P_F} \frac{1}{T_A} T_F \right) h_B = u_F \tag{B.14}$$
$$\frac{P_A}{P_F} \frac{1}{T_A} (u_A - h_B) T_F + h_B = u_F \tag{B.15}$$

To simplify notation we introduce the parameter Q:

$$Q T_F + h_B = u_F \quad \text{where} \quad Q \equiv \frac{P_A}{P_F} \frac{1}{T_A} (u_A - h_B) \tag{B.16}$$

As mentioned, this equation cannot be solved analytically because the variable u_F is a complicated function of the temperature T_F, the pressure P_F and the molar fraction of the mixture. The molar fraction for the mixture is most easily expressed as the molar fraction of substance A.

$$u_F = f(P_F, T_F, y_B) \quad \text{where} \quad y_A = \frac{n_A}{n_F} = \frac{P_A}{P_F} \frac{T_F}{T_A} \tag{B.17}$$

Using equations B.16 and B.17 the final temperature of the gas mixture, and the molar fraction can be determined. This can then be fed back into the ideal gas law to retrieve the total amount of moles of pressurant needed.

Using this method to analyse the same example as in the previous section, (ullage volume initially at 1 bar and 100 K; pressurized to 35 bar by helium from a 200 bar, 293 K tank) but now initially having oxygen vapour in the ullage, the temperature in the ullage volume rises to 430 K. The replacement of the gas in this case thus lowers the temperature rise by 20 K. The temperature rise however is still very substantial.

Using this method, most of the non-ideal gas effects introduced by using mixtures are taken care of. However the effect of heat transfer still remains. General heat transfer equations can easily be obtained from textbooks such as that from Incropera et al. [15].

Mass transfer is another major issue that needs to be dealt with. Gas can condense from the ullage volume onto tank walls and on the propellant surface, pressurant gas can diffuse into the propellant and propellant can evaporate into the ullage gas. If a ullage section is initially filled with propellant vapour and is pressurized, this vapour in the ullage will not directly condense as it is heated up by compression. If it cools down at the walls, vapour may condense again. If the surface of the propellant is stirred and/or heated propellant may evaporate again. Overall, if the ullage volume is sufficiently stirred, and is allowed to get into thermal equilibrium with the propellant vapour, the ullage gas will be fully saturated with the propellant vapour. At that point a molar fraction of propellant will be present in the ullage volume as dictated by Raoult's law[15] and the definition of partial pressures. The molar

fraction is than equal to the ratio of the total gas pressure and the vapour pressure of the pure propellant vapour, as shown in equation B.18.

$$y_A = \frac{P_A}{P_{A,sat}}$$

(B.18)

Also some amount of the pressurant will dissolve into the propellant. However, when the substances are chosen correctly, this is usually a very minor effect. Reaction balance coefficients for specific mixtures can be found in literature, such as the paper by Robson[53] for a large selection of propellants and pressurants, and Dresar[27] for the specific case of helium and liquid nitrogen.

B.2. Analytical approach to pressurized expulsion

It is possible to estimate analytically the amount of pressurant gas required for expulsion of all propellant from the tank. The derivation of the analytical equation is introduced by Sutton[58], and a similar equation is given by E. Ring[52]. The equations are slightly different because of the inclusion of the compressibility factor (Z) by Ring in his equation. The assumptions involved with the derivation of this equation, and the exact steps to get to it are not directly clear from the books by Sutton and Ring. Therefore the equation leads to confusion now and then, with questions on its validity and on when and where it is applicable[65]. To hopefully clear up the situation completely, this section gives the full, step by step, derivation of the pressurant gas mass equation of Sutton and Ring.

First, in section B.2.1 the main equation is worked out, starting from an energy balance, assuming no heat transfer. All assumptions and derivations are given step by step. After this follows section B.2.2 to explain the version of the equation that Ring uses and the problem that this equation has. Section B.2.3 goes back to the equation of Sutton to develop formulas for all other important system parameters. Then finally, developing beyond the work of Ring and Sutton in section B.2.4, it is shown how the equations would evolve if instead of no heat transfer, perfect heat transfer is assumed.

B.2.1. Derivation by Sutton

For the derivation the system is divided in two main sections: a pressurant tank and a ullage section in the propellant. Gas flows from the pressurant tank into the ullage volume. The pressurant tank has a constant volume but a changing pressure. The ullage volume is at a constant pressure (because of the pressure regulator) but is changing in volume, as propellant is forced out of the tank. The ullage volume starts at zero and ends at the full propellant tank volume. Next to these pressure and volume assumptions, it is assumed that the gas can be treated as an ideal gas and that there is no heat or mass transfer anywhere in the system to or from the gasses.

The derivation starts with a simple energy balance equating the energy at the start and at the end of the process. In the following equations the subscript 0 refers to the situation before the start of the pressurized expulsion. The subscript $pres$ refers to the pressurant tank, and the subscript u to the gas in the ullage volume, both at the end of expulsion. The value V_{prop} is the total volume of the propellant tank.

$$E_{start} = E_{end}$$

(B.19)

$$U_0 = U_{pres} + U_u + W$$

(B.20)

$$m_0 c_v T_0 = m_{pres} c_v T_{pres} + m_u c_v T_u + P_u V_{prop}$$

(B.21)

Equation B.20 is basically a statement of the first law of thermodynamics: $\Delta U = Q - W$. The heat transfer it zero, so the change in internal energy of the system equals the amount of work done by the system. Equation B.21 is where Sutton starts his derivation[58]. On the left is the energy in the gas at the start of the pressurized expulsion. It is assumed the gas is only present in the pressurant tank. On the right the energy at the end is summed with three terms. The first is the energy in the pressurant tank at the end of the expulsion, the second then energy in the gas in the propellant tank, and the third term is the work done by the pressurant gas during the expulsion. As the pressure in the propellant tank is assumed to be constant during the process, the work done by the gas is simple the multiplication of this pressure with the propellant tank volume. Using the ideal gas law, $PV = mRT$, equation B.21 can

be rewritten to:

$$m_0 c_v T_0 = \frac{c_v P_{pres} V_{pres}}{R} + \frac{c_v P_u V_{prop}}{R} + P_u V_{prop} \tag{B.22}$$

$$m_0 c_v T_0 = \frac{c_v}{R} \left(P_{pres} V_{pres} + P_u V_{prop} + \frac{R}{c_v} P_u V_{prop} \right) \tag{B.23}$$

$$m_0 = \frac{1}{RT_0} \left(P_{pres} V_{pres} + \left(1 + \frac{R}{c_v} \right) P_u V_{prop} \right) \tag{B.24}$$

Using the ideal gas relations $c_p = c_v + R$ and $\gamma = c_p/c_v$, this can be rewritten to:

$$m_0 = \frac{1}{RT_0} \left(P_{pres} V_{pres} + \gamma P_u V_{prop} \right) \tag{B.25}$$

Again the ideal gas law can be used (applying it on the start situation): $V_{pres}/(RT_0) = m_0/P_0$.

$$m_0 = \frac{P_{pres} m_0}{P_0} + \gamma \frac{P_u V_{prop}}{RT_0} \tag{B.26}$$

$$m_0 \left(1 - \frac{P_{pres}}{P_0} \right) = \gamma \frac{P_u V_{prop}}{RT_0} \tag{B.27}$$

$$m_0 = \frac{P_u V_{prop}}{RT_0} \left(\frac{\gamma}{1 - P_{pres}/P_0} \right) \tag{B.28}$$

Equation B.28 is the equation presented by Sutton and gives the required pressurant mass as a function of the starting pressure and temperature of the pressurant tank, and the volume and pressure of the propellant tank[58].

B.2.2. Derivation by Ring (Including compressibility)

As is done by Ring, it is possible to include the compressibility factor Z in the equation to include for some non-ideal effects of the pressurant gas[52]. The derivation runs in the same manner up to equation B.25. After this equation the gas law for the start situation is written as: $V_{pres}/(RT_0) = Z_0 m_0/P_0$. Using this formulation and developing the equation further leads to the equation presented by Ring:

$$m_0 = \frac{P_u V_{prop}}{RT_0} \left(\frac{\gamma}{1 - Z_0 P_{pres}/P_0} \right) \tag{B.29}$$

The compressibility factor is a simple correction on the ideal gas formula to try and correct for certain non-ideal gas effects such as the size of the molecules and their mutual attraction force. For Helium the value for Z at room temperature ranges between 1 at 1bar and 1.095 at 200bar (data from CoolProp).

Because it includes at least some non-ideal gas effects, it could be expected that the formula from Ring would better predict the amount of pressurant gas required. However this is not always the case. During calculations for this thesis it was found out that in certain cases this "correction" is actually detrimental to the equation's predictive power. If the ratio P_{pres}/P_0 of pressurant tank pressure at the start and end is a number close to unity, the equation severely over-predicts the amount of pressurant required. This can be best illustrated with an example.

Imagine a system where the pressurant tank is filled with helium at room temperature and at 200 bar pressure. This means $P_0 = 200$ bar and $Z_0 = 1.095$. After the pressurization of a propellant tank is completed, the tank still has a pressure of 170 bar left, so $P_{pres} = 170$ bar. This is a situation that might occur in test setups, where the pressurant tank is oversized compared to the propellant tank to facilitate multiple tests before a refill is required. In the equation of Sutton (B.28) the term $1/(1 - P_{pres}/P_0)$ would work out to a value of 6.67. If the equation of Ring (B.29) is used the term would instead look like $1/(1 - Z_0 P_{pres}/P_0)$ and filling in the numbers gives a value of 14.4. This results in a more than twofold increase in predicted pressurant mass between the two equations. Clearly this goes beyond what would be expected of a "correction" for some small non-ideal gas effects. Because of the compressibility factor the term below the division bar first goes to infinity when the pressure ratio approaches unity (at the point where $P_{pres}/P_0 = 1/Z_0$). Eventually the equation even turns out negative pressurant gas masses.

From this example it can be concluded that, although the idea of correcting for some non-ideal effects seems nice, it can have some unexpected backlash. The correction of Ring should not be used when the pressure ratio for the pressurant is expected to be close to one. This is especially of concern for systems in test setups but may also be relevant for pressure fed systems. For a pressure fed system starting at $P_0 = 200$ bar and ending at $P_{pres} = 50$ bar the formula of Ring predicts 3.3% more helium usage than the formula of Sutton. If this is indeed a valid correction would need to follow from actual testing, and even then it must be considered if the small difference it produces is worth the risk. Use equation B.29 with caution.

Following on this, it is possible to ask what the magnitude of uncertainties concerning real-gas effects actually are. It is possible to cut the derivation presented by Sutton short and to solve the equation for initial mass mostly by iterative solutions using real-gas properties from a database (CoolProp). It turns out that the deviation between the two methods is not more than 5% in the large majority of the cases (analysed over a range of cases for different start and end pressures and temperatures). If it does deviate more, this only occurs when the ratio P_{pres}/P_0 is very close to unity. So it turns out that also the equation of Sutton needs to be used carefully in some situations.

B.2.3. Further development
From equation B.28 the further unknowns of the system can be derived. The volume of the pressurant tank can be gotten from the start situation equation of state:

$$V_{pres} = \frac{m_0 R T_0}{P_0} \tag{B.30}$$

The temperature in the pressurant tank at the end (T_{pres}) can be gotten with the isentropic expansion relations, as within the pressurant tank such an expansion takes place.

$$T_{pres} = T_0 \left(\frac{P_0}{P_{pres}} \right)^{\frac{1-\gamma}{\gamma}} \tag{B.31}$$

Likewise, the mass left in the pressurant tank at the end of the process (m_{pres}) can also be found using isentropic relations:

$$m_{pres} = m_0 \left(\frac{P_{pres}}{P_0} \right)^{1/\gamma} \tag{B.32}$$

The mass in the propellant tank can be found with a simple mass balance: $m_0 = m_u + m_{pres}$.

$$m_u = m_0 - m_{pres} \tag{B.33}$$

$$m_u = m_0 \left(1 - \left(\frac{P_{pres}}{P_0} \right)^{1/\gamma} \right) \tag{B.34}$$

And finally the temperature of the gas in the propellant tank can be gotten with the equation of state:

$$T_u = \frac{P_u V_{prop}}{R m_u} \tag{B.35}$$

$$= \frac{P_u V_{prop}}{R m_0} \frac{1}{1 - \left(P_{pres}/P_0 \right)^{1/\gamma}} \tag{B.36}$$

$$T_u = T_0 \frac{1}{\gamma} \frac{1 - P_{pres}/P_0}{1 - \left(P_{pres}/P_0 \right)^{1/\gamma}} \tag{B.37}$$

B.2.4. Including heat transfer
Sections B.2.1 and B.2.3 give the equations for the most simple case: No heat transfer at all in the system. This is the most important analytical case, and the standard reference case for the calculation of the collapse factor (see section B.3). However this is likely far from the real situation where heat transfer might occur between the pressurant tank and the pressurant, and between the ullage gas and

the propellant plus propellant tank. A general situation involving heat transfer can be described by adding a total heat transfer Q to equation B.21:

$$m_0 c_v T_0 = m_{pres} c_v T_{pres} + m_u c_v T_u + P_u V_{prop} - Q \tag{B.38}$$

If heat transfer in the system now is taken into account, this can be most easily characterized by two parameters. The first is the polytropic coefficient k for the expansion process in the pressurant tank. When $k = \gamma$ the process is adiabatic and when $k = 1$ the process is isothermal. Any values in-between give values for more or less heat transfer from pressurant tank to pressurant gas. The second parameter is the final temperature T_F of the ullage gas. It is again assumed the ullage gas is homogeneous in temperature. This final temperature will be somewhere between that of the initial pressurant gas, T_0, and the propellant tank temperature. Using these extra two parameters, the gas mass in the pressurant tank at the end, m_{pres}, can be specified using the polytropic relations, and the gas mass in the propellant tank at the end, m_u, can be fully specified using the ideal gas law:

$$m_{pres} = m_0 \left(\frac{P_{pres}}{P_0} \right)^{1/k} \tag{B.39}$$

$$m_u = \frac{P_u V_{prop}}{R T_F} \tag{B.40}$$

These two values can then be used in the mass balance of the system to calculate the total pressurant mass required at the start:

$$(m_0)_Q = \frac{P_u V_{prop}}{R T_F} \frac{1}{1 - \left(P_{pres}/P_0 \right)^{1/k}} \tag{B.41}$$

If desired, this value can be plugged back into the equation for m_{pres}. Also it can be used again in equation B.38 to find the value of Q, which might be an interesting parameter to evaluate the heat flows in the system.

B.3. Tank collapse factor

The tank collapse factor is a figure of merit that gives and indication of how efficient a tank pressurization system is making use of the available pressurant gas. The tank collapse factor is defined as the ratio of the actual gas mass flowing into the tank during pressurization and expulsion versus the ideal gas mass flowing into the tank[20]. In equation form this can be written as:

$$K \equiv \frac{(m_u)_{real}}{(m_u)_{ideal}} \tag{B.42}$$

The ideal ullage mass in this case is defined by the equations of Sutton (B.28 and B.34). Normally the value of K is estimated for a system, which allows for the calculation of the real ullage mass. However, it can also be turned around: The collapse factor can be estimated by using an analytical equation for $(m_u)_{real}$. The most general equation for this is equation B.40, which is basically the ideal gas law. Using this, and the ideal ullage mass from the equations of Sutton, this leads to an estimation equation for the collapse factor:

$$K = \frac{P_u V_{prop}}{R T_F} \left[\frac{P_u V_{prop}}{R T_0} \left(\frac{\gamma \left(1 - \left(P_{pres}/P_0 \right)^{1/\gamma} \right)}{1 - P_{pres}/P_0} \right) \right]^{-1} \tag{B.43}$$

$$= \frac{T_0}{T_F \gamma} \frac{1 - P_{pres}/P_0}{1 - \left(P_{pres}/P_0 \right)^{1/\gamma}} \tag{B.44}$$

Of course this collapse factor estimation does not take into account any mass transfer. This estimation equation allows to determine the maximum and minimum values for the collapse factor by inserting the minimum and maximum values for T_F. The minimum value that can be expected will be equal to the

temperature of the propellant. The maximum temperature that can be expected is equal to the initial temperature T_0. That is the temperature that would be gotten in the ullage if the expansion process in the pressurant tank is isothermal and there is no heat loss in the propellant tank.

As an example, let's consider a liquid oxygen tank ($T_{prop} = 90$ K) that is pressurized with helium to $P_u = 30$ bar. The helium tank is initially at $P_{pres} = 200$ bar and $T_0 = 293$ K. Using equation B.44 this results in a minimum collapse factor of $K = 0.75$ and a maximum of $K = 2.45$. The minimum value is actually lower than one. This is logical, because the estimation of an isothermal process in the pressurant tank means that heat is drawn into the system from the environment.

Students-to-space rocket simulation

This appendix summarizes the simulation results from a "student-to-space" rocket simulation case. The case is that of a pressurization system for a sounding rocket aiming for space using liquid oxygen. The input parameters have been taken as an approximation of those found in chapter 2. The analysis conducted is the same as that for the test setup case as discussed in section 3.4, and the conclusion are the same as well. The results here are presented just as is, for the interested reader.

Table C.1 gives an overview of the simulation settings. An extra parameter introduced here is the pressure regulator gas flow multiplier. This is a linear multiplier that can be applied to the gas flow estimate from the pressure regulator class (section 3.1.3). This was introduced because it was found that the pressure regulator used during the physical tests, and thus the one modelled in the code, is by far not suited for usage in a larger rocket. It just cannot deliver the flow of helium to maintain anything close to a desired tank pressure. It was found that when taking the gas flow to be 10 times as large, the simulations produce acceptable tank pressure histories.

Table C.2 gives the main numerical output parameters as produced by the differen simulations.

The average pressure and temperature are again plotted figures C.1 and C.2 respectively.
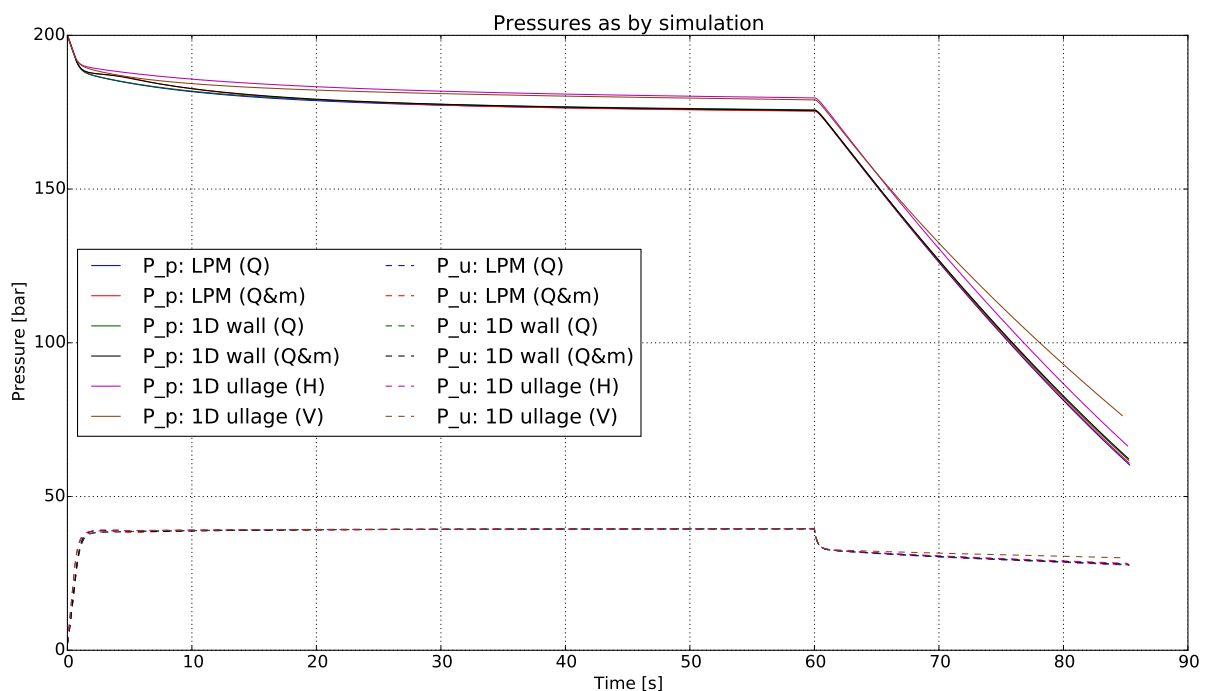
Figure C.1: Pressure versus time in the ullage and pressurant tank for the "students to space" rocket simulation.

Table C.3 gives the overview of the sensitivity analysis results.

Table C.1: The most important initialization parameters for the conducted simulations.

Parameter	Value	Unit
Timing		
Timestep	10	ms
Pressurization time	60	s
Propellant		
Propellant	Oxygen	-
Initial pressure	2	bar
Initial temperature	90	K
Propellant tank		
Diameter	0.32	m
Inner length	2.3	m
Wall thickness	5	mm
Bulkhead thickness	30	mm
Ullage fraction at start	0.1	-
Number of wall segments	50	-
Top bulkhead initial temperature	100	K
Number of ullage sections (start)	5	-
Number of ullage sections (end)	50	-
Ullage initial temperature	100	K
Pressurant		
Pressurant	Helium	-
Initial pressure	200	bar
Initial temperature	293	K
Force constant temp. inflow?	False	-
Pressurant tank		
Volume	80	L
Inner length	2.3	m
System		
Exit orifice diameter	14	mm
Pres. regulator set pressure	40	bar
Pres. regulator mass flow multiplier	10	-

Table C.2: The main system parameter resulting from the simulations for the "students to space" rocket simulation.

|		Collapse factor [-]	Expulsion time [s]	Avg. tank pressure [bar]	Inflowing gas mass [kg]	Pressurant pressure (end) [bar]
1	LPM (Q)	1.35	25.3	30.1	1.35	60.2
2	LPM (Q&m)	1.34	25.3	30.1	1.34	60.8
3	1D wall (Q)	1.32	25.3	30.2	1.33	61.8
4	1D wall (Q&m)	1.32	25.2	30.3	1.33	62.3
5	1D ullage (H)	1.27	25.2	30.4	1.28	66.4
6	1D ullage (V)	1.13	24.7	31.5	1.15	76.3

Fluid temperatures as by simulation
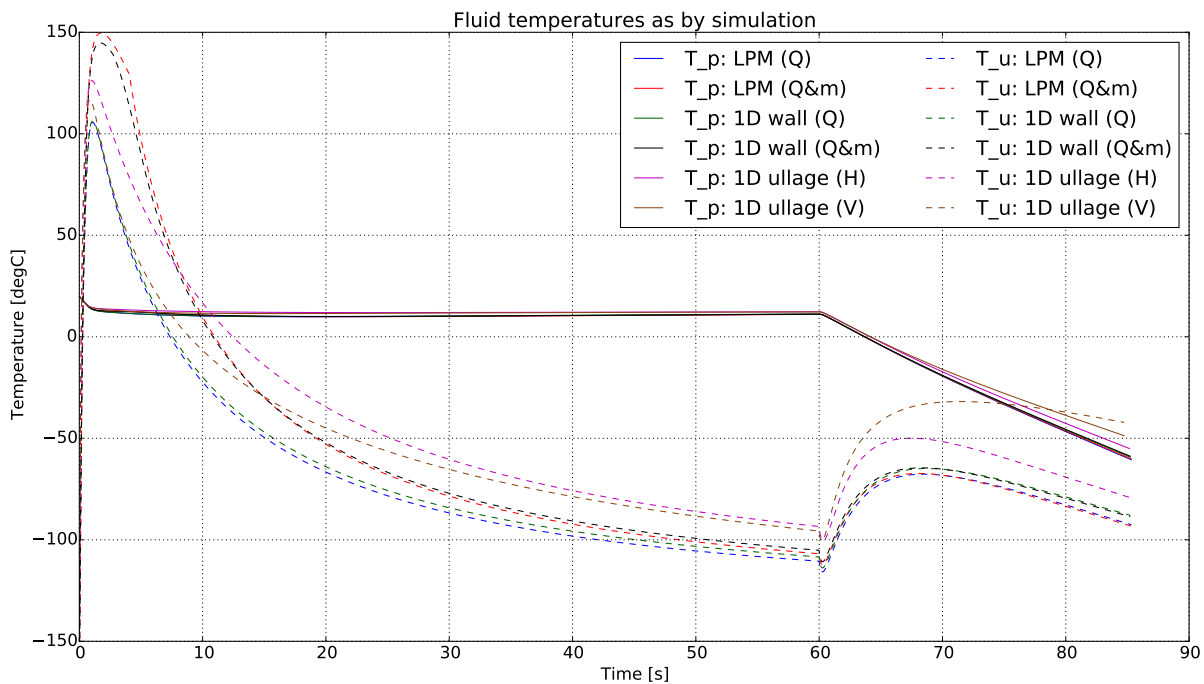
Figure C.2: Temperature versus time in the ullage and pressurant tank for the "students to space" rocket simulation.

Table C.3: Results of the sensitivity analysis. Changes in the parameters are expresed as percentual change with respect to the nominal output of the simulation. Differences lower than 0.5% have been removed from the table.

		Collapse factor [-]	Expulsion time [s]	Avg. tank pressure [bar]	Inflowing gas mass [kg]	Pres. pressure (end) [bar]
Nominal result		1.35	25.3	30.1	1.35	60.2
Timestep	-50%	-1%	-1%	–	–	1%
	+100%	-1%	-1%	–	–	1%
Pres. Reg. Rise time	-50%	-1%	-1%	–	–	1%
	+100%	-1%	-1%	–	–	1%
Pres. Reg. Mass flow	-10%	–	–	-3%	-2%	5%
	+10%	-1%	-2%	1%	2%	-3%
Heat transfer	-50%	-8%	-2%	1%	-6%	5%
	+100%	8%	–	-3%	7%	-4%
Tank diameter	-10%	1%	-20%	1%	-20%	36%
	+10%	-3%	22%	-2%	22%	-33%
Tank length	-10%	–	-10%	1%	-11%	19%
	+10%	-1%	11%	-1%	11%	-18%
Initial ullage fraction	-10%	-2%	1%	–	–	1%
	+10%	1%	-1%	–	1%	–
Pressurant tank volume	-10%	-2%	–	-1%	1%	-17%
	+10%	1%	–	–	–	16%
Pressurant tank pressure	-10%	-2%	1%	-1%	–	-23%
	+10%	–	–	1%	1%	25%
Pressurant tank temperature	-10%	-3%	–	-1%	7%	4%
	+10%	2%	–	–	-5%	-3%
Pres. Reg. Set pressure	-10%	2%	5%	-9%	-8%	16%
	+10%	-3%	-4%	8%	8%	-14%
Orifice diameter	-10%	1%	21%	3%	7%	-9%
	+10%	-2%	-16%	-4%	-5%	9%

D
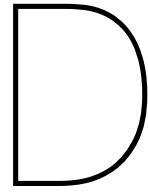
Test procedures

Included in the following pages are the test procedures used during the axial injection tests on the 17th of January 2017. The procedures have been written in cooperation by Rob Hermsen, Juan Mussini, Daniel Schwerig and Mathijs van de Poel. The procedures have been checked and approved by the DARE safety board. The procedures have been generated using the DARE template for test procedures developed by Daniel Schwerig.

Cryogenic Tank Pressurization test 1: Radial injection

Test Procedures

Authors:
Rob Hermsen, Juan Mussini,
Daniel Schwerig, Mathijs van de Poel

Version:
V 2

Monday 16th January, 2017

Color labeling

Color	Meaning	Dangers associated
	Pre test day phase	None
	System setup phase	None
	Systems check phase	Pneumatic actuation lines pressurized
	Pressure change warning	Pressure change
	Handling of cryogenic fluids / systems with cryogenic temperatures phase/warning	Cryogenic temperatures
	Major warning	Various
	Minor warning	Various

Abbreviations

BV	Bleed valve
CGR	Compressed Gas Regulator
CP	Command post
FV	Fill valve
LN2	Liquid nitrogen (cryogenic liquid)
MV	Main valve
N2	Nitrogen gas
OSO	Operational Safety Officer
SUP	Test supervisor: Michel van den Brink (3ME)
TC	Test Conductor
TO	Test Operator
TOD	Tank Opening Device

A - Pre testday operations			
ID	**Check**	**Description**	**Comments**
A1		Assemble system (tank + feed system):	
A2		Find small N2 bottle + pressure regulator for pneumatic actuation	
A3		Ensure that there is enough pressure on the small N2 bottle for actuation	
A4		Prepare 3 copies of this document	
A5		Ensure transport is available (cart)	
A6		Calibrate the load cells	
A7		Zero the pressure sensors (software calibration) and record the zero-ing value	
A8		Test-run all valves	
A9		Test-run the procedures	
A10		Make sure team members and safety officers are available	
A11		Collect all items from the packing list	
A12		One day before test: Position RIO onto test bench	
A13		One day before test: Connect sensors and actuators to RIO	
A14		One day before test: Charge the batteries of the camera	
A15		One day before test: Check weather prediction for test day and evaluate if test can continue	

System State:
- Test setup assembled with RIO attached
- All equipment and tools set ready for transport to test site

B - Initial Setup			
ID	**Check**	**Description**	**Comments**
B1		Position test bench onto test location (Place test bench feet onto wooden plates)	
B2		Set up CP table and laptop	
B3		Open text/excel file log to note down important events and observations along with timestamps	
B4		Let CP note the weather conditions in the log (check temperature with thermometer, check windspeed online)	
B5		Check Dewar readiness with SUP (Dewar should be filled with LN2 by SUP)	
B6		Check availability of cryo compatible safety gloves with SUP	
B7		Check availability of oxygen deficiency detection devices with SUP	
B8		Assist SUP in moving the dewar near the test setup.	
B9		Place wooden plates on grass over which the dewar can be moved towards the testbench	
B10		Place dump-box in front of system exhaust	
B11		Remove tape from main exhaust orifice	
B12		Remove tape bleed valve exhaust	
B13		Attach small N2 bottle + regulator to pneumatic actuation lines	
B14		Attache pressurant bottle load cell platform to RIO (second load cell connection)	
B15		Measure the weight of the He bottle with the person scale. Report this value to CP so that it can be noted down.	
B16		Setup He pressurant bottle on measurement platform and losely secure with chain at test bench	
B17		Attach pressure regulator to He bottle	
B18		Attach pressurant hose to pressure regulator	
B19		Roll out power cable from 3ME to CP	
B20		Roll out power cable from CP to RIO	
B21		Roll out data cable from CP to RIO	
B22		Attach USB power cable to capacitive sensor	
B23		Turn on RIO	
B24		Check connection with RIO	

B25		Check that all sensors give a read-out (i.e. are not maxed out or at zero voltage output. Check for noise fluctuations in the value.)	
B26		Set of test location with red-white tape/chain	
B27		Insert pegs into ground for securing the test bench	
B28		Attach tension bands between pegs and test bench	
B29		Install camera's on test setup (Do not turn on)	
B30		Gather all people and discuss location layout • Recap overall course of the procedures • Explain/show escape path in case of detection of oxygen deficient atmosphere	

System State:
- The run tank with feed system is set up
- The pressurization lines are connected but not yet pressurized
- The sensors and valves are connected to the RIO
- The test location is set of with red-white tape

C - Pre-test operations			
ID	**Check**	**Description**	**Comments**
C1		Clear the area, only OSO, TC, TO and SUP are allowed on location	
C2		Make sure phones are turned off or left at CP	
C3		Make sure test location is properly closed off (discuss with SUP)	
C4		Make sure area is secure	
C5		Make sure no cables on the ground are a trip hazard	
C6		Check that system is securely attached to ground	
C7		Visually inspect test setup for possible loose connections in feed system or sensor cables	
C8		Check bolted connections at all feed system parts for hand-tightness	
C9		Check all feed-system connections (hand-tight)	
C10		Check correct orientation of BV, FV and MV (arrow on valves pointing away from tank.)	
C11		Check that the small N2 bottle + CGR are correctly set up	
C12		Check that the He bottle + CGR are correctly set up	
C13		Check that the He bottle is positioned centrally on the measurement platform. (The top plate of the platform should not be touching any of the aluminium rods on the side).	
C14		Check that the dump-box has been correctly set up	
C15		Check that the tape has been removed from the main exhaust orifice	
C16		Check that the tape has been removed from the BV exhaust	
C17		Remove plastic cap from the pressure relief valve	
C18		Check that no parts are resting against the test-bench section measured by the load-cell	
C19		Check that no parts are resting against the He bottle, other than the securing chain from the test bench.	
C20		Check that the He bottle is not leaning against the test bench.	
C21		Inform CP of the completion of the pre-test operations	

System State:
- The run tank with feed system is set up
- The pressurization lines are connected but not yet pressurized
- The pressurant bottle is connected but still unopened
- The sensors and valves are connected to the RIO
- The test location is set of with red-white tape
- The movable dewar is filled with liquid nitrogen (60L, at between 1 to 3 bar, at around -196°celsius)
- The movable dewar is positioned near the test setup.

		D - RIO systems check	
ID	**Check**	**Description**	**Comments**
D1		Inform CP of the start of the RIO systems check	
D2		Make sure all persons on test location wear safety glasses	
D3		Check that RIO is turned on and in safe mode	
D4		Check with CP if they are ready for the systems check (LabView program running)	
D5		Check with CP if all sensors give sensible read-outs: • Temperature sensor TC0 should give a value near environment temperature. • Temperature sensors TC1 through TC15 should all give values near 18 degC (room temperature in the LaikaLab). • All other sensors should give values that show slight noise fluctuations	
D6		Ask CP to start low-speed data acquisition	
D7		Ask CP to zero the tank load cell	
D8		Calibrate the tank load cell with test mass 1 (put test mass at top of the aluminium tank holding structure for at least 10 seconds)	
D9		Calibrate the tank load cell with test mass 2 (put test mass at top of the aluminium tank holding structure for at least 10 seconds)	
D10		Ask CP to zero the pressurant load cell	
D11		Calibrate the pressurant load cell with test mass 1 (put test mass at top of the gas bottle for at least 10 seconds)	
D12		Calibrate the tank load cell with test mass 2 (put test mass at top of the gas bottle for at least 10 seconds)	
D13		Ask CP to set both pressure sensors to atmospheric pressure	
D14		Turn RIO to "arm"	
D15		Check Fill Valve actuation (solenoid, listen for click during actuation)	
D16		Make sure the N2 cylinder CGR is closed	
D17		Make sure the N2 cylinder CGR-V is closed	
D18		Slowly open the small N2 cylinder completely	
		The N2-CGR is now pressurized with N2 cylinder pressure—	
D19		Set N2-CGR pressure to 7 bar	

D20		Slowely open the N2-CGR valve	
		The pneumatic actuation lines are now pressurized with 7 bar of nitrogen—	
D21		Check for leaks in the pneumatic actuation line and fix in necessary	
D22		Make sure MV closes and opens properly (request actuation from CP)	
D23		Make sure BV closes and opens properly (request actuation from CP)	
D24		Make sure PV opens and closes properly (request actuation from CP)	
D25		Make sure MV is powered off (and thus opened)	
D26		Make sure BV is powered off (and thus opened)	
D27		Make sure PV is powered off (and thus closed)	
D28		Make sure the He cylinder CGR is closed	
D29		Make sure the He cylinder CGR valve is closed	
D30		Slowly open the He cylinder completely	
		The He-CGR is now pressurized with He cylinder pressure—	
D31		Set He-CGR pressure to 25 bar	
D32		Slowely open the He-CGR valve	
		The pressurant line up to PV is now pressurized with 25 bar of Helium—	
D33		Check for leaks in the connections at the He-CGR and at PV with leak detection spray. If leaks are found: 1. Close the He-CGR valve 2. Ask CP to open PV for 5 seconds to depressurize the line 3. Tighten the leaking connection 4. Slowely open the He-CGR valve again and recheck for leaks. 5. Repeat this process if needed	
D34		Close the He-CGR valve	
D35		Step back from the test bench	
D36		Ask CP to open PV for one second to depressurize the pressurant line	
D37		Close the He-CGR valve	
D38		Turn the RIO to "safe"	

D39		Inform CP of the end of the RIO systems check	

System State:
- The actuation lines are pressurized
- The RIO is ready for measurements and actuation
- The run tank is ready to be filled with liquid nitrogen
- The movable dewar is filled with liquid nitrogen (60L, at between 1 to 3 bar, at around -196°celsius) and positioned near the test bench

E - Filling the run tank			
ID	**Check**	**Description**	**Comments**
E1		Inform CP of start of filling of the run tank	
E2		Check if dewar is properly secured (level ground, wheel locks)	
E3		Remove plastic cap from FV connection port	
E4		Check that all personnel handling the dewar are wearing cryogenic safety gloves	
E5		SUP: Connect dewar hose to FV connection port	
E6		Set the RIO to "arm"	
E7		Check if the area is cleared	
E8		Ask CP to close MV (powered)	
E9		Check with CP that BV is open (unpowered)	
E10		Ask CP to open FV (powered)	
E11		SUP: Slowly open the dewar fill valve partially	
Cryogenic liquid now flows into the run tank—			
When FV, BV, and MV are closed, the tank is fully sealed off. Pressure will start to rise due to evaporation of the nitrogen in the tank.—			
E12		Retreat to CP	

E13		Monitor and control the filling process. Monitor by: • Monitor the load cell, tank mass should be increasing slowly. Continue with next point on procedures if tank mass reaches 22.3kg or does not increase anymore. • Monitor pressure sensors: These should indicate values between 1 and 3 bar. • Monitor thermocouples: These should show decreasing temperatures. They should settle around temperatures of -190degC. • Visually monitor the test setup for any vapor clouds which are not originating from the bleed valve exhaust. If such clouds are observed: assess situation and possibly order CP to close the fill valve and open the main valve. Control by: • Let LN2 flow for 5 minutes. • Close fill valve and bleed valve and let the system sit for 5 minutes to let temperature gradients balance out. • Open bleed valve to depressurize, then open fill valve again for 5 minutes. • Repeat untill all thermocouples show values around or below -190 deg C or untill the dewar is empty. At that point, continue with the next point on the procedures.	
E14		Ask CP to close FV (unpowered)	

System State:
- The run tank is completely chilled down and (partially) filled with LN2
- The fill valve is closed
- The main valve is closed
- The bleed valve is opened
- The dewar is connected to the run tank
- The cryogenic liquid is below 3 bar of pressure

F - Disconnecting the dewar			
ID	Check	Description	Comments
		Disconnecting the dewar will be under guidance of SUP—	
F1		Approach system (only OSO, SUP, TC, TO). WARNING: DO NOT DIS-ARM THE RIO.	
F2		Make sure the person that will disconnect the dewar is wearing cryo-compatible safety gloves and safety goggles or a face shield.	
F3		Close dewar self-pressurization system	
F4		Close dewar hose-valve	
F5		Disconnect dewar hose from fill line connection. Watch out for LN2 coming from the line. Let this spill onto the ground.	
		The connection may be very tight due to different thermal expansion coefficients of the two connected pieces. Discuss situation with SUP if the connection cannot be loosened.—	
F6		Move dewar back to CP	
F7		Discuss next point of action: • If the tank is not filled to 90% fill level (22.3kg) with LN2 or not chilled down to temperature below -190 degC: Refill the dewar (SUP) and restart from part E: Run tank filling. • If the tank is filled to 90% fill level (22.3kg) with LN2: continue with the procedures	

System State:
- The dewar has been disconnected and moved to CP
- The run tank is filled with LN2 at around atmospheric pressure
- The bleed valve is opened

G - Pressurization and expulsion			
ID	**Check**	**Description**	**Comments**
G1		Approach system (only OSO, SUP, TC, TO). WARNING: DO NOT DIS-ARM THE RIO.	
G2		Check if the area is secure	
G3		Turn on top bulkhead GoPro and hand held camera on tripod	
G4		Provide calibration step by placing test mass 1 onto the pressurant cylinder for 10s	
G5		Provide calibration step by placing test mass 2 onto the pressurant cylinder for 10s	
G6		Check that the He-CGR valve is closed	
G7		Ask CP to cycle PV once to check its functioning	
G8		Ask CP to ensure PV is closed (unpowered)	
G9		Read out He cylinder pressure and ask CP to note this pressure.	
G10		Slowly open the He-CGR valve	
The pressurization line up to PV is now pressurized with 25 bar helium—			
G11		Clear the area	
G12		Ask CP to close the bleed-valve	
The tank is now fully closed. Pressure will start to rise due to evaporation of the nitrogen in the tank.—			
G13		Consult with OSO and SUP about a go-ahead on pressurization and LN2 expulsion	
G14		Confirm with CP that the following automatic timer values have been set: • Pres. valve delay = 5s • Pressurization time = 60s • Expulsion time = 50s	
G15		Turn on the GoPro facing the expulsion orifice	
G16		Ask CP to start high-speed data recording	
G17		Ask CP to switch system to automatic mode	
Tank pressurizaiton followed by LN2 expulsion—			
Large scale nitrogen evaporation will occure. May cause an oxygen deficient environment.—			

G18		Start countdown for pressurization and expulsion at T-10	
G19		CP start the automated sequence at T-5	
G20		At T=+50s: Start LN2 expulsion countdown from -10seconds	

<table>
<tr><td colspan="4" style="background:#f44;">

Automated sequence:
- **T=+0s: Start of pressurization of tank (PV opening)**
- **T=+60s: Start of LN2 expulsion (MV opening)**
- **T=+110s: End of LN2 expulsion (MV and PV closing, BV opening)**
—
</td></tr>
</table>

G21		Leave system standing for 1 minute	
G22		Ask CP to switch system to low speed data recording	
G23		Ask CP about system status (tank mass and pressure)	
G24		Ask CP to confirm that PV is closed (unpowered)	
G25		Ask CP to open MV to dump any remaining LN2	

The whole system now contains gaseous N2 at atmospheric pressure. LN2 may still be left in the fill line. This will slowly evaporate. The whole system is still at cryogenic temperatures.—

| G26 | | Approach the test bench | |

Watch out for possible oxygen deficiency in the atmosphere.—

Do not touch any part of the system without cryogenic compatible gloves—

G27		Turn off the cameras	
G28		Read out He cylinder pressure and ask CP to note this pressure.	
G29		Close the He cylinder	
G30		Ask CP to open PV for 5 seconds to depressurize the pressurization line	
G31		Return to CP	
G32		Ask CP to stop data recording	
G33		Ask CP to "Stop all loops"	
G34		Ask CP to start retrieving test data from the cRIO and to back-up this data on USB	

| G35 | | Discuss options for the rest of the test day:
• Refill the tank and do another test (max 3 fills and empties): Fill the dewar again and restart from part E: Run tank filling.
• Stop for the day and pack up: Continue with the next phase. | |

System State:
- The system is depressurized except for the valve actuation lines
- The run tank is empty from LN2 except for maybe small amounts in the fill line
- All valves are now unpowered (MV and BV are open, FV and PV are closed)
- The tank system is still at cryogenic temperatures: Do not touch exposed metal surfaces on the tank or feed system.

ID	Check	Description	Comments
H - Packing up			
H1		Close the small N2 cylinder	
H2		Ask CP to cycle the BV to depressurize the actuation lines	
H3		The area is now secured. Everyone can approach the test bench	
Do not touch exposed metal surfaces on the tank or feed system without cryogenic compatible gloves.—			
H4		Assess system temperature and associated risks during clean-up	
H5		Put plastic cap back on fill valve connection	
H6		Put plastic cap back on pressure relief valve	
H7		Back up test data from LABView	
H8		Clean-up and pack everything back in.	
H9		Transport back to lab	
H10		After sufficient time for system temperature to normalize: put tape back on BV and MV exhausts.	
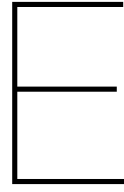
E Data processing

E.1. Statistical coefficients

For statistical analysis a number of coefficients are used within the report to indicate the accuracy of a measurement or the accuracy of a fit. This section gives a quick overview of the definitions used. In the following equations n is the number of samples, y_i is the i-th value from the dataset under analysis, and f_i is the value resulting from the fitted function for the dataset. For standard error of estimate, m is the number of parameters that are fitted to the data for the fitting function under consideration (i.e. for linear fits $m = 2$).

$$\text{Average:} \qquad \bar{y} = \frac{1}{n} \sum_i^n y_i \tag{E.1}$$

$$\text{Standard error:} \qquad \sigma = \sqrt{\frac{1}{n-1} \sum_i^n (y_i - f_i)^2} \tag{E.2}$$

$$\text{Standard error of the mean:} \qquad \sigma_{\bar{y}} = \frac{\sigma}{\sqrt{n}} \tag{E.3}$$

$$\text{R}^2 \text{:} \qquad R^2 = 1 - \frac{\sum_i^n (y_i - f_i)^2}{\sum_i^n (y_i - \bar{y})^2} \tag{E.4}$$

$$\text{Relative Standard Error[65]:} \qquad RSE = \sqrt{\frac{1}{n-m} \sum_i^n \left(\frac{y_i}{f_i} - 1 \right)^2} \tag{E.5}$$

Uncertainties are in general calculated via the methods described in JCGM 100:2008 [38].

E.2. Moving average filter

Moving average filters applied on the data are implemented in Python code by means of the algorithm below. The window size supplied to the function should be an odd number. The input data is mirrored at the start and end of the data set to reduce distortion of the filtered data at the edges. The basic algorithm (excluding the mirroring) has been reproduced from the book "Digital Signal Processing"[55].

```python
# Import packages
import numpy as np

# Moving average filter function definition
def movingAverageFilt(data, windowSize):
```

```
6         """Applies a moving average filter with the given window size over
              the given data. windowSize should be an odd, positive, integer
              number. Data can be a python list type or a numpy array."""
7
8         # Compute half-window size
9         p = (windowSize - 1)/2
10
11        # Convert data to list type
12        data = list(data)
13
14        # Mirror data before start and after end of data
15        dataExtended = data[p:0:-1] + data + data[-2:-p-2:-1]
16
17        # Initialize the filtered data array
18        avgFilt = np.zeros(len(data))
19        avgFilt[0] = sum(dataExtended[0:windowSize])
20
21        # Loop through the data
22        for i in np.arange(1,len(data)):
23            avgFilt[i] = avgFilt[i-1] + dataExtended[i+windowSize-1] -
                  dataExtended[i-1]
24
25        # Divide by windowSize and return filtered value
26        return avgFilt/windowSize
```

E.3. Thermocouple data processing

The thermocouple data output by the NI9213 module is in volts. It outputs 16 channels (numbered 0 to 15) for the 16 thermocouples, plus an autozero channel and a cold junction compensation (CJC) channel. To process the data to get temperature values, a number of steps need to be taken for each data sample.[1]

First the resistance of the internal thermistor that is in the NI9213 needs to be computed. This is done via equation E.6. In this equation U_{CJC} is the voltage output of the sample. The values of the various constants are specified by National Instruments.

$$R_t = \frac{10000 \cdot U_{CJC} \cdot 32}{2.5 - U_{CJC} \cdot 32} \tag{E.6}$$

Using this resistance the CJC temperature (in degree Celsius) can be computed via equation E.7. The constants in this equation are taken from the NI provided LabView code

$$T_{CJC} = \frac{1}{A + B \ln R_t + C \left(\ln R_t\right)^3} - 273.15 - D \quad \text{where:} \begin{cases} A = 1.2873851 \cdot 10^{-3} \\ B = 2.3575235 \cdot 10^{-4} \\ C = 9.497806 \cdot 10^{-8} \\ D = 1 \end{cases} \tag{E.7}$$

This temperature is taken as the CJC temperature which is applied uniformly over all thermocouple channels. It is thus assumed that all terminals of the NI9213 are at the same temperature. From this temperature the associated voltage generated by the cold-junction is calculated. This is done via the conversion values specified in NIST Monograph 175 on thermocouples[19]. Temperature to voltage conversion for T-type thermocouples is done by equation E.8 and for K-type thermocouples via equation E.9. The voltage is calculated in millivolt and the temperature needs to be given in degree Celsius. The values for the coefficients are specified in table E.1 for T-type thermocouples and in table E.2 for K-type thermocouples.

---

[1]See the specifications of National Instruments on `http://zone.ni.com/reference/en-XX/help/370984R-01/criodevicehelp/9213_converting/`.

$$U = c_0 + c_1 T + c_2 T^2 + c_3 T^3 + \ldots + c_n T^n \tag{E.8}$$

$$U = c_0 + c_1 T + c_2 T^2 + c_3 T^3 + \ldots + c_n T^n + a_0 e^{a_1 (T - a_2)^2} \tag{E.9}$$

The thermocouple output voltage (in volts) is now added to this CJC voltage (in millivolts), and the NI9213 autozero voltage (in volts) is subtracted from this.

$$U[\text{mV}] = U_{CJC} + 10^3 \cdot (U_{TC} - U_{autozero}) \tag{E.10}$$

Then as final step this voltage is converted to a temperature. Again using the NIST Monograph 175 specifications[19]. The conversion is done via equation E.11. The coefficients for this equation are given in table E.3 for T-type thermocouples and in table E.4 for K-type thermocouples.

$$T_{TC} = c_0 + c_1 U + c_2 U^2 + c_3 U^3 + \ldots + c_n U^n \tag{E.11}$$

Table E.1: NIST temperature to voltage conversion values for T-type thermocouples using equation E.8.[19]

Temperature range:	-270°C to 0°C	0°C to 400°C
$c_0 =$	0.0	0.0
$c_1 =$	$3.874\,810\,636\,4 \times 10^{-2}$	$3.874\,810\,636\,4 \times 10^{-2}$
$c_2 =$	$4.419\,443\,434\,7 \times 10^{-5}$	$3.329\,222\,788\,0 \times 10^{-5}$
$c_3 =$	$1.184\,432\,310\,5 \times 10^{-7}$	$2.061\,824\,340\,4 \times 10^{-7}$
$c_4 =$	$2.003\,297\,355\,4 \times 10^{-8}$	$-2.188\,225\,684\,6 \times 10^{-9}$
$c_5 =$	$9.013\,801\,955\,9 \times 10^{-10}$	$1.099\,688\,092\,8 \times 10^{-11}$
$c_6 =$	$2.265\,115\,659\,3 \times 10^{-11}$	$-3.081\,575\,877\,2 \times 10^{-14}$
$c_7 =$	$3.607\,115\,420\,5 \times 10^{-13}$	$4.547\,913\,529\,0 \times 10^{-17}$
$c_8 =$	$3.849\,393\,988\,3 \times 10^{-15}$	$-2.751\,290\,167\,3 \times 10^{-20}$
$c_9 =$	$2.821\,352\,192\,5 \times 10^{-17}$	…
$c_{10} =$	$1.425\,159\,477\,9 \times 10^{-19}$	…
$c_{11} =$	$4.876\,866\,228\,6 \times 10^{-22}$	…
$c_{12} =$	$1.079\,553\,927\,0 \times 10^{-24}$	…
$c_{13} =$	$1.394\,502\,706\,2 \times 10^{-27}$	…
$c_{14} =$	$7.979\,515\,392\,7 \times 10^{-31}$	…

Table E.2: NIST temperature to voltage conversion values for K-type thermocouples using equation E.9.[19]

Temperature range:	-270°C to 0°C	0°C to 1372°C
$c_0 =$	0.0	$-1.760\,041\,368\,6 \times 10^{-2}$
$c_1 =$	$3.945\,012\,802\,5 \times 10^{-2}$	$3.892\,120\,497\,5 \times 10^{-2}$
$c_2 =$	$2.362\,237\,359\,8 \times 10^{-5}$	$1.855\,877\,003\,2 \times 10^{-5}$
$c_3 =$	$-3.285\,890\,678\,4 \times 10^{-7}$	$-9.945\,759\,287\,4 \times 10^{-8}$
$c_4 =$	$-4.990\,482\,877\,7 \times 10^{-9}$	$3.184\,094\,571\,9 \times 10^{-10}$
$c_5 =$	$-6.750\,905\,917\,3 \times 10^{-11}$	$-5.607\,284\,488\,9 \times 10^{-13}$
$c_6 =$	$-5.741\,032\,742\,8 \times 10^{-13}$	$5.607\,505\,905\,9 \times 10^{-16}$
$c_7 =$	$-3.108\,887\,289\,4 \times 10^{-15}$	$-3.202\,072\,000\,3 \times 10^{-19}$
$c_8 =$	$-1.045\,160\,936\,5 \times 10^{-17}$	$9.715\,114\,715\,2 \times 10^{-23}$
$c_9 =$	$-1.988\,926\,687\,8 \times 10^{-20}$	$-1.210\,472\,127\,5 \times 10^{-26}$
$c_{10} =$	$-1.632\,269\,748\,6 \times 10^{-23}$	…
$a_0 =$	…	$1.185\,976\,000\,0 \times 10^{-1}$
$a_1 =$	…	$-1.183\,432\,000\,0 \times 10^{-4}$
$a_2 =$	…	$1.269\,686\,000\,0 \times 10^{2}$

Table E.3: NIST voltage to temperature conversion values for T-type thermocouples using equation E.11.[19]

	Temperature range:	-200°C to 0°C		0°C to 400°C	
	Voltage range:	-5.603mV to 0.0mV		0.0mV to 20.872mV	
$c_0 =$		0.0		0.0	
$c_1 =$		2.594 919 2	$\times 10^1$	2.592 800	$\times 10^1$
$c_2 =$		$-2.131 696 7$	$\times 10^{-1}$	$-7.602 961$	$\times 10^{-1}$
$c_3 =$		7.901 869 2	$\times 10^{-1}$	4.637 791	$\times 10^{-2}$
$c_4 =$		4.252 777 7	$\times 10^{-1}$	$-2.165 394$	$\times 10^{-3}$
$c_5 =$		1.330 447 3	$\times 10^{-1}$	6.048 144	$\times 10^{-5}$
$c_6 =$		2.024 144 6	$\times 10^{-2}$	$-7.293 422$	$\times 10^{-7}$
$c_7 =$		1.266 817 1	$\times 10^{-3}$	$\ldots$	

Table E.4: NIST voltage to temperature conversion values for K-type thermocouples using equation E.11.[19]

	Temperature range:	-200°C to 0°C		0°C to 400°C	
	Voltage range:	-5.891mV to 0.0mV		0.0mV to 20.644mV	
$c_0 =$		0.0		0.0	
$c_1 =$		2.517 346 2	$\times 10^1$	2.508 355	$\times 10^1$
$c_2 =$		$-1.166 287 8$		7.860 106	$\times 10^{-2}$
$c_3 =$		$-1.083 363 8$		$-2.503 131$	$\times 10^{-1}$
$c_4 =$		$-8.977 354 0$	$\times 10^{-1}$	8.315 270	$\times 10^{-2}$
$c_5 =$		$-3.734 237 7$	$\times 10^{-1}$	$-1.228 034$	$\times 10^{-2}$
$c_6 =$		$-8.663 264 3$	$\times 10^{-2}$	9.804 036	$\times 10^{-4}$
$c_7 =$		$-1.045 059 8$	$\times 10^{-2}$	$-4.413 030$	$\times 10^{-5}$
$c_8 =$		$-5.192 057 7$	$\times 10^{-4}$	1.057 734	$\times 10^{-6}$
$c_9 =$		$\ldots$		$-1.052 755$	$\times 10^{-8}$

E.4. System state parameter

The system state of the test setup is recorded by the LabView program. The program records the state of various valves and software variables. A total of 12 variables are recorded. All but one of these variables are boolean values and can thus be represented by one bit. The only recorded variable that is not a boolean is the "System state" parameter that can have one of five values, and can thus be represented using 3 bits. A total of 14 bits is thus required to record the state of all variables. The LabView program takes the values of all boolean variables as bits and concatenates these into one binary number. Added to these are the 3 bits for the "System state" parameter. The number is padded with zeros to form a 16 bit unsigned integer. This integer is stored in the data file. Post processing of the data splits the integer back into its individual bits and extracts from this the values of the different variables. The list of which bit in the number corresponds to which variable is given in table E.5.

The boolean values for the valves represent not the state of the valve, but whether or not the valve is powered by the cRIO. I.e. a value of 0 means the valve is unpowered, a value of 1 means the valve is powered. Thus for a normally opened valve a 0 means the valve is opened, a 1 means the valve is closed.

E.5. Setting all time parameters

All sensor outputs need to have an associated timestamp with them to make logical sense of the data and to compare data coming from different sensors. All time parameters as presented in the report are derived from the counters associated with each variable set and the measurement frequency specified for the sensors. The measurement frequencies are specified in the LabView code by specifying the number of ticks between measurements of the 40MHz onboard clock in the cRIO.

The thermocouple data, pressure sensor data, and load cell data all have their own counter which is generated on the cRIO FPGA. The system state parameter is sampled by the cRIO RT-control loop, but has the load cell counter added to each of its measurements. The capacitive sensor is sampled by the FDC1004 chip and an Arduino. The Arduino adds a measurement counter to each measurement,

Table E.5: System state variable bit breakdown. The system state is represented by 3 bits. These three bits combined can take on values 0 through 4 (decimal), which represent: 0=Manual, 1=Standby, 2=Pressurization, 3=Expulsion, 4=Depressurization.

Bit #	Variable
(LSB) 0	Fill valve (relay 5)
1	Main valve (relay 1)
2	Bleed valve (relay 3)
3	Pressurization valve (relay 4)
4	Arm switch (0=safe, 1=armed)
5	Record data
6	Recording speed high
7	Depressurized
8	Emergency Shutdown
9	Automated Sequence Enabled
10	Automated Sequence Running
11 12 13	System State (3 bit binary number. Bit #11 is the LSB. Bit #13 is the MSB. See caption.)
14	*Not used*
(MSB) 15	*Not used*

and subsequently the cRIO adds a copy of the load cell counter to each capacitance measurement again when the cRIO processes it. (See section E.5.2).

The measurement frequency can be set to either a "low-speed" (LS) or a "high-speed" (HS) recording mode. Generally all preparation during tests is done at low-speed recording, while pressurization and expulsion is done at high-speed. The recording speed is switched to high around 60 s before the start of expulsion and this switch is recorded in the system state parameter. The time parameter of the system state is used to specify the start and end times of the high speed recording. These start and end times are then used to adjust the time-step in generating the timestamps for the sensor data. The capacitive sensor does not have different measurement frequencies between low-speed and high-speed. See table E.6 for an overview of all measurement frequencies during the radial and axial injection tests.

Table E.6: Measurement frequencies for low and high speed recording for all sensors. (* = See section E.5.2)

Sensor type	Low-speed		High-speed	
	#ticks [10^6]	f [Hz]	#ticks [10^6]	f [Hz]
Load cell	8	5	0.8	50
Pressure sensor	8	5	0.8	50
Thermocouples	40	1	10	4
System state	8	5	0.8	50
Capacitive sensor	-	20.046*	-	20.046*

E.5.1. Setting t=0s
For all tests a t=0s time needs to be defined to facilitate comparison of the different sensor outputs. For all radial and axial injection tests the t=0s time has been defined by the moment that the pressurization valve is given the signal to open, as recorded in the system state parameter. This event occurs a certain amount of time Δt_{start} after start of the data acquisition. This Δt_{start} is subtracted from all time variables. Table E.7 gives an overview of all Δt_{start} variables and total measurement times for all radial and axial injection tests.

E.5.2. Capacitive data measurement frequency
During the analysis of the axial injection test data it was discovered that the measurement frequency set into the Arduino, which does the sampling, did not match the observed measurement frequency. The

Table E.7: Total measurement time and time between start of measurements and opening of the pressurization valve for pressurization and explusion (t=0s).

Test	Δt_{start} [s]	Total meas. time [s]
rad1	9979.64	10455.80
rad2	2302.86	2957.58
rad3	2306.24	3019.20
ax1	10039.16	10758.04
ax2	2744.44	3334.20
ax3	2045.14	2613.64
vtx	11864.82	13189.58

corrected measurement frequencies, as used in the report, are specified in table E.8. These frequencies were derived with the assumption that the cRIO performs measurements exactly on the frequency that is specified. The measurement frequencies given in the table are gotten by comparing the "CapSampleCounter" and "LC_counter" values over the timespan from $\approx$10s after the start of measurements till t=-180s. The frequency for the vortex tube test was not determined from the measurements but taken as average of the observed frequencies during the axial tests.

Table E.8: Set vs observed measurement frequencies for the capacitive sensor.

Test	Set frequency [Hz]	Observed frequency [Hz]	Observed dt [s]
ax1	20.0	20.0454	0.0498868
ax2	"	20.0467	0.0498836
ax3	"	20.0476	0.0498814
vtx	"	20.047	0.049882

E.6. Sensor calibration

For the load cells and pressure sensors calibration is needed to correlate the output voltage of the sensors to a sensible measurement value in kilogram or bar respectively.

Pressure sensors

The pressure sensors were calibrated by means of a pressure gauge and a compressor at pressure values between 1 bar and 6 bar (absolute). The values are given in table E.9. Uncertainty in the values due to measurement error in the electrical system is <0.15 bar. Uncertainty due to the inaccuracies in the pressure dial in the compressor and read-out of the dial values is estimated to be <0.5 bar.

Table E.9 gives a value for b as the atmospheric pressure offset during calibration. The pressure offset used for the data of the tests is determined per test by taking the average value of the pressure sensor read-out from t=200s till the end of measurements. During this time both sensors see atmospheric pressure (assumed to be 1.01 bar). Uncertainty in the atmospheric pressure (<0.05 bar) is thus added on top of the total uncertainty in pressure values. The total value of b as determined by the data is given for each test in table E.10.

Load cells

The tank load cell (LC1) is a 500lb (227kg) minature inline load cell from Futek, type number LCM300. The pressurant cylinder load cell (LC2) is a Scaime ZFA s-beam load cell rated to a maximum of 100 kg. The load cells have been calibrated when assembled within the test setup.

A total of three test masses plus the unloaded case were used for the calibration curves. The uncertainty in the masses of the test masses is estimated to be <0.01 kg. Uncertainty in the electronic measurement is <0.09 kg for LC1 and <0.045 kg for LC2. The calibration values and the resulting linear calibration curves are given in table E.11.

Just like the pressure sensors, the load cells are zero-ed per test to calibrate for measurement data. This is only done for LC1, as for LC2 only the relative difference between start and end of pressurization and expulsion is needed. The total offset values for LC1 are given in table E.12. These values are

Table E.9: Calibration values used for the pressure sensors. The inaccuracy in the electrical measurements (incl. noise) is on average <0.15 bar. Inaccuracies in the reference pressure dial and readout of this dial is estimated to be <0.5 bar.

P [bar]	U [mV]
1	4.00
2	4.13
3	4.31
4	4.48
5	4.64
6	4.75

Linear fit: $P = aU + b$	
a	6388 [bar/V]
b	-24.51 [bar]
R^2	0.995
RSE	0.052

Table E.10: Total atmospheric pressure offset values as determined for each pressure sensor for each test. The values are determined by averaging the pressure sensor output over the range t=200s till end of measurements. Standard deviations in the average are <0.1 bar for PS1 and <0.12 bar for PS2.

Test	PS1 (tank)	PS2 (He line)
rad1	-24.60	-24.26
rad2	-24.57	-24.26
rad3	-24.57	-24.29
ax1	-24.59	-24.28
ax2	-24.59	-24.29
ax3	-24.58	-24.29
vtx	-23.68	-23.98

obtained by averaging the LC value of the unloaded case in the measurement data. The times over which is averaged are indicated in the table as well.

Table E.11: Calibration values used for the load cells. The inaccuracy in the electrical measurements (incl. noise) is on average <0.09 kg for LC1 and <0.045 kg for LC2. Inaccuracy in the test masses is estimated to be <0.01 kg

M [kg]	U_{LC1} [mV]	U_{LC2} [mV]
0.00	-0.4597	-0.0321
1.34	-0.4713	-0.0722
2.53	-0.4819	-0.1077
14.06	-0.5854	-0.4526

Linear fit: $M = aU + b$		
a	-111646 [kg/V]	-33430 [kg/V]
b	-51.293 [kg]	-1.072 [kg]
R^2	1.0	1.0
RSE	0.011	0.00

Table E.12: Total load cell offset values as determined for LC1 for each test. The values are determined by averaging the load cell output over the indicated time range. Standard deviations in the average are <0.1 kg. The zero position for the vortex tube test was determined very much at the start of the test because no zero value was present near the end of the data set.

Test	Offset [kg]	t_{start} [s]	t_{end} [s]
rad1	-49.95	350	476 (=end)
rad2	-50.04	350	620
rad3	-50.02	350	620
ax1	-50.02	550	719 (=end)
ax2	-49.98	350	590 (=end)
ax3	-50.01	350	569 (=end)
vtx	-54.51	-9800	-8500

E.7. Data glitches

The data of the various tests contain a number of data "glitches" where the data shows unexpected behaviour that is due to errors in the measurement setup (e.g. software glitches or faulty electrical connections) and which do not relate to a physical process in the test setup. This section lists all the data glitches that were noted during the data analysis, and how they were corrected for (if they were corrected).

E.7.1. First exposure test (02-12-2016)

Capacitive sensor

The capacitive sensor dropped to a low, fairly noise-free level from around t=-1100s till t=-100s. The level is not a clipped minimum value in the measurement range. It is slowly increasing over the timespan that it occurs. Why this glitch occurs cannot be determined.

E.7.2. Radial injection tests (16-01-2017)

Capacitive sensor (all tests)
The capacitive sensor was not functioning properly during the tests as the measurement range for the capacitive sensor board was not configured for the proper range of sensor version 2. The data is clipped at a maximum value of 24058pF for most of the time. At the start of the first test the value is fluctuating around 2850pF. During this time the sensor connector was plugged in the wrong way round and this measurement is thus the measurement of capacitance of the central rod of sensor version 2 to the tank wall, which is fairly constant. This measurement is of no value.

Thermocouples (tests 1 and 2)
Thermocouple TC2 jumps to minimum and maximum values various times. This is probably to a faulty connection in the cable that disconnected at random times. The jumps occur at test 1 about 10 minutes before start of pressurization, and during the expulsion phase. They also occure at test 2 at the start of filling.

Load cell (tests 1 and 3)
The pressurant mass data is overall very noisy and jumps to maxima and minima often, likely due to a faulty connection in the cable. This connection was repaired for the axial injection tests on the following day. The noise is due to vibrations in the test bench.

System states (test 1)
The data recording variable has the value "false" from the start of measurements at t=-9980s till t=-9766seconds and between t=-8725s and t=-8573s. This is a glitch because this variable can logically not be false, because if it would be, the LabView VI should not be recording data. Why this value does however show true is unknown and is likely a glitch in LabView or the cRIO itself.

E.7.3. Axial injection tests (17-01-2017)

Capacitive sensor (all tests)
During this test capacitive sensor version 1 was used. Unfortunately the range was also not fully properly set for this version as it is clipped again at the maximum value of 24058pF.

Thermocouples (all tests)
Thermocouple TC14 loses connection quite often and for prolonged periods of time from the start of filling (t≈-8140s) till approximately halfway through filling (t≈-7040s). This is also likely due to a faulty physical connection.

System states (test 1)
The data recording variable has the value "false" from the start of measurements at t=-10039s till t=-9899seconds and between t=-8416s and t=-8268s. See section E.7.2.

Pressure sensors (test 2)
The pressure sensor data shows a glitch in the counter values at indices 19553, 19554, 19555, 19556, and 19557. Before and after these indices the counter progresses linearly, incrementing with one for each subsequent value. However at these indices the counter shows randomly varying larger numbers. These affected five counter values were changed from their random values of [59403., 59700., 58468., 59744., 58600.] to [20067., 20068., 20069., 20070., 20071.]. This correction changes the counter back to a linear, monotonically increasing sequence, with the exception that the value 20072 is not present in the sequence. This is the only dropped data point in the whole measurement sequence.

Just like the counter, the feed line pressure sensor (PS2) has a similar glitch at exactly these 5 points. The measurement values suddenly drop with around 44.6bar. The values keep on varyingly randomly around their average value, so it is likely no broken physical connection. The data points were removed and replaced by a linear interpolation between the data points at index 19552 and index 19558. The values at these data points are 23.8263bar and 23.843bar respectively. The timespan these five measurement points represent is 0.1s. All variations that could have occurred within this time are expected to be well within measurement noise. No glitch is observed in the data of the tank pressure sensor (PS1)

Why this glitch occurred is not clear. It is most likely some artefact occurring within LabView, the cRIO, or the pressure sensor module of the cRIO.

E.7.4. Vortex injection tests (21-02-2017)

Thermocouples

Thermocouples TC3, TC4 and TC10 show a few points in time where the value jumps to its upper bound during the filling and cool-down.

System states

Just like in the other tests, the bit indicating data recording is at "false" at the start of the measurements and switches a few more times before settling at the logical value of True around t=-140min. It remains at that value for the rest of the recording.

Load cell

The load cell measurements were in general very noise due to the chatter of the fill valve. The signal however also showed a number of glitches, specifically around the t=-45min mark. During pressurization, from approximately t=+42s till t=+60s the signal unexpectedly shows a high increase in noise and a few glitches around t=60s. Where this comes from is not known. It does not seem to have a physical explanation. It might be an electrical error.

Pressure sensor

The counter value of the pressure sensors has a number of strange jumps after approximately t=+400s. This seems to occure at the switch from high-speed recording back to low-speed recording. As it occurred well beyond the test time it was decided to not investigate further.
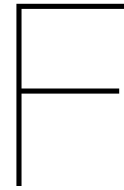
Man-hours spent on production

Table F.1 gives an approximate overview of the amount of man-hours spent on preparing the test setup. This includes machining, processing and assembly. It does not include design work done on parts.

Table F.1: Overview of the approximate amount of man-hours spent on construction of the test setup.

Description	Hours spent
Test bench: Cutting and machining of aluminium profiles and assembly	25
Tank construction: Machining tank wall and bulkheads, fixing seals, assembly.	90
Diffuser production	10
Tank insulation	10
Gravel box	10
Sensor adapter development: Development of potting equipment. Glue tests. Construction of test samples. Construction of test adapters.	40
Feed system: part acquisition and processing	75
cRIO and sensor hardware development: Hardware modifications on the cRIO. Production of capacitive sensor.	80
Measurement and actuation: LabView Software development. Capacitive sensor software development	100
Subsystem testing: Adapter pressure tests. Tank air pressure tests. Tank water pressure test.	20
System assembly: Final assembly of the whole system.	20
Vortex tube: Production and assembly of parts	15
Total	495

G

EUCASS 2017 abstract

The research conducted for this master thesis research has been summarized and rewritten for the 7th European Conference for Aeronautics and Space Sciences (EUCASS). The paper is titled "Pressurization system for a cryogenic propellant tank in a pressure-fed high-altitude rocket" and has been submitted for the symposium 'Propulsion Physics for Air-Breathing and Rocket Engines'. The co-author is Ir. B.T.C. Zandbergen. The abstract has been approved by the organization, and the paper has been written and submitted to the organization. The abstract that was originally submitted for the paper has been reproduced below here.

Pressurization system for a cryogenic propellant tank in a pressure fed high-altitude rocket
Rob Hermsen (*r.j.g.hermsen@student.tudelft.nl*), and Barry Zandbergen
(*b.t.c.zandbergen@tudelft.nl*) *Faculty of Aerospace Engineering, Delft University of Technology, Kluyverweg 1, 2629 HS, Delft, the Netherlands*

This paper describes the practical investigation of a simple, low-cost pressurization system for a small cryogenic propellant tank. The pressurization system is developed for high-altitude rocket applications by the student society Delft Aerospace Rocket Engineering (DARE) of Delft University of Technology. DARE has the aim to be the first student society in the world to launch a rocket into space with a self-designed rocket engine. For the next generation of DARE high altitude rockets, DARE initiated the cryogenic project to investigate the usage of cryogenic propellants, most specifically liquid oxygen[1]. Development is focused on the usage of a pressure fed system where high pressure helium is used to expel the liquid oxygen from the tank.

The goal of the present investigation is to determine the amount of pressurant gas required for pressurized expulsion of the propellant, and to investigate the effects of different types of pressurant injectors. This is done by creating and evaluating 1D simulations of the system and validating these simulations with a test setup. Cryogenic propellant pressurization and the effect of different pressurant injectors has been investigated in the past[2]. However these investigations often focused on low pressure (P<10bar), high volume (V>200L) tanks, while high pressure, low volume tanks are of interest in the investigation. Because of the effects of higher pressures and scale changes on heat transfer it is hypothesized that axial injection of the pressurant will be more beneficial for pressurant gas consumption in high-pressure, low-volume tanks compared to the commonly used radial injection method. Furthermore it is hypothesized that the usage of pressurant gas can be reduced even further by splitting the pressurant gas stream by means of a vortex tube (or "Hilsch tube"[3]) into a cold and a warm gas stream.

---

[1] Jeroen Wink, Ralph Huijsman, Luka Denies, Robert Werner, Rob Hermsen, Adriaan Schutte, Angelo Cervone and Barry Zandbergen. *Cryogenic Rocket Engine Developments at Delft Aerospace Rocket Engineering*, 2016. SP2016-3124644
[2] DeWitt, Stochl and Johnson. *Experimental evaluation of pressurant gas injectors during the pressurized discharge of liquid hydrogen*, 1966. NASA Lewis Research Center
[3] Huzel and Huang. *Design of liquid propellant rocket engines, (section 8.7)*, 1992.

192 G. EUCASS 2017 abstract

The hypotheses are tested by using the three different types of injection (radial, axial and vortex) on a hardware test setup. The hardware test setup that has been constructed for this investigation uses a 30 liter tank containing liquid nitrogen, pressurized with helium to 25 bar. During the test, pressure, mass and fill level are measured versus time. Also thermocouples at 15 different locations within the tank and out on the tank wall determine temperature distribution vs. time. These thermocouple readings allow a clear insight in the temperature distribution within the ullage gas. The measurement setup and the test results will be presented and analyzed in the paper and inferences will be drawn on the amount of pressurant required, the effect of tank size and the effect of different types of injectors. The test data will be used as basis to better understand the thermodynamic processes in the tank ullage volume, which can be used to improve 1D simulations of the process. The data will be used as validation data for these 1D simulations models. The understanding of the thermodynamic process gained from the data combined with the simulation efforts will result in sizing rules applicable to the pressurization system for small, high-pressure, cryogenic propellant tanks.